Title
The Aerodynamics of Deforming Wings at Low Reynolds Number

Author
Medina, Albert

Publication Date
2013

Peer reviewed|Thesis/dissertation

University of California
Los Angeles

The Aerodynamics of Deforming Wings at Low Reynolds Number

A dissertation submitted in partial satisfaction
of the requirements for the degree
Doctor of Philosophy in Mechanical Engineering

by

Albert Medina

2013

Abstract of the Dissertation

The Aerodynamics of Deforming Wings at Low Reynolds Number

by

Albert Medina

Doctor of Philosophy in Mechanical Engineering

University of California, Los Angeles, 2013

Professor Jeff D. Eldredge, Chair

Flapping flight has gained much attention in the past decade driven by the desire to understand capabilities observed in nature and the desire to develop agile small-scale aerial vehicles. Advancing our current understanding of unsteady aerodynamics is an essential component in the development of micro-air vehicles (MAV) intended to utilize flight mechanics akin to insect flight. Thus the efforts undertaken that of bio-mimicry. The complexities of insect wing motion are dissected and simplified to more tractable problems to elucidate the fundamentals of unsteady aerodynamics in biologically inspired kinematics. The MAV's fruition would satisfy long established needs in both the military and civilian sectors. Although recent studies have provided great insight into the lift generating mechanisms of flapping wings the deflection response of such wings remains poorly understood. This dissertation numerically and experimentally investigates the aerodynamic performance of passively and actively deflected wings in hover and rotary kinematics. Flexibility is distilled to discrete lines of flexion which acknowledging major flexion lines in insect wings to be the primary avenue for deformation. Of primary concern is the development of the leading-edge vortex (LEV), a high circulation region of low pressure above the wing to which much of the wing's lift generation is attributed. Two-dimensional simulations of wings with chord-wise flexibility in a freestream reveal a lift generating mechanism unavailable to rigid wings with origins in vortical symmetry breaking. The inclusion of flexibility in translating wings accelerated

from rest revealed the formation time of the initial LEV was very weakly dependent on the flexible stiffness of the wing, maintaining a universal time scale of four to five chords of travel before shedding. The frequency of oscillatory shedding of the leading and trailing-edge vortices that develops after the initial vortex shedding was shown to be responsive to flexibility satisfying an inverse proportionality to stiffness. In hover, an effective pitch angle can be defined in a flexible wing that accounts for deflection which shifts results toward trend lines of rigid wings. Three-dimensional simulations examining the effects of two distinct deformation modes undergoing prescribed deformation associated with root and tip deflection demonstrated a greater aerodynamic response to tip deflection in hover. Efficiency gains in flexion wings over rigid wing counterpart were shown to be dependent on Reynolds number with efficiency in both modes increasing with increased Reynolds number. Additionally, while the leading-edge vortex axis proved insensitive to deformation, the shape and orientation of the LEV core is modified. Experiments on three-dimensional dynamically-scaled fruit fly wings with passive deformation operating in the bursting limit Reynolds number regime revealed enhanced leading-edge vortex bursting with tip deflection promoting greater LEV core flow deceleration in stroke. Experimental studies on rotary wings highlights a universal formation time of the leading-edge vortex independent of Reynolds number, acceleration profile and aspect ratio. Efforts to replicate LEV bursting phenomena of higher aspect ratio wings in a unity aspect ratio wing such that LEV growth is no limited by span but by the LEV traversing the chord revealed a flow regime of oscillatory lift generation reminiscent of behavior exhibited in translating wings that also maintains magnitude peak to peak.

The dissertation of Albert Medina is approved.

Xiaolin Zhong

Pirouz Kavehpour

Chris Anderson

Jeff D. Eldredge, Committee Chair

University of California, Los Angeles

2013

To my mother...

Table of Contents

List of Figures

List of Tables

Acknowledgments

This dissertation would not have possible without the support and guidance of my advisor, Professor Jeff D. Eldredge. Professor Eldredge supplied wisdom and freedom to pursue a range of research endeavors. Most importantly he gave me the opportunity to perform this work and for that I am greatly indebted. I must also thank the members of my committee: Professor Mark Frye of the Behavioral Algorithms and Circuits laboratory, Professor Pirouz Kavehpour of the Complex Fluids and Interfacial Physics laboratory, and Professor Xiaolin Zhong of the Hypersonics and Computational Aerodynamics laboratory. I owe a great debt of gratitude to Professor Haecheon Choi of Seoul National University and Professor Anya Jones of the University of Maryland for making their resources and facilities available. I am thankful to my friends and colleagues at UCLA who have been nothing but supportive. I would like to thank my sister, Maribel Salcido, my brothers, Jesus, Ruben and Daniel Medina for their everlasting love and support. And lastly, I would like to thank my mother for her unconditional love and support, for having the strength to fill the roles of mother and father, for the many life lessons, and for enduring her many struggles so that I would not have to.

Vita

2007	Bachelors of Science (Aerospace Engineering), University of California, Los Angeles.
2008	Masters of Science (Mechanical Engineering), University of California, Los Angeles.
2007-2008	Graduate Student Researcher, Fusion Laboratory, University of California, Los Angeles.
2008-2013	Graduate Student Researcher, Biolocomotion Laboratory, University of California, Los Angeles.
2008-2011	Teaching Assistant, University of California, Los Angeles.
2011-2012	Resident Scientist/Teacher, Emerson Middle School.
2007-2009	Instructor: CEED Engineering 87, University of California Los Angeles.
2007-2010,2012	Instructor: BREES, University of California Los Angeles.
2013	Reviewer: Journal of Fluids and Structures.
2013	Referee: Journal of Fluid Mechanics.

Publications

N. B. Morley, A. Medina, M. A. Abdou, Measurements of specific electrical contact between SiC and lead-lithium eutectic alloy, Fusion Science and Technology, 56: 195-200 (2009)

J. D. Eldredge, J. Toomey, A. Medina, On the roles of chord-wise flexibility in a flapping wing with hovering kinematics, Journal of Fluid Mechanics, 659: 94-115 (2010)

CHAPTER 1

Introduction

Flapping flight has gained much attention in the past decade. Nature has demonstrated the breadth of maneuverability achieved by flapping wing configurations. The necessity to better understand the force generating mechanisms has been been accelerated by the desire to construct micro air vehicles. Such vehicles could see applications in both military and civilian sectors. Military agencies see the potential for surveillance and reconnaissance, allowing soldiers to fly over enemy-occupied territory without putting personnel in harms way, survey a landscape such as a ridge to ensure safe passage from potential threats, and real time intel on the battlefield. All this would be accomplished discretely as the size of the micro air vehicle is rather small in comparison to conventional aircraft. In fact, estimates place the MAV comparable in size to a large insect, making the MAV extremely portable. Currently performing this role is the Small UAV (SUAV) which is a hand-launch unmanned aerial vehicle carried by infantrymen. However, despite its portability, the SUAV still posses a considerable task to transport with wing spans often in the rang of 0.8-1.6m. In the civilian sector, MAVs are a good candidate for air quality sampling, search and rescue missions and disaster management among others. Additionally, micro air vehicles are significantly cheaper to produce given the size and material needed to produce.

Currently in the works are rotary and flapping wing MAVs. The former utilize multiple rotors thrusting downward to maintain flight. Of interest in this dissertation is flapping flight at low Reynolds number ranging from 10^2 to 10^4, a regime in which insects have proven the best candidate. What makes this field particularly engaging is the departure from classical aerodynamics. According to classical theory "bumblebees cannot fly" [105]. Of course we

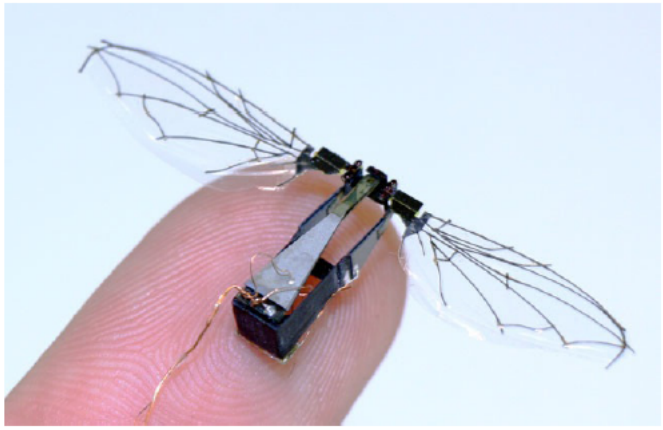

Figure 1.1: Harvard microrobotic fly [92].

know this to be false, but such a statement serves to demonstrate conventional aerodynamics are not suited for our particular application. Instead, flapping wings rely heavily on unsteady mechanisms and operate at considerably higher angles of attack, typically $\alpha > 30°$. In the classical sense, one would equate this to a loss of lift and increased drag, treating lift and drag as independent entities. However, as unsteady phenomena would have it, operating at higher angle of attack results in a lift inseparable from drag. The two are one in the same, manifestations of the same fluid mechanic phenomena: the pressure force acting normal to the wing [23]. This load distribution makes insects very adaptable to perturbations of the surroundings and highly maneuverable. We will designate lift as the component of the resultant pressure force that acts opposite to gravity.

It is not our desire to completely mimic an insect but to draw inspiration and a deeper understanding of the force generating mechanisms from. It is not clear if insect wings as we encounter them in nature are optimized for forward flight or hovering. That is to say a given set of wings may serve multiple purposes related to other aspects of survival. So although their primary purpose is flight their evolutionary path may have included broader criteria. This is not specific to the aerial creatures, even in aquatic settings we see pectoral fins used for the burial of fertilized eggs. Focus in our study will be primarily on hovering kinematics, wherein the body of the insect remains fixed in space, subjected to its own wake

in an otherwise stationary fluid. In a given stroke, the wing will have translated or heaved in one direction creating a wake, only to reverse direction and translate once again, resulting in the wing-wake interactions.

The wings we are interested in exhibit a degree of flexibility, portraying elastic deformation when loaded. Universal amongst the insect kingdom is a vein-membrane wing structure. The veins run from base to the tip, dispersing or fanning-out along the span. Along the leading-edge there exists a coalescence of veins resulting in a "spar" member to which the wing derives much of its stiffness. Additionally we see major flexion lines along which much of the wing deflection is designated to. Aside from muscles internal to the body at the base, there are no active muscular structures in the wing themselves. This results in passive deformations in flight, fluid-solid interactions in which the behavior of the fluid and that of the solid depend on one another. Naturally the question arises as to which degree does the fluid force determine the wing shape and vice versa.

1.1 Classical Lift

Before embarking on flapping wings, it may best serve the reader to begin with a short review of classical aerodynamics pertaining to lift and see how such theories are inapplicable for our purposes. Aircrafts operate in Reynolds number $O\left(10^6 - 10^7\right)$ and angle of attack $\alpha < 15^\circ$. The flow often remains laminar with a thin boundary layer, lending the airfoils to potential flow theory. The lift is given by the Kutta-Joukowski theorem under steady state conditions as:

$$L' = \rho \mathrm{U} \Gamma \tag{1.1}$$

where the prime denotes lift per unit span and Γ the circulation. This circulation arises from satisfying the Kutta condition: at the onset of motion the airfoil has two stagnation points, one point on the bottom face closer to the leading edge and one above closer to the trailing. Viscosity in the boundary layer effectively shifts the upper surface stagnation point to the trailing edge of the airfoil, ensuring the oncoming flow separated above and

(a) Start-up vortex formation (b) 3D vortex ring

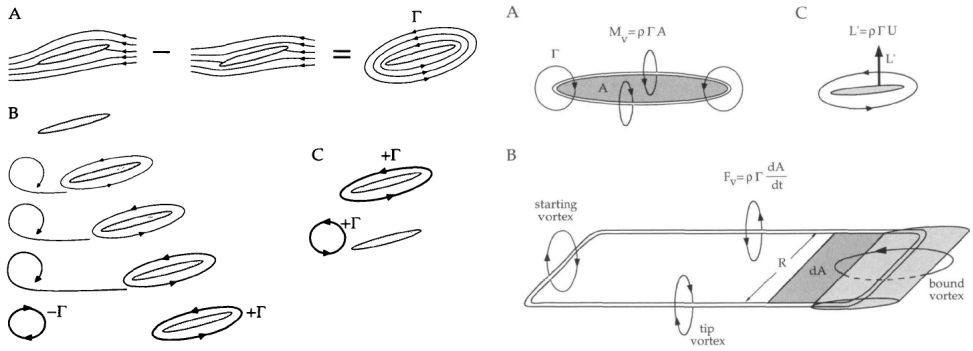

Figure 1.2: Steady-state theory lift [23].

below the airfoil meets back together with equal velocity in both direction and strength at the sharp trailing edge of the airfoil [23]. This action creates bound circulation on the airfoil and, accordingly to Kelvin's circulation theorem, also creates circulation of equal and opposite sign in the wake deemed the start-up vortex. In a three dimensional configuration this is best visualized as a circulation ring with the bound and start-up vortex attached via circulation produced by the tip of the wings. From equation (1.1) alone, it becomes clear lift is dependent only on bound circulation, independent of the wake. For an aircraft, a runway provides enough distance between the wing and the start-up shed vorticity which, according to potential theory, has an effect inversely proportional to distance, rendering the starting vortex inconsequential to the aircraft.

This is in stark contrast to flapping wing mechanics.

1.2 Flow Separation

Fluid flow separation is a phenomena in which flow detaches from a solid surface and does not reattach itself. The flow-dividing stream line, which separates flow above and below an airfoil, is met perpendicularly under the airfoil at a stagnation point near the leading-edge. Under the right circumstances, this streamline will detach from the above the wing from the solid surface, meaning the solid surface no longer acts as an isolated streamline. Rather, the dividing-streamline is now a mixture of the body surface and the newly formed wake. The

fluid in the wake takes on the form of eddies and vortices in a region significantly thickened adjacent to the wing. Prior to separation the flow traversed parallel to the surface from leading-edge to trailing-edge, now the flow is marked by pockets of flow reversal where the fluid has reversed direction. Such a phenomena is associated with loss of lift and increased drag particularly from pressure drag due to the pressure differential developed between the lower and upper surface of the wing. The onset of separation can be brought about by many factors such as an adverse pressure gradient and geometric aberrations.

1.3 Unsteady Mechanisms

Steady-state theory is insufficient in capturing the mechanisms employed by flapping wings. Under this theory it is not uncommon to find an insect is theoretically incapable of sustaining its own weight in flight. We know this to be false but it leaves open the question as to how insects are able to do so. The answer is in the use of unsteady fluid mechanics such as delayed stall, wake capture and added mass.

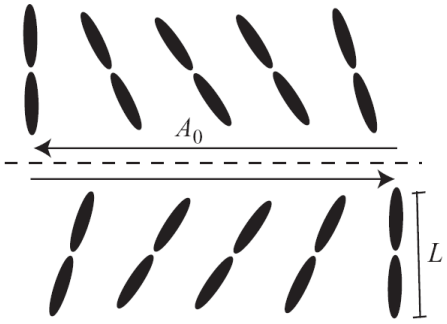

Figure 1.3: Sample symmetric hovering kinematics of a rigid wing. A single stroke involves a downstroke and an upstroke with the wing undergoing pitch reversal in preparation for the subsequent half-stroke.

Given a two-dimensional wing translating from rest at high angle of attack, we have established the formation of a trailing edge vortex with circulation strength satisfying Kelvin's circulation theorem. To reiterate, this starting vortex is ignored under steady state as it does

not influence the airfoil. However in flapping each half-stroke is on the order of a couple of chord lengths. Under these conditions the starting vortex's proximity renders it influential on the circulatory growth on the wing by means of the velocity it induces. This is known as the Wagner effect and solutions only approach steady state approximations after roughly seven chords lengths of travel [23].

1.3.1 Delayed Stall

Operating at elevated angle of attack also introduce another important phenomena to the leading-edge of the wing. Most fixed-wing aircraft operate at $\alpha < 15°$, beyond which there exists a critical angle of attack where flow separation occurs. It is here we must be mindful of the flight pattern: fixed-wing craft wish to continue to translate whereas flapping wing creatures wish to reverse direction after heaving. Should a wing continue to translate at high angles of attack the separated flow will develop drag and loss of lift, termed stall. However the process of stalling is not an instantaneous one. A flapping wing, or biofoil, translates a finite distance in a given half-stroke, the time duration in translation coincides with the time necessary for a stall to develop. Consequently, biofoils can develop transient circulatory forces much greater than those attainable in steady-state. This has been terms delayed or dynamic stall.

The separated flow at the leading-edge of the airfoil develops into an attached vortex commonly referred to as the leading-edge vortex. This vortex grows in strength, fed by the free-shear layer developed at the point of separation and remains located at the leading-edge upper surface of the wing. The flow is separated from the leading-edge and temporarily reattaches to the upper surface further down the chord. Just as in stall, dynamic stall is the development of a "bubble" of enclosed vorticity created by flow separating and reattaching, the likes of which is attenuated at greater angles of attack [23]. The difference between stall and dynamic stall is in stall the "bubble" is given ample amount of time to pinch off, the leading-edge vortex is shed after which the flow behind the wing is that of stalled conditions. During the attachment period the leading-edge vortex produces a suction, generating greater

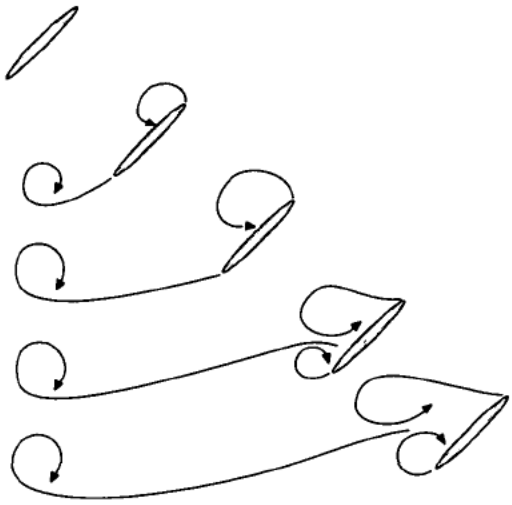

Figure 1.4: Impulsive start of an airfoil at high angle of attack [23].

lift from the pressure differential across upper and lower surfaces.

1.3.2 Wing-Wake Interaction

Wing-wake interaction is a common occurrence in both nature and engineering applications wherein we observe a foil encountering its own wake or a wake induced by another foil. Some of which are avoided, for instance, the mandated waiting time given commercial aircraft to be cleared for takeoff, ensuring the wake of the previous craft to takeoff has significantly dissipated. This is not to imply all interactions prove detrimental. One such example is migrating birds flying in a "'v"'-formation. Each wing experiences an up-wash induced by other wings' wakes in the group by means of tip vortices, reducing induced drag and power demands [46]. Such a flight formation has also been implemented in cargo and military aircraft, reducing fuel consumption.

In a tandem wing configuration, such as that of the dragonfly, two wings operate in the same plane (in the two-dimensional limit). Under going hovering the wings are separated by a vertical distance approximately 1.25 chord lengths. The down-wash and wake of the fore wing is certainly encountered by the hind wing. However, the fore wing does not flap in isolation, unperturbed. The fore wing experiences changes in flow conditions due to the

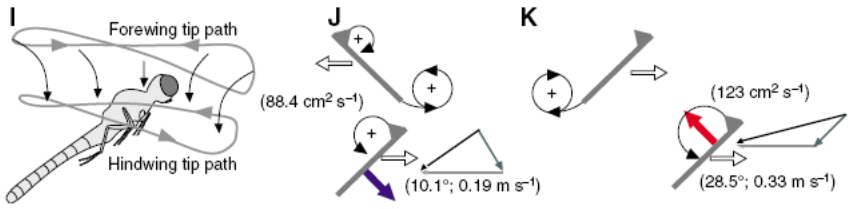

Figure 1.5: Tandem wing configuration and resultant force pending fore-hind wing phase [65].

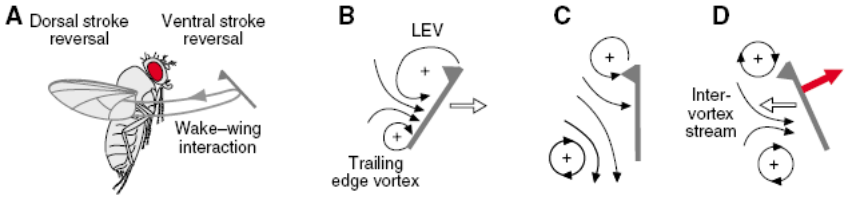

Figure 1.6: Wake capture mechanism at stroke reversal [65].

in-wash of fluid caused by the presence of the hind wing. In estimating the power necessary to produce identical values of mean lift, hovering with four wings with the hind wings leading fore wing motion by 25% of the stroke cycle requires 22% less power than hovering with two fore wings [66].

It has become clear wing-wake interactions can prove beneficial if properly implemented. We are interested in single winged flight configurations so the question remains as to how such wings may benefit from an established wake. One such mechanism proposed is the wake-capture mechanism wherein the wing 'recylces' kinetic energy imparted to the wake. At the end of a half-stroke the biofoil has created a leading and trailing edge vortex system. This counter rotating vortex dipole is believed to accelerate the fluid, increasing the apparent velocity of the fluid with respect to the wing as it begins the subsequent half-stroke after stroke reversal [65]. However, force peaks at the start of the half-stroke once believed to be the results of wake-capture appear closely related to the rapid acceleration of the wing, indicating wake-capture may be negligibly small [94].

More recently experiments have compared the forces generated at the beginning of the

first stroke with those of the fourth stroke and determined although the force peaks were due to the rapid accelerations, they were augmented by wake effect [12] [115]. The wake effect roles depends on the kinematics of the wing, how the wing encounters the wake. In some cases it has been reported the mean lift coefficient is decreased by nearly 18% and the mean drag coefficient increased by 10% for half-strokes with developed wakes compared to start-up half-strokes [115]. The wake is creating a downwash which makes sense intuitively, in order to maintain a vertical force the biofoil must impart momentum into the fluid downward. Although the mean lift coefficient may have decreased, the instantaneous lift coefficient at the start of a half-stroke may contain a peak greater than that produced in a start-up stroke.

1.3.3 Added Mass

As noted in previous section, researchers observe a force signature closely related to the accelerations of the biofoil. Just as unsteady as the wake discussed thus far so too is the velocity of the wing. When examining a submerged body accelerating or decelerating in a fluid the body encounters an added mass effect. Because a body, or in this case a biofoil, cannot occupy the same physical space as the fluid simultaneously, the body must move a volume of the surrounding fluid when the body is in motion. In doing so, the surrounding fluid is accelerated or decelerated resulting in an addition to the inertia, the fluid traveling now with the body acts as added mass. This is to say a body must be accelerated with enough power to accelerate the body-fluid system, experiencing a reaction force from the fluid in the process.

In an inviscid problem, an accelerating body experiences a fluid reaction force in the form of virtual added mass of fluid. This virtual mass adds to the inertial force acting on the body. In the two-dimensional limit the reaction forces are represented by the following:

$$\begin{bmatrix} F_{x,A} \\ F_{y,A} \end{bmatrix} = \begin{bmatrix} M_{xx} & M_{xy} \\ M_{yx} & M_{yy} \end{bmatrix} \cdot \begin{bmatrix} \dot{U} \\ \dot{V} \end{bmatrix} \tag{1.2}$$

where $F_{x,A}$ and $F_{y,A}$ are the fluid reaction forces acting on the body, M_{ij} is the virtual fluid mass, and $\dot{U}$ and $\dot{V}$ the acceleration in x and y direction respectively ('$\cdot$' indicating

differentiation with respect to time). Virtual mass is dependent on the geometry of the solid body, for example, an elliptical body of semimajor axis a and semiminor axis b will experience virtual masses $M_{xx} = \rho\pi a^2$, $M_{yy} = \rho\pi b^2$, and $M_{xy} = M_{yx} = 0$.

In the viscous problem, shear stresses are reintroduced. As such, when a body is accelerated from rest in a stagnant fluid, the combination of the impulse associated with the instantaneous appearance of a surface vortex sheet and the displaced fluid inertia collectively account for the reaction force of the fluid [29].

1.4 Kinematics

Hovering poses perhaps the most energy costly maneuver as there is no ambient wind or forward flight speed to aid in lift generation. Nondimensional numbers often cited in flapping flight are Reynolds number and Strouhal number:

$$\mathrm{Re} = \frac{f_{\mathrm{flap}} c A}{\nu} \tag{1.3}$$

$$St = \frac{f_{\mathrm{flap}} c}{U_o} \tag{1.4}$$

where f_{flap} is the stroke frequency, c the chord length, A the stroke amplitude, and U_o the free stream velocity. The way we have defined Re here is specific to hovering. One should also note U_o is zero in hovering, there is no free stream or insect body velocity and therefore St is irrelevant.

A flapping wing is characterized by three degrees of freedom: instantaneous stroke position, $\phi(t)$, instantaneous angle of attack, $\alpha(t)$, and instantaneous stroke deviation, $\theta(t)$. Our task is complicated considerably by the amount of variables present and their various combinations, such as: stroke amplitude, pitch amplitude, deviation amplitude, frequency, chord length, aspect ratio and phase in pitch and deviation. The inclusion of another wing in tandem would only add further. In order to develop a fundamental understanding of the underlying physics, we will first draw attention to two-dimensional single flapping wing.

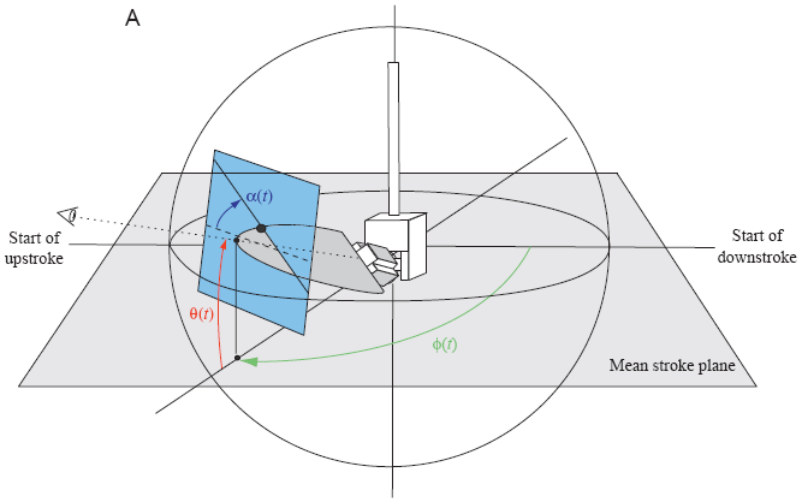

Figure 1.7: Degrees of freedom in a flapping wing [90].

Two-dimensional studies have proven instrumental in identifying force mechanisms, and phenomena uncovered in these studies has proven applicable in three-dimensional studies.

Faced with so much variety it seems natural to question to what capacity might a given parameter and kinematic bear influence in force production and performance.

1.5 Amplitude

Two-dimensional simulation conducted by Eldredge *et al.* on an elliptical wing showed a clear preference in hovering stroke amplitude [49]. With stroke amplitudes A_o/L varied from 0.67 to 5.33, the lift increased monotonically with amplitude, where A_o is stroke amplitude and L is the reference chord length. Near $A_o/L \approx 3$ mean lift per stroke appears to reach a maximum value which appears to plate for the larger amplitudes. When the mean lift is normalized by power consumption, it appears a stroke amplitude of 3 to 4 chords is desired for peak efficiency. Although the mean lift generated for larger stroke amplitudes is constant (for rigid wings), the temporal signature of the lift as well as the efficiency may differ.

In determining parametric effects on performance, Berman *et al.* tested the hypothesis that insects move their wings in a manner which minimizes the metabolic cost during

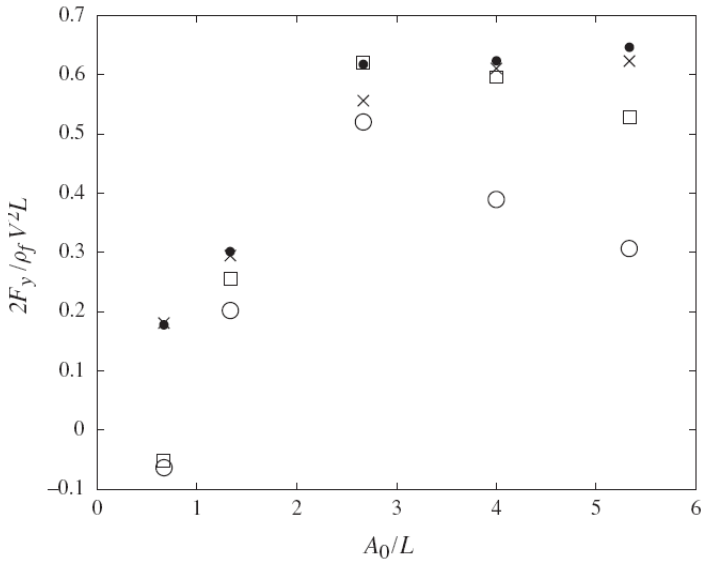

Figure 1.8: Mean lift (• - rigid wing, × - flexible wings) [49].

hovering flight [9]. All parameters are determined based on power specifications, including stroke amplitude. Insects of varying weight are tested including a fruity fly (*Drosophila melanogaster*), bumblebee (*Bombus terrestis*) and hawkmoth (*Manduca sexta*). A three-dimensional wing is modeled by an elliptical cross section along the chord with a chord length that was assumed to vary like a half-ellipse. The total force on the wing is determined with blade-element assumption wherein the total force is the summation of the forces on each infinitesimal blade segment. Aerodynamic forces of each segment were calculated using a model previously formulated by Pesavento & Wang [79].

The criteria for optimization was to determine the value of kinematic parameters which would account for the least amount of power consumption under the condition that the lift produced was sufficient to support the insects' weight. Negative power is consider negligible and elastic storage in the wing is also considered negligible although it has been measured to be on the order of 10% (Dickinson & Lighton 1995). The optimal solutions are found via a hybrid optimization algorithm combining aspects of a genetic algorithm and a gradient-based optimizer [9].

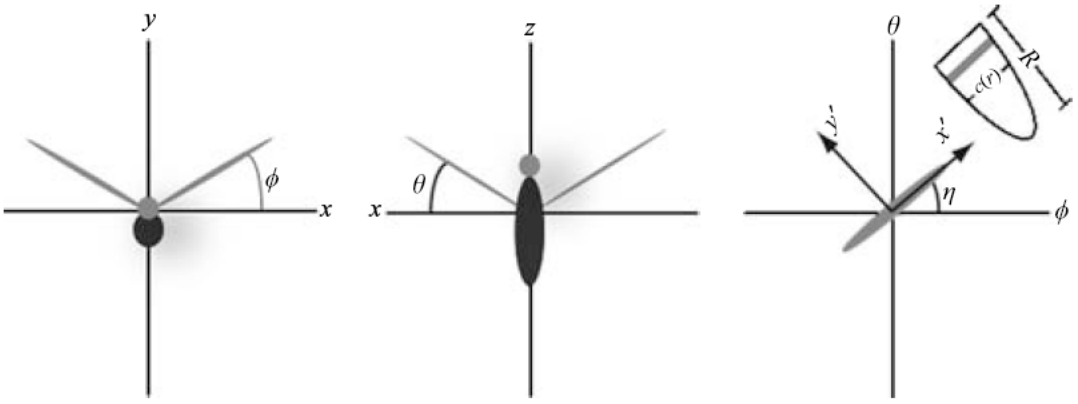

Figure 1.9: Elliptical wing model. All species considered share the same planform [9].

The resulting kinematics predicted optimal hovering with stroke amplitude of 180°, the maximum allowable by any given wing. Intuitively this would makes as a greater stroke amplitude would benefit from a greater translational period where the LEV is produced. However, taking the insects' physiology into consideration and the discrepancy becomes apparent. Measured stroke amplitudes are known to be 150°, 116° and 121° for the fruit fly, bumblebee and hawkmoth respectively. This may highlight our desire to draw inspiration from rather than mimic an insect in hover. With physiological constraints removed we could potentially engineer a wing and kinematic system requiring less power per unit mass of the insect.

A study by Wang *et al.* sought to determine the unsteady forces of flapping wings and their relative importance [107]. Implementing a three-dimensional flapper undergoing sinusoidal flapping and a two-dimensional numerical model, the sinusoidally varying strokes studied allowed for the relative contributions of some of the dynamic effects to be theoretically estimated. Such estimates include relative contributions to quasi-steady forces from wing rotation and acceleration and estimates of wing inertia relative to fluid force.
The robotic apparatus consisted of a Plexiglas wing with planform cut to that of a *Drosophila* wing. Flapping kinematics were restricted to the horizontal plan as to reduce the number of parameters and DPIV imaging was conducted at $0.65R$ where R is the total wing span, corresponding to the spanwise location in which previous studies have shown the greatest

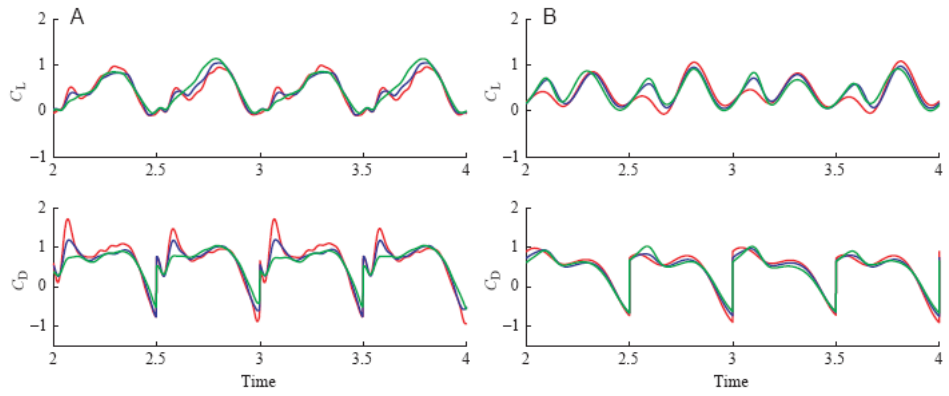

Figure 1.10: Force coefficients for amplitudes $A_o/c = 2.8$(red), 3.6(blue) and 4.2(green) for (A) 3D experimental and (B) 2D computational results [107].

circulation. The two-dimensional numerical model represented the wing as an elliptical body in which the Navier-Stokes equation governing the vorticity was solved.

Reynolds numbers Re varied from 75 to 115 and frequency f constant at $0.25Hz$. With a phase between pitch reversal and stroke reversal of $\phi = \pi/4$ the experimental lift coefficients were 0.93, 0.99, 0.95 and 0.93 at $A_o/L = 2.8$, 3.6, 4.2 and 4.8 respectively and the corresponding computational lift coefficients were 1.07, 1.0, 0.9 and 0.9. So the two approaches showed good agreement. For the range of amplitude studied here, $A_o/L = 3 - 5$, the lift coefficients have a weak dependence on stroke amplitude. According to Eldredge *et al.* [49] all cases studied here are well within the regime of relatively constant lift coefficient. Wang *et al.* hypothesizes that perhaps additional mechanisms are unnecessary to maintain an attached LEV for wings traversing less than 4 chord lengths. This is in part in response to a study of a two-dimensional wing at $\alpha = 45°$ and $Re = 10^3$ which does not show a temporal drop in its force signature until 4 chords of travel, after which the wake develops a von Karman street [106].

In a study by Chen *et al.* we see a nearly constant leading-edge vortex shedding time [16]. The two-dimensional computational study focused on leading-edge vortex growth and shedding time [16]. The infinitely thin two-dimensional flat plate was fixed at angles of

attack from 10 to 60° for $Re = 100$. The plate is then displaced with a power law velocity profile expressed non-dimensionally as:

$$\hat{U}\left(\hat{t}\right) = \hat{t}^{\beta} \tag{1.5}$$

where β ranges from 0 to 5. The incompressible Navier-Stokes equations were solved using an immersed boundary projection method in a reference frame fixed to the plate. It should be noted the authors prefer presenting results in a nondimensional form that is generally insensitive to instantaneous velocity, for example, time $\tilde{t}$ is now defined as:

$$\tilde{t} \equiv \frac{1}{c}\int_0^t U\left(\tau\right) d\tau \tag{1.6}$$

This will non-dimensionalize based on chord lengths traveled by the plate. Special attention is given to the case of $\alpha = 30°$. Once the added mass contribution to force is removed, the peaks in lift associated with leading-edge vortex production are isolated. Their exact nature appears to depend on β. Chen *et al.* concluded that although the peaks in lift varied in magnitude and timing, the temporal bounds from the start of the peak to the end appeared to be universal, completing around $\tilde{t} \approx 4.5$ [16]. This completion is interpreted as the leading-edge vortex separation from the plate. For the various velocity and acceleration profiles it appears the formation and the subsequent shedding of the leading-edge start-up vortex time is constant (Figure [1.11]).

Additionally, Chen *et al.* found for values of $\beta \leq 1$ the lift coefficient curves nearly collapse and the nature of the peaks appear to be insensitive to β. Once the first few start-up vortices formed and shed, a regular pattern of shedding vortices developed in the wake. The non-dimensional frequency of shedding $\tilde{f}$ appeared to be dependent on β but when plotted against instantaneous Reynolds number a linear relationship arises that holds for both steady and accelerating plates (Figure [1.12]). This provides convincing evidence that Re, and not acceleration, is responsible for the long-time dynamics of the flow. Additionally, Chen *et al.* determined that the same independence of acceleration is present in the lift coefficient oscillation minimum and maximum. The quasi-steady state of long-time lift coefficient is

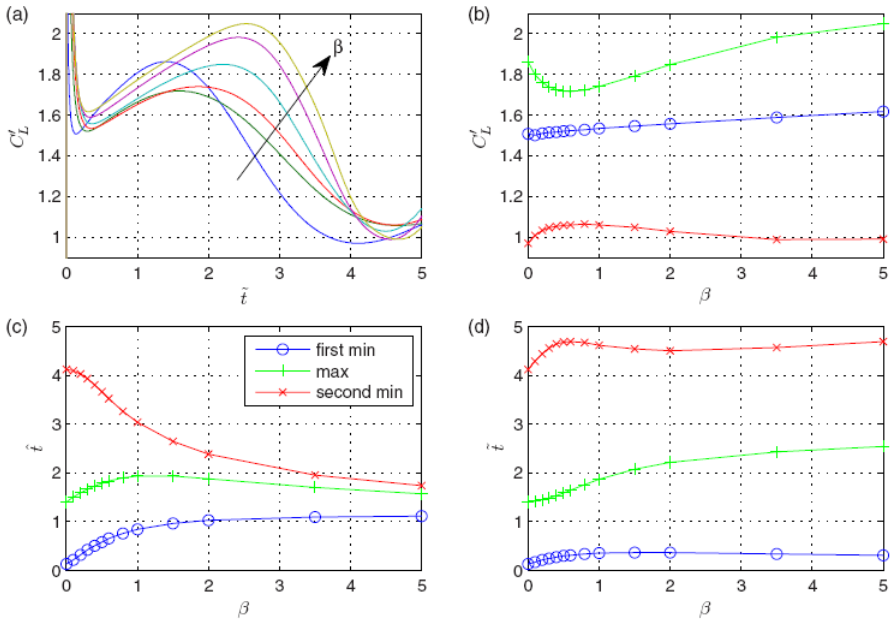

Figure 1.11: Lift augmentation analysis for $\beta = 0.0$, 0.5, 1.0, 2.0, 3.5 and 5 utilizing chord length scaled time $\tilde{t}$ [16].

determined by Re.

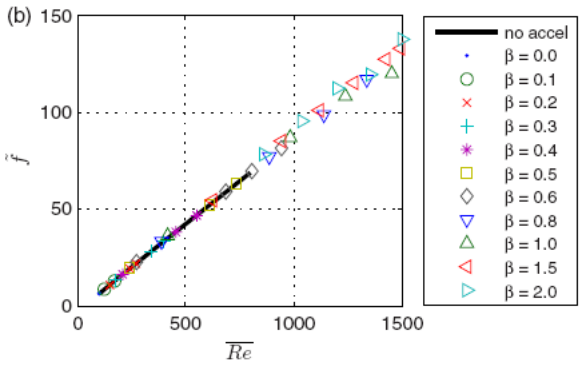

Figure 1.12: Frequency of force oscillation for all powers of β [16].

1.6 Phase

A translating wing at α will generate lift. However in flapping flight a typical wing stroke is composed of two translating regions, upstroke and downstroke, as well as two rotational regions, pronation and supination. Referring back to Wang *et al.*'s study [107], we wish to examine the effect of phase between pitch reversal and stroke reversal as well as the role of wing rotation. As a half-stroke comes to an end, the wing must rotate about an axis spanning from the base to the tip of the wing, reversing its pitch. It must adjust its angle of attack $\alpha(t)$ in preparation for the reverse half-stroke. Of interest is the phase ϕ dependency on force generation with ϕ values $\pi/4$, 0 and $-\pi/4$ corresponding to advanced, symmetrical, and delayed rotation with respect to translation. In the case of delayed rotation the wing begins to translate with an angle of attack greater than $\pi/2$ which results in downward lift. Although this seems contrary to our current goals it should not be dismissed entirely as Wang *et al.* reasons such a maneuver may still be useful in flapping flight as it may provide a means for wings to reduce the force on the wing. Unlike the advanced and symmetrical cases, delayed exhibits flow separation from the leading-edge quickly in stroke.

Once again in comparing the three-dimensional experimental results to two-dimensional numerical results modeled as a projection of a wing at 70% span, the lift agrees quite well for advanced and symmetrical cases, however the lift of the delayed case shows a clear phase delay of the computational results with respect to the experimental. This phase delay only occurs after the first stroke. The results indicate average lift depends sensitively on the rotation phase ϕ as opposed to the weak dependence on stroke amplitude.

In the rotational regions, pronation and supination, the wing undergoes rapid rotation to reverse pitch in preparation for the subsequent halfstroke heave. As Dickinson *et al.* states, these brief regions of rotation are capable of producing significant lift at stroke reversal [22]. To demonstrate this, Dickinson *et al.* constructed a wing apparatus comprising of a mechanical wing capable of flapping and a tank for the ambient fluid. The wing was modeled after that of a fruit fly, *Drosophilia melanogaster*. Moving this wing in a heave of 180° at

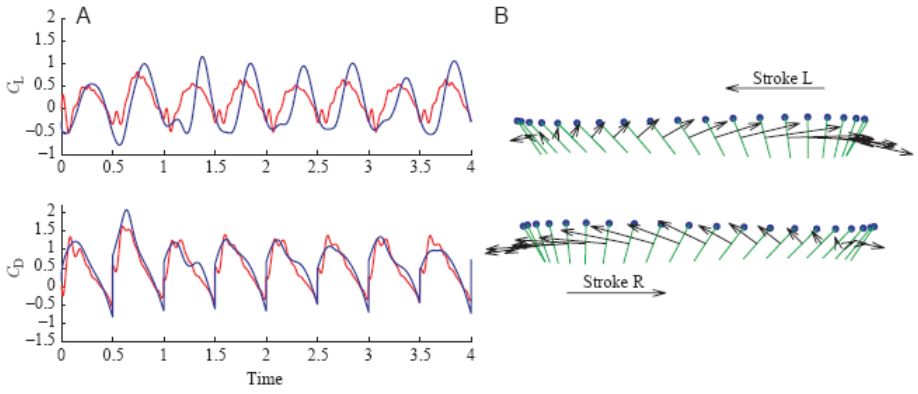

Figure 1.13: Phase delay $\phi = -\pi/4$ (A) Force coefficients for experimental (red) and computational (blue) (B) Force vectors superimposed on wing kinematics [107].

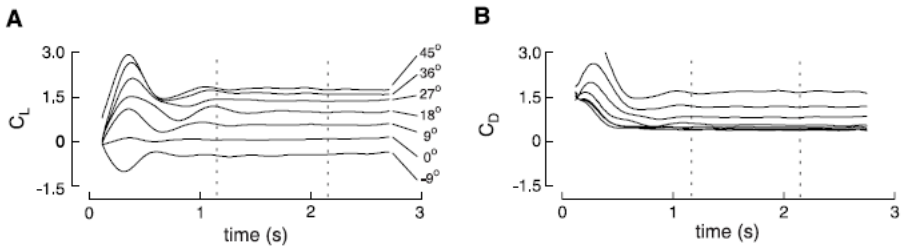

Figure 1.14: Transient response to heaving at constant α [22].

constant velocity and angle of attack provided a means to calculate lift and drag coefficient, C_L and C_D, corresponding to translation. After initial transients the three-dimensional wing produces relatively stable constant coefficients.

In estimating the contribution of wing rotation to force generation, the wing is placed in hovering kinematics and the recorded translational coefficients subtracted from its force history. The time course of rotational lift shows significant spikes at pronation and supination. At work here is rotational circulation.

Rotational circulation is akin to the Magnus effect wherein a rotating object such as a cylinder pulls the air within the boundary layer as it spins. The cylinder in this case would serve as a source of circulation. Now if such a cylinder were to be translating, by Kutta-Joukowski theorem, a force would be generated. The direction of force however depends on

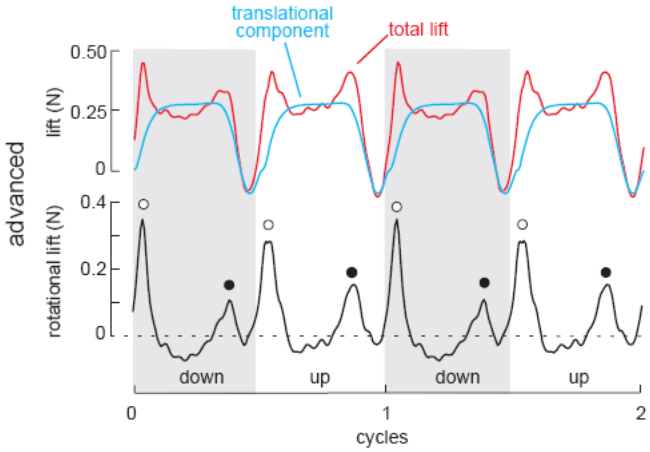

Figure 1.15: Rotational lift contribution. Advanced case displayed here with rotation preceding stroke reversal by 8% of wingbeat cycle. ∘ - transients attributed to wake-capture, • - transients attributed to rotational circulation [22].

the direction of rotation and translation. This direction of rotation and translation emphasis the importance of phase between heave and pitch reversal. Dickinson *et al.* verified the effects of phase by systematically changing the phase between heave and pitch reversal for simplified kinematics [22]. It was shown when when pitch reversal lead heave reversal, wing rotation produced a positive lift peak. When pitch reversal lagged heave reversal the opposite held true, a negative peak in lift was generated, due to the leading-edge of the wing rotating into the oncoming fluid. This explains the positive force transients produced by rotational circulation for advance and symmetrical phases. The net aerodynamic forces are found to largely act perpendicular to the wing surface indicating the shear forces are much smaller than pressure forces. Given the flat nature of the wings studied, we see a component of the resultant rotational circulation provide for lift and drag.

1.7 Frequency

The frequency at which wings flap can attenuate performance as well. For instance, the greater the frequency for a given wing, the greater the Reynolds number in hovering. The

translational acceleration too may increase due to the decrease in time allocated to take a wing from rest to translation. This also pertains to deceleration at the end of a half-stroke. With this apparent increase in acceleration profile, increased frequency may increase the role of inertial and added mass effects influential on the biofoil. We must also be mindful of the wake characterized by counter rotating vortex dipoles which act to convect themselves in the fluid. Frequency of flapping may determine the nature of force produced by wake interaction depending on the convection speed of the wake.

In minimizing energy consumption in fruit fly, bumblebee and hawkmoth using a hybrid of clustering genetic algorithm and a Powell simplex algorithm, Berman *et al.* found optimal frequencies to be 234Hz, 122Hz and 19Hz respectively [9]. These values are within or only slightly above frequencies exhibited by the insects. So it appears frequency decreases with increasing mass.

Frequency selection is not restricted to hovering. Although our focus is in hovering maneuvers, to better understand the parametric effects of flapping it is best we broaden our scope to forward flight of flapping wings. Evident among flying and swimming creatures is the frequency variation in flapping and undulation. Wang numerically modeled a two-dimensional elliptical wing, the motion of which consists of the superposition of a mean forward motion and a sinusoidal flapping motion, using a Navier-Stokes solver [106]. Preliminary tests maintaining a Reynolds number $Re = 1000$ and Strouhal number $St = 0.16$ indicate a clear distinction among performance with some f or St_c more favorable than others, where St_c is the reduced frequency. In lift production, all cases are symmetric about zero, making the mean lift zero as expected in symmetric flapping. Of concern in this particular case is the thrust coefficient which appear to be asymmetric about the zero axis. Thrust efficiency and coefficient reach a maximum at reduced frequency $St_c \approx 1$, where thrust efficiency is the time-averaged thrust efficiency from von Karman & Bergers (1963) [106].

Examining the vortex dynamics of a wing translating at a constant angle of attack $\alpha = 40°$ at $Re = 1000$ reveals a time scale τ associated with LEV production, after which the lift

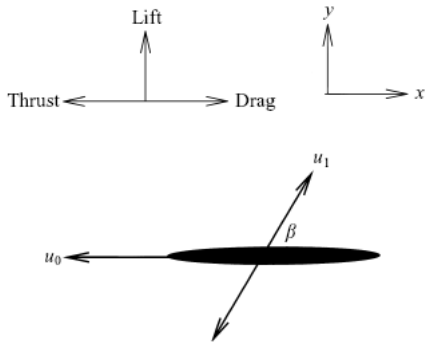

Figure 1.16: Forward flight flapping model, $\beta = \pi/2$ [106].

coefficient obtains a steady value before von Karmon street is developed. This gives a time scale, τ, to which the flapping frequency can be compared. The wing should flap slowly enough to promote the growth of the vortex. It seems in forward flight the frequency also determines the angle of attack, in a given half-stroke the angle of attack increases from $0°$ to a maximum angle in a span of one-fourth the period. To produce thrust, Wang determines the maximum angle of attack should be within $45 - 60°$ with Strouhal number St_a between $0.16 - 0.27$. Wang notes an increase in thrust coefficient with increasing St. Furthermore, at higher values of St the maximum thrust coefficient is achieved for $St_c \approx 0.7$ independent of St with thrust efficiency following a similar trend.

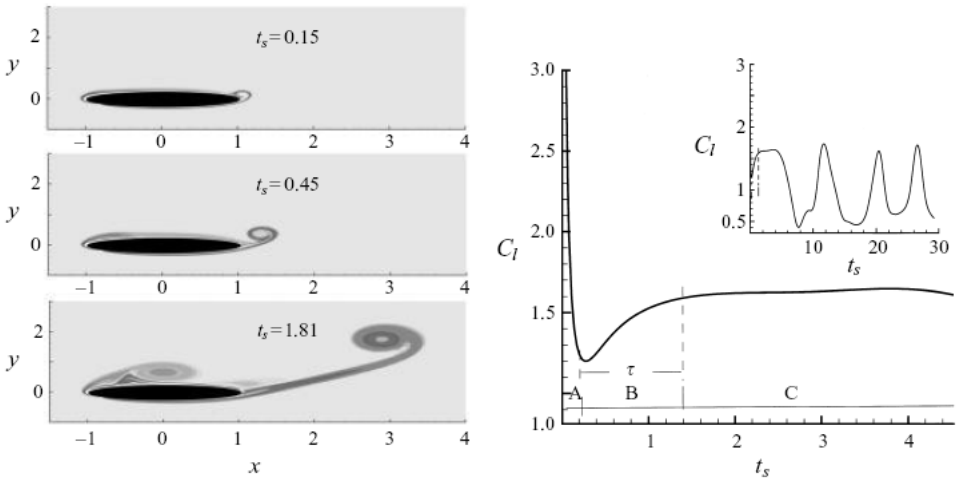

Figure 1.17: Lift coefficient and contour plot of impulsively started ellipse, $\alpha = 40°$ and $Re = 1000$ [106].

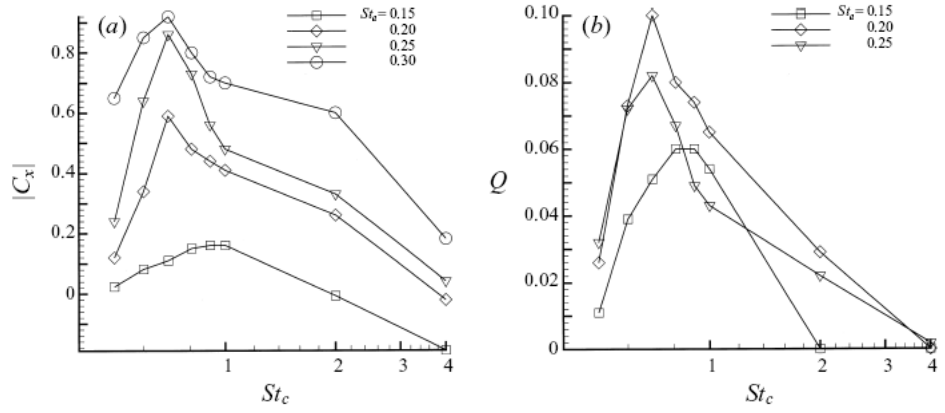

Figure 1.18: Thrust coefficient (a) and efficiency (b) as a function of St_c for a given St [106].

1.8 Quasi-Steady Modeling

Common methods for calculating two-dimensional lift and drag for a foil make use of dimensionless force coefficients:

$$L' = \frac{1}{2} C_L U^2 \rho c \tag{1.7}$$

$$D' = \frac{1}{2} C_D U^2 \rho c \tag{1.8}$$

where C_L and C_D are the lift and drag coefficient respectively, U is the velocity of the airfoil with respect to the fluid, ρ is the density of the fluid, and c is the chord length of the airfoil. The primed terms, L' and D', indicate force per unit span. The coefficients are time-invariant parameters determined by the airfoil's geometry, Reynolds number at which it operates and angle of attack [23]. Derivation of such equations required constant velocity flight with no deviations in flightpath, a stark contrast to hovering kinematics. However, this does not restrict their use to steady kinematics. The forces generated by an airfoil for a given set of kinematics, marked with unsteady velocity and angle of attack, may be estimated by utilizing the equations at discretized time increments with C_L and C_D data measured prior [23]. Such an approach is termed "'quasi-steady state"'. This method is not without problems.

Quasi-steady state analysis results may bear little resemblance to wind tunnel results for a flapping airfoil. The force coefficients are not constant but rather display complex time histories [23]. Additionally, quasi-steady state analysis does not take into account wake interaction between the airfoil and shed vorticity. It only considers the bound circulation, the circulation resulting from the fluid acceleration above the airfoil. The magnitude of the bound circulation depends on the geometry and angle of attack of the airfoil. The greater the angle of attack, the greater circulation needed to shift the upper surface stagnation point to the trailing edge. In fact, this approach assumes a starting vortex in the far field of the wake having no effect on the airfoil. Quasi-steady estimates of drag are found to undershoot the measured drag near stroke reversal owing in part to added mass [90].

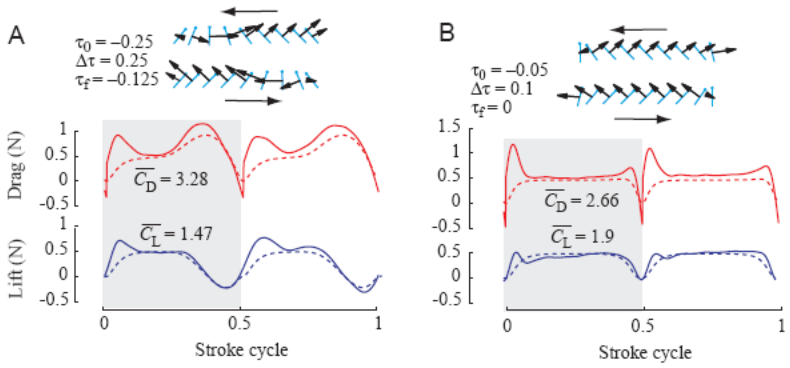

Figure 1.19: Drag (blue) and lift (red) for measured values (solid lines) and quasi-steady model (broken lines) (A) advance rotation and (B) symmetric rotation [90].

Despite its shortcomings, the model proves useful as a means of estimating unsteady force trends. The overlay of the quasi-steady model provides a means of decomposing the aerodynamic forces into its constituent components. All deviations from the quasi-steady estimate represent unsteady effects. Measured force trajectories display peaks at the beginning and end of each half stroke that are either absent or smaller in the quasi-steady predictions. It is at the beginning and end of a stroke where most of the translational acceleration and rotational dynamics are most prominent. In determining the governing quasi-steady lift and drag coefficients, a wing at constant α and velocity is impulsively translated or swept in a 180° arc for two and three-dimensional wings respectively. After initial transients the resulting force attains a nearly constant value before the onset of von Karman shedding. This is conducted for a desired Reynolds number and repeated for various angles of attack. From this data quasi-steady lift and drag coefficients can be determined as a function of angle of attack.

In general, force coefficients are greater in the measured unsteady case than predicted by the quasi-steady estimates employed by Sane *et al.* [90]. The maximum in lift coefficient reported is also shifted by approximated 10° in the force signature and lift-to-drag ratios for the quasi-steady model appear to overestimate aerodynamic efficiency and fail to be attenuated by stroke amplitude. On rotational timing, for symmetric rotation (in phase)

the force signature is better estimated by the quasi-steady approximations than advanced and delayed phase. Perhaps owing to the kinematics closely resembling those implemented in determining the quasi-steady relations.

1.9 Stroke Deviation

Stroke deviation refers to the degree in which a given airfoil deviates from a plane of interest, in the case of hovering we concern ourselves with the horizontal plane. In optimization studies in which power consumption necessary to actuate flapping wings in hovering per unit mass, it was found stroke deviation in the form of figure-8 motion played a less crucial roll in the largest (hawkmoth) and smallest (fruit fly) insects studied [9]. In fact, the resultant kinematics appear largely sinusoidal in the horizontal plane, or rather lean more toward a triangular waveform. In the intermediately massed insect (bumblebee), the figure-8 deviation was much more pronounced. In conducting this study, Berman assumes a universal wing planform geometry for all species [9]. In reality, the insects selected exemplify the breadth of variety of geometries found in insect wings. Perhaps allowing specific wing geometries would help bridge the variance in stroke deviation observed for intermediate massed insects.

Flapping deviations from the horizontal plane are highly sensitive to the direction of deviation at the start of the stroke. For both oval and figure-8 motions, a wing that deviates upward will experience a reduced angle of attack whereas a wing moving downward will experience the opposite [90]. Additionally, a wing moving downward at the start of translation will experience greater wake influence as the wing is moving toward the descending vorticity field of the previous stroke. Although the impact of stroke plane deviation is clear in the time course of lift and drag, the impact on mean force coefficients remains quite small. The effects of deviation tend to average themselves out over the course of a full stroke [90].

1.10 Scaling

Biological studies often cite Reynolds and Strouhal numbers, conveying fluid behavior and influence of morphology of the wing on the fluid. In an effort to couple both the morphology and kinematics of the locomotory system to the Navier-Stokes equation, Lentick *et al.* identified dimensionless numbers representing rotational accelerations in the flow due to the wing kinematics and morphology by means of non-dimensionalizing the Navier-Stokes equation with respect to the surface of a wing undergoing flapping, spinning or translation kinematics as illustrated in Figure [1.20] [67].

Such a coordinate change to the wing surface requires the proper velocity transformation:

$$\mathbf{u}_{inert} = \mathbf{u}_{loc} + [\mathbf{u}_{body} + \mathbf{\Omega}_{wing} \times \mathbf{r}] \tag{1.9}$$

$$\mathbf{a}_{inert} = \mathbf{a}_{loc} + [\mathbf{a}_{ang} + \mathbf{a}_{cen} + \mathbf{a}_{Cor}] \tag{1.10}$$

where

$$\mathbf{a}_{ang} = \dot{\mathbf{\Omega}} \times \mathbf{r} \tag{1.11}$$

$$\mathbf{a}_{cen} = \mathbf{\Omega} \times (\mathbf{\Omega} \times \mathbf{r}) \tag{1.12}$$

$$\mathbf{a}_{Cor} = 2\mathbf{\Omega} \times \mathbf{u}_{loc} \tag{1.13}$$

Here $\mathbf{u}$ is velocity, $\mathbf{a}$ is acceleration and Ω is angular velocity. Subscript *inert* indicates reference to inertial frame, *loc* to local wing reference frame, *ang* denotes angular, *cen* centripetal and *Cor* Coriolis. The resulting non-dimensional transformed Navier-Stokes is as follows:

$$\frac{D\mathbf{u}}{D\mathrm{t}} + \frac{\dot{\Omega}Rc}{U^2}\dot{\mathbf{\Omega}} \times \mathbf{r} + \frac{\Omega^2 Rc}{U^2}\mathbf{\Omega} \times (\mathbf{\Omega} \times \mathbf{r}) + \frac{\Omega^2 Rc}{U^2}2\mathbf{\Omega} \times \mathbf{u} = -\frac{P_o}{\rho U^2}\nabla P + \frac{\mu}{\rho U c}\nabla^2 \mathbf{u} \tag{1.14}$$

where the acceleration of the body is neglected assuming steady flight. The current state of equations are generalized to include forward flight by the insect [67]. Additionally, it is assumed the wing is flapping in a sinusoidal motion with amplitude Φ_o and frequency

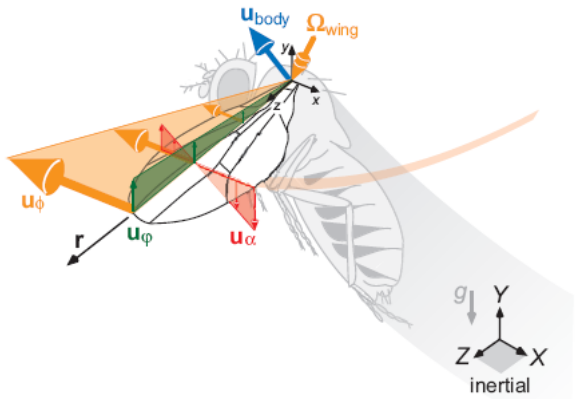

Figure 1.20: Forward flight wing kinematics [67].

f. Under these conditions, Lentick *et al.* decided to simplify the governing Navier-Stokes equation to better interpret the dimensionless groups' scale factors by time averaging the values of $\mathbf{\Omega}$, $\dot{\mathbf{\Omega}}$ and wingtip speed U resulting in a NS equation for forward flapping flight:

$$\frac{D\mathbf{u}}{D\mathrm{t}} + \frac{1}{J^2+1}\left(\frac{1}{A^*}\dot{\mathbf{\Omega}}\times\mathbf{r} + \frac{1}{AR}\mathbf{\Omega}\times(\mathbf{\Omega}\times\mathbf{r}) + \frac{1}{AR}2\mathbf{\Omega}\times\mathbf{u}\right) = -Eu\nabla P + \frac{1}{Re}\nabla^2\mathbf{u} \quad (1.15)$$

in which J is the advance ratio, $A*$ the dimensionless stroke amplitude of the wing, AR is the aspect ratio of the single wing, Re is Reynolds number, and Eu the Euler number which Lentick *et al.* has deemed irrelevant in incompressible flows:

$$J = \frac{U_{body}}{4\Phi_o R f} \quad (1.16)$$

$$A^* = \frac{\Phi_o R}{c} \quad (1.17)$$

$$AR = \frac{R}{c} \quad (1.18)$$

Under such a representation, it is much easier to see how accelerations scale, such as Coriolis scaling inversely to aspect ratio. This analysis also lends itself to hovering kinematics wherein the advance ratio, J, is zero:

$$\frac{D\mathbf{u}}{D\mathrm{t}} + \frac{1}{A^*}\dot{\mathbf{\Omega}}\times\mathbf{r} + \frac{1}{AR}\mathbf{\Omega}\times(\mathbf{\Omega}\times\mathbf{r}) + \frac{1}{AR}2\mathbf{\Omega}\times\mathbf{u} = -Eu\nabla P + \frac{1}{Re}\nabla^2\mathbf{u} \quad (1.19)$$

Lentick *et al.* concluded flapping wings induce three rotational accelerations that diffuse into the wing's boundary layer: angular, centripetal and Coriolis. Such accelerations could prove

significant in the development of leading edge vorticity and lift. Additional non-dimensional groups have been identified as angular acceleration number C_{ang}, centripetal acceleration number C_{cen} and Rossby number Ro:

$$C_{ang} = \frac{U^2}{\dot{\Omega}^2 Rc} \tag{1.20}$$

$$C_{cen} = \frac{U^2}{\Omega^2 Rc} \tag{1.21}$$

$$Ro = \frac{U^2}{\Omega^2 Rc} \tag{1.22}$$

The angular acceleration number is a measure of the unsteadiness of the flow induced by the rotational acceleration of the wing, the centripetal acceleration number measures the centripetal acceleration due to the wing's rotation, and Rossby number measures the Coriolis acceleration induced by the relative motion of fluid with respect to the rotating wing [67]. Forward flight works to reduce rotational accelerations, $J > 1$. Hovering, characterized by $J \approx 0$, provides the extreme case exhibiting maximal rotational accelerations. Such accelerations are though to contribute to the stability of the LEV observed in three-dimensional flapping.

1.11 LEV Stability

The aerodynamic performance of a biofoil in hover is largely explained by the presence of a stable leading-edge vortex. Although the LEV has been visualized both experimentally and numerically, the phenomena governing its stability remains poorly understood. Toomey *et al.* has shown rotation rate to be the primary control of lift generation in two-dimensional wings, perhaps indicating the rotation rate plays a role in LEV stability [100]. Expressing the Navier-Stokes equations in a rotating frame attached to a wing's surface, Lentick *et al.* has determined the angular acceleration may in fact help to stabilize the leading-edge vortex.

In two dimensional studies the only component available is the angular acceleration in pitch. However in three dimensions we recover angular velocities and accelerations pertaining to stroke, pitch and deviation. Therefore three dimensional configurations may offer greater

stability. Dickinson *et al.* observed force coefficients measured by the 3D wing apparatus to be slightly smaller than the transient force coefficients corresponding to a 2D wing undergoing the same translating motion [22]. However, Dickinson *et al.* found the 3D coefficients were greater than the steady-state 2D coefficients. Beyond the initial transients, the 3D wing produces relatively stable constant coefficients. It is widely believed the axial flow down the span of a wing in a 3D configuration works to convect momentum out of the core of the leading edge thereby stabilizing the LEV in a process termed vortex stretching. In doing so the axial flow would effective reduce the strength of the LEV and perhaps prolong the separation process.

$$\frac{D\omega}{Dt} = \underbrace{(\omega \cdot \nabla)\,\mathbf{V}}_{\text{vortex stretching}} + \nu\nabla^2\omega \tag{1.23}$$

This may explain why the 2D transient produced greater coefficients: the lack of axial flow. In fact, Dickinson *et al.* proposes the loss of energy from the core of the leading edge vortex probably works to limit the force generation of the 3D case to below that of the 2D case. In effect, making the two-dimensional lift coefficients per unit span the benchmark to which three-dimensional cases may not surpass as demonstrated in Figure [1.21].

In visualizing the three-dimensional LEV process, van den Berg *et al.* constructed a flapper apparatus with a dynamically scaled hawkmoth wing [101]. The hawkmoth is on the larger end of the aerial insect spectrum in size but despite its relatively large size it still maintains the ability to hover and may present a threshold of flapping wing hovering ability in nature. The focus here was the leading-edge vortex formation and evolution during a single downstroke. For analytical purposes the spiral vortex was represented as an ellipse with width w and height h recorded. Laser sheet techniques were used on the wing to examined the leading edge vortex at four positional angles and up to five spanwise positions per position angle.

At the onset of downstroke with stroke position $\phi = 50°$, just after pronation, there was no leading edge vortex present. For positional angle $\phi = 30°$ a leading edge vortex is clearly observed. Its size smaller at the base of the wing and tended to increase with radial distance

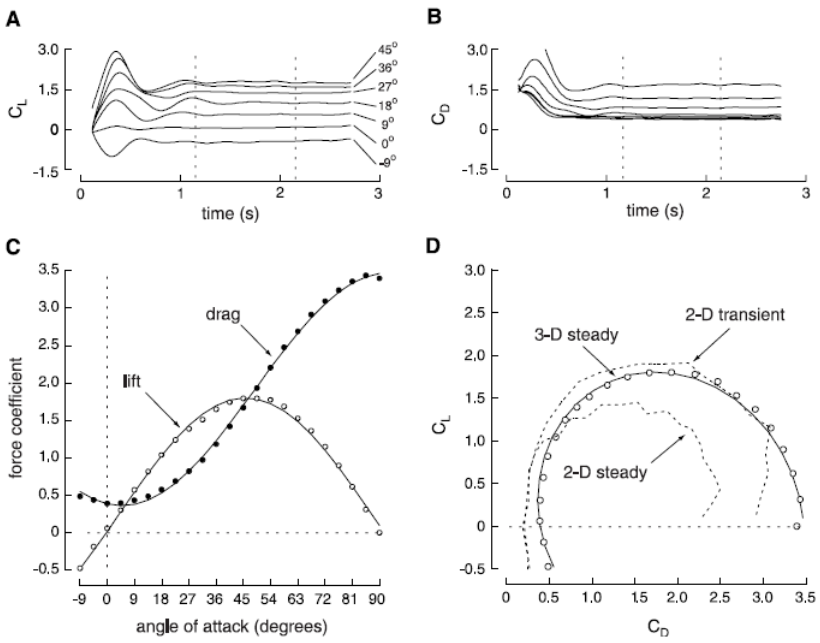

Figure 1.21: Three-dimensional wing heaving at constant α, quickly accelerated from rest to constant velocity. (A) Lift and (B) drag coefficient. (C) Average force coefficients as angle of attack, averaging excludes transients. (D) Polar representation, influence of induced drag on 3D wing manifests itself as small right shift in the curve relative to 2D data. [22].

down the span. For instance the height with respect to the wing surface increases by a factor of 3.5 between radial positions $0.25R$ and $0.63R$ where R is the total spanwise length of a wing. Additionally noted is the cross sectional shape of the vortex, seemingly changing from oval at $0.25R$ to circular at $0.63R$ and beyond. The circular shape may indicate the portion of the LEV no longer being subjected to shearing, effectively detached from the surface of the wing. The center of the vortex also experiences attenuation, moving away from the surface of the wing down the span from 1.3% to 5.8% of R, increasing 4.5 times greater. From wing base to wing tip it also becomes apparent that the vortex center shifts further back from the leading edge of the wing from 3.2% to 6.4% of R. The leading edge vortex does not traverse the entire length of the wing, often around $0.63R$ to $0.75R$ the LEV separates from the wing surface and is incorporated into the tip vortex. We see here early on in the downstroke the LEV showing signs of instability: increased size and location from the wing surface down

the span.

Further along the downstroke at $\phi = 0$ the LEV has amassed greater strength and size. The distance of the vortex center to surface of wing has grown from 3.2% to 15% of R at $0.25R$ and $0.75R$ respectively. The vortex center has also moved further back along the chord at each radial location examined, 4.3% to 8.6% of R from $0.25R$ to $0.75R$. Furthermore, the gradient of this distance with respect to the radial direction has also increased. Finally $\phi = -36$ the wing is decelerating at this point with the wing oriented in the vertical direction with $\alpha \approx 90°$. It was observed that the vortex center distance from the wing surface has decreased by $10 - 20\%$ between $0.25R$ and 0.63 from values reported for $\phi = 0°$. In the downstroke from $\phi = 0°$ and $\phi = -36°$ the LEV separates from the wing surface between $0.63R$ and $0.75R$ only to be replaced by a smaller LEV. This new LEV is developed by the same mechanics of the first. The new LEV is much weaker as the wing is already decelerated prior to supination. It seems hawkmoth wings, for the duration of a stroke, develop a leading edge vortex that is initially characterized by an elliptical cross-section with center located close to the leading edge. As the stroke continues the cross-section gradually turns circular down the span of the wing and the LEV is swept along the chord depending on radial position. Eventually the center of the vortex becomes far removed from the wing surface and leading edge and as the wing decelerates the LEV separates. Ultimately, it was estimated that the circulation in the LEV alone accounted for approximately 2/3 of the total lift required to support a hawkmoth.

It is clear aerodynamic forces in flapping wings are largely attributed to the presence of a leading edge vortex formed above the wing. To gain fundamental insight to the stability of such vortices Lentink *et al.* expresses the Navier-Stokes equations in a reference frame fixed to the wing's surface [68]. This explicitly shows the accelerations that may govern the LEV

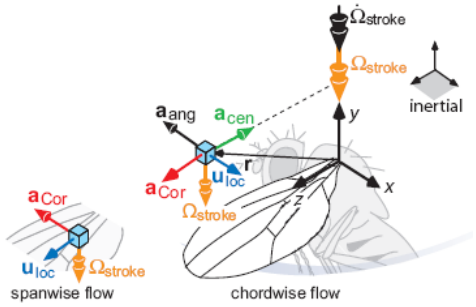

Figure 1.22: In the wing-bound frame, the fluid experiences three accelerations due to wing kinematics: angular, centripetal, and Coriolis acceleration [68].

dynamics: angular, centripetal and Coriolis accelerations.

$$\mathbf{a}_{ang} = 1/A^* \cdot \dot{\mathbf{\Omega}} \times \mathbf{r} \tag{1.24}$$

$$\mathbf{a}_{cen} = 1/Ro \cdot \mathbf{\Omega} \times (\mathbf{\Omega} \times \mathbf{r}) \tag{1.25}$$

$$\mathbf{a}_{Cor} = 1/Ro \cdot 2\mathbf{\Omega} \times \mathbf{u}_{loc} \tag{1.26}$$

where $\mathbf{\Omega}$ is the angular velocity, A^* the dimensionless stroke amplitude and Ro the Rossby number. Lentick *et al.* has previously postulated that perhaps rotation may be key to LEV stability [67]. Of the Navier-Stokes accelerations, both the centripetal and Coriolis accelerations are deemed 'quasi-steady' in that they do not depend on angular acceleration but on angular velocity $\mathbf{\Omega}$ of the wing. This is in contrast to the angular acceleration which is dependent on on changes in angular velocity $\dot{\mathbf{\Omega}}$ [68].

The implications of the acceleration terms during flapping are immediate: at the mid-stroke when LEV stability is at issue both $\mathbf{a}_{cen}$ and $\mathbf{a}_{Cor}$ are maximal as $\mathbf{\Omega}$ is at a maximum. A given stroke can be approximated as a sinusoidal function, reaching a maximum angular velocity at midstroke and a minimum in $\dot{\mathbf{\Omega}}$. This analysis would suggest LEV stability is mediated by rotational accelerations rather than unsteady acceleration $\mathbf{a}_{ang}$ [68]. With the dimensionless groups identified as A^* and Ro, Lentink *et al.* perform a series of flow visualizations and force measurements on a dynamically scaled fly wings (*Drosophila melanogaster*) revolving with $Ro = 2.9$ and translating wings with $Ro = \infty$. A stable leading edge vortex

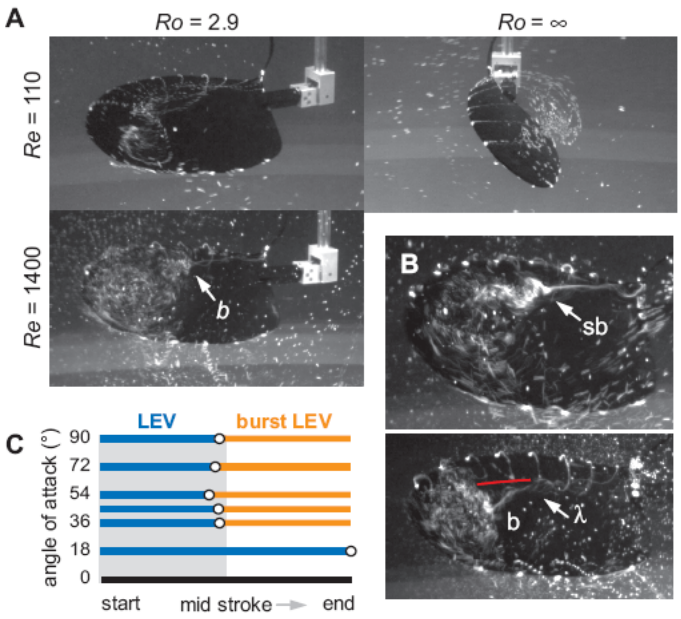

Figure 1.23: (A) Influence of Rossby number for wing undergoing rotational or translational reciprocal motion at $\alpha = 36°$. (B) LEV exhibiting bursting at $Re = 1400$ at midstroke for $\alpha = 45°$ (top panel) and $\alpha = 18°$ (bottom panel). (C) Onset of LEV bursting for reciprocally revolving wing ($Ro = 2.9$) at $Re = 1400$ [68].

was observed in unidirectional revolving wing with $A^* = infty$ and $Ro = 2.9$ as well in a reciprocally revolving wing with $A^* = 3.5$ and $Ro = 2.9$ but not in the case of unidirectionally translating wing with $A^* = \infty$ and $Ro = \infty$ or reciprocally translating wing with $A^* = 3.5$ and $Ro = \infty$. Reciprocating motion is not sufficient to provide stability. It appears low Ro is required from revolving propeller-like motion, with Ro $O\,(1)$ desirable in hovering flight, as demonstrated in Figure [1.23] [68].

For the case of unidirectional revolving wings, at $Re \approx 1000$ for $\alpha \geq 18°$ the LEV would experience bursting. Force measurements indicate such bursting does not result in a loss of performance. In fact it seems to elevate the force coefficients at higher Re. This bursting feature may work to reduce the separation distance, the distance normal to the wing from the surface to the LEV center, thus ensuring stability. The means by which the LEV bursts remain unclear. Experiments on unconfined vortical flows reported experienc-

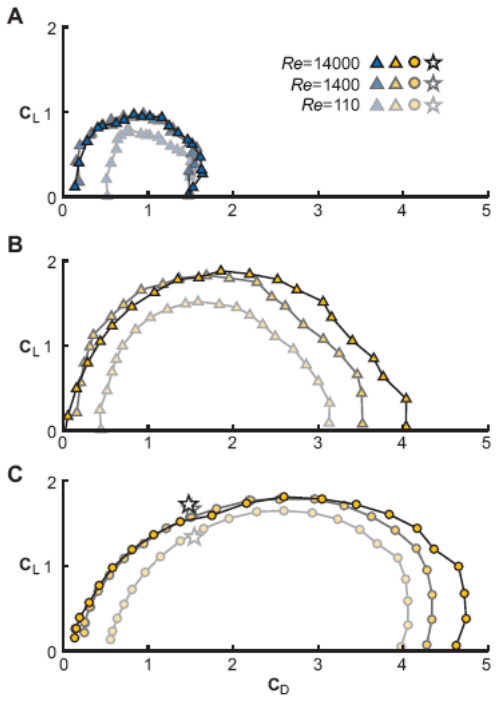

Figure 1.24: Lift and drag augmentation varies little with Re. (A) Unidirectionally translating wing, (B) Unidirectionally translating wing, (C) Reciprocally rotating wing ($\alpha = 45°$) [68].

ing vortex breakdowns wherein the vortex core would abruptly enlarge following a sudden deceleration of axial flow within the vortex core [54]. However, flapping wing configurations reportedly experience axial flow external to the LEV core.

Current hypotheses attribute LEV stability in a flapping wing to that of delta wings of high speed aircraft, wherein a strong axial flow stabilizes the symmetric vortices along the top of the craft. In such a configuration, the leading-edge vortex and tip vortices are one in the same. However, Lentick *et al.*'s preliminary tests using a dynamically scaled fly wing (*Drosophila melanogaster*) at Re = 110 and 1400 were conducted to determine whether tip effects or wing sweep alone could stabilize a leading edge vortex [68]. For sweep angles of 0 to 60° and angles of attack from 0 to 90°, results show a purely translating wing very quickly shed the LEV indicating the presence of a tip vortex alone is insufficient to stabilize an LEV. Additionally, swept wing configurations are also incapable of stabilizing LEV. However

Lentink *et al.* did experience elevated lift coefficients and stable LEV production when the wing was rotated about its base as in the case of flapping. This would indicate LEV stability in insect flight is not attributed to the same mechanisms found in delta wing aircraft [68].

This does not necessarily exclude tip vortices from the stability process. This may indicate the effect of tip vortex influence depends on the aspect ratio and span of the wing. Birch *et al.* put forth two possible explanations as to the prolonged leading-edge vortex attachment in three-dimensional flows [11]. The first of which is the existence of base-to-tip spanwise flow formed in the spiral vortex limits the growth of the leading-edge vortex by removing momentum from the vortex core. This can also be described as vortex stretching in which the vortex is elongated by spanwise flow. Alternatively, Birch *et al.* hypothesizes a downward velocity induced by the tip vortex. Such a flow may reduce the effective angle of attack of the wing and thereby attenuate the growth of the LEV [11]. Both hypotheses are tested with a robotic flapper dynamically scaled to mimic the *Drosophila* wing. Just as expected, observed is a spanwise flow drive by the pressure gradient from the variation of local stroke velocity along the length of the wing. From DPIV the peak spanwise velocities approached nearly 40% of the wing-tip velocity in the rear two-thirds of the wing as illustrated in Figure 1.25. The spanwise flow remained relatively low within the leading-edge vortex itself. It appears then that spanwise flow is not strictly confined to the LEV core but rather appeared as a sheet along the chord.

To test if the detected core flow was sufficient to provide the necessary stability, two "teardrop" fences were placed on the wing as to disrupt any possible axial flow. One test placed these fences at the front of the wing to coincide with the LEV core and another test placed these fences at the trailing edge to disrupt the broad posterior sheet of spanwise flow (Figure 1.26). The former placement had almost no effect on the structure or attachment of the LEV whereas the latter placement showcased a 25% drop in net force. It would seem the posterior flow external to the LEV promoted growth rather than retard it for the sake of stability. Finally, Birch *et al.* construct a circular wall coinciding with the tip of the wing during stroke (Figure 1.27). Such a wall was thought to remove the effects of tip vortex on

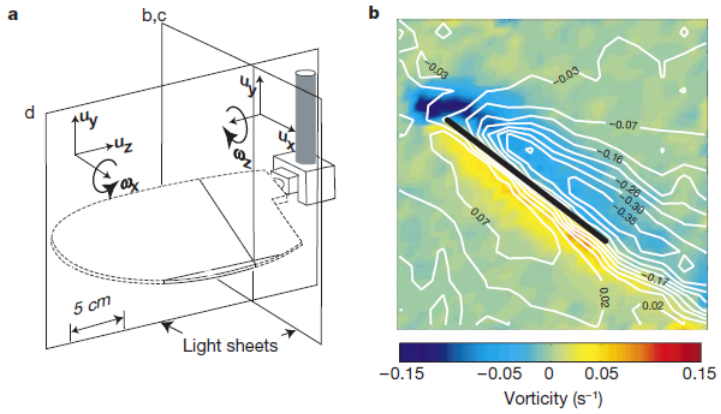

Figure 1.25: (a) Wing apparatus (b) Spanwise velocity contour plot at $0.48R$ superimposed on vorticity plot [11].

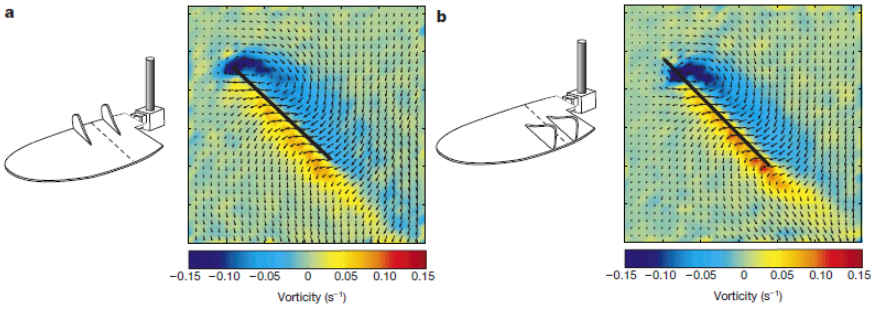

Figure 1.26: LEV remains attached despite forward and rearward fencing. Vorticity fields correspond to $0.48R$. [11].

the LEV attachment. This showed no effect on the dynamics of the LEV attachment but did increase the strength of the LEV by 14% corresponding to an 8% increase in force.

Birch *et al.* suggests the net aerodynamic performance is limited by the strength of the LEV rather than the structure or stable attachment to the wing during the stroke. Nevertheless, this study provides convincing evidence of the tip vortex effect on the leading-leading edge vortex. In an experiment conducted by Ringuette *et al.* examining tip vortices on a free-end translating flat plate it was observed the tip vortex contributes substantially to the overall plate force. Although results varied depending on aspect ratio, they show that the interaction of the tip vortex and the LEV generated a high transient drag peak, whereas

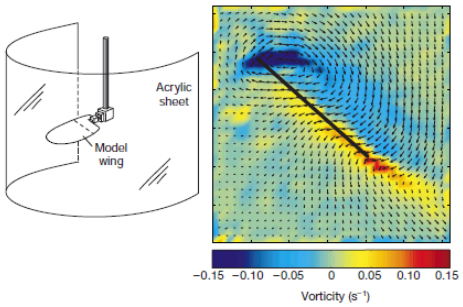

Figure 1.27: Wall designed to remove tip vortex effects. LEV dynamics remain unchanged but strength is increased. Vorticity field corresponds to $0.48R$. [11].

suppressing the flow around the tip results in lower drag. Suppressing the flow around the tip worked to significantly lower the drag. The influence of tip vortex on the force coefficient increases with decreasing aspect ratio. Perhaps this gives reason as to why tip vortices were negligible in previous studies.

1.12 Wing Structure

As nature would have it we find that wings undergo deformations controlled largely by the architecture of the wing, making the study of the structure and stiffness of a biofoil an important one. Birds for example will experience deformations dominated by muscular activation all along the leading edge of the wing which can alter both the span of the wing as well as the effective lifting area. In decreasing a lifting the lifting area, the local stiffness of the wing is increased due to the overlapping of feathers. Insects on the other hand physiologically do not have muscular structures extending into the wings, flapping is achieved by muscular actuation located at the base. This means deformations experienced by the wing are passive responses to the aeroelastic effects. The passive response is thought to be a result of the venation of the wing which may determine the wings flexural stiffness and modes of deformation. Thus, the architecture of a given wing determines its effective flight regime.

Insect wings are extremely diverse, however there are commonly shared traits. Generally

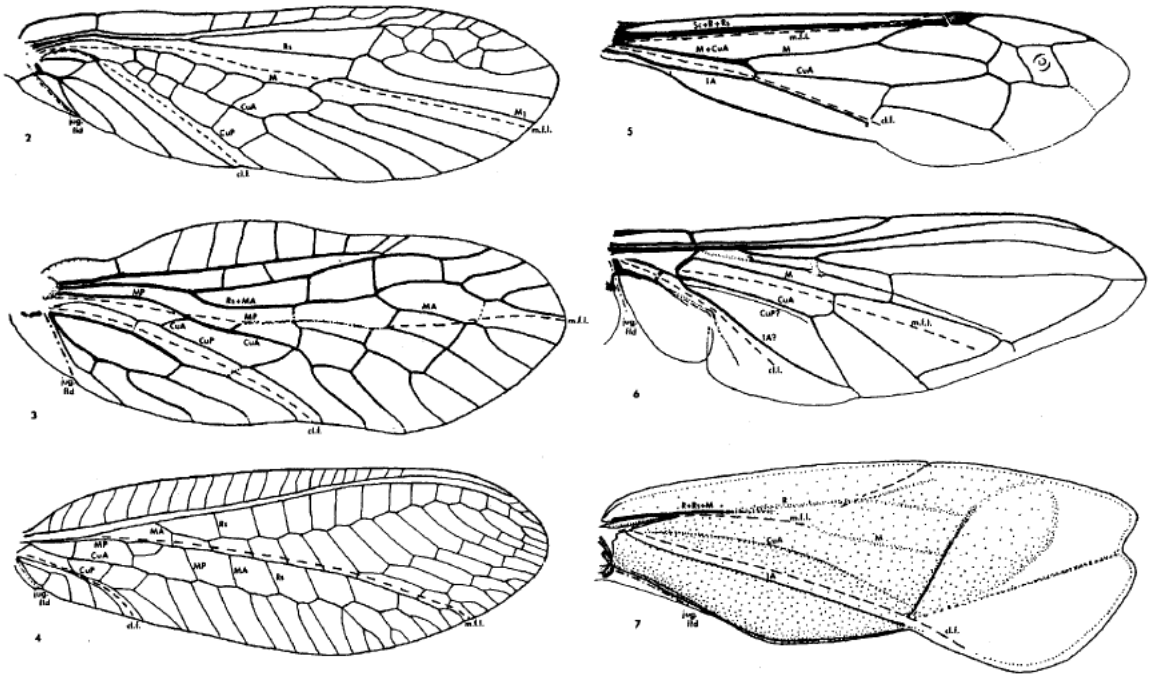

Figure 1.28: Selection of forewings showcasing representative venation patterns and median flexion lines [112].

speaking, most wings consist of a membrane supported by venation. This venation pattern consists of longitudinal veins running from base to tip. Additionally, these veins increasingly spread or fan along the span of the wing. The wing owes much of its rigidity to the coalescence of veins running along the leading edge of the wing. This clustering or thickening of longitudinal veins in the vicinity of the leading-edge results in a 'spar' member capable of withstanding greater loads. The veins themselves are not uniform but rather take on a tubular structure with variable diameter size [113]. Depending on species, we also see cross-veins running along the chordwise direction. With much of the wing support located at the leading-edge much of the wing is susceptible to bending and twisting. Some relief can be had by means of flexion lines along which the wing experiences major deflections, isolating major bending to radially running lines [111].

Because of the mixed media composition of the wing (membrane and veins) and the variability in veins geometry it is difficult to measure a flexural stiffness. However static load

tests conducted on 16 species wings by Combes *et al.* revealed overall wing flexural stiffness did not significantly differ from dorsal to ventral side of the wing in spanwise or chordwise direction in any species tested [17]. Of all the size variables tested the overall spanwise stiffness was most strongly correlated to the wing span. Similarly, the overall chordwise stiffness was most strongly correlated to the chordlength than any other size variable. The measurements also reveal a large anisotropy with spanwise stiffness approximately 1-2 orders of magnitude larger than chordwise flexural stiffness with the spanwise stiffness scaling strongly with the cube of the wing span and the chordwise stiffness scaling with the square of the chord length [17].

A finite element model of a male *Manduca sexta* wing allowed the control of individual member stiffnesses which were subjected to static point forces, static pressure loads and dynamic loading tests [18]. Displacement in the spanwise and chordwise direction of the live wings tested were reproduced fairly well by the exponential fit of the flexural stiffness. Such a stiffness distribution saw most of the deflection confined to the outer third of the wing for static point forces and much of its displacement at the tip of the wing with bending in both the spanwise and chordwise directions for pressure loads [18]. Confinement of deflection to the outer portion of the wing is in good agreement with point force tests on the forewing of *Panorpa germanica* by Ennos *et al.* [33]. The exponential stiffness distribution may be the result of vein tapering in diameter from wing base to tip [111].

1.13 Flexibility and Passivity

Nature has demonstrated the breadth of maneuverability achieved with flapping wing configurations. Such wings are largely characterized by a degree of flexibility, allowing them to twist and bend when loaded. We see greater degree of deformation in the tip region where aerodynamic loads are greatest. It seems camber can do little to attenuate bending in flapping or produce any dorsal/ventral bending asymmetry [18]. We see much of the bending

reserved for the chordwise direction while twisting occurs about the radial axis. Such elastic behavior could provide a means for a wing to reduce its aerodynamic load. Additionally, it may prevent fracture should the insect encounter a collision. In examining a flexible rod in a two-dimensional flow, Alben *et al.* found with increasing flow speeds the drag on the rod transitioned from the classical U^2 scaling to a reduced $U^{4/3}$ drag law by means of streamlining [2]. It becomes apparent the effects of flexibility can potentially be profound. Returning to flapping wings, this bending behavior could determine the nature in which flexible wings interact with the wake in hover.

Highly characteristic of flapping wings is the largely passive manner in which the wings deflect by means of inertial and fluid forces. The wing contains no means to actively prescribe instantaneous shape beyond muscular actuation at the base of the wing, leaving much of the mechanics passive. This presents a unique situation which asks to what degree does the fluid force determine the wing shape and vice versa. Daniel *et al.* addresses the question as to whether or not bending in a wing is largely determined by inertial or fluid forces [20]. It has long been held the instantaneous bending in a wing during flapping was a direct result of a combination of the two forces. Of interest was the hawkmoth, which Daniel *et al.* found the inertial-elastic moments at times during the stroke to be 10 times great than those of fluid dynamic moments. The importance of fluid dynamic moment, however, appeared to increase with increasing wing beat frequency. The hawkmoth represents the larger end of the aerial insect spectrum and operates at the lower limit of wing beat frequency, thus bending by both inertial-elastic and fluid dynamic forces still plays an increasingly important role in smaller insects operating at larger frequencies [9].

Thus far we have seen the force generating mechanisms employed by flapping wings. Furthermore, we begin to see a degree of passivity which places more emphasis on wing design. For example, in the extreme case of a free falling elliptical body, Anderson *et al.* showed the passive behavior resulted in fluttering or tumbling depending on the geometry of the body, the thickness ratio. Although this is a falling body, the local velocity experienced is comparable that experience by flapping wings. However, in flapping wings, the leading

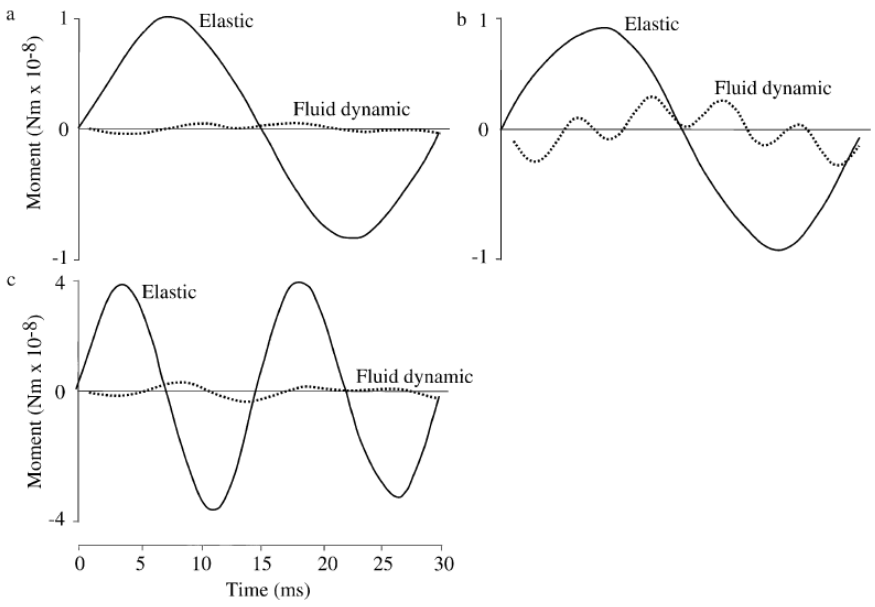

Figure 1.29: Moment contributions by inertial-elastic and fluid forces (a) Wing beat frequency $30hz$ (b) Increased chord length to $3cm$ reduces relative importance of inertial-elastic forces (c) Increased frequency $60hz$ also slightly reduces relative importance of inertial-elastic forces. Inertial-elastic forces still dominate. [20].

edge often remains rigid, leaving much of the deflection and thus the passive components anterior to the wing. The rigid leading-edge usually defines the general angle of attack of the wing with bending occurring further down the chord.

Toomey *et al.* addressed the effects of low order chordwise flexibility on the force signature and shape of a two-dimensional wing in hover [100]. It is found decreasing the time allocated to translational and rotational transitions has an immediate impact on the deflection angle of the wing and the mean lift production whereby both of are increased. This would give reason to believe the wing rotation rate during pitch reversal and timing and the corresponding deflection are the primarily controls the generation of lift. In fact lift force signature closely resembled that of the deflection in the wing. This would indicate force is closely related to the deflection and therefore the instantaneous shape of the wing. Vanella *et al.* also conducted a numerical study similar in configuration, a two-dimensional sinusoidal hovering wing with passive low order chordwise deflection. It was found that a flapping frequency

one-third the natural frequency of the wing produced the greatest lift to drag ratios, ranging from 28 to 21% greater than that of a rigid wing undergoing the same kinematics for the Reynolds numbers tested. Vanella *et al.* attributes the performance increase of flexible wings to an enhanced wake capture mechanism in which a stronger flow around the wing at stroke reversal is present resulting in a stronger trailing edge vortex shed at the end of the stroke.

Passivity is not reserved to chordwise flexibility. As noted earlier a given wing may experience twisting along the radial axis, indicating passivity may be extended to pitch and pitch reversal. Bergou *et al.* explored this idea with a rigid two-dimensional biofoil in flapping where the pitch of the wing was left passive, unprescribed. Operating under such conditions would leave the stroking kinematics active but pitch passive, perhaps reducing energy consumption, ultimately extending flight time. The resulting power consumption indicates passive pitch reversal produced negative power during both pronation and supination with inertial and, to a larger extent, aerodynamic forces contributing to passive pitch.

Although our focus is hovering, passivity proves important in forward flight as well. In forward flight, where the wake is effectively washed down stream, passive deflection of a wing can prove critical to performance. Heathcote *et al.* showed that an airfoil, consisting of 66% flexible material (Carbon Maganese), flapping in a freestream (or rather plunging in this case) generated vortices greatly dependent on plate thickness and thus on plate stiffness and flexibility [42]. The vortex strength, mode of shedding and spatial distribution of vortices depended on stiffness of the airfoil. Ultimately, the stiffness in this case dictated the degree of passivity exhibited by the airfoil.

Thus far we have reviewed the force generating mechanisms in flapping wings and have demonstrated the implications of flexibility and passivity employed by such wings. We now proceed to observe the effects of wing deformation on aerodynamic performance in a series of simplified kinematics pertinent to flapping flight.

CHAPTER 2

Problem Statement

This work numerically and experimentally investigates the development and robustness of vortical structures about low aspect ratio wings in response to deformation at low Reynolds number in biologically-inspired kinematics. Among the vortical structures present considerable attention is given to the leading-edge vortex and the effects wing deformation may entail on LEV formation and lifting performance. This study begins with two-dimensional simulations using the viscous vortex particle method. Of interest is the hover maneuver which offers a unique opportunity to observe strong wing-wake interactions and the aeroelastic response of a flexible wing. Proposed MAVs are intended to operate with wings comparable to those of insects with comparable scale and lift requirements. Inherent in insect wing structure is a degree of flexibility which makes the wing susceptible to passive deformation. In examining the effects of flexibility a lift mechanism unavailable to rigid wings is identified. Flexibility is introduced in a low-order sense and initially reserved for chordwise deflections. Passivity is then extended to pitch of a rigid wing about a predetermined pitch axis.

The leading-edge vortex is largely responsible for the force generated on a wing operating at elevated angles of attack so it is imperative that this vortex remain attached and not separate or shed prematurely. However if the kinematics are restricted to purely translational, relaxing the stroke reversal requirement of hovering, at large convective times there develops a Karman vortex street stemming from the asymmetry in vortical strength and size at the leading and trailing-edge. Two-dimensional high-fidelity simulations of translating wing at fixed angle of attack examine the attenuation of force transients and the adjustment to shedding characteristics in response to passive deflection. Translating wings are

also explored with the flow physics modeled implementing the lower-order techniques of the Brown-Michael equation. This inviscid model idealizes both the leading and trailing-edge vortex as point vortices in the wake while the wing is represented as an array or panel of point vortices representing bound circulation. Though inviscid the Brown-Michael approach still maintains much of the physics exhibited in high-fidelity simulations.

The scope of this study is now expanded for the inclusion of three-dimensional wings and focus is shifted to both passive and active deformation in flapping. The discussion at hand so too expands to take in account key flow phenomena absent in two-dimensional studies, namely axial flow and the presence of a tip vortex. Axial flow, driven from wing root to tip, has long been postulated to induce vortex stretching whereby the flow acts to remove or convect momentum from the LEV core, prolonging the separation process. Of course stretching requires that the axial flow experience a velocity gradient. Thus numerical simulations on flapping wings in hover examine wings undergoing distinct modes of active deformation as a novel approach to axial flow control.

The wings considered are now of finite span and see the development of a tip vortex. The influence of the tip vortex on the LEV remains elusive. Given its proximity it has been hypothesized as being responsible for 'pinning down' the leading-edge vortex to the wing surface through the flow field the tip vortex induces. Efforts to remove the tip vortex effects reportedly resulted in an increase in lift [12] while others have determined the tip vortex insignificant [68]. The degree of influence may be the result of the wing planform geometry and aspect ratio. As such this work examines the formation of the tip vortex and determine conditions under which it proves beneficial to lift production numerically and experimentally. Additionally, we wish examine the response of tip vortex strength and shape to deflections at the wing tip.

Flexibility in three-dimensional wings is presented in the lower-order limit in a manner similar to two-dimensional wings presented. Experimental efforts include hover kinematics on a dynamically-scaled fruit fly (*Drosophila melanogaster*) wing. In testing the operation limits of low aspect ratio wings, the fruit fly wing is examined at Reynolds number associated

with the bursting limit of the leading-edge vortex. The effects of passive deformation in flapping present themselves in this Reynolds number regime as LEV enlargements for select deflection modes. The discussion of passive deflection effects is further advanced in extending passivity to pitching in hover. Finally, biological constraints are neglected as rectangular wings are considered in rotary kinematics. Force measurements on wings over a the course of a complete sweep revolution at elevated Reynolds numbers provide further insight into the nature of LEV bursting and LEV saturation. The inclusion of trailing-edge deflection demonstrates how passivity may promote saturation by virtue of dynamic augmentation of the effective chord length.

CHAPTER 3

Methodology

3.1 Computational

3.1.1 Viscous Vortex Particle Method

Two-dimensional viscous flow simulations are performed using the viscous vortex particle method developed by Eldredge *et al.* [30, 28]. The viscous vortex particle method (VVPM) solves the Lagrangian form of the Navier-Stokes equations for vorticity. Vorticity-carrying particles are utilized as computational elements rather than Eulerian grid-based methods. Particles convect at the local flow velocity carrying with them vorticity. For two-dimensional flow, the vorticity exists only orthogonal to the flow plane, reducing the problem to one of convection and diffusion.

The viscous vortex particle method's treatment of vorticity as a primary quantity makes it well suited for study of vortical structures created by flapping and afford a distinct advantage in efficient computation of the rotational regions of the flow over grid-based methods which use interpolation between grid points to determine the desired field quantities. The velocity of the flow includes particle induced velocity, velocity due to vortex sheet on the body surface, velocity induced by surface deformation, and the free stream velocity [118].

Of great significance of the method is the robust handling of the couple dynamics in the fluid-body interactions. The wings considered are modeled as rigid elliptical bodies constrained to one another via torsional springs, as depicted in Figure 3.1, and will studied will experience large-scale deformation in response to external, inertial-elastic and fluid dynamic forces. The dynamics of the fluid and of the body call for simultaneously solving the

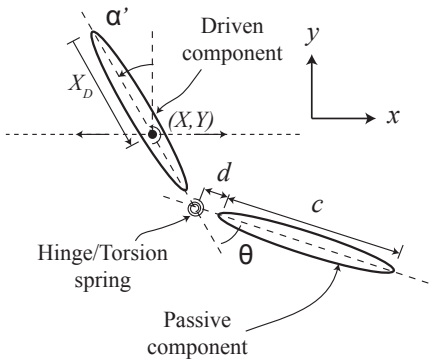

Figure 3.1: Two-dimensional hinged wing model: rigid elliptical constrained to one another via torsional springs and dampers. X, Y denote pivot point of reference body, α' angle of attack of reference body [49].

full Navier-Stokes and elasticity equations of the body which are joined by kinematic and dynamic constraints at their interface [29].

3.1.2 Immersed-Boundary Finite-Volume Method

Three-dimensional flapping wing simulations are conducted using the immersed-boundary finite-volume method developed by Kim *et al.* [59]. The method is based on a finite-volume approach on a staggered grid using a fractional-step method and is well suited for simulating internal and external flows of complex geometries in its introduction of mass sources and sinks as well as momentum forcing to a body surface. Momentum forcing and mass sources/sinks applied ensure the no-slip condition is enforced on the immersed surface and continuity is satisfied.

Unlike an unstructured grid method, the immersed-boundary method considers a body in the flow field a kind of momentum forcing in the Navier-Stokes equations rather than a real body. In this manner a wide range of complex geometries may be easily handled with simple orthogonal grids which typically do not coincide with the solid body surface. Given the freedom from grid constraints an immersed-boundary may also be set in motion without the need to regenerate grids in time thus reducing computational expense over unstructured

grid methods.

To accommodate for the momentum forcing by an immered-boundary surface the Navier-Stokes equation are adjusted to include a discrete-time momentum forcing term. Convection terms are treated by a third-order Runge-Kutta method and diffusion terms with a second-order Crank Nicolson method. Forcing terms are enforced in a staggered fashion and applied only to the immersed body surface or inside the body. For a stationary body, forcing points which coincide with the immersed boundary are set to zero. However, as often is the case, forcing points exist inside the body and require second-order linear and bilinear interpolations dependent on whether neighboring forcing points also exist inside the body.

In applying momentum forcing the velocity at forcing points inside the body obtain a velocity equal and opposite to that of external grid points in the fluid. However, this results in cells with a net influx or outflux of mass into the cell, violating continuity. Therefore, it is necessary to introduce a source/sink term in teh continuity equation for the cell to satisfy mass conservation.

3.2 Experimental

3.2.1 Flapper Apparatus

Experiments on flapping wings were performed at the University of California, Los Angeles in a $1\text{m} \times 1\text{m} \times 0.6\text{m}$ acrylic tank as shown in Figure 3.2. Reynolds numbers considered range $\text{Re} = O\left(10^2\right) - O\left(10^4\right)$. The working fluid of choice was water held at room temperature, $20°C$, Table 3.1. Insect wings normally operate in air and the fluid choice acts to increase fluid viscosity over that of air thereby allowing experiments to be conducted at reduced speeds, simplifying data acquisition. Force measurements conducted on the insect scale would prove rather noisy and imaging techniques would require strobe or illumination sheets operating at frequencies slightly reduced from the stroke frequency. In order to maintain the same fluid behavior across multiple scales Reynolds number matching dictates the reduction

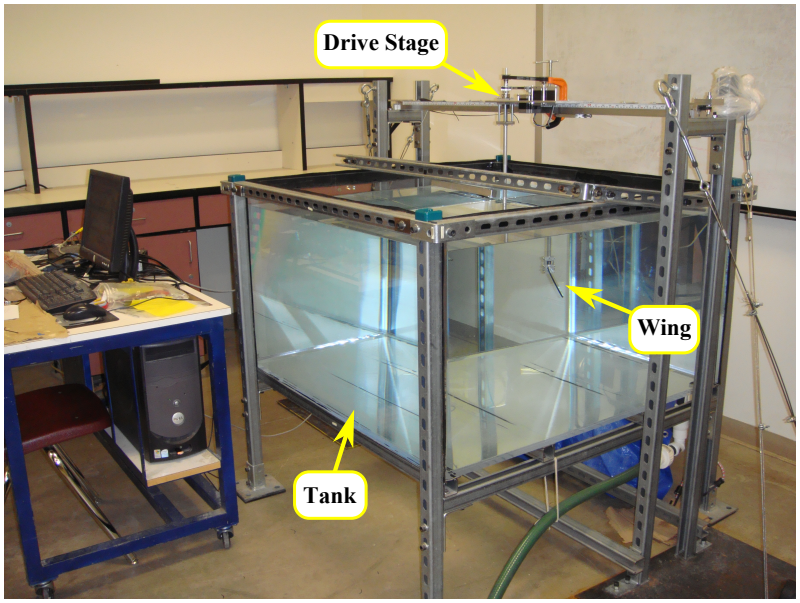

Figure 3.2: Tank and flapping wing apparatus.

in speed must also be met with an enlargement in size. Therefore wings considered are dynamically-scaled to larger sizes over those of typical insect wings. The tank is more than sufficient to accommodate a wing and its corresponding support structure in additional to several chord lengths ensuring wall interference is not an issue.

Affixed above the tank is the motion-control drive stage mounted on a rail spanning the length of the tank as shown in Figure 3.4. The rail system allows easy adjustment and reconfiguration of the wing, though for the experiments of interest the stage was situated mid-tank. The stage houses the stepper motors and supports the submerged test body. More specifically the control stage connects to the test body via coaxial aluminum rod and tube running vertically and terminating at a 90° bevel gear box which then supports the wing at the base. The rod and tube are allowed to rotate independently with each communicating to their respective dedicated stepper motors via drive belts. Rotation of the tube corresponds to rotation of the entire test body about the tube central axis, providing for a heaving or sweep motion about a stationary axis. Actuation of the inner rod directly utilizes the bevel gear resulting in a pitching motion of the wing. The combination of the two motors can replicate the hovering and rotary maneuvers with motion only restricted to the horizontal

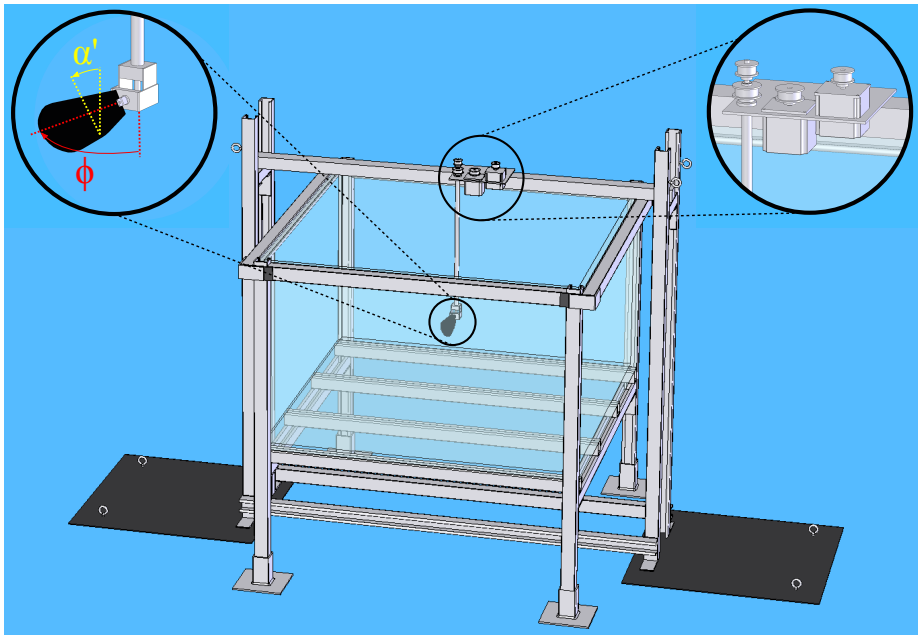

Figure 3.3: Tank and flapping wing apparatus design.

plane.

Stepper motor control is achieved via a BiStep2A 2-Amp Stepper Motor Controller board capable of driving single or dual stepper motor configurations, each of which being either unipolar or bipolar. The board is interfaced with LabView via National Instruments BNC-2110, operating in the step/direction mode. This mode requires a digital signal to specify the direction of actuation of a motor (clockwise or counter-clockwise) and a square digital waveform providing an actuation frequency. Each low to high transition of the square waveform corresponds to a microstep of the motor. The frequency of microsteps f_{ms} to be taken over the time step size Δt was determined by:

$$f_{ms} = \frac{(\theta_{t+\Delta t} - \theta_t) \cdot (\Psi) \cdot (200\text{steps/rev}) \cdot (\text{rev}/360^\circ)}{\Delta t} \tag{3.1}$$

where θ_t and $\theta_{t+\Delta t}$ are angular positions determined by discretized kinematics, Ψ is the microstep size by which a full step is discretized, and Δt is the time step size of kinematic discretization. In this manner the desired kinematics are discretized into a series of mi-

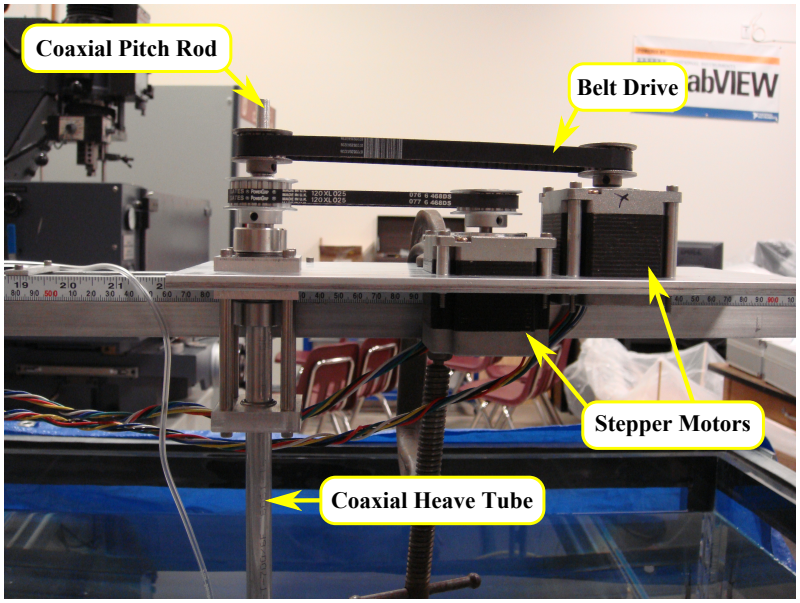

Figure 3.4: Flapping apparatus drive stage. Hover maneuver is achieved by a combination of heaving and pitching via independent actuation of dedicated stepper motors driving a coaxial rod and tube.

crosteps with the speed of kinematics determined by the frequency of microsteps taken. Input kinematics for the test body are read from output files of Matlab script.

The test bodies considered are dynamically-scaled fruit fly (*Drosophila melanogaster*) wings, Table 3.1. Under examination are three distinct wing configuration with variable stiffness: rigid wing, root-flexion wing, and tip-flexion wing as shown in Figure 3.6. The rigid wing may be thought of as the limiting case of infinite stiffness and should serve to produce baseline data for comparative purposes. As previously noted flexibility is viewed in the lower-order limit, hence the emphasis of major flexion lines. Flexion lines are represented experimentally by the inclusion of a hinge allowing for passive deflection. Additionally, torsional springs are positioned about the hinge offering torsional resistance or elasticity. The root-flexion wing allows for a segment of the root constituting 32% of the wing area to passively deflect under inertial-elastic and fluid forces applied. Similarly, the tip-flexion wing allows for nearly 37% of the wing area to deflection about a hinge near the wing tip. Flexion lines permit the relative hingewise movement of whole areas of a wing, allowing, for

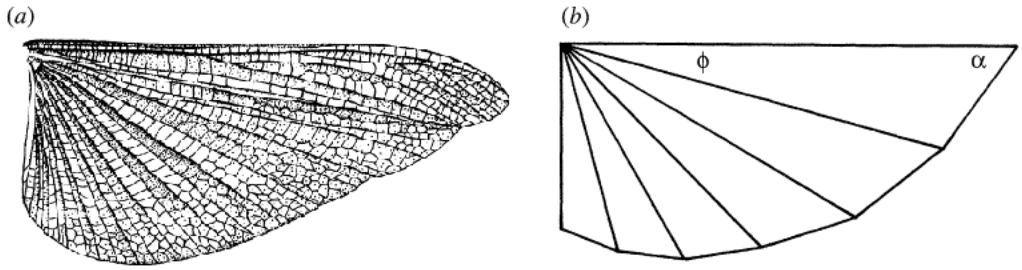

Figure 3.5: (a) Locusta migratoria hindwing (b) Logarithmic spiral fit [114].

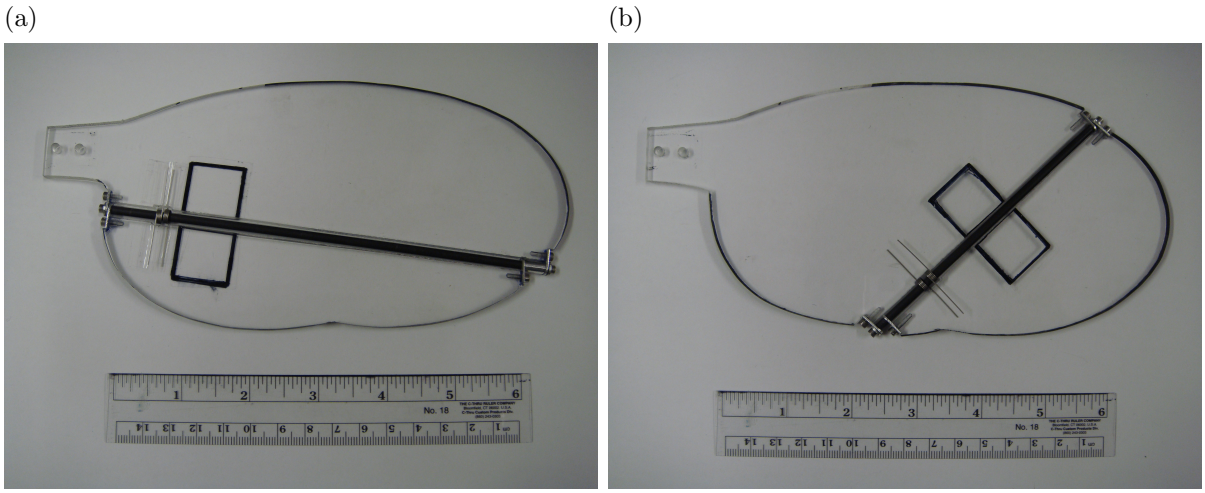

Figure 3.6: Dynamically-scaled fruit fly (*Drosophila melanogaster*) wings with passive (a) root and (b) tip deflection about a hinge that transects the wing. Torsional springs provide resistance. The rigid wing counterpart shares the same planform with the exclusion of a hinge.

example, alteration of camber at different stages of the stroke [112].

Previous studies have concerned themselves with the construction of a venation pattern within a wing to achieve flexibility [97] [92]. However, ultimately this pattern gives rise to major lines of flexion achievable with rigid members constrained to one another via hinge. The approach undertaken here forgoes the vein-membrane construction altogether while maintaining similar passive behavior. Flexioin modes were selected to represent and isolate different flexible phenomena observed in insect wings. Root deflection is characteristic of low aspect ratio wings $AR \leq 3$, while tip deflection is most predominant at larger aspect ratios.

Deflection history:

Resultant deformation in flapping in both flexion configurations is reconstructed via image analysis. A single CCD camera operating at 30Hz was used to capture the deflection about the hinge of the 5th stroke cycle. Aiding in determining the deflection angle were 2cm $\times$ 2cm square markers situated on each side of the hinge. The experiment was then physically modeled in SolidWorks cading software and matched to image captures of the experiment. Frame by frame the model was configured to align with overlays of experimental flapping images, including the deflected portion of the wing. In this manner the angle of deflection is easily calculated over the course of a representative stroke.

Dye Visualization:

Dye visualization was conducted to provide qualitative insight into vortical structure formation and phenomena about the flapping wings. Running along the leading-edge of the wing a (material) tube was affixed of outer diameter 1/8in and inner diameter 1/16in. External to the tank the free end of the dye tube connected to an injection syringe operating manually. The fixed end was sealed off and two additional holes $\approx$ 1/32in in diameter were added running parallel to the length of the tube spaced 1cm apart. Opting to inject dye in this manner, which may seem a minor detail, was intended to proceed with injection while minimizing artificially inducing an axial flow velocity component beyond the merits of the flapping wing on its own accord. Images capturing was conducted using both a CCD camera and high speed Phantom (model) camera alternatively operating at 30Hz and 100Hz respectively. The dye used for flow visualization was a mixture combining four parts blue dye, one part rubbing alcohol (get scientific name), and one part dairy creamer (check mixture ratios).

Particle Image Velocimetry:

Single-sheet particle image velocimetry was conducted about flapping wings. The working fluid was seeded with nearly neutrally-buoyant silver-coated glass spheres of 10μm diame-

ter and specific gravity of SG = 1.1. A vertical laser sheet produced by a New Wave Solo III Nd:YAG laser illuminating seeding particles via reflection. A high speed 2 megapixel Phantom v9.1 camera positioned perpendicular to the tank and the laser sheet captures the seeding particle movement flowing about the flapping wing. The image plane is coincident with the laser sheet with laser sheets oriented to capture chordwise planes along the span. To reduce laser reflection and illumination of the wing and apparatus all immersed bodies were treated with a black adhesive coating and subsequently sanded to produce a matte black finish. PIV techniques include both single and double exposed images. Flow fields were determined from images processed processed using the MatPIV toolbox package in Matlab and in LaVision DaVis software.

3.2.2 Rotary Wing Apparatus

Rotary wing experiments were performed at the University of Maryland in an 18in $\times$ 18in $\times$ 18in glass tank as shown in Figure 3.7. Tests include two separate working fluids offering a range of Reynolds numbers $\mathrm{Re}_{3/4b} = O\left(10^3\right) - O\left(10^4\right)$. The first fluid was water at $20°C$, just as before. The second fluid was a 50/50 mixture by volume of water and glycerin maintained at $20°C$, Table 3.2. The mixture proved miscible with no indication of dissociation between the two constituent fluids. Of interest here is the Reynolds number regime associated with LEV bursting. Use of pure glycerin as working fluid would have made for Reynolds numbers well below the intended mark, thus the addition of water was necessary to reduce the viscosity. The kinematics considered are strictly rotational, completing one full revolution of 360°. Wall effects were negligible on the wing considering the tank size accommodated the wing and sever additional chord lengths. Further, the kinematics no longer required several stroke cycles for the flow to become fully developed as is the case in hover kinematic studies.

As before, affixed above the tank is motion-control drive stage housing the stepper motor, driver and stainless steel drive shaft as shown in Figure 3.8. The shaft extends from the control stage where it is fixed by a bearing, traversing the entire depth of the tank where it

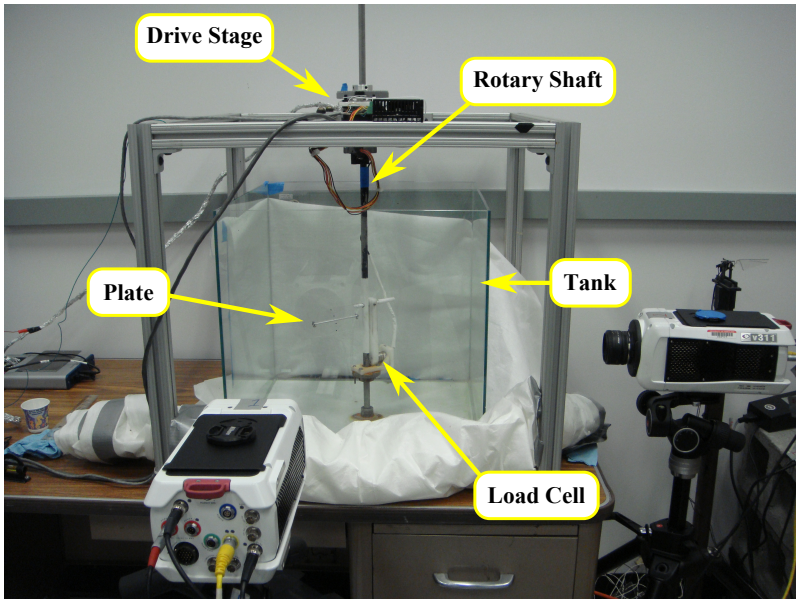

Figure 3.7: Rotary wing apparatus.

is held in place by a fixed bearing and is belt-driven with a 6:1 gear ratio from the motor. The kinematics in this system are restricted to one degree of freedom: rotation about the shaft. Therefore tests are conducted at fixed angle of attack. The wing is mounted from the leading-edge to an aluminum rod which runs clear through a bore in the drive shaft with attention given to ensure the rod does not come into contact with the shaft. Riding a collar about the shaft is a force balance which does not reside coaxially with the support rod of the wing. Rather the balance is offset further down the shaft to a depth below that of the wing in order to minimize its influence on the flow field. The force balance then communicates with the wing via stiff vertical column attached to the balance and extending to the support rod of the wing. Forces experienced on the wing are now transferred directly to the balance.

The stepper motor is actuated by a driver operating in step/direction mode. The driver communicates with LabView script via a National Instruments DAQ card. The desired kinematics are discretized in Matlab to produce a series of high/low signals with a low-to-high transition interpreted as a microstep in the designated direction. In this manner, the kinematics may easily be changed pending the input file from Matlab into LabView. The DAQ card also records force, moment and angular position data at a sample rate of 1000Hz.

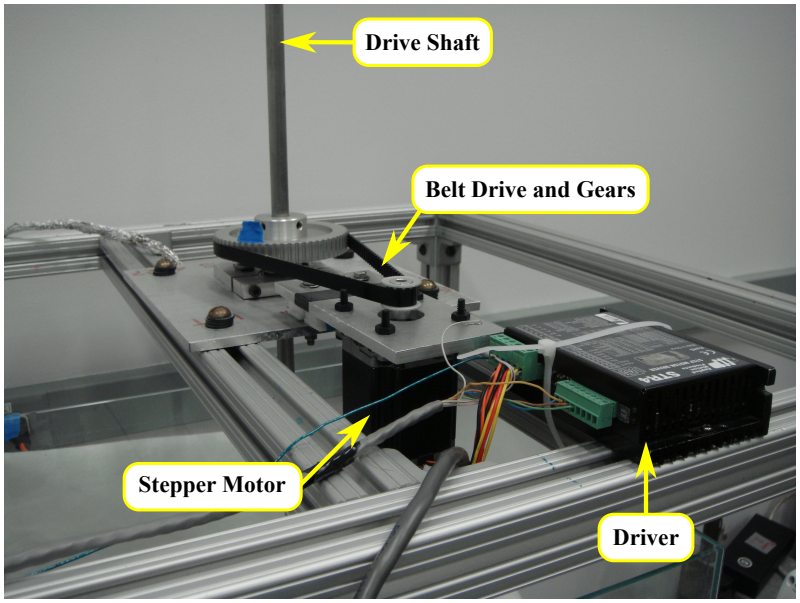

Figure 3.8: Rotary wing apparatus drive stage. A single stepper motor drives the rotary shaft producing a sweeping motion of the plate at fixed angle of attack.

The stepper motor was equipped with an optical encoder reading angular position output.

The wings tested are defined by a rectangular planform, neglecting biological geometric considerations as variability among creatures is vast as shown in Figure 3.9. This includes aspect ratios of $AR = [1, 2]$ with rigid and flexible wing counterparts represented, Table 3.2. Flexibility is confined to a single hinge introduced at the mid-chord position of the wing, running the span of the wing parallel to the wing leading-edge. At any given point during the revolution 50% of the wing are is susceptible to deflection, uniformly altering the wing's effective chord length defined as the distance between the leading and trailing-edge. It should be noted the hinge does not contain any torsional resistance such as springs or dampers leaving deflection to be determined by inertial and fluid forces.

Force Measurement:

The National Instruments DAQ card also records force and moment at a sample rate of 1000Hz. Force and moment data is provided by the ATI Nano 17 IP-68 six degree-of-freedom load cell supporting the wing. Force measurements are first taken with each wing

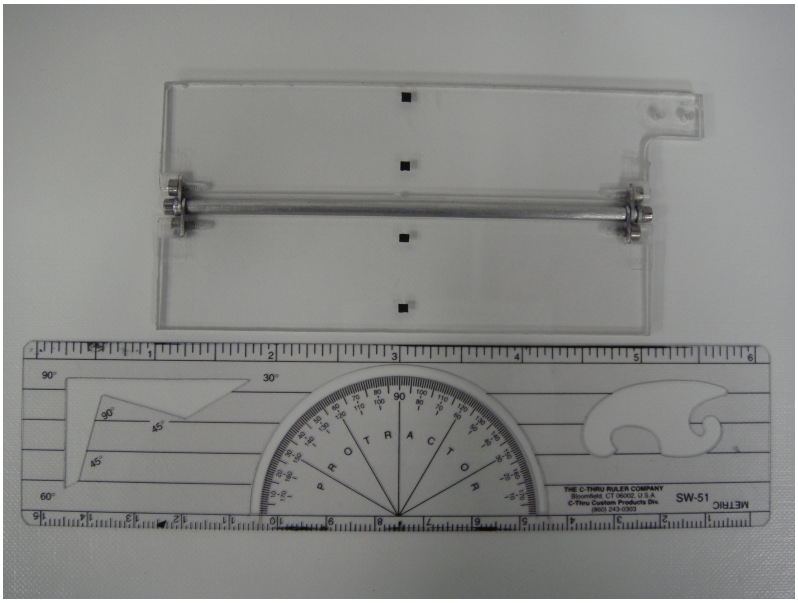

Figure 3.9: Representative rectangular hinged plate of $AR = 2$. Deflection is isolated to the midchord position via the inclusion of a hinge running the entire span connecting two planar bodies. Rigid plate counterparts consist of a single planar body with the exclusion of the hinge.

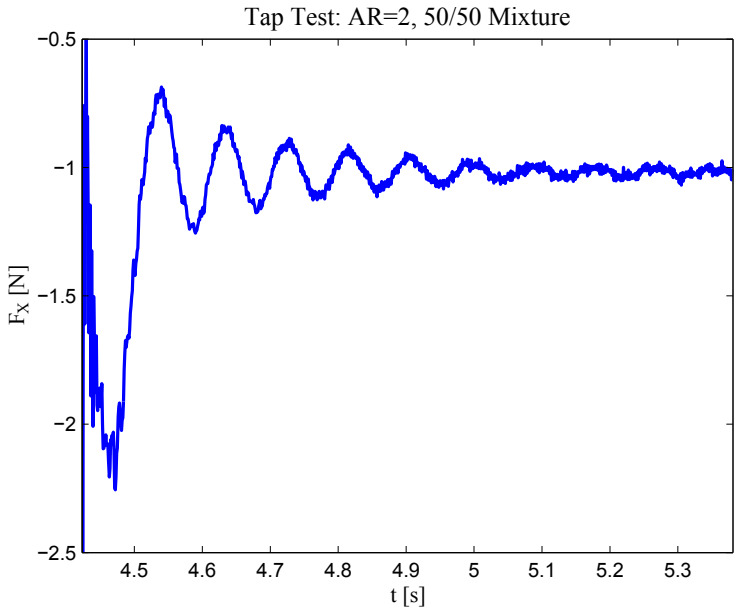

Figure 3.10: Tapping tests on a rigid plate of $AR = 2$ submerged in a 50/50 mixture of water and glycerin by volume. The vibrational frequency response of the wing is to be removed using band-stop filters.

operating in air for a total of 10 runs. The data is then averaged and represents the inertial forces of the plate kinematics to be subtracted later. Once the working fluid is added a series of tapping tests are conducted on the stationary plates to examine the harmonic frequency response as reflected in the recorded data as shown in Figure 3.10. A low-pass Butterworth filter of 30Hz is used to remove electrical noise and other high frequency noise sources from each experimental run. After the low-pass filter is applied, the data is averaged over $5 - 10$ consecutive runs. The inertial forces are then subtracted from the data and a band-stop filter is applied to remove the natural frequency response of the plate in the fluid.

Motion Tracking:

Given the passive nature of the hinged plates there stands a need to quantify the deflection history in response to fluid and inertial forces. The scale of the plates considered do not lend themselves to optical encoder mounted at the hinge that are also capable of operating completely submerged. The necessity of a non-invasive solution to quantify deflection throughout

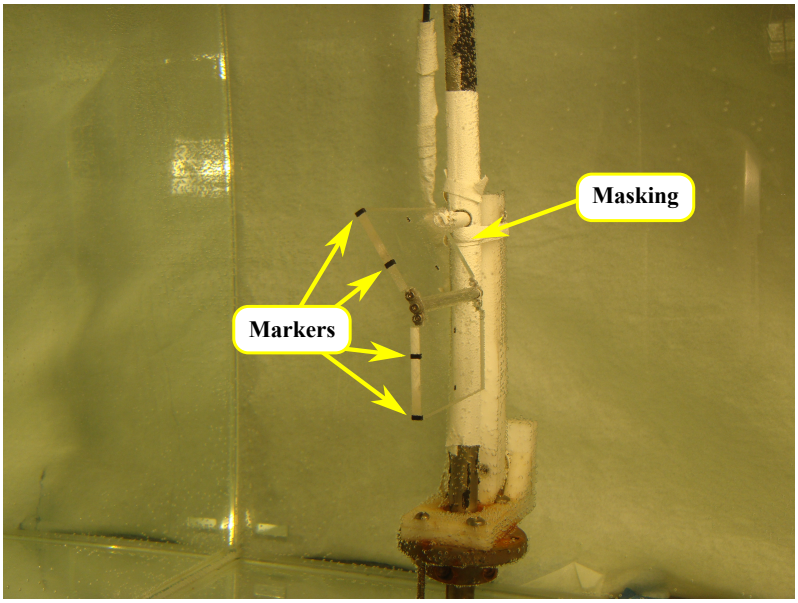

Figure 3.11: Motion tracking markers about the tip of an $AR = 1$ plate. Masking of supporting structure with white adhesive removed background noise during imagine processing with the use of appropriate flood lighting during experimentation.

the stroke cycle that would not induce secondary flow phenomena or interrupt flow fields characteristic of the plate left only high-speed motion capturing and three-dimensional reconstruction methods available. Three-dimensional reconstruction follows high-speed motion captures of the revolving plates. Of interest in the captured images are four markers placed along the tip of the wing running from leading-edge to trailing-edge with each constituent body of the plate carrying two markers spaced 0.75in or 0.50in for $AR = 1$ or $AR = 2$ respectively as shown Figure 3.11.

The experimental setup now includes the use of two high-speed Phantom v311 1 megapixel cameras oriented perpendicular to two adjacent tank walls as shown in Figure 3.12. Images are captured simultaneously at 250hz. To avoid obstruction of imaging by the rotary shaft the tank was divided into quadrants with the two cameras focused only on a single common quadrant. To capture a complete revolution by the wing each experiment was run a total of four times with each consecutive run's initial plate position offset by 90° from the last. The

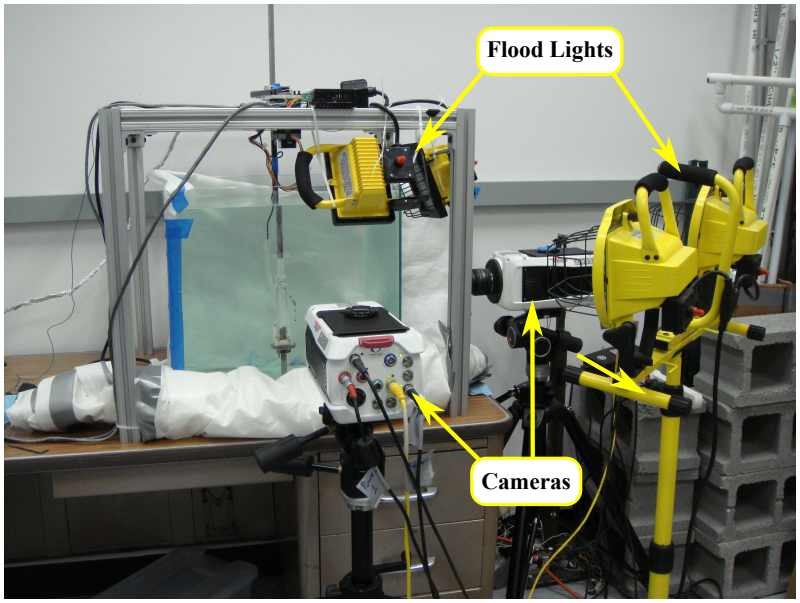

Figure 3.12: Motion tracking experimental setup. High-speed cameras oriented 90° to one another, facing perpendicular to adjacent faces of the tank capture the plate's motion. Flood lighting ensures images are over-exposed thus masking or removing background image noise. The plate is currently revolving out of plane with the rotary axis located to the left of the image.

deflection angle calculation requires that only the markers be captured in any given image. As such, supporting structures are masked with white adhesive as shown in Figure 3.11. Further, a series of floods lights deployed about the tank work to over-expose the images and wash out undesirable masked objects including the background and supporting sturctures, leaving the markers largely accounting for the objects captured as shown in Figure 3.13.

Images are then converted to binary by intensity threshold σ_T. Each image pixel is indexed and its intensity is compared to the threshold with pixels of intensity satisfying $I > \sigma_T$ being converted a value of 1 (white) and pixels of intensity $I < \sigma_T$ converted to 0 (black). With the binary image constructed, adjacent black components are connected to determine the silhouette of bodies within the image. Body or silhouette sizes external to predetermined threshold sizes are discarded. Of the image bodies identified the four markers

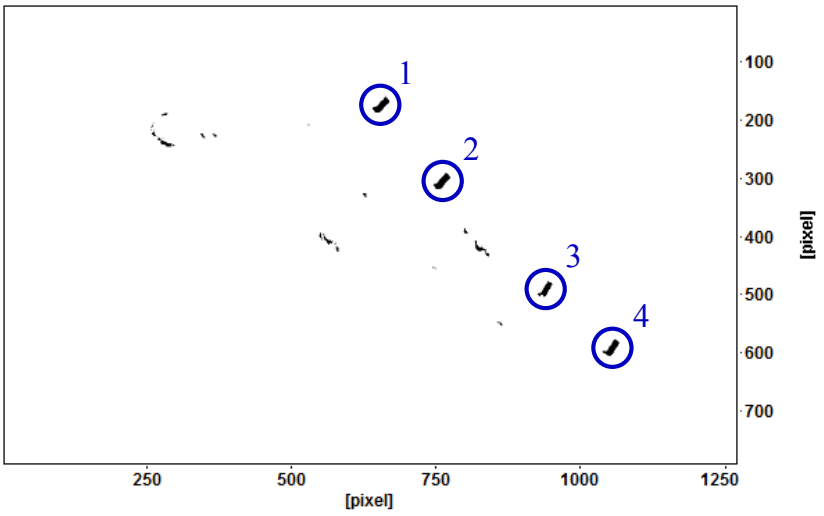

Figure 3.13: Image of $AR = 1$ plate revolving at $\mathrm{Re} = 10^4$ captured by a camera positioned in front of the tank. Flood lighting over-exposes the image and washes out undesirable elements pertaining to the background and supporting structures. The four markers along the wing tip remain predominant and easily identifiable in the resulting image.

are manually selected as the bodies to be tracked from image frame to frame. The marker positions within an image are quantified as the centroid of a marker's silhouette.

Subsequent positions of the specified markers are determined based on proximity threshold of their centroid position at t_{n-1} to body centroids determined in the next frame at t_n. In this manner the four markers' evolution within the image plane are determined for both cameras with u_{ij} and v_{ij} image space coordinates where subscripts i and j specifying body and camera, respectively. Through the collinearity of the camera sensor (image plane), the lens and the markers' position in the laboratory reference frame it is possible to relate a marker's position in the image plane with an array in the laboratory reference frame as proposed by Koehler *et al.* [61]. The map between the laboratory reference frame and the image space follows:

$$u_{ij} = \frac{-d_j \left(r_{j11} \left(x_i - x_{0j} \right) + r_{j12} \left(y_i - y_{0j} \right) + r_{j13} \left(z_i - z_{0j} \right) \right)}{\left(r_{j31} \left(x_i - x_{0j} \right) + r_{j32} \left(y_i - y_{0j} \right) + r_{j33} \left(z_i - z_{0j} \right) \right)} \tag{3.2}$$

$$v_{ij} = \frac{-d_j \left(r_{j21} \left(x_i - x_{0j} \right) + r_{j22} \left(y_i - y_{0j} \right) + r_{j23} \left(z_i - z_{0j} \right) \right)}{\left(r_{j31} \left(x_i - x_{0j} \right) + r_{j32} \left(y_i - y_{0j} \right) + r_{j33} \left(z_i - z_{0j} \right) \right)} \tag{3.3}$$

where $r_{j\mathrm{xx}}$ are components of the rotation matrix R_j between the laboratory reference frame and the image space reference frame. Finally, the four markers are reconstructed in laboratory space with their global position determined by the intersection of the two arrays provided by the two cameras from their stemming from their respective points of view. The two arrays pinpoint the global positions of the markers in the laboratory. With the markers positions determined throughout the stroke there remains the small matter of determining the deflection angle defined as the angle between two vectors, the first of which is determined in three-dimensional space as the vector passing through the two markers on the plate's leading body and the second of which runs through the two markers on the plate's trailing body.

Table 3.1: Flapper Apparatus

Aspect Ratio	$AR\ \left(\frac{b^2}{S}\right)$	2.36
Planform Area	S	$0.0134\,\mathrm{m}^2$
Span	b	$0.1778\,\mathrm{m}$
Chord	$\bar{c}\ \left(\frac{S}{b}\right)$	$0.0757\,\mathrm{m}$
Thickness	w	$0.4445\,\mathrm{cm}$
Root Standoff	r_s/c	0.86
Root Deflection Area	S_r/S	0.319
Tip Deflection Area	S_t/S	0.368
Wing Density	ρ_acrylic	$1173.8\,\mathrm{kg/m}^3$
Fluid Density	ρ_water	$998\,\mathrm{kg/m}^3$
Kinematic Viscosity	ν_water	$1.0 \times 10^{-6}\,\mathrm{m}^2/\mathrm{s}$
Heave Tube Diameter	D_H	$0.50\,\mathrm{in}$
Pitch Rod Diamter	D_P	$0.25\,\mathrm{in}$
Torsional Spring Stiffness	K	$0.035\,\mathrm{Nm}$
Seeding Sphere Diameter	D_S	$10\,\mu\mathrm{m}$
Seeding Sphere Specific Gravity	SG	1.1

Table 3.2: Rotary Wing Apparatus

Aspect Ratio	$AR\ \left(\frac{b}{c}\right)$	[1, 2]
Planform Area	S	[9, 8] in^2
Span	b	[3, 4] in
Chord	c	[3, 2] in
Thickness	w	$0.125\,\text{in}$
Root Standoff	r_s/c	0.50
Deflection Area	S_def/S	0.50
Wing Density	ρ_acrylic	$1173.8\,\text{kg/m}^3$
Fluid Density	ρ_water	$998\,\text{kg/m}^3$
	ρ_mixture	1085.6, kg/m^3
Kinematic Viscosity	ν_water	$1.0 \times 10^{-6}\,\text{m}^2/\text{s}$
	ν_mixture	$5.49 \times 10^{-6}\,\text{m}^2/\text{s}$
Shaft Diameter	D_shaft	$0.50\,\text{in}$
Rod Diameter	D_rod	$0.25\,\text{in}$

CHAPTER 4

Two-Dimensional Flexible Wings

4.1 Introduction

Th effects of flexibility in two-dimensional wings are studied numerically in a series of kinematics intended to distill the role of passive deflection in flapping wing flight. Biological wings are inherently flexible given the asymmetric architecture and variable material density. The wings are void of internal muscular actuation and are driven at the base and resulting deformation is the passive response of the wing to inertial-elastic and fluid forces. The wing is modeled as an articulated body with constituent elliptical rigid bodies constrained to one another via torsional springs and dampers allowing for chordwise bending of the wing. The leading body of the wing is prescribed kinematics with the remaining bodies free to passively respond. The aerodynamic impact and vortical formation times are assessed in a series of configurations and maneuvers including freestream tests, acceleration from rest studies and hover kinematics. These studies help characterize the effects of flexibility force generation and power consumption and in the process identify mechanisms unavailable to rigid wing counterparts. Simulations are conducted using the viscous vortex particle method with dynamic coupling of the fluid-body interactions developed by Eldredge [29, 118].

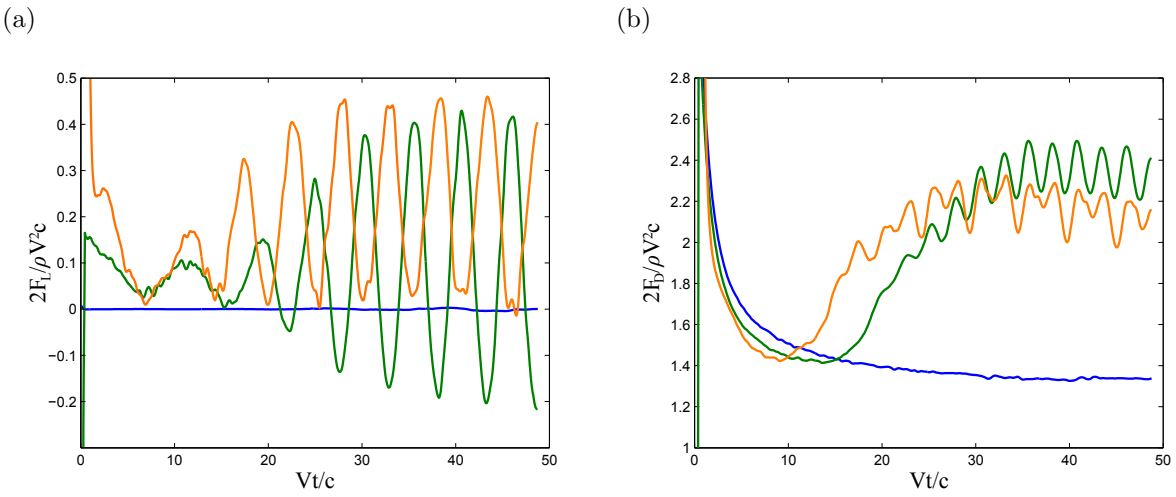

Figure 4.1: Rigid and flexible normal wing response to freestream flow at $Re = 100$. Wings: rigid (——), single hinge (——), double hinge (——).

4.2 Flexible Wing in a Freestream

4.2.1 Shedding Frequency

As exhibited in nature, insect wings are characterized by a degree of flexibility. Additionally, we see these wings operating at large angles of attack ($\alpha > 30°$), experiencing both leading and trailing-edge vortices. Before embarking on placing these wings in various flight kinematics it is only natural that we ask the question as to how the inherent flexibility may attenuate the shedding frequency of leading and trailing-edge vortices. In a bid to isolate flexibility effects and observe the wing at a high angle of attack, we simulate multiple wings using the viscous vortex particle method situated normal ($\alpha = 90°$) to a freestream flow at $Re = 100$. Under such conditions the wing is perpendicular to the oncoming flow.

The wings tested include a rigid wing and two flexible wing configurations, composed of two and three elliptical bodies constrained to one another via torsional springs as shown in Figure 3.1. In accordance with insect wings, the leading portion of the wing, or rather the leading body of the multi-body flexible wings is designated as the active body with a vertical orientation, leaving subsequent bodies in the wing to passively deflect. Results for wings of density ratio $\rho_b/\rho = 5.0$ described by Table 4.1 are shown in Figure 4.1, where

ρ_b is the body density, ρ is the reference fluid density, V is the freestream velocity and c is the chord. The resulting lift of the rigid single body wing remains zero, producing purely drag as anticipated for a symmetric unperturbed wake. Drag smoothly approaches an asymptotic value characteristic of the development of two counter-rotating vortices of the same strength in the wing wake. However, both flexible wings exhibit oscillatory lift and drag signatures, akin to vortex induced vibration studies. The flexible components deflect under the influence of the flow and effectively break the vortical symmetry experienced by the rigid single component wing. This break in wing geometric symmetry prompts asymmetry between leading-edge and trailing-edge vortical strengths, with the former having the greater strength resulting in a net upward lift in both flexible wing configurations. In both flexible cases it takes approximately 28 chords for the oscillatory behavior to fully develop. The drag of the rigid wing, apart from the initial transient spike at the start of the simulation, smoothly approaches a limit.

Table 4.1: Freestream Normal Wings

	Major Axis (a/c)	Minor Axis (b/c)
Single Body	0.5	0.05
Double Body	0.245	0.049
Triple Body	0.16	0.03
	Torsional Stiffness ($K/\rho V^2 c^2$)	Torsional Damping ($R/\rho V c^4$)
Double Body		
hinge #1	0.375	0.0275
Triple Body		
hinge #1	0.375	0.0275
hinge #2	0.2669	0.019574

It is here we identify a lift mechanism unavailable to rigid wings: deflection induced vortical-symmetry breaking. As will be demonstrated in the Section 4.3.2, a flexible wing

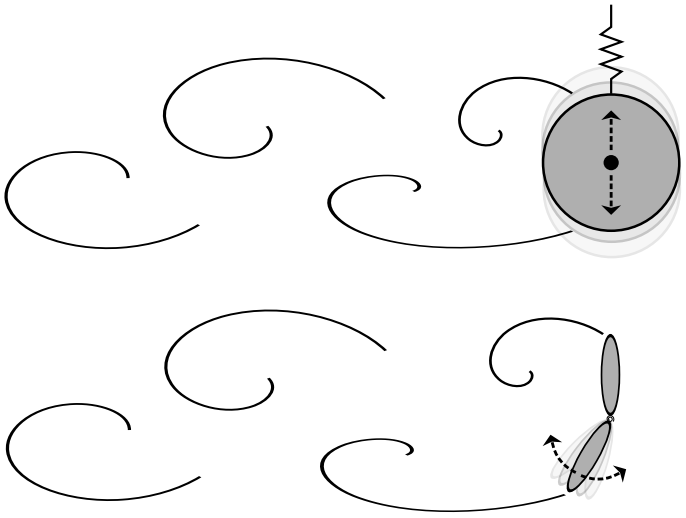

Figure 4.2: Vortex induced vibration modes of a single degree of freedom cylinder with an extensional spring and a passive wing trailing edge with a torsional spring.

will better benefit from such a mechanism operating at elevated angles of attack.

4.2.2 Vortex Induced Vibration

The freestreams studies have shown oscillatory forces and correspondingly oscillatory orientations of the wings tested where peaks and troughs experienced in force were concurrent with maximum and minimum deflections of the hinges. In this light such deflection behavior could be interpreted as vortex induced vibration. We seek now to draw analogies between our wing configurations, more specifically a double-body flexible wing, and the classical problem of an undamped cylinder mounted on an extensional spring in a nominally two-dimensional flow oscillating in response to vortex shedding [10]. The one degree of freedom allotted the cylinder is motion perpendicular to the flow. Similarly the flexible maintains a fixed angle of attack in the leading body of $\alpha = 90^\circ$ while the trailing body is allowed one degree of freedom to passively deflect about the hinge at midchord of the double-body wing as illustrated in Figure 4.2.

Figure 4.3 compares the frequency response of the flexible wing of varying hinge stiffness

to that of the cylinder as a function of reduced velocity U^* [1]. Reduced velocity is defined as $U^* = U/f_n D$ where f_n is natural frequency as defined by

$$\hat{f}_n = \frac{1}{2\pi}\sqrt{\frac{\hat{K}}{\hat{m}_{body} + \hat{m}_{added}}}, \tag{4.1}$$

nondimensional body mass $\hat{m}_{body}$ is defined as

$$\hat{m}_{body} = \pi \frac{\rho_{body}}{\rho_{fluid}} \frac{a}{c} \frac{b}{c}, \tag{4.2}$$

nondimensional added mass of the fluid $\hat{m}_{added}$ is defined by

$$\hat{m}_{added} = \pi \frac{\rho_{fluid}}{\rho_{fluid}} \frac{b^2}{L_{ref}^2}, \tag{4.3}$$

nondimensional spring stiffness $\hat{K}$ is defined as

$$\hat{K} = \frac{K}{\rho V^2 c^2}, \tag{4.4}$$

f^* is the ratio of the oscillatory frequency of the immersed body to the natural frequency, and m^* is the density ratio of the immersed body to the fluid. The cylinder is characterized by synchronization of oscillatory frequency and natural frequency near unity for higher mass ratios and elevated values of f^* with greater lock-in U^* range of the oscillation response for low mass ratio bodies. The double-body wing was tested for a single density ratio of $m^* = 5$ and variability of U^* was achieved via varying torsional spring stiffness. As opposed to the cylinder which exhibited lock-in over a range of reduced velocities for a given m^*, the wing shows no signs of lock-in or plateau regions despite the constant mass ratio between tests. The behaviors it seems are not strictly analogous. The difference arises fundamental difference in shedding mechanics. A cylinder in a freestream naturally develops von Karman street at appropriate Reynolds number. On the other hand, a given wing at appreciable attack angle will naturally encounter asymmetry between the LEV and TEV. Flexibility further promotes this asymmetry in deflecting the trailing-edge thereby further reducing the TEV feeding sheet.

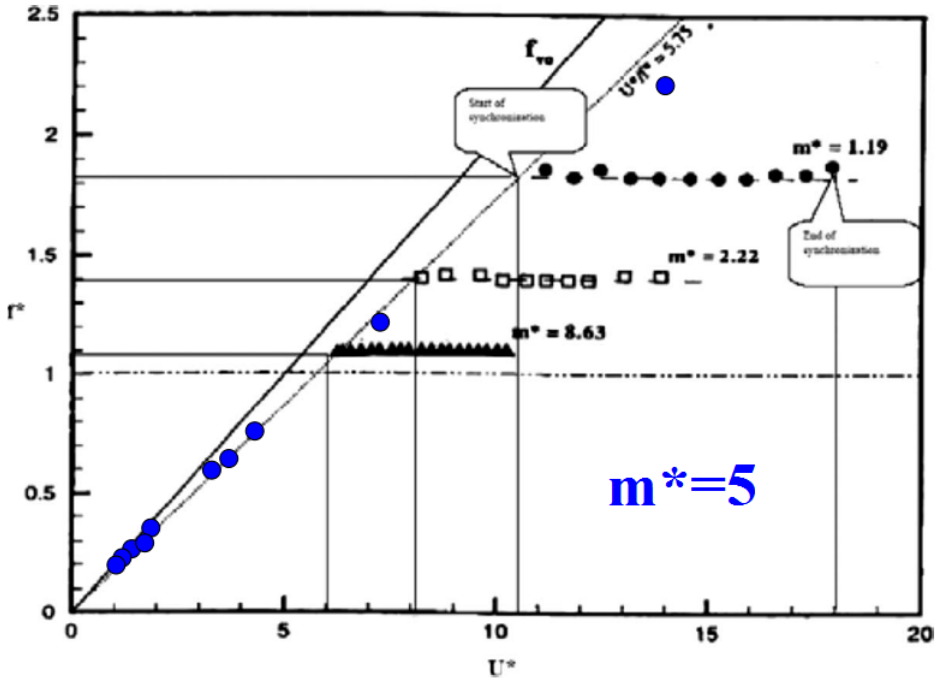

Figure 4.3: Frequency response comparison between a flexible wing of varying torsional stiffness and a cylinder of varying mass ratios in variable freestream reduced velocity U^* [1].

4.2.3 Effects of Torsional Stiffness

The previous section examined a two-component wing undergoing midchord deflection in response to freestream flow. The leading body was fixed at a prescribed angle of attack and the trailing body was free to revolve about the hinge. Here the effects of torsional spring stiffness on aerodynamic load, more specifically on lift, are examined. However, as opposed to prior simulations maintaining fixed α of the leading or reference body, passivity is now extended to pitch. The reference body is allowed passive rotation about its centroid, coincident with a torsional spring of stiffness $\hat{K}_P$. The equilibrium position of the reference body is normal to the flow ($\alpha = 90°$) when unloaded. The loaded configuration is the result of aerodynamic loads and restoring moments of torsional springs $\hat{K}_P$ and $\hat{K}_H$ where the pitch angle is now acquired rather than prescribed.

To facilitate selection of torsional strength combinations an effective stiffness value $\hat{K}_{eff}$

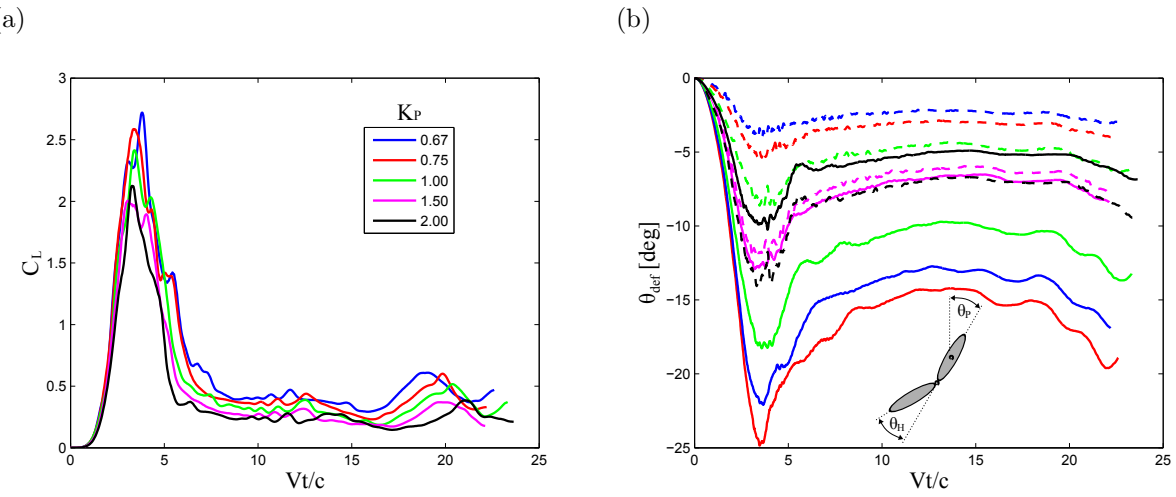

Figure 4.4: (a) Lift and (b) deflection behavior of a two-body wing with passive pitch and hinge deflection for $\hat{K}_{eff} = 0.5$. Deflection: pitch angle with respect to vertical θ_{P} (——), hinge angle θ_{H} (– – –).

is defined as a corollary to extensional springs in series. The torsional springs may be viewed as a series of torsional spring elements determining the orientation of the trailing body. Under this argument simulations are limited to two effective stiffnesses $\hat{K}_{eff} = [0.5, 1.0]$ defined by

$$\frac{1}{\hat{K}_{eff}} = \frac{1}{\hat{K}_P} + \frac{1}{\hat{K}_H}. \tag{4.5}$$

Figure 4.4(a) show lift behavior of a wing in an impulsively started flow at Re = 100 for $\hat{K}_{eff} = 0.5$. All pitch stiffnesses K_P tested are in qualitative agreement. Lifting trends experience a include a substantial peak approximately $\hat{t} \approx 3.5$. The transient peak subsides near $\hat{t} = 6.5$ as lift now maintains a largely steady value before the onset of a secondary peak in lift near $\hat{t} = 16$ and terminating near $\hat{t} = 21.4$. In general it appears there appears an inverse relationship between $\hat{K}_P$ and C_L.

Lifting trends are reflected in the pitch and deflection angles as shown in Figure 4.4(b). Both the pitch and deflection angle experience spikes coincident with those found in lift. With the exception of $\hat{K}_P = 2.0$, pitch angle exceeds the trailing-body deflection angle. The first peak in lift and deflection angles is largely driven by impulsive nature of the flow. However the second peak in lift is much more representative of a leading-edge vortex formation time

(a) (b)

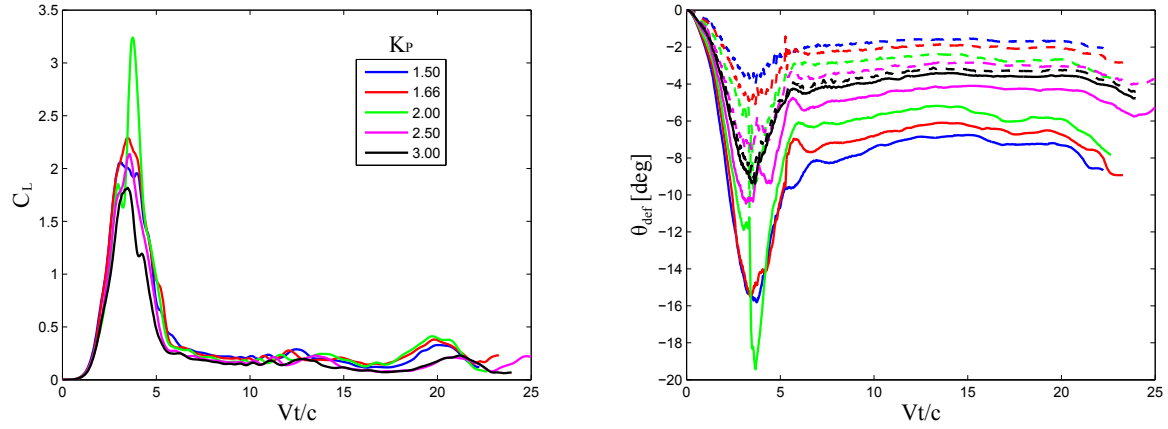

Figure 4.5: (a) Lift and (b) deflection behavior of a two-body wing with passive pitch and hinge deflection for $\hat{K}_{eff} = 1.0$. Deflection: pitch angle with respect to vertical (——), hinge angle (– – –).

one could expect to encounter in wings operating elevated angle of attack. For the duration of the second peak there is in general an increase in pitch angle. It is difficult to distinguish cause and effect between the two however the rise in lift is characteristic of the enlargement of the leading-edge vortex and with this growing vortex its suction influence on pitch orientation potentially grows aft of the pitch axis of he leading-body, contributing further to clock-wise rotation. Similar trends are continued in Figure 4.5 for $\hat{K} = 1.0$ though with what appears to be spurious behavior in the transient peak for $\hat{K}_P = 2.0$.

4.2.4 Leading-edge Vortex Shedding Frequency

It has long been established biological fliers take advantage of unsteady flow phenomena, most notably dynamic stall, to generate sufficient lift. The process of dynamic or delayed stall is not an instantaneous one and the reciprocating motion of a flapping wing occurs on smaller time scales than that associated with fully stalled conditions. Stall is separation of flow about an airfoil resulting in loss of lift. To better characterize the process of stall or rather the LEV formation and shedding a wing of fixed angle of attack is accelerated from

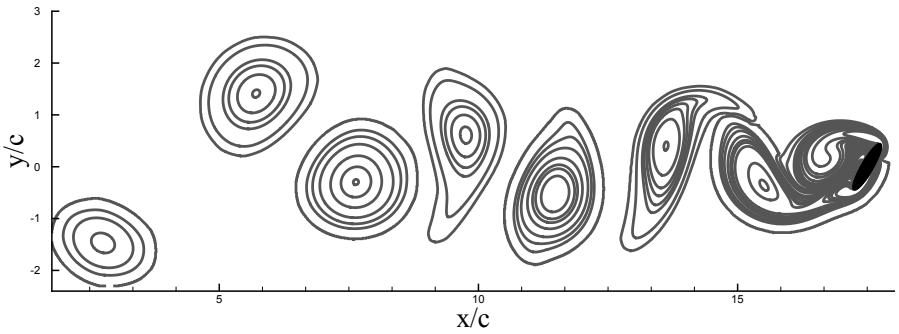

Figure 4.6: Vortex shedding pattern of a rigid single-component wing translating at $\alpha = 60°$ with $\beta = 0$.

rest following the power-law velocity approach of Chen *et al.* [16]:

$$\hat{U} = \hat{t}^{\beta} \tag{4.6}$$

where β values less than unity are reminiscent of acceleration profiles of flapping wings in nature.

The work of Chen *et al.* is expanded upon with the inclusion of chordwise flexibility at the midchord position for two-component wings. Flapping flight permits the formation of a single LEV so consideration here is given to the time scale of LEV development. Time is nondimensionalized by

$$\tilde{t} = \frac{1}{c} \int_0^t U(\tau)\, d\tau \tag{4.7}$$

where focus is now shifted to the number of chords traversed and adding insensitivity to instantaneous velocity [16]. Vortex shedding is demonstrated in Figure 4.6 for a rigid single-component wing.

Figures 4.7, 4.8 and 4.9 demonstrate the effects of flexibility on quasi-steady vortex shedding about an accelerating airfoil with velocity power law constant $\beta = 0.0$, $\beta = 0.25$ and $\beta = 0.5$ respectively. Vortex shedding is interpreted as the frequency at which lift oscillates. The rigid wing behavior is consistent with that reported by Chen *et al.* in that the initial transient peak concludes within a well defined range of $\tilde{t} = 3.6 - 4.1$ chords

traversed. For an impulsive start (Figure 4.7) the formation time of the initial vortex is consistently $\tilde{t} = 4 \pm 0.04$ for all attack angles considered, $\alpha = [30°, 45°, 60°]$. The greatest variability in rigid wing initial shedding comes from $\beta = 0.25$ in Figure 4.8 where signs of attack angle dependency surface: shedding time shows proportionality to angle of attack. The range of initial LEV shedding is minor for $\beta = 0.5$ (Figure 4.9).

The effects of flexibility on initial LEV shedding are negligible for $\beta = 0.0$ and $\alpha = 30°$ with all wing torsional stiffnesses in agreement with the rigid counterpart shown in Figure 4.7(a) despite the degree of deflection experienced for the lower spring stiffnesses. Given the relatively low attack angle the deflection does little to influence initial LEV saturation. Increasing angle of attack prompts greater deflection and influence on shedding time for $K = 0.015$ which now experiences a reduction of approximately 13% while the remaining flexible configurations remain in continued agreement with the rigid wing. Lift magnitudes generated are directly proportional to the torsional spring stiffnesses with the greatest stiffness performing similarly to the rigid wing. A disparity between the stiffest wing and rigid wing lift becomes evident with $\beta > 0$. Similarly, it is for power law value $\beta = 0.5$ that initial LEV shedding time demonstrate proportionality to their stiffnesses as shown in Figure 4.9.

The oscillatory nature of lift production reflects long-time quasi-steady vortex shedding. After initial transient peaks a regular pattern of vortex shedding is established. The frequency of shedding is not constant with the exception of $\beta = 0.0$. The response of shedding frequency for long-time wake formation as function of instantaneous Reynolds number are shown in Figure 4.10 for $\alpha = [45°, 60°]$. The frequency and Reynolds number normalization proposed by Chen *et al.* are

$$\tilde{f} = \frac{\mathrm{Re}_{\mathrm{ref}} \sin^2 \alpha}{\hat{t}_2 - \hat{t}_1} \tag{4.8}$$

and

$$\overline{\mathrm{Re}} = \mathrm{Re}_{\mathrm{ref}} \frac{\tilde{t}_2 - \tilde{t}_1}{\hat{t}_2 - \hat{t}_1}, \tag{4.9}$$

respectively, where subscripts denote time stamps between two consecutive peaks in lift and $\hat{t}$ is time normalized by a reference velocity. The dependency of $\tilde{f}$ on $\overline{\mathrm{Re}}$ maintains a linear profile provided by least-squares fit. The affect of chordwise deflection is to increase

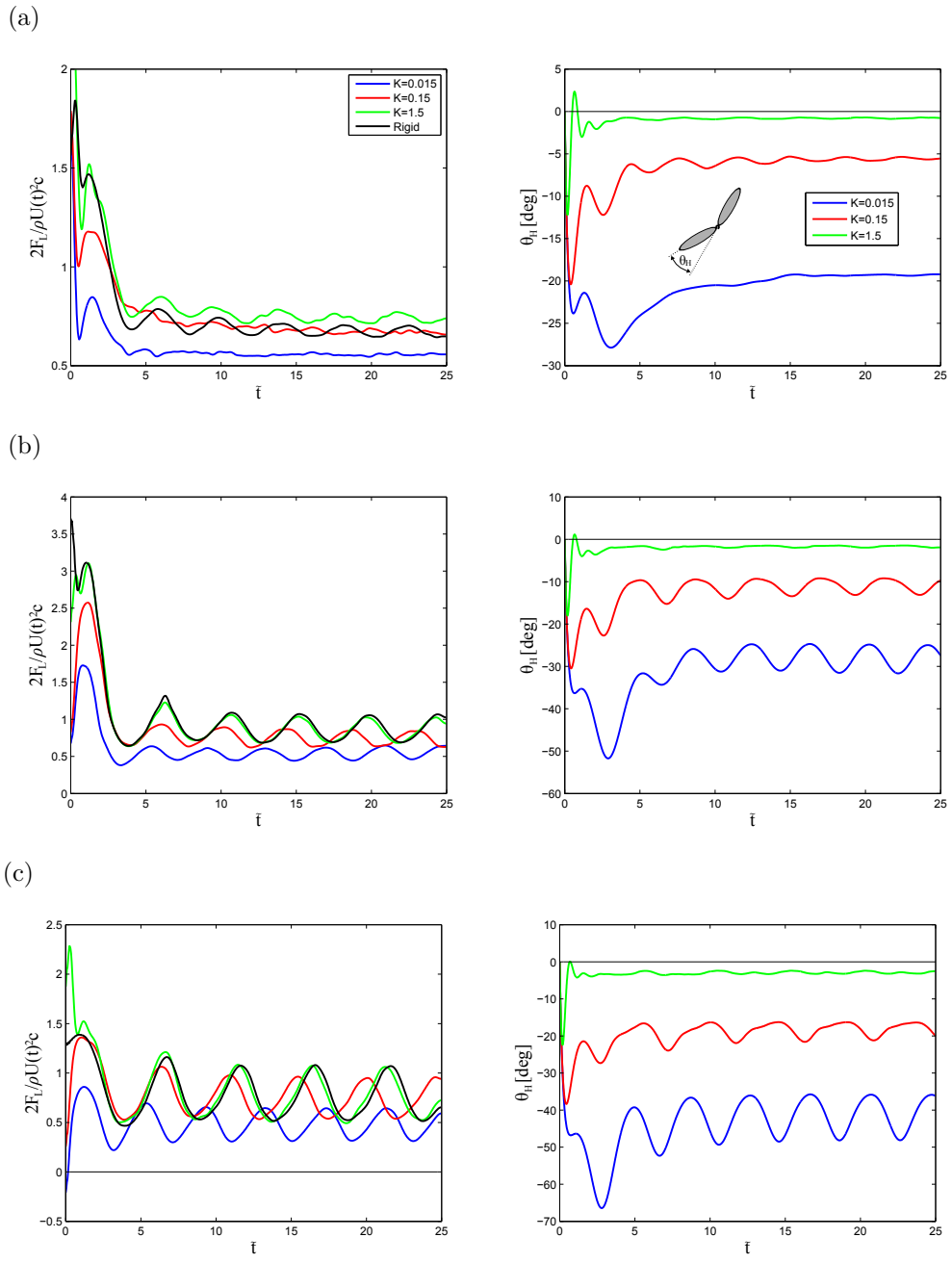

Figure 4.7: Effects of passive trailing deflection on lift peaks behavior of an accelerating wing of velocity power law constant $\beta = 0.0$. Angle of attack: (a) $\alpha = 30°$, (b) $\alpha = 45°$, (c) $\alpha = 60°$. Lift response of the airfoil is shown in the left column and deflection history is shown on the right. Time normalization is based on chords traversed, $\tilde{t}$.

(a)

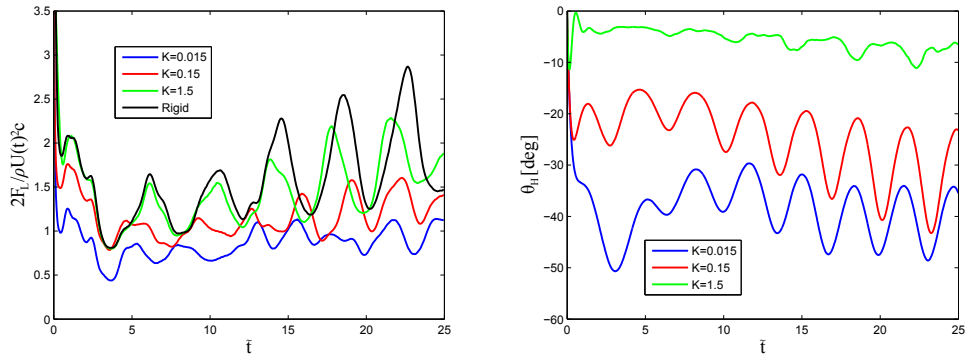

(b)

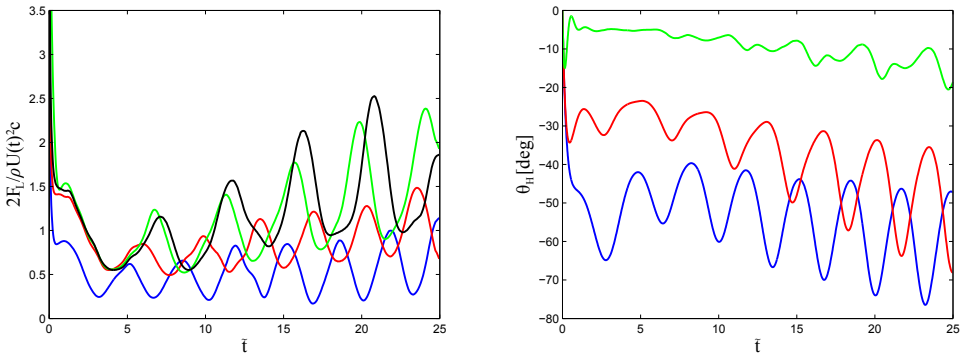

Figure 4.8: Effects of passive trailing deflection on lift peaks behavior of an accelerating wing of velocity power law constant $\beta = 0.25$. Angle of attack: (a) $\alpha = 45°$, (b) $\alpha = 60°$. Lift response of the airfoil is shown in the left column and deflection history is shown on the right. Time normalization is based on chords traversed, $\tilde{t}$.

(a)

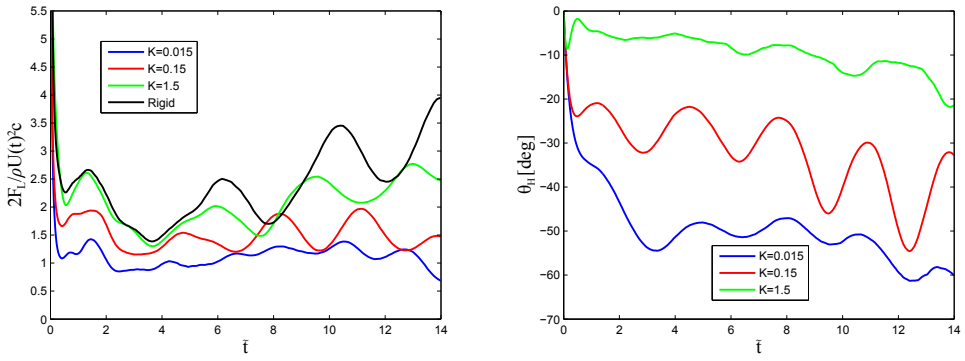

(b)

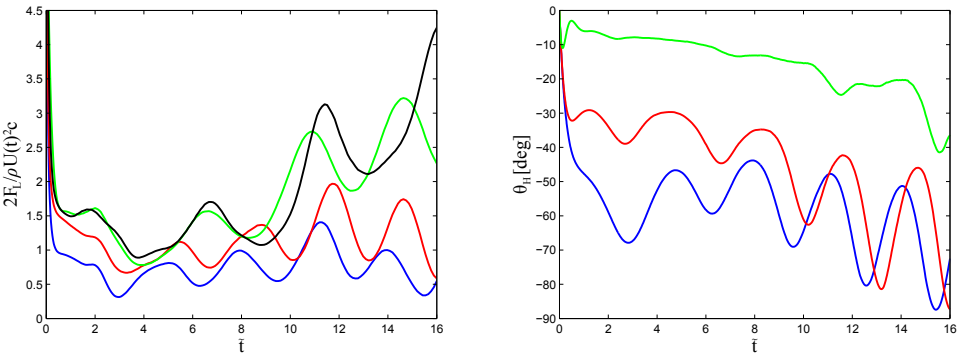

Figure 4.9: Effects of passive trailing deflection on lift peaks behavior of an accelerating wing of velocity power law constant $\beta = 0.5$. Angle of attack: (a) $\alpha = 45°$, (b) $\alpha = 60°$. Lift response of the airfoil is shown in the left column and deflection history is shown on the right. Time normalization is based on chords traversed, $\tilde{t}$.

(a) (b)

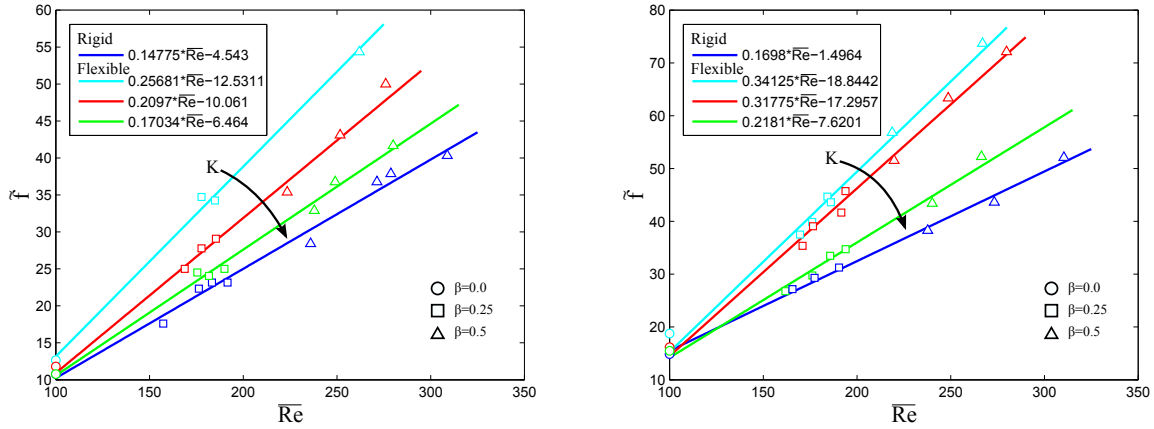

Figure 4.10: Frequency of lift oscillation for rigid and flexible wings at $\mathrm{Re}_{\mathrm{ref}} = 100$ for all velocity power law constants considered. Angle of attack: (a) $\alpha = 45°$, (b) $\alpha = 60°$. Torsional spring stiffness of the double component wing are $\hat{K} = [0.015, 0.15, 1.5]$.

vortex shedding time $\tilde{f}$ for a given instantaneous Reynolds number without loss of shedding frequency independence of acceleration profile or β value.

4.3 Flexibility in Hover

4.3.1 Pitch Phase

The effects of flexibility are now examined in a representative case of a three-component flexible wing (Table 4.3) undergoing passive deflection in hover kinematics. The inclusion of a third body into the flexible wing provides an additional degree of freedom through which the deflection response of the wing may approach that of a fully elastic membrane. Performance is compared to a single-body rigid wing. Hover is accomplished by sinusoidal heaving following:

$$X = -A\cos(2\pi f t) \tag{4.10}$$

where A is the heave amplitude and f the frequency. Pitch about an axis $0.16c$ aft the

leading-edge maintains a constant angle of attack of $\alpha = 45°$ for the majority of the stroke following a hyperbolic tangent waveform:

$$\alpha' = -\frac{\pi}{2} + \frac{\pi}{4}\tanh\left[n\sin\left(2\pi ft - \Phi\right)\right] \tag{4.11}$$

where α' is the pitch angle, n is a smoothing constant, and Φ is the pitch phase. When $\Phi = 0$ pitch is coincident with stroke reversal and is said to be inphase or symmetric. Nondimensionalization is based on the wing chord as reference length $L_{ref} = c$, maximum rotational velcoity as reference velocity $V = \dot{\alpha'}c$ and time normalized by $T_{ref} = c/V$. The pitch axis is confined to a horizontal axis and a given pitch maneuver constitutes 20% of the stroke cycle period.

Table 4.2: Kinematic Parameters

Heave Amplitude	A/c	2
Angle of Attack	α	45°
Smoothing Constant	n	5
Pitch Phase	Φ	0
frequency	f	0.0405

Figure 4.12(a) demonstrates the effects of flexibility on lift generation in hover at Re = 100 with pitch phase $\Phi = 0$ over a representative halfstroke. The lift profiles appear comparable with differences most pronounced during pitch. In fact the greatest similarity stems from the midstroke where, as indicated in Figure 4.12(b), the flexible wing hinges return to a nearly undeflected state where the flexible wing no longer exhibits significant camber. At that point the flexible wing resembles the rigid wing and this physical resemblance is reflected in lift. The deflection history of both hinges remain in sync for the duration of the stroke in that the leading hinge deflection profile is mirrored in the trailing hinge. It is important to note the hinge deflection angle is measure between two consecutive bodies in a wing and the angle between the trailing body and the actively prescribed leading body would be the summation of both hinge angles.

Table 4.3: Flexible Wing

Number of Bodies	N_b	3
Number of Springs	N_s	2
Body Major Axis	a/c	0.16
Body Minor Axis	b/c	0.03
Leading Hinge Stiffness	$K_1/\rho V^2 c^2$	0.42
Trailing Hinge Stiffness	$K_2/\rho V^2 c^2$	0.08
Leading Hinge Damping	$R_1/\rho V c^4$	0.0275
Trailing Hinge Damping	$R_2/\rho V c^4$	0.0195
Hinge Distance	d/c	0.01

As noted above the rigid and flexible wing differ in lift production primarily during pitch. Though the leading reference body undergoes symmetric pitch with $\Phi = 0$ the wing camber often lags stroke reversal with inertial-driven deflection. As a result the wing trailing edge motion can be likened to a whipping motion where the rotational velocity of the trailing edge is that of the leading body in addition to this trailing fling rotational velocity. Vanella *et al.* argued this whip-motion bore little influence on the leading-edge vortex but proved instrumental in strengthening shear layers strength of the end-of-stroke trailing-edge vortex [102]. This may offer explanation to early lift behavior where the flexible wing is able to recover some lift during pitch over that produced by the rigid wing at the start of the halfstroke. Further, the lift peak reduction of the flexible is more gradual than that of the rigid wing at pitch completion at the start of the stroke. This is the result of the prolonged attachment of the end-of-stroke trailing-edge vortex experienced by the flexible wing as shown in Figure 4.11 which enhances wake-capture mechanisms in generating a greater flow toward the wing from the strengthened trailing-edge vortex and the deflected camber also reorients the zero-lift direction. At halfstroke's end the dynamic camber of the flexible wing may work to reduce rotational circulation about the wing. Additionally, the wing compliance may also sacrifices downward momentum at stroke reversal. These devises coupled offer insight into

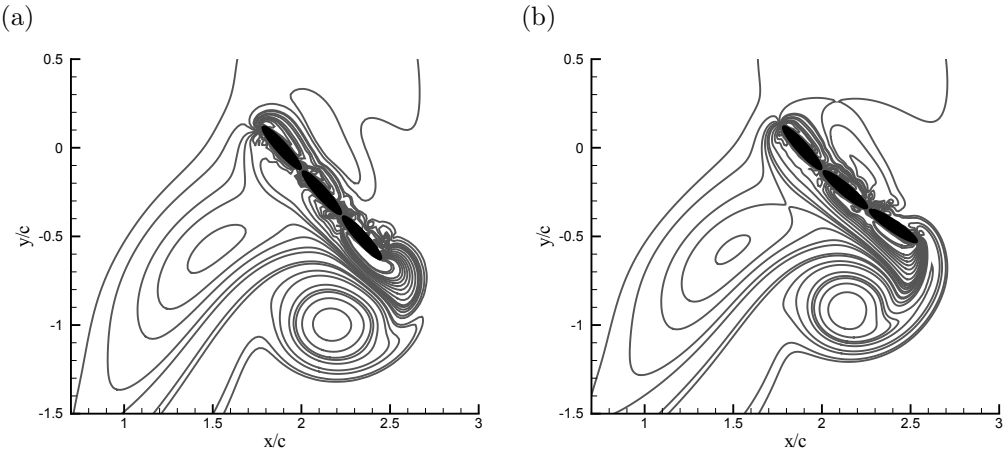

Figure 4.11: Vorticity field about (a) rigid and (b) flexible wings in hover shortly after stroke reversal, $t/T = 3.55$, at $\alpha = 45°$. Reynolds number Re = 100.

the reduction in lift by the flexible wing during pitch at halfstroke's completion. Ultimately the flexible would producer slightly greater$\overline{C}_L$ and experience gains in lift production per unit driving power, $\overline{F}_L V/\overline{P}$, as shown in Table 4.4.

The inclusion of passive hinges has demonstrated potential benefits of flexible wings over rigid counterparts in hover. Hover is the most energy costly of maneuvers in flapping flight and gains in lift to power ratio achievable by flexibility are encouraging. To asses the effects of dynamic camber at different points in the stroke, pitch is shifted from its stroke-symmetric phase of $\Phi = 0$ to $\Phi = \pm\pi/5$. This phase shift of the pitch profile isolates the entirety of a single pitch reversal maneuver to a given halfstroke. Phase of $\Phi = \pi/5$ shifts pitch to initiate coincident with the start of a given halfstroke and phase $\Phi = -\pi/5$ shifts pitch to complete at the end of a given halfstroke. Figure 4.13(a) shows lift during a representative halfstroke of hover for flexible wings of all phases Φ. Figure 4.13(b) depicts the deflection history of the wings' hinges. Phase-shifted deflection profiles do not differ greatly from general features identified in the symmetric profile. All profiles are largely defined by the deflection spike near $\alpha' = 0$ followed by a secondary fling spike in the opposite direction, albeit shifted according to Φ. The phase does not incite radically new modes of deflection.

The resulting effects on lift are much more drastic in that lift does not follow the same

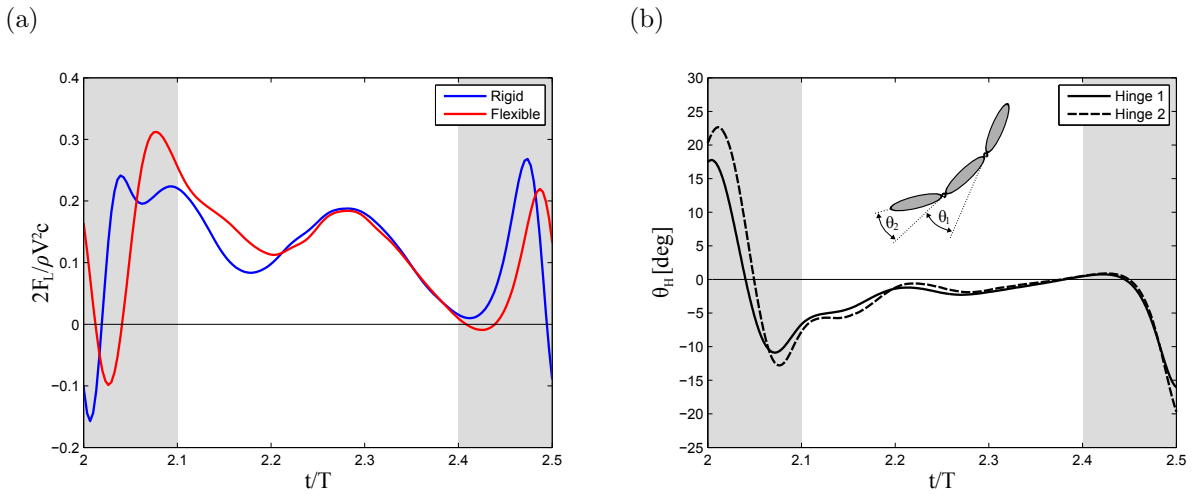

Figure 4.12: (a) Lift comparison between rigid and flexible wings and (b) deflection history of flexible wing hinges over a representative halfstroke. Leading hinge is Hinge 1 and trailing hinge is Hinge 2. Reynolds number Re = 100 and pitch phase is coincident with stroke reversal with $\Phi = 0$. T is the stroke period. Shaded regions indicate pitch maneuver.

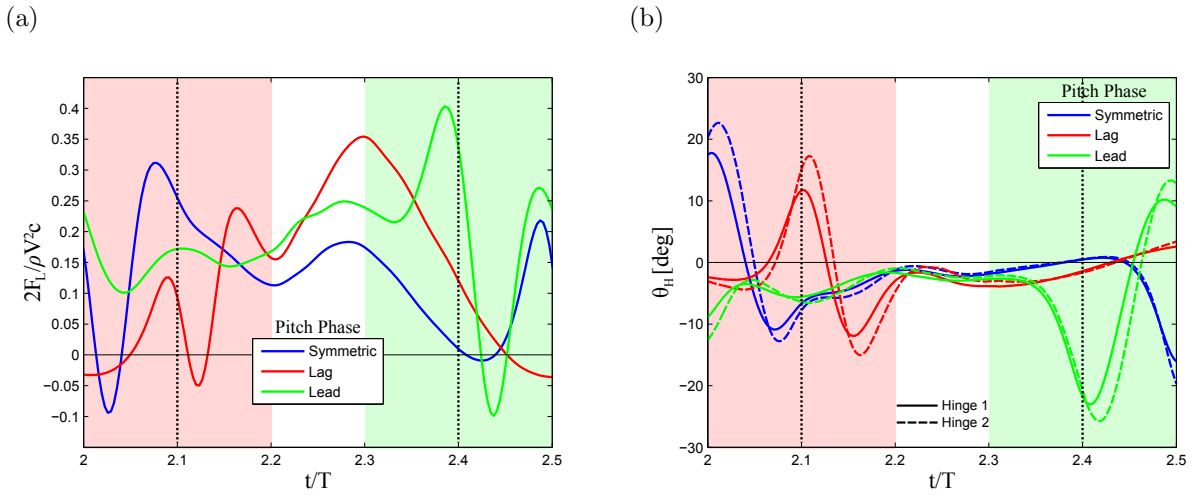

Figure 4.13: (a) Lift comparison between flexible wings of varying pitch phase Φ and (b) corresponding deflection history of flexible wing hinges over a representative halfstroke. Leading hinge is Hinge 1 and trailing hinge is Hinge 2. Reynolds number Re = 100. Phase: symmetric $\Phi = 0$, lag $\Phi = \pi/5$, and lead $\Phi = -\pi/5$. T is the stroke period. Shaded regions indicate pitch maneuver and dotted lines indicate the point lag and lead pitch angles are $\alpha' = 0$ as well as indicate the pitch regions for symmetric phase.

simplified profile-shift behavior as deflection. Pitch phase lag experiences a reduction in early lift over that of symmetric pitch which is characterized by a maximum near pitch completion. Peak lift is achieved approximately 60% of the halfstroke duration and smoothly dissipates with wing deceleration. Pitch phase lead is the most capable of operational configurations with modification to lift over phase symmetry resulting in a much more uniform performance for much of the stroke duration. Given its phase lead the flexible wing begins heave oriented with the desired angle of attack.

Table 4.4: Hover Performance: Rigid and Flexible Wings

	Φ	$\overline{C}_L$	$\overline{P}$	$\overline{F}_L V/\overline{P}$
Rigid	0	0.1219	0.1041	0.5854
Flexible	0	0.1237 (+1.45%)	0.0954 (−8.45%)	0.6487 (+10.81%)
	$\pi/5$	0.1315 (+7.79%)	0.0885 (−15.09%)	0.7432 (+26.94%)
	$-\pi/5$	0.1860 (+52.53%)	0.1454 (+39.59%)	0.6397 (+9.26%)

Figure 4.14 demonstrates the effects of pitch phase on the vorticity field generated by the flexible wing. For lead phase the wing completes pitch prior to stroke reversal. This primes the wing orientation for ease of accommodation of the leading-edge vortex of the previous halfstroke which is re-encountered on reversal. The deflection in chord provides one avenue for encountered vortices to be swept under the wing. Additionally, the trailing-edge undergoes a whip motion during pitch which significantly enhances shear layers feeding the trailing-edge vortex. The strength of this trailing-edge vortex aids in the transfer and integration of the previous leadinge-edge vortex into the wake, where it feeds into the newly formed trailing-edge vortex at the start of the next halfstroke and in conjunction with the trailing-edge vortex formed during pitch creates a vortex dipole with a trajectory directed slightly downward thereby imparting downward momentum into the fluid. In a symmetric phase the wing still benefits from ease of integration of the previous halfstroke LEV being swept under the wing however given the timing of pitch there is a tendency for the global velocity of the wing trailing-edge to reduce given the velocity of the leading reference body

now heaving in the opposite direction. What amounts is a dipole in the wake stemming from the trailing-edge with a greater imbalance between the two dipole elements, the counter-clockwise component being the stronger of the two. As such, the trajectory is directed upwards. For the lag phase the orientation of the wing at the start of the next halfstroke encounters the previous halfstroke LEV in a manner that deflects the LEV upward toward the wing leading edge. Pitch then splits the vortex into two with one portion being swept to the bottom of the wing and lingering for a period of time and the other portion is sent over the leading edge in proximity to the newly formed counter-rotating leading-edge vortex of the current halfstroke.

4.3.2 Elevated Angles of Attack

Having identified a lift mechanism characteristic of flexible wings, we now subject the single component rigid wing and the triple component flexible wing to hovering kinematics. High fidelity simulations using viscous vortex particle method of a three component two-dimensional wing in hover revealed the passive response to pitch amplitude [118] [49]. A number of pitch amplitudes $\alpha^{'}$ were tested $(90^{\circ} - \alpha)$. Heave and pitch were actively prescribed for the leading elliptical body component of a modeled wing, leaving the torsional hinge between bodies free to passively deflect. In the case of a rigid wing, the active body is the sole body in the system. Flapping wings characteristically operate at elevated angles of attack, inducing flow separation and LEV formation. The oscillatory nature of a stroke in hover requires that the wing reverse pitch at the end of translating the stroke amplitude in preparation for the translation of the subsequent half-stroke. The pitch amplitude $\alpha_o^{'}$ controls the degree to which the flapping wing adopts an aerodynamic angle of attack in each direction of heaving. As such, it is expected to control the development of the leading-edge vortex, and the degree to which this vortex contributes positively to lift, with the pressure force generated acting normal to the surface of the wing. A heaving rigid wing with little pitching remains nearly vertical, and in its most extreme case ($\alpha_o^{'} = 0$) will generate negligible lift apart from the small net contribution from the edges if vertical symmetry is

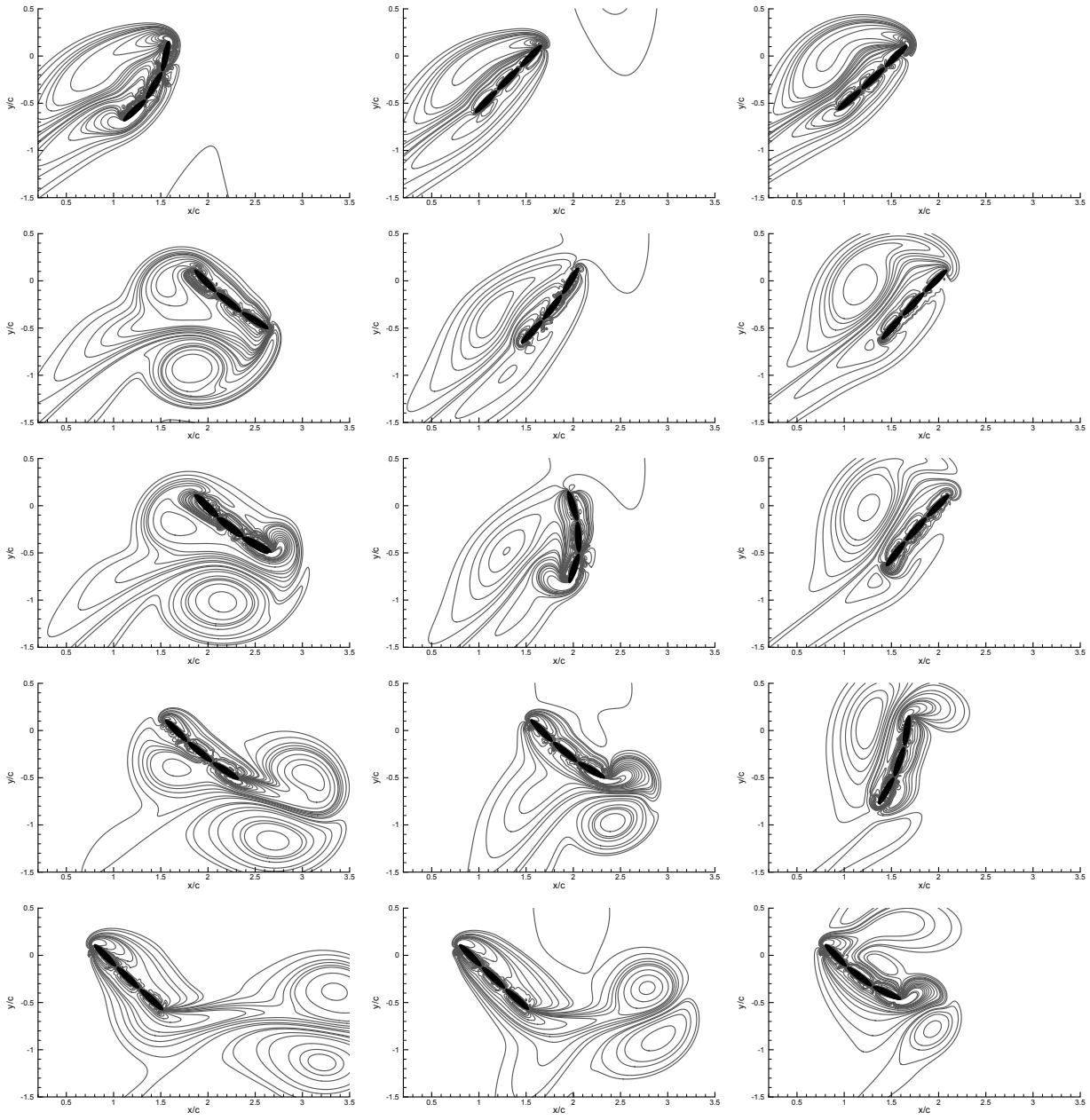

Figure 4.14: Comparison of vorticity field generated by a flexible wing during pitch at stroke reversal for varying pitch phases. Columns: lead phase ($\Phi = -36°$), symmetric phase ($\Phi = 0$), lag phase ($\Phi = 36°$). Rows: $t/T = [3.39, 3.47, 3.51, 3.59, 3.67]$.

broken.

Figure 4.15 depicts the mean lift and flapping efficiency of a three-component (flexible) versus a single-component (rigid) wing undergoing flapping kinematics about a pitch axis at $X_D/L = 0.16$ with phase lead $\phi = 36^\circ$ and heaving amplitude $A_o/L = 4$. The wing rotation occupies 40% of half the stroke period T_s, with the velocity profile employed this amounts to wing rotation spatially accounting for 35% of a half-stroke, ensuring that the pitch angle is nearly constant for most of each half-stroke in heave.

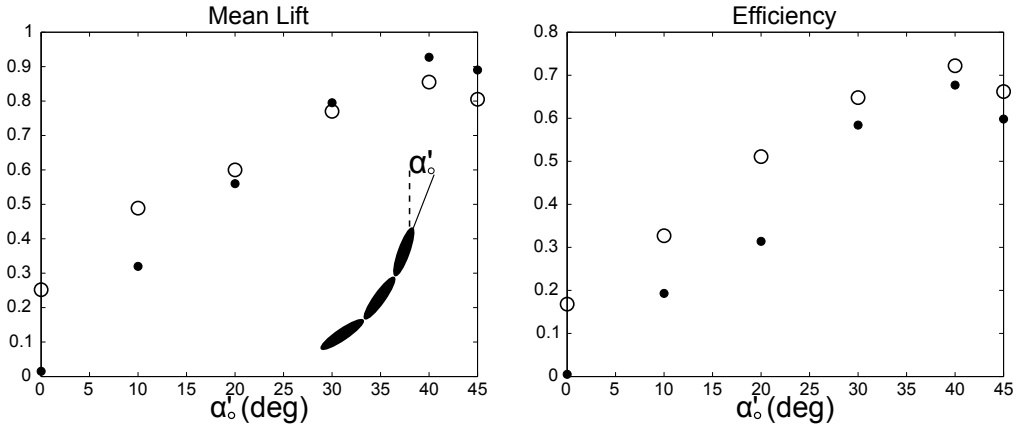

Figure 4.15: Stroke-averaged lift and efficiency for pitch amplitudes defined by the leading edge of the wing [49]. Wings: rigid (○), flexible (●).

Though the rigid wing produces slightly more lift at larger pitch amplitudes, the flexible wing generates larger lift at smaller pitch amplitudes, and in particular, non-zero lift at zero pitching. Furthermore, the efficiency of the flexible wing is larger than that of the rigid wing at all pitch amplitudes. Figure [4.15] shows that wing flexibility can potentially provide an opportunity for lift generation that is unavailable for a rigid wing flapping at small $\alpha^{'}$. During each heaving phase of the stroke, the flexible portion of the wing deflects opposite the direction of motion in an apparent streamlining mechanism, providing the wing with a somewhat smaller effective angle of attack. This passive mechanism for changing the effective angle of attack is very similar to passive pitching of a rigid wing, explored recently by Bergou, Xu & Wang [7].

In describing the current flexible wing, one would have to note the three elliptical body lengths and thickness ratios as well as the deflection angles of each hinge. This can be quite troublesome, particularly in the limit of a wing composed of many constituent bodies. In an effort to easily account for the wing and its deflection, an effective pitch angle, $\tilde{\alpha}$, can be quantified by measuring the angle of a line intersecting the centroids of the first and last constituent bodies of the flexible wing. The lift and efficiency are plotted versus the r.m.s. amplitude of this angle (and of the original pitch angle of the single-component wing) in figure [4.16]. The lift and efficiency trends exhibited by the two wings agree well over the entire range, except for a slightly lower lift and higher efficiency in the flexible wing at the largest angles. There is essentially a collapse of the two wing performances. This would indicate in constructing an MAV the power pertaining to rotating a rigid wing may be reduced by employing flexibility at a reduced pitch amplitude. One application of these wings would then be in descending maneuvers from hovering. Flapping the flexible wing at lower pitch amplitude would require less power since removing the active rotation of the wing yet still produce the lift required from an equivalent rigid wing, allowing for the insect or MAV to descend gracefully.

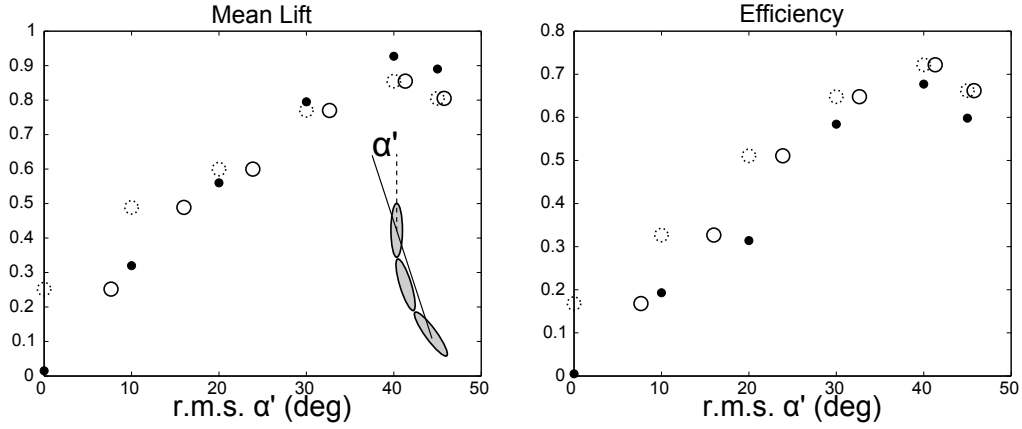

Figure 4.16: Stroke-averaged lift and efficiency for pitch amplitudes defined by the effective body deflection [49]. Wings: rigid (○), flexible (●). Dashed circles indicate flexible wing values prior to shifting.

It is interesting to note with the rotation interval fixed, as pitch amplitude is decreased

so too is the role of rotational circulation on the wing. Thus at lower pitch amplitudes performance variances are increasingly due to passive deflection. The effects of flexibibility are therefore better isolated operating under these conditions.

The ability to deflect was also found to determine the wing-wake interactions. Upon pitch reversal, the wing experiences the greatest hinge deflection. As the passive components of the wing are now rotating in accordance with the leading-edge member, they attain a greater angular velocity at the trailing-edge than observed by a rigid wing. This whip of the tail creates a greater shear layer which is rolled-up into the trailing edge area. Additionally, the deflected wing provides for a means for the shed leading-edge vortex to pass, or rather be swept, beneath the wing. Coupled with the increased velocity induced by the rolled-up trailing shear layer the deflected wing sees a shed vortex more easily passed at stroke reversal. Such a feat proves favorable as this ensures the production of the LEV in the subsequent stroke remains largely separated from the oppositely strengthened shed LEV. The rigid wing however can encounter a shed LEV which distributes vorticity above and below the heaving wing. The portion distributed below the wing experiences a greater residence time, lingering on this surface until eventually being washed downward.

4.3.3 Passivity in Pitch

We have seen how a flexible and rigid wing's performance may collapse due to the establishment of an effective pitch amplitude. This pitch was developed by passive means so to explore this concept further we examined an entirely rigid wing undergoing passive pitch in hover. Maintaining the same pitch axis $X_D/L = 0.16$ and stroke amplitude $A_o/L = 4$ as before, the rigid wing is prescribed hover motion in the horizontal plane at $Re = 100$, leaving the pitch and pitch reversal passive. The wing is outfitted with a torsional spring about its pitch axis to facilitate restoration of the wing to an aerodynamically neutral state (from half-stroke to half-stroke), a vertical orientation with $\alpha^{'} = 0$. Deflection of the body will be determined by the balance of aerodynamic, elastic and inertial forces. To determine the sensitivity of the aerodynamics to the wing configuration and vice versa the spring stiff-

ness was varied over two orders of magnitude, effectively controlling the 'stiffness' of a wing undergoing twisting about the radial axis.

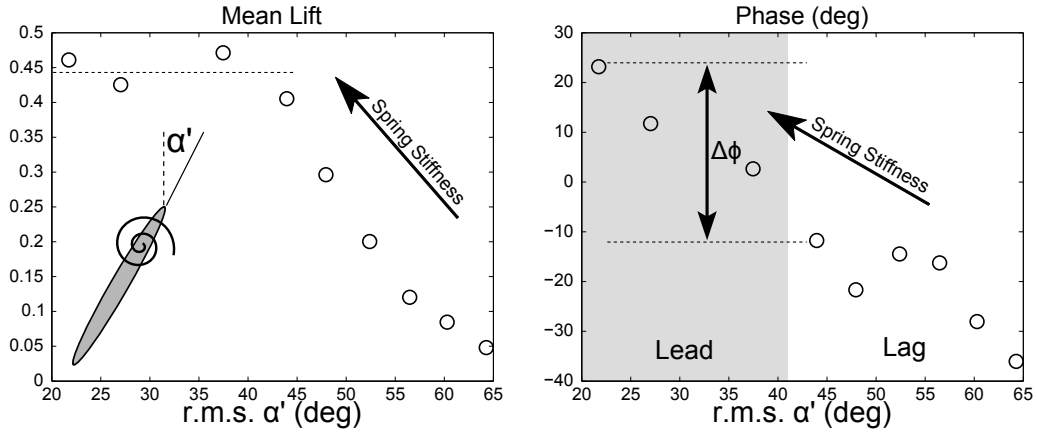

Figure 4.17: Stroke-average lift and pitch phase for various wing stiffnesses, K ($0.015 \leftrightarrow 1.5$)

It becomes apparent too little stiffness does not make for effective lift generation. The wing orients itself parallel to the flow with $\alpha^{'} \approx 90°$, and with the wings symmetric geometry this makes for an ineffective lifting surface. With increasing stiffness we see a lift increase. Additionally, increase in spring stiffness is met with a decrease in pitch amplitude. For intermediate to higher end stiffnesses, the lift develops a plateau region in which the average lift generated is insensitive to r.m.s. pitch amplitude. Additionally, passivity lends itself to phase as well, stroke reversal is not guaranteed to coincide with pitch reversal despite the restoring force exerted by the spring. When nearing the end of a half-stroke, the wing decelerates to a stop before reversing direction. Although the velocity returns to zero the aerodynamic forces do not diminish. The wake still presents an influence on the orientation due to its proximity and strength. Increasing stiffness was found to make for a transition from phase lag to lead. It is interesting to note that the lift plateau's constituent points span both the lag and lead regions, with a difference in phase of $\Delta\phi \approx 40°$. This would indicate passivity in pitch also greatly reduces sensitivity to phase.

So far the low performance of the smaller spring stiffnesses has been attributed to large pitch amplitude, however, the lack of strong wing-wake interactions may also prove detrimen-

tal. The low angle of attack makes for a weak trailing edge vortex. The wing still develops a counter rotating dipole in the wake, upon pitch reversal (which lags heave reversal) the wing gradually rotates approximately 140° producing a weak leading-edge vortex. Due to the high pitch amplitude during translation, the leading-edge vortex growth is mitigated and is convected downstream along the wing's upper surface. This roughly places the leading and trailing-edge vortices in a vertical alignment with comparable strengths. Ultimately less momentum is imparted on the fluid in the downward vertical direction.

4.4 Conclusion

Passive wing deformation has proven influential on both leading-edge vortex shedding frequency at large convective times and on force production. Freestream studies have demonstrated a vortex-symmetry breaking mechanism unavailable to rigid wings oriented normal to the flow wherein the counter-rotating vortices are no longer of the same strength due to a difference in shear-feeding layers at the leading and trailing edges. Two-dimensional wings eventually experience shedding of vortical structures when saturation is achieved. For sufficient convective times this shedding is periodic and the formation of a von Karman street is typically observed. A flexible wing accelerating from rest following a power law velocity profile demonstrated the effects of wing deflection on shedding frequency which includes increased shedding frequency with decreasing torsional spring stiffness. Additionally, the flexible still maintained a linear dependent of shedding frequency on Reynolds number and with the exception of the least stiff torsional spring all other flexible wings considered did not greatly alter the formation of the initial leading-edge vortex formed at the onset of motion. Passive chordwise deformation in hover has been shown to prolong attachment of the end-of-stroke vortex and strengthen its circulation thereby enhancing the flow induced by the vortex and the wake capture mechanism at stroke reversal. These effects were only strengthened further with pitch phase leading stroke reversal which increases the global "whipping" velocity of the passive trailing edge of the wing. External to the pitch portions of the kine-

matics the flexible wing produced forces similar to that of the rigid wing given its largely undeflected state. In attempting to bridge the performance and efficiency behavior of rigid and flexible wings an effective pitch angle was quantified by a line segment spanning from the centroids of the flexible wing's leading and trailing bodies. Plotting the flexible wing's lift and efficiency under the newly defined effective pitch resulted in a shift of the flexible wings data to lie on a trend line associated with the rigid wing. It appears the effects of flexibility in hover are predominant during pitch when deflection is greatest driven by both inertial and aerodynamics loads, though the inclusion of passive deformation also has long term effects in the development and shedding of vortical structures and hover kinematics typically do not include stroke amplitudes sufficiently large for such behavior to take effect.

CHAPTER 5

Three-Dimensional Wings In Hover: Prescribed Deformation

5.1 Introduction

Passive chordwise deflection in two-dimensional wings has been shown to promote greater frequency of leading-edge vortex shedding in accelerating wings. Freestream studies show the flexible wing's ability to disrupt symmetry in vorticity between the leading and trailing-edge vortices with the leading edge held normal to the flow field, a feat unavailable to rigid counterparts. In the reciprocating motion of hover, flexibility resulted in a fling motion of the trailing edge at stroke reversal producing greater shear layers with prolonged separation from the trailing edge which promotes greater wake-capture mechanisms. Despite proving influential on shedding, it has been shown trailing edge deflection does not effect the leading-edge vortex strength. However, in three-dimensional flight the wings are subject to axial flow and a tip vortex and vortical structures formulated are tantamount to a vortex ring system with a strong interdependence among all constituent components. In this light, the effects of deformation on aerodynamic performance and leading-edge vortex development are studied about a three-dimensional wing undergoing the hover maneuver. This study does not concern itself with the nature of flexibility but rather the resulting effects deformation may have on aerodynamic performance and vortical structure development. In a bid to distill the complicated nature of wing deformation into a simple context, deformation is confined to one of two lines of flexion with origins in deformation observed in biological counterparts. Flexion lines allow for a segmental portion of the tip or root of the wing to deflect following prescribed

sinusoidal motion. This work is not intended to draw specific conclusions on specific species of insect and planform area is idealized as rectangular. Simulations numerically solving the three-dimensional incompressible Navier-Stokes equations use the immersed-boundary finite-volume method developed by Kim *et al.* [58]. Previous studies have examined the effects of wing deformation on flight performance in the context of prescribed camber and twist measured from wing motion and deformation of in vivo insects [26, 117, 103]. Given the degree of insensitivity of LEV circulatory strength to chordwise deflection demonstrated in two-dimensional wings this study seeks to examine which facet of the leading-edge vortex is altered in response to generalized deformation modes and to what extent.

5.2 Wing Geometry and Deformation Modes

Wings of rectangular planform with aspect ratio $AR = b^2/S = 2$ and thickness $w/c = 0.1$ where b is the wing span measured from root to tip, c is the chord length, and S the planform area. The wing is situated at a standoff distance of $r_s = 0.4c$ from the rotation axis and the pitch axis is located $y' = 0.16c$ aft of the wing leading edge. The deflection modes selected are derived from general deformation exhibited in biological fliers. Deflection is prescribed a priori and is confined to one of two isolated lines of flexion about which a segmental portion of the wing will rotate as shown in Figure 5.1. Of interest are two distinct flexion configurations about the root and tip in comparison to the a rigid wing which remains planar. The first deflection mode configuration consists of a flexion line funning largely in the spanwise direction allowing for deflection of the wing root. Mode two consists of a flexion line oriented largely in the chordwise direction stemming from the leading edge at the wing tip. Both modes allow for a deflection area which accounts for 24% of the total planform area.

Wings undergo hover kinematics with no deviation from the horizontal plane with heave following

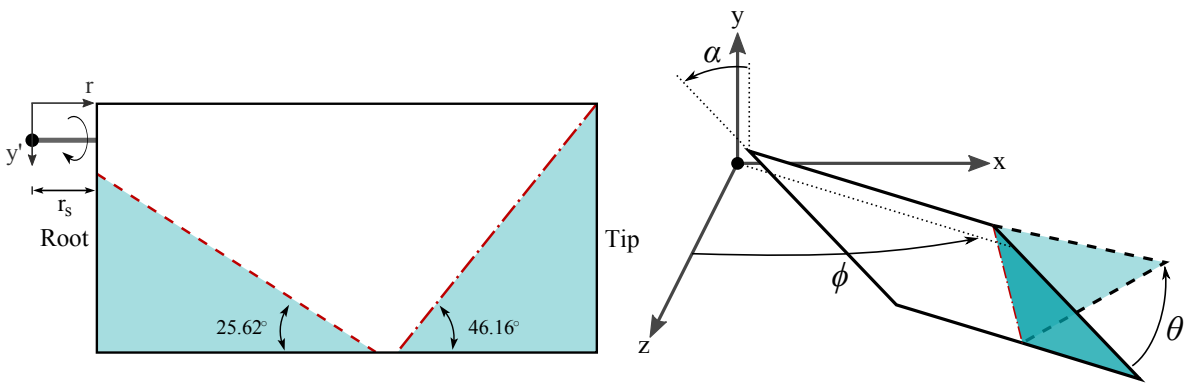

Figure 5.1: Flexion line configurations (left) superimposed onto the rectangular wing: root (– – –) and tip (– · –). Deflection modes (right) in heaving. Each deflective area constitutes $0.24S$ of planform area.

$$\phi(t) = \phi_m \cos(2\pi f t). \tag{5.1}$$

Pitch is determined by a hyperbolic tangent waveform,

$$\alpha(t) = \frac{\alpha_m}{\tanh C_\epsilon} \tanh\left[C_\epsilon \sin(2\pi f t)\right], \tag{5.2}$$

with pitch reversal duration and profile determined by C_ϵ [9]. Lastly, deflection about the root or tip follows a sinusoidal waveform given by

$$\theta(t) = \theta_m \sin(2\pi f t - \Phi). \tag{5.3}$$

Kinematic profiles over the course of a representative stroke are depicted in Figure 5.2 and Reynolds number is defined as $\mathrm{Re} = V_{\mathrm{tip}} c/\nu$.

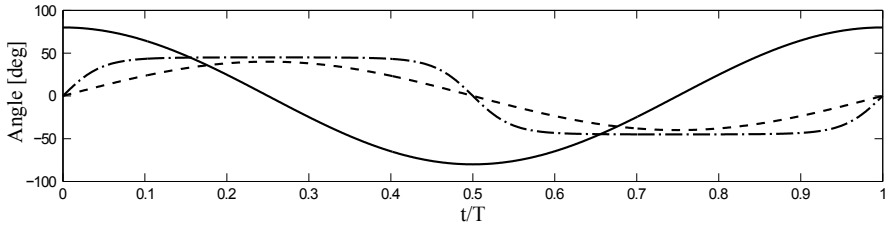

Figure 5.2: Sweep (——), pitch ($-\cdot-$), and deflection ($- - -$) kinematics over a period for $\Phi = 0$.

Table 5.1: Kinematic Parameters

Heave Amplitude	ϕ_m	80°
Pitch Amplitude	α_m	45°
Deflection Amplitude	θ_m	40°
Pitch Duration	C_ϵ	3.3
Deflection Phase	Φ	$[0, \pi/4, \pi/2, \pi, -\pi/4]$

5.3 Force Modification via In-Phase Deformation

Investigation of wings flapping at Re = 100 with in-phase deflection $\Phi = 0$ of amplitude $\theta_m = 40°$ demonstrated the effects of deflection on force generation. Figure 5.4 shows the temporal evolution of lift and drag during a representative halfstroke after the fluid has become fully developed for rigid, root flexion and tip flexion wing configurations. All wings experience the same profile trends differing only in magnitude with the greatest differences experienced by the deflection wings approaching the midstroke. In-phase deflection of $\Phi = 0$ places the maximum deflection coincident with the midstroke. Additionally, the plates return to an undeflected state at stroke reversal. Correspondingly, the greatest similarity between the plates' forces is observed near stroke reversal. Resulting lift profiles are characterized by a major jump extending much of the halfstroke surrounded by two smaller peaks. The peak at the beginning of stroke can be attributed in part to wake-capture and the latter peak to rotational circulation brought about by the pitch maneuver at midstroke's end [22]. The tip

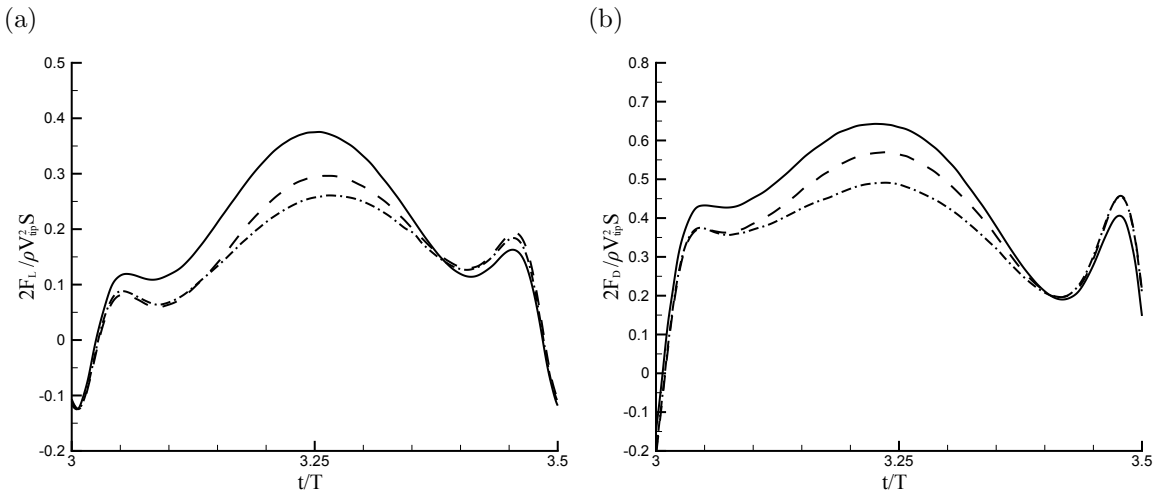

Figure 5.3: Temporal variation in (a) Lift and (b) Drag coefficient of three wing deflection configurations at Re = 100: Rigid (——), Root (− − −), Tip (− · −). Deflection amplitude $\theta_m = 40°$, deflection phase $\Phi_{\text{def}} = 0$.

deflection wing augments the aerodynamic forces to a greater extent than root deflection. The greater modifications of force in response to tip deflection may suggest the effects of deflection are more pronounced when deflection is introduced in areas of higher local velocity, namely the tip.

Forces at Re = 10^3 preserve major features identified for Re = 100 with some key modifications as shown in Figure 5.4. Lift retains a profile dominated by a parabolic signature for the majority of the halfstroke. The latter peak corresponding to rotational circulation of pitch remains largely unchained with C_L values comparable to those experienced at Re = 100. The initial peak associated with wake-capture now appears less distinct from the greater lift profile with reductions in peak coefficients for the rigid and root flexion wings, peaks are now incorporated to a greater extent into the greater lift parabolic. Conversely, tip deflection maintains a distinctive initial peak with an increased C_L maximum that also experiences a temporal shift. Between the rigid wing and two deflection wing configurations now exists a greater disparity in lift coefficient. Further, the lift of the deflection plates is in greater agreement than drag with the root deflection wing producing greater drag. This would indicate tip flexion as a favorable flexion mode among the two presented at Re = 10^3 given

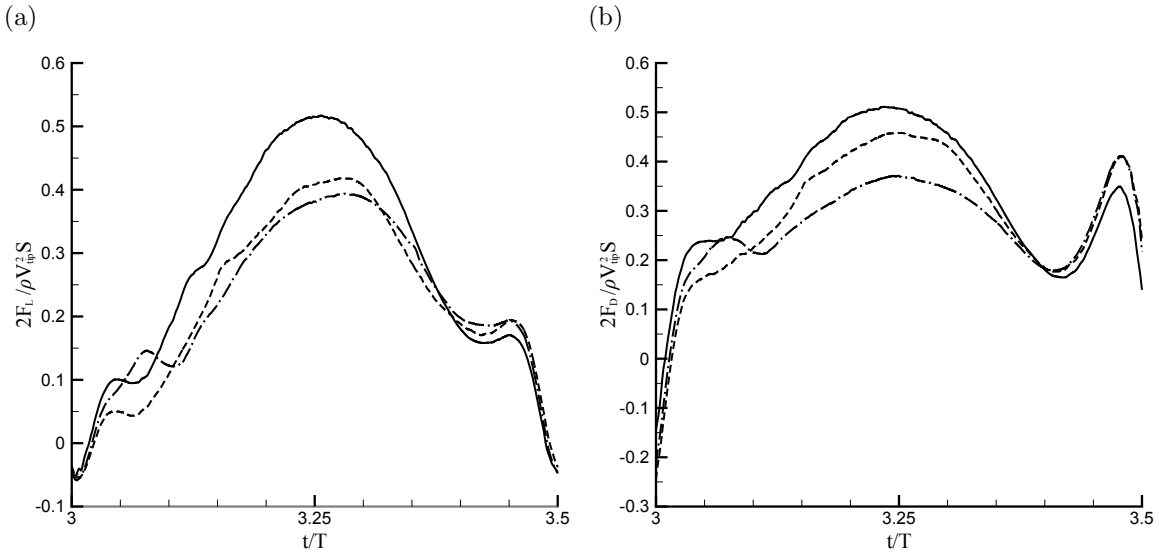

Figure 5.4: Temporal variation in (a) Lift and (b) Drag coefficient of three wing deflection configurations at Re = 1000: Rigid (——), Root (− − −), Tip (− · −). Deflection amplitude $\theta_m = 40°$, deflection phase $\Phi_{\text{def}} = 0$.

the comparable lift and significant drag reduction. Overall, the increase in Reynolds number by an order of magnitude was met by an increase in C_L and a reduction in C_D for all configurations, indicating a reorientation of the resultant aerodynamic load on the wings from that of Re = 100.

Examination of the vortical structures induced in flapping offers a sense of the deflection influences on vortical strength and development. Figure 5.5 shows the vortical structures identified by the λ_2 criterion for flapping at Re = 100. The most notable difference in regards to the tip vortex among the deflection wings compared to the rigid wing vortical development resides in the tip flexion case shown in Figure 5.5(c). The tip vortex here appears thicker. The tip deflection reduces the flux of vorticity into the tip vortex as evidenced by the dissipative time scale of the shed tip vortex of the previous halfstroke in the wake. Despite the circulatory strength reduction the tip deflection also works to shift the tip vortex inboard toward the wing root, thereby increasing the leading-edge vortex and tip vortex proximity and promoting an earlier merger of the two vortical structures along the span than that experienced by a rigid counterpart.

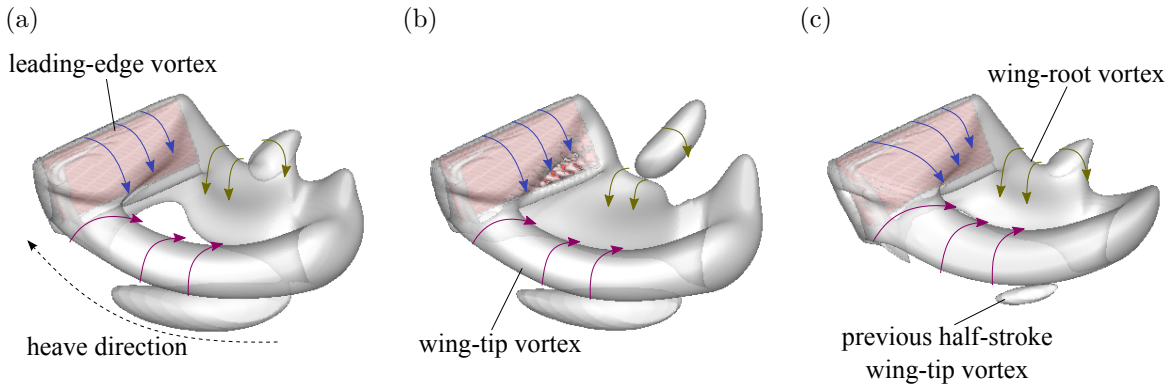

Figure 5.5: Three-dimensional vortical structures at $t/T = 3.37$, following the midstroke at Re = 100: (a) Rigid (b) Root deflected (c) Tip deflected. Angle of attack $\alpha = 45°$, deflection amplitude $\theta_m = 40°$, deflection phase $\Phi = 0$. Vortical structures isosurface of $\lambda_2 = -0.03$ [51].

In a given halfstroke the leading-edge, tip, root and starting vortex are often viewed as a single closed loop vortex system. Stereoscopic DPIV experiments by Poelma textitet al. also showed the flow structure around a rotating wing is a vortex loop made up of a leading-edge vortex, tip vortex, starting vortex and a root vortex [81]. Simulations on translating low aspect ratio wings by Taira and Colonius found the leading-edge vortex and tip vortex remain separate vortical entities, lacking the closed loop system of rotating wings [95]. Of these loop components there exists a thinning of the starting-vortex segment, with the root flexion wing accounting for the greatest variability. Additionally, root deflection provides an avenue for wing-woot vortex separation as shown in Figure 5.5(b).

Vortical fields at Re = 10^3 shortly after midstroke are as shown in Figure 5.6. In addition to the primary components of the vortex loop system, the leading-edge, root, starting, and tip vortex, the wings at this Reynolds number host a number of secondary vortices existing on scales a fraction of those loop constituent vortices. The wing tip appears to be a significant source of instabilities taking the form of of sporadically formulated sub-structures stemming from the wing tip and encircling and overlapping the tip vortex. In the case of tip deflection at midstroke in Figure 5.6(c) much of the chaotic nature of the sub-structures is suppressed by the reduced shear at wing tip and replaced with a sleeve-like structure that remains in

the vicinity of the shear feeding wing tip.

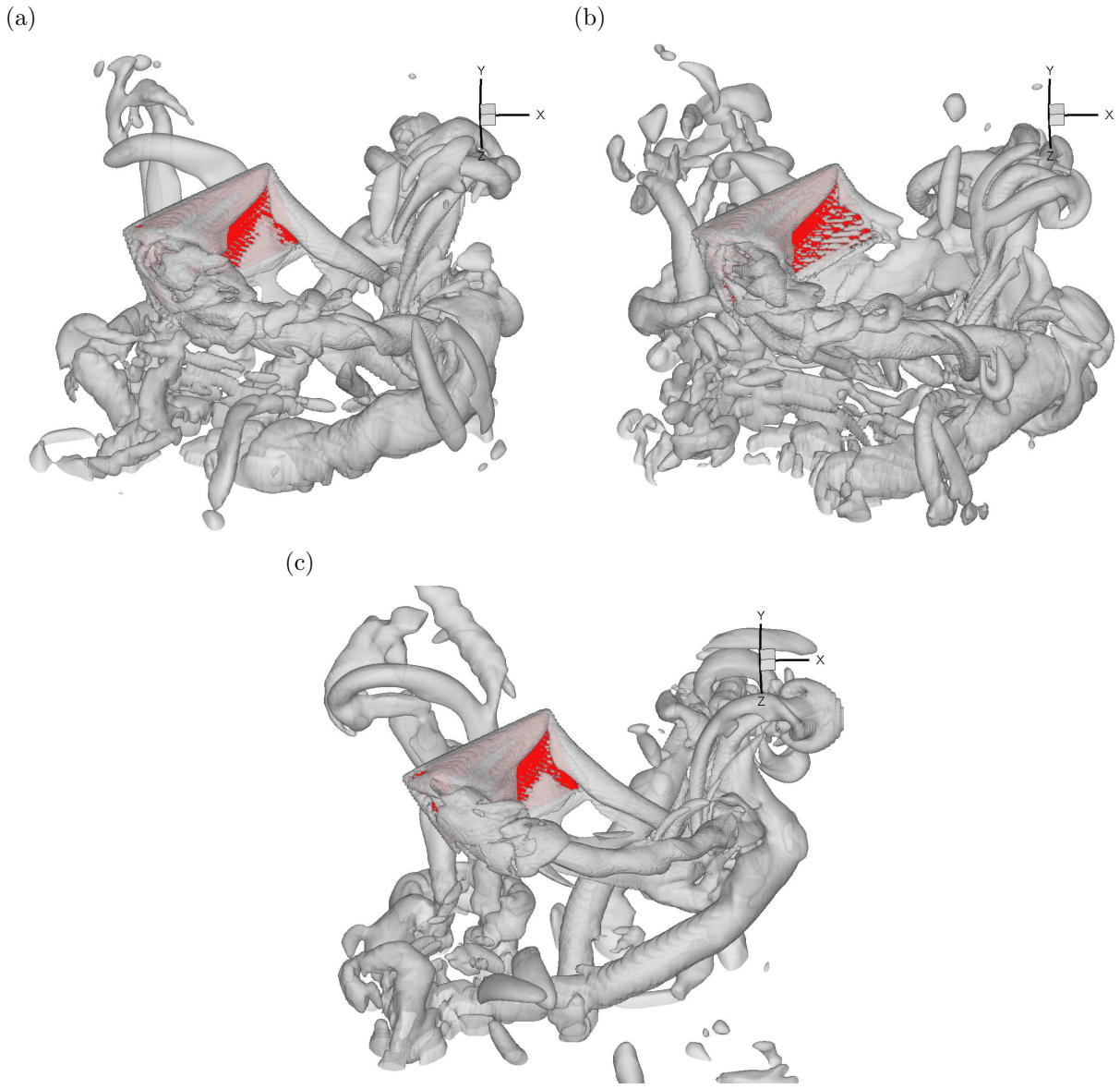

Figure 5.6: Three-dimensional vortical structures at $t/T = 3.37$, following the midstroke at Re = 1000: (a) Rigid (b) Root deflected (c) Tip deflected. Angle of attack $\alpha = 45°$, deflection amplitude $\theta_m = 40°$, deflection phase $\Phi = 0$. Vortical structures isosurface of $\lambda_2 = -0.03$ [51].

5.4 LEV Axis and Core Response to Deformation

Use of λ_2 isosurfaces and other vortical identification algorithms have proven vital in expanding our knowledge on various flow phenomena, however, other flow features may become obscured. To aid in highlighting flow features associated with the LEV response to deflection-induced perturbations, identification of the LEV axis line and core is conducted following the approach of Graftieaux *et al.* where a vortex axis is identified by the Γ_1 criterion [38],

$$\Gamma_1(P) = \frac{1}{S}\int_{M\in S} \frac{(\mathrm{PM}\wedge U_M)\cdot z}{\|\mathrm{PM}\|\cdot\|U_M\|}\mathrm{d}S. \tag{5.4}$$

$|\Gamma_1|$ reaches a maximum near the vortex center which is interpreted as the vortex axis with values in the range of 0.9 and 1.0 due to normalization. Similarly, the LEV core is identified as a region of flow dominated by rotation attached to the upper surface of the wing corresponding to $|\Gamma_2| > 2/\pi$,

$$\Gamma_2(P) = \frac{1}{S}\int_{M\in S} \frac{\left[\mathrm{PM}\wedge(U_M-\tilde{U}_P)\right]\cdot z}{\|\mathrm{PM}\|\cdot\|U_M-\tilde{U}_P\|}\mathrm{d}S. \tag{5.5}$$

Figure 5.7 demonstrates the agreement between the velocity and vorticity field with the LEV axis and core about midspan of a rigid wing. The axis is encircled by the local velocity field and the axis is compliant with the vortical region of the LEV.

Other methods of axis detection include points in the flow where velocity is parallel to the real eigenvector of the velocity gradient tensor as outlined by Rutten and Pagendarm [89]. The guiding assumption in this approach is the real eigenvector is sufficiently indicative of the rotation axis of the local fluid element. The axis line is then constructed by streamline integration origination from the previously discovered axis element.

Figure 5.8(a) examines the spatial evolution of the LEV axis about the flapping wings along the span for Re = 100, $\theta_m = 40^\circ$ and $\Phi = 0$ to reveal the axes behave nearly identically throughout the stroke among the rigid, root deflection and tip deflection plate configurations.

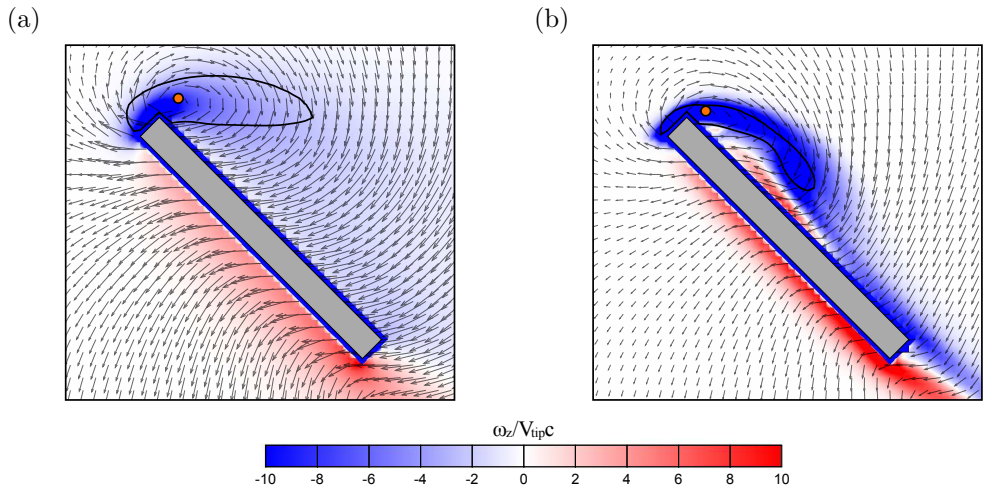

Figure 5.7: Flow and vorticity fields and corresponding LEV axis and core about a rigid plate at midspan at midstroke, $t/T = 3.25$: (a) Re = 100 and (b) Re = 1000. Contours of spanwise vorticity, velocity field (→), LEV axis as defined by maximum $|\Gamma_1|$ (●), LEV core boundary as defined by $\Gamma_2 = 2/\pi$ (——).

The evolutionary path of all axes largely follow the adhere to the plate leading edge with slight deviation with increasing spanwise location. Computational studies on revolving wings at fixed angle of attack by Harbig *et al.* report dual LEV structures. However, the stroke amplitude and Reynolds number considered support only a single axis. With negligible variation among the three plate configurations, the leading-edge vortex axis is best characterized as insensitive to deflection.

Upon increasing Reynolds number to Re = 10^3, the wings still support a single LEV axis, a consequence of stroke amplitude or formation time afforded to the vortical structures by the kinematics selected as shown in Figure 5.8(b). The spatial evolution of axes about the rigid, root deflection and tip deflection wings continue to exhibit negligible differences. As is the case with Re = 100, the axes at Re = 10^3 remain in the vicinity of the wing leading edge, though the axes now recedes further from the leading edge in approaching the wing tip resulting in greater variability over that of Re = 100. Although the axes depicted in Figure 5.8(b) correspond to $\Phi = 0$, the behavior extends to other deflection phases tested and the figure remains representative of all deflection phases considered in Table 5.1.

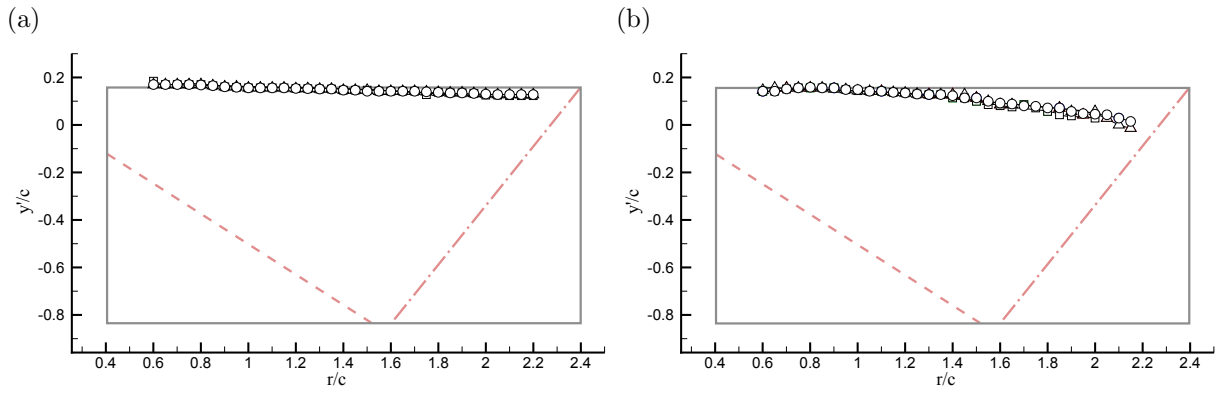

Figure 5.8: Leading-edge vortex axis spatial evolution about a plate at midstroke, $t/T = 3.25$. (a) Deflection amplitude $\theta_m = 40°$, Reynolds number $Re = 100$, (b) $\theta_m = 40°$, $Re = 1000$. Rigid ($\triangle$), root deflection ($\square$), tip deflection ($\bigcirc$). Flexion lines highlighted on the rigid plate planform: Tip ($- \cdot -$), Root ($- - -$).

In contrast to the axis, the LEV core proves sensitive to deflection as shown in Figure 5.9. For Re = 100 and in-phase deflection phase $\Phi = 0$ root deflection near the wing base is responsible for a reduction in LEV core size as demonstrated in Figure 5.9(a). Tip deflection, however, experiences a core similar to that of the rigid plate which would indicate the effects of tip deflection are minimal in regards to core size near the wing root. All wing configurations share the general trend of experiencing core size growth with span, culminating in a maximum near $r^*/b = 0.7$ as shown in Figure 5.9(b). Beyond this spanwise position approaching the wing tip both the rigid and root flexion wings experience significant reductions in core size as shown in Figure 5.9(c). Conversely, the tip flexion wing supports prolonged enlargement of the LEV core. Further, the deflection state of the wing is directly reflected in the orientation of the resulting core which appears to rotate in a direction congruent with the wing's deflection. At Re = 10^3 the aforementioned trends are continued as shown in Figure 5.10 with a greater discrepancy now between the rigid and root deflection wings. Cores presented also appear elongated in response to greater shearing of the fluid.

Although core formation among the plates may appear may be equal or very similar in size for a given spanwise position, the resulting circulatory strength of the cores can vary and

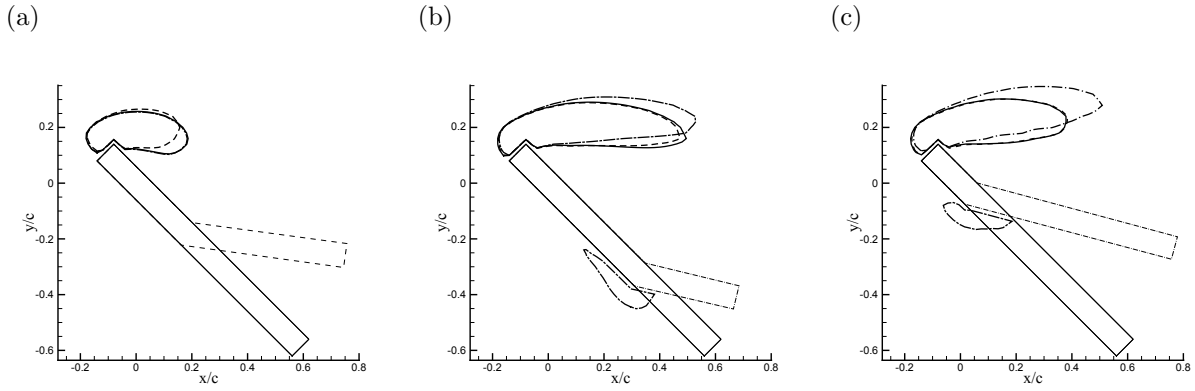

Figure 5.9: Leading-edge vortex core ($|\Gamma_2| > 2/\pi$) spanwise evolution during midstroke. Radial position: (a) $r^*/b = 0.1$, (b) $r^*/b = 0.7$, (c) $r^*/b = 0.9$. Core contour and plate geometry: Rigid (——), Root (– – –), Tip (– · –). $\theta_m = 40°$, $\Phi = 0$,Re = 100. Note: $r^* = (r - r_s)$ with $0.0 \leq r^*/b \leq 1.0$.

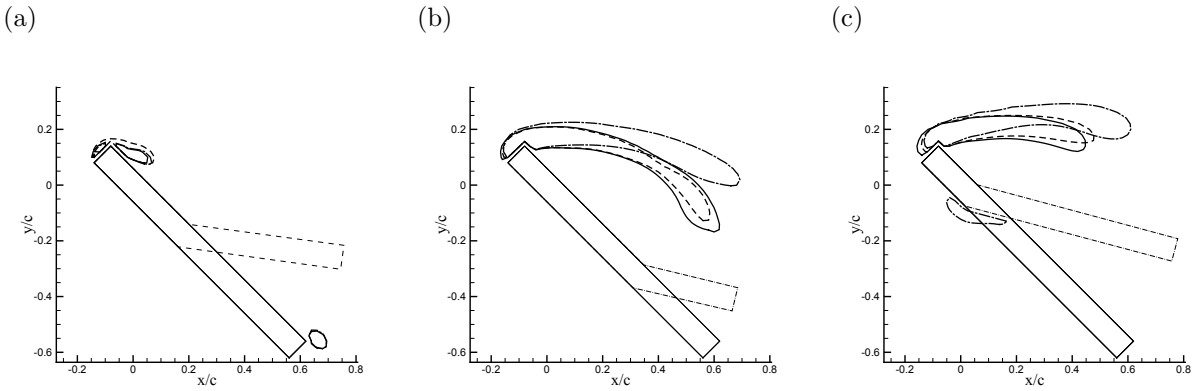

Figure 5.10: Leading-edge vortex core ($|\Gamma_2| > 2/\pi$) spanwise evolution during midstroke. Radial position: (a) $r^*/b = 0.1$, (b) $r^*/b = 0.7$, (c) $r^*/b = 0.9$. Core contour and plate geometry: Rigid (——), Root (– – –), Tip (– · –). $\theta_m = 40°$, $\Phi = 0$,Re = 1000.

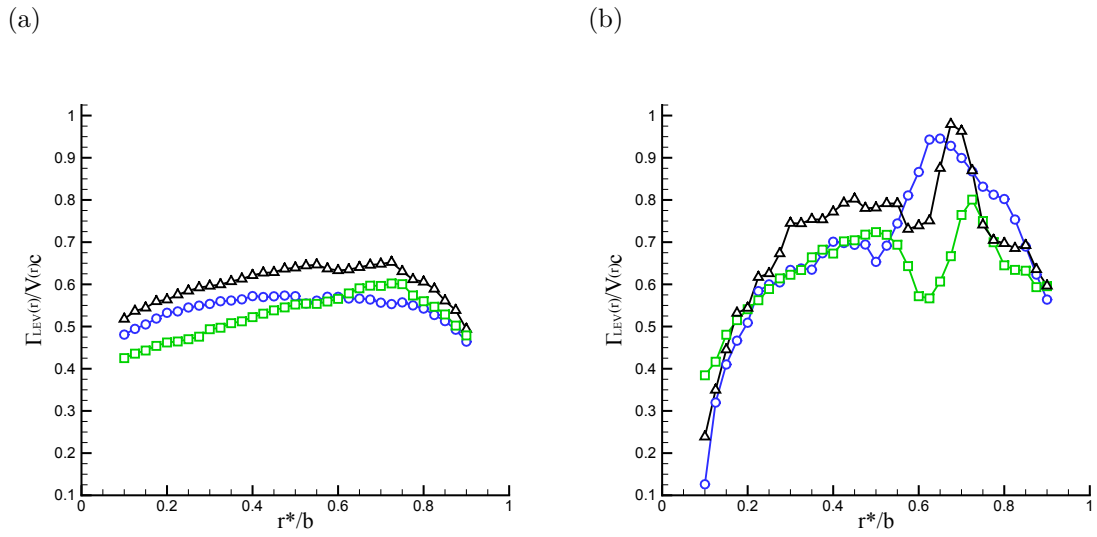

Figure 5.11: Leading-edge vortex circulation Γ_{LEV} about a plate at midstroke, $t/T = 3.25$. (a) Re = 100 and (b) Re = 1000: Rigid (△), Root deflection (□), Tip deflection (◯). Deflection amplitude $\theta_m = 40°$ and phase $\Phi = 0$. Note: $\mathrm{r}^* = (\mathrm{r} - \mathrm{r}_s)$ with $0.0 \leq \mathrm{r}^*/\mathrm{b} \leq 1.0$.

differ in behavior in response to the deflection modes as shown in Figure 5.11. The leading-edge vortex circulation, Γ_{LEV}, is normalized by local velocity of the wing to remove effects from velocity variability along the span from the profiles presented. For Re = 100 in Figure 5.11(a) the rigid wing experiences parabolic growth in circulation until reaching a maximum near $0.75b$, beyond which the circulation reduces to values below that of the circulation at the wing root. Root deflection leads to circulation growth that appears much more linear to achieve a maximum near $0.75b$ before a near linear reduction approaching the wing tip. Tip deflection produces a largely symmetric parabolic circulation profile with a maximum at the midspan position $0.5b$. Figure 5.11(b) shows the resultant circulation behavior for Re = 10^3. Similar behavior between the rigid and tip deflection wing performance is observed near the root until $0.2b$, beyond which the tip deflection plate now performs as the root deflection plate does until span of $0.47b$. Further along the span all plates diverge in behavior to develop distinctive profiles.

At Re = 10^3 in the vicinity of $0.7b$ span all plates experience a variation of a distinct spike in circulation. Spike maximums from $0.675b$, $0.725b$, and $0.65b$ for rigid, root deflection and

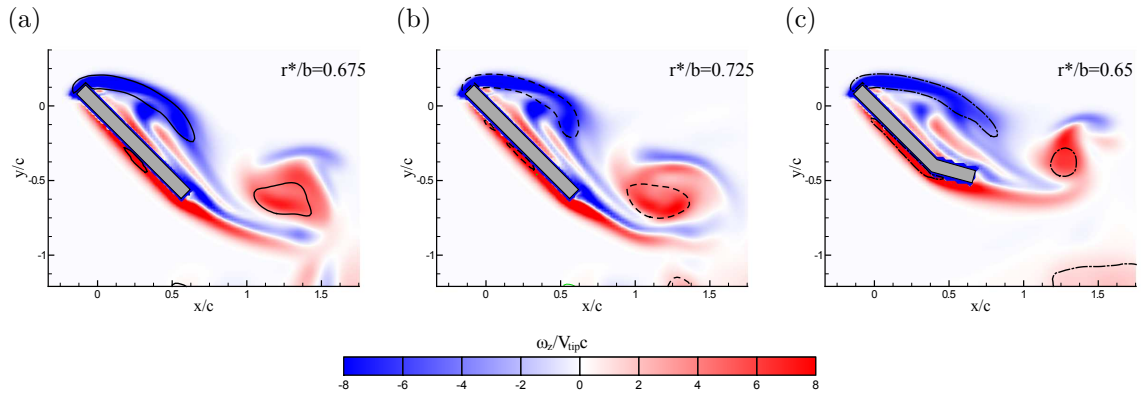

Figure 5.12: Vorticity contours at spanwise positions corresponding to maximum leading-edge vortex circulation at Re = 1000: (a) rigid, (b) root, and (c) tip. Lines indicate $|\Gamma_2|$ contours of $2/\pi$.

tip deflection plate respectively. These spike maxima are accompanied by vortical structure size increases and LEV core growth as shown in Figure 5.12. Additionally, as noted by Jardin *et al.*, there is also the development of a strong trailing-edge vortex in the vicinity of the wing tip thought to promote instabilities in the LEV [50]. The newly formed TEV remains in close proximity to the wing trailing edge for approximately 30% of the span originating at the tip and is the result of the tip vortex being redirected inboard after clearing the wing chord producing a spanwise component that merges with shear layers present along the wing trailing edge. The tip vortex formation differs from that at Re = 100 which occupies a region of the fluid outlined by the wing tip trajectory. The resulting TEV formation near the wing tip also accommodates a region of fluid with an influx of counter-rotating vorticity, secondary to the eruption layer near the leading edge.

5.5 Axial Flow

The selected deflection modes were initially proposed as a means to favorably modify axial flow behavior in flapping via deflection-induced channeling and incorporation into the leading-edge vortex for low Reynolds numbers. With the inclusion of flow into the LEV the

potential for bursting is present at lower Reynolds number which has been shown to enhance force production at higher Reynolds numbers, where the term lower Reynolds number is reserved for Re = $O(10^2)$ [68]. It was initially believed to, at the very minimal, enhance LEV stability at lower Reynolds numbers by the axial flow working to remove or convect momentum from the LEV core. However, studies have shown stability Rossby number and quasi-steady acceleration terms to play principal roles in LEV development and attachment to the wing surface.

Vorticity fields and axial flow contours at Re = 100 are presented in Figure 5.13. On inspection of the rigid wing, an axial flow maximum develops near the trailing edge for the entirety of the span. As indicated in Table 5.2 axial flow at Re = 100 monotonically increases with span. Flexion wings also experience maximum axial flow seemingly attached to the trailing edge. Root deflection entertains two maxima near the wing root over the length of span hosting a deflection segment of wing, though this bifurcation appears to be heavily reliant on the thickness of the wing as shown in Figure 5.13(b). Near the wing tip the root flexion wing experiences flow field reminiscent of the rigid wing. Although the proximity of the axial flow maximum to the leading edge of the plate is increased via root deflection, the maximum still remains localized at the trailing edge and offers no more integration into the leading-edge vortex than the rigid wing. The same behavior holds true for tip flexion, with the radial position dependency now reversed by the root flexion wing as shown in Figure 5.13(c). It appears despite the low aspect ratio of the wing much of the deflection effects remain localized in their respectively radial positions.

At Re = 10^3 there exists a shift of axial flow maxima from the trailing edge to the leading edge. Figure 5.14(a) shows the axial flow maximum shift naturally, unabetted by an means of deflection for the rigid wing. The deflection wings follow suit with an axial flow well integrated into the LEV core. It is worth noting flexion wings off more variability from their rigid counterpart in the flow visualized at sections of the flexion wing that are undeflected than observed at Re = 100. Referring to Table 5.2 the axial flow maxima do not monotonically increase with span but rather achieve a maximum prior to $0.75b$ and begins to

decrease. Of the three wings it is the root flexion wing that experiences the greater core flow at midspan and three-quarter span positions adding validity to the idea of root deflection channeling axial flow.

Table 5.2: Axial Flow Maxima $(w_z/V_{\text{tip}})\,|_{\max}$, $\Phi = 0$, $\theta_m = 40°$

		$r^*/b = 0.25$	$r^*/b = 0.50$	$r^*/b = 0.75$
Re = 100				
	Rigid	0.399	0.486	0.551
	Root	0.380	0.473	0.534
	Tip	0.383	0.438	0.460
Re = 1000				
	Rigid	0.596	0.908	0.812
	Root	0.568	0.940	0.929
	Tip	0.565	0.823	0.828

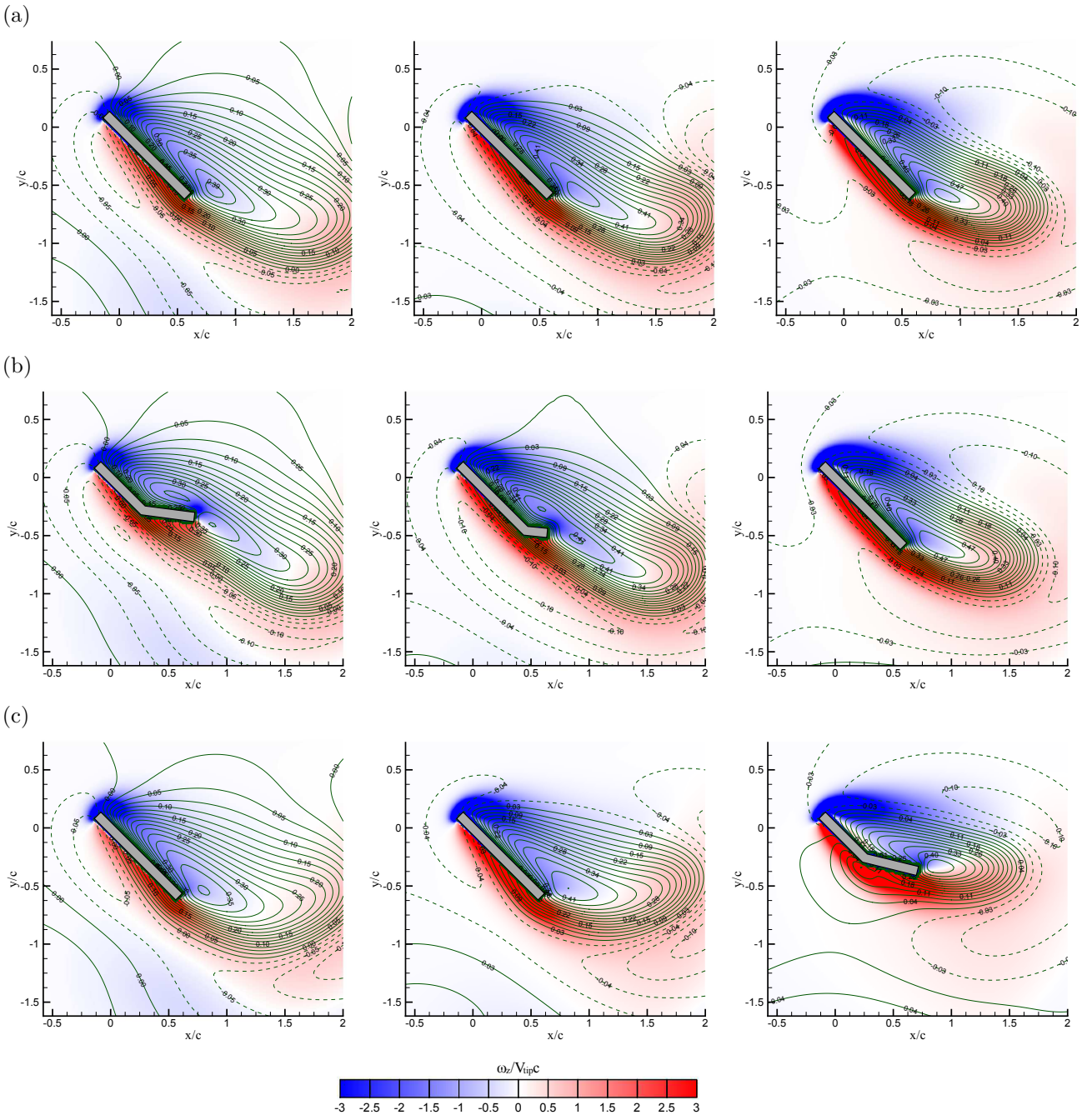

Figure 5.13: Vorticity (flood) and axial flow field (contours) about (a) rigid, (b) root flexion and (c) tip flexion wings at midstroke at Re = 100. Axial flow: outboard flow (——), inboard flow (– – –). Columns correspond to cross sectional plans at spanwise position $r^*/b = 0.25$, $r^*/b = 0.50$, and $r^*/b = 0.75$, respectively.

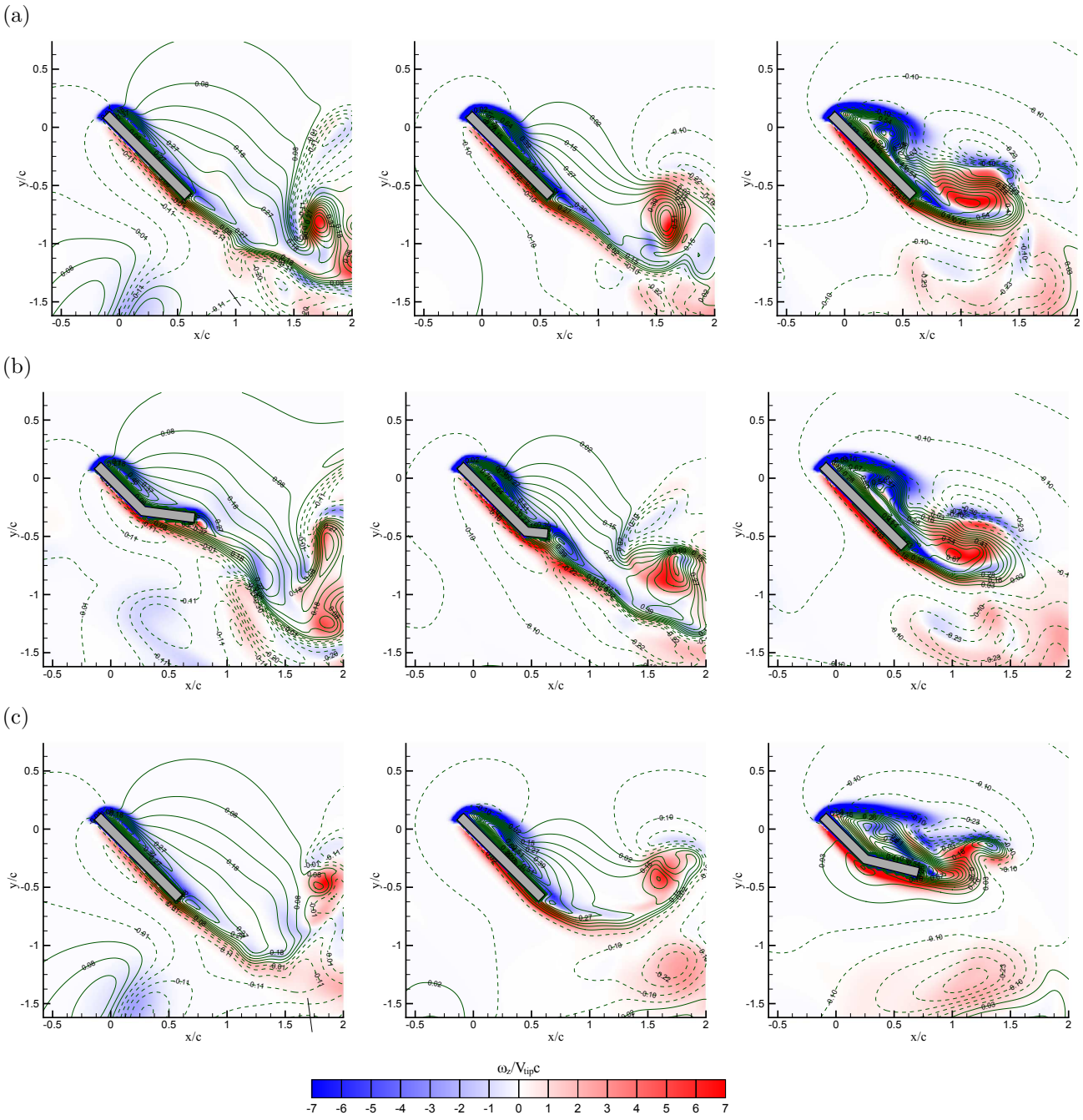

Figure 5.14: Vorticity (flood) and axial flow field (contours) about (a) rigid, (b) root flexion and (c) tip flexion wings at midstroke at Re = 10^3. Axial flow: outboard flow (——), inboard flow (– – –). Columns correspond to cross sectional plans at spanwise position $r^*/b = 0.25$, $r^*/b = 0.50$, and $r^*/b = 0.75$, respectively.

5.6 Effects of Deflection Phase on Performance

Deflection maximum is now shifted to different parts of the stroke via Φ of Equation (5.3) at Re = 100. In both the root and tip flexion wings in-phase deflection of $\Phi = 0$ the least time-averaged lift, $\overline{C}_L$, as shown in Figure 5.15 and summed up in Table 5.4. Minimum $\overline{C}_D$ also corresponds to in-phase deflection for tip flexion in Figure 5.15(b), whereas root flexion is characterized by a minimum at $\Phi = 45°$ with deflection maximum occurring after midstroke. In the instance of $\Phi = 180°$ the root flexion wing is capable of producing greater lift than the rigid plate which has been unachievable thus far for a flexion wing. The root's deflection imparts positive camber on the wing and increases its ability to impart downward momentum into the fluid. The $\overline{C}_L$ for both flexion wings increases with increasing Φ but the performance gap between the two flexion configurations widens with Φ as well. Conversely, $\overline{C}_D$ of the two flexion wings converges with increasing Φ, ultimately producing the same drag at $\Phi = 180°$.

The stroke average aerodynamic power, $\overline{P}$, and efficiency ratio, η_D/η_R are plotted in Figure 5.15 where where efficiency is defined as the mean lift per unit power, $\overline{F}_L V_{\text{tip}}/\overline{P}$ and subscript D and R indicate deflection wing and rigid wing respectively. Plate deflection prompts reduction in power in both root and tip configurations. Power consumption is lessened by as much as 18.6% for root deflection with $\Phi = 45°$ from that of the rigid wing and by as much as 31.7% for tip deflection with $\Phi = 0$. These power reductions equate to gains in efficiency as great as 14.9% for the root flexion wing with $\Phi = 90°$ over the rigid wing and 19% for tip flexion with $\Phi = 45°$. With the exception of in-phase deflection of the root flexion wing, the deflection modes prove more efficient than the rigid counterpart for the phases considered.

Flight at Re = 10^3 sees considerable reduction in power consumption and gains in efficiency at midstroke phases. The root flexion wing previously required less power than a rigid wing at Re = 100 with $\Phi = 0$ but was also marked with a reduction in efficiency. Operations at Re = 10^3 now report 8.2% gain in flight efficiency accompanied with an even

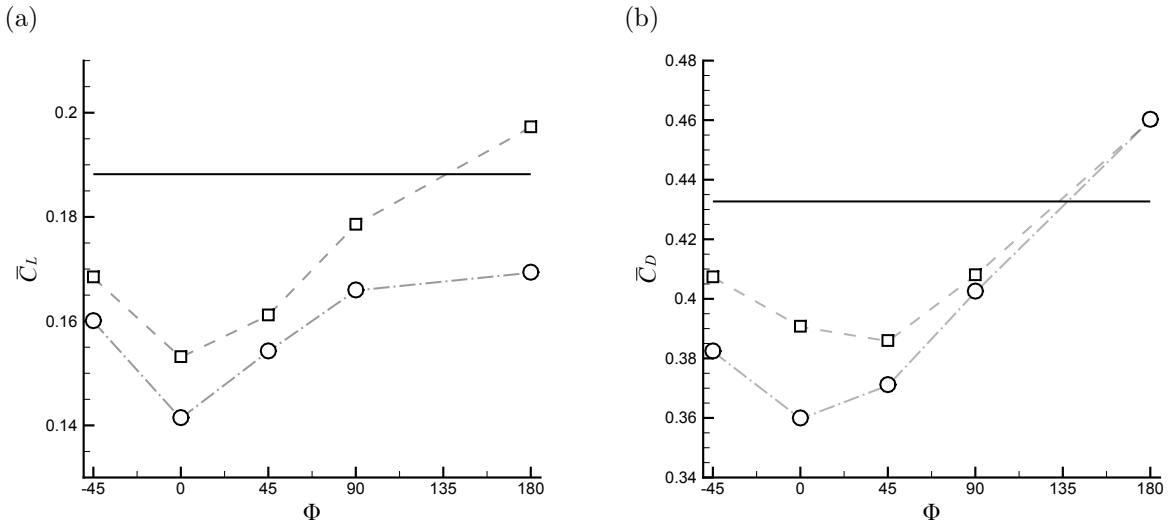

Figure 5.15: Time-averaged (a) Lift and (b) Drag coefficient with deflection phase $\Phi = [-45°, 0°, 45°, 90°, 180°]$: Rigid (——), Root (□), Tip (◯) plate configurations. Reynolds number Re = 100, deflection amplitude $\theta_m = 40°$, heave amplitude $\phi_m = 80°$.

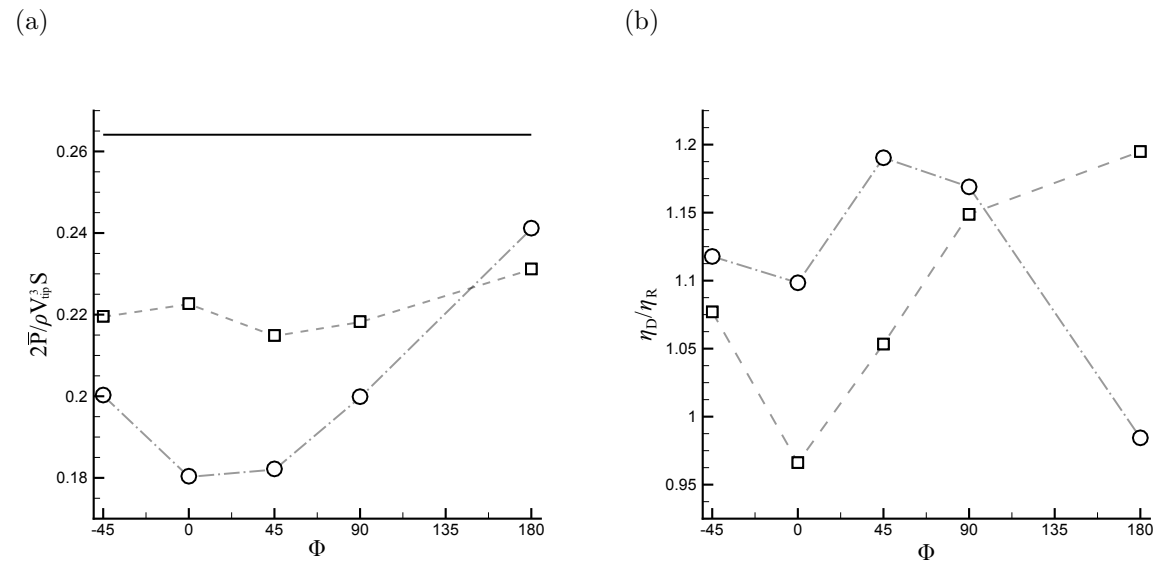

Figure 5.16: (a) Stroke-averaged power, $\overline{P}$, and (b) efficiency ratio in hover. Rigid (——), Root (□), Tip (◯). η_D indicates deflection plate efficiency and η_R rigid plate efficiency.

Table 5.3: Flapping Performance, $\theta_m = 20°$

Case	Φ_{def}	$\overline{C}_L$	$2\overline{P}/\rho V_{\text{tip}}^3 S$	η
Rigid	–	0.1899	0.2641	0.7192
Root	0	0.1722 (−9.3%)	0.2606 (−1.3%)	0.6608 (−8.1%)
	$\pi/4$	0.1758 (−7.4%)	0.2582 (−2.2%)	0.6810 (−5.3%)
	$\pi/2$	0.1856 (−2.3%)	0.2605 (−1.4%)	0.7124 (−0.93%)
	π	–	–	–
	$-\pi/4$	0.1795 (−5.5%)	0.2639 (−0.08%)	0.6804 (−5.3%)
Tip	0	0.1710 (−9.9%)	0.2395 (−9.3%)	0.7142 (−0.69%)
	$\pi/4$	0.1750 (−7.8%)	0.2397 (−9.2%)	0.7302 (+1.5%)
	$\pi/2$	0.1817 (−4.3%)	0.2536 (−3.9%)	0.7166 (−0.35%)
	π	0.1902 (+0.16%)	0.2336 (−11.5%)	0.8142 (+13.2%)
	$-\pi/4$	0.1789 (−5.8%)	0.2527 (−4.3%)	0.7078 (−1.6%)

greater reduction in power consumption of 24.6% as tabulated in Table 5.5. Trends for root flexion with phase $\Phi = 180°$ mirror those of $\text{Re} = 100$ but are boosted to greater percentages. The same holds true for tip flexion at $\Phi = 0$ where power and efficiency percentages are boosted with efficiency quadrupled. Tip deflection into the direction of motion with $\Phi = 180°$ was met with a drop in efficiency from that of the rigid plate at $\text{Re} = 100$, though now at $\text{Re} = 10^3$ experiences an increase in operational efficiency while maintaining power reduction. The trade-off of course is lift production with reductions as great as 18.4% for root deflection with $\Phi = 0$, however, at $\Phi = 180°$ the root flexion wing is still demonstrates its ability to impart greater downward momentum than the rigid wing and produce elevated lift.

Table 5.4: Flapping Performance, $\theta_m = 40°$, Re = 100

Case	Φ	$\overline{C}_L$	$\overline{C}_D$	$2\overline{P}/\rho V_{\text{tip}}^3 S$	η
Rigid	–	0.1899	0.4327	0.2641	0.7192
Root	0	0.1547 (−18.5%)	0.3908 (−9.7%)	0.2227 (−15.6%)	0.6948 (−3.4%)
	$\pi/4$	0.1628 (−14.2%)	0.3860 (−10.8%)	0.2149 (−18.6%)	0.7576 (+5.3%)
	$\pi/2$	0.1803 (−5.1%)	0.4081 (−5.7%)	0.2183 (−17.3%)	0.8262 (+14.9%)
	π	0.1987 (+4.6%)	0.4602 (+6.4%)	0.2312 (−12.5%)	0.8594 (+19.5%)
	$-\pi/4$	0.1701 (−10.4%)	0.4074 (−5.8%)	0.2196 (−16.8%)	0.7746 (+7.7%)
Tip	0	0.1425 (−24.6%)	0.3601 (−16.8%)	0.1804 (−31.7%)	0.7901 (+9.8%)
	$\pi/4$	0.1560 (−17.8%)	0.3712 (−14.2%)	0.1822 (−31.0%)	0.8562 (+19.0%)
	$\pi/2$	0.1680 (−11.5%)	0.4026 (−6.9%)	0.1999 (−24.3%)	0.8406 (+16.9%)
	π	0.1707 (−10.1%)	0.4603 (+6.4%)	0.2412 (−8.7%)	0.7080 (−1.6%)
	$-\pi/4$	0.1610 (−15.2%)	0.3825 (−11.6%)	0.2003 (−24.2%)	0.8038 (+11.8%)

Table 5.5: Flapping Performance, $\theta_m = 40°$, Re = 1000

Case	Φ	$\overline{C}_L$	$2\overline{P}/\rho V_{\text{tip}}^3 S$	η
Rigid	–	0.2707	0.2375	1.1398
Root	0	0.2209 (−18.4%)	0.1791 (−24.6%)	1.2334 (+8.2%)
	π	0.2972 (+9.8%)	0.2015 (−15.1%)	1.4749 (+29.4%)
Tip	0	0.2218 (−18.1%)	0.1365 (−42.5%)	1.6249 (+42.6%)
	π	0.2528 (−6.5%)	0.2084 (−12.3%)	1.2131 (+6.5%)

5.7 Heave Amplitude in Hover

The heave amplitude plays a significant role in determining the degree of interaction between a flapping plate and the wake. Low heave amplitudes leave the plate operating in the vicinity of the wake for the duration of the halfstroke. Additionally, smaller heave amplitudes may also have implications on the size and strength of the leading-edge and tip vortices and their corresponding dynamics and subsequent interaction with a reversing plate. The flexion modes have already demonstrated their ability to modify the surrounding flow field. Though how these modifications scale with heave amplitude are unknown. To offer some insight stroke-averaged lift and drag responses to heave amplitude are sought here with the objective of determining any departures in force coefficient trends from the rigid wing which would indicate the development of phenomena not represented at $\theta_m = 80^\circ$ in the flexion wings. Heaving amplitude is reduced from $\phi_m = 80^\circ$ in increments of 20° to $\phi_m = 40^\circ$, Figure 5.17.

With reduction the wake becomes increasingly influential, proving beneficial to lift production. The same holds true for the time-averaged drag coefficient, satisfying an inverse proportionality with heaving amplitude. Of the range of heave amplitudes presented there appears to be no immediate departure from trends displayed by the rigid wing lift and drag coefficients for the flexion wings. This would suggest the flexion modes do not take advantage of the reduced heave amplitude in a manner unavailable to the rigid wing and do not incite additional flow phenomena differing drastically.

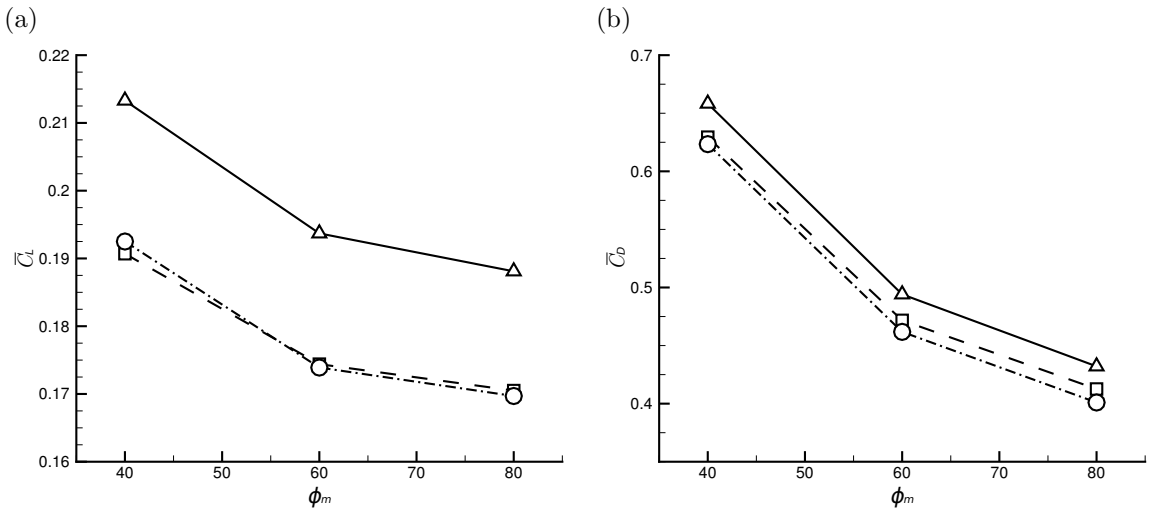

Figure 5.17: Time-averaged (a) Lift and (b) Drag coefficient: Rigid (△), Root (□), Tip (◯). Heave amplitudes include $\theta_m = [40°, 60°, 80°]$, deflection phase $\Phi_{\text{def}} = 0$.

5.8 Reynolds Number

The Reynolds number associated with smaller aspect ratio wings, ($AR \leq 3$), is typically on the order of $Re = O(10^2)$. In a bid to investigate operational limitations low aspect ratio wings the rigid, root and tip flexion plates are subjected to Reynolds numbers range $Re = O(10^2) - O(10^3)$ for reduced deflection amplitude $\theta_m = 20°$. All three plates monotonically increase in time-average $\overline{C}_L$ with increasing Re, Figure5.18(a), the slope of which decreases with Re. The averaged lift coefficient appears to plateau or approach performance saturation as it nears $Re = 10^3$ in all cases. The asymptotic nature of the stroke-averaged force coefficients with Reynolds number verifies Re = 10^3 as an appropriate maximum Reynolds number to consider for the aspect ratio $AR = 2$ wings. The root and tip flexion plates also perform very similarly in terms of average lift production for Reynolds numbers range, offering a maximum difference between the two of just 3% at $Re = 562.3$. Deflection amplitudes of $\theta_m = 40°$ presented above have demonstrated greater variability between tip and root flexion wings.

On the other hand, the time-averaged drag coefficient scales inversely to Reynolds number. It may be worth noted the convergent nature of the drag coefficient between the two

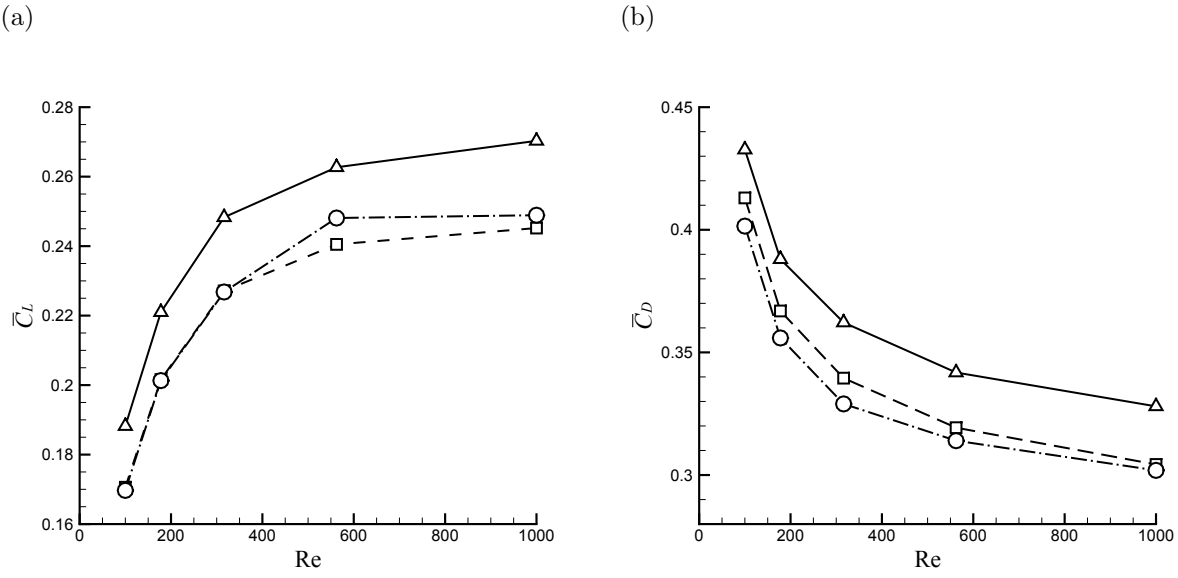

Figure 5.18: Time-averaged (a) Lift and (b) Drag coefficient with Reynolds number Re = [100, 177.8, 316.2, 562.3, 1000]: Rigid (△), Root (□), Tip (◯). Deflection amplitude $\theta_m = 20°$, deflection phase $\Phi_{\text{def}} = 0$, heave amplitude $\phi_m = 80°$.

flexion plates. Though the two flexion configurations behave very similarly, the difference in $\overline{C}_D$ between tip and root flexion maintains a visibly steady value until reaching Reynolds numbers $Re > 500$, beyond which the two drag values approach one another, Figure 5.18(b). High-fidelity simulation on low aspect ratio revolving wings by Garmann *et al.* also showed lift increases with Reynolds number up until a saturation point [35].

5.9 Trailing-Edge Deflection: Effective Attack Angle

Trailing-edge defleciton is now prescribed about the mid-chord position via flexion oriented along the span extending from base to tip. In this manner the plate experiences a uniform cross section for all radial positions. In examining chord-wise deflection Eldredge *et al.* found passive deflection to effectively shift lift and efficiency of a flexiible wing to trends similar to that of a rigid wing operating at a lower angle of attack, with the flexible wing requiring less actuation than the rigid counterpart [49]. This shift is achieved by quantifying an effective pitch angle. Similarly, in introducing chord flexion to a three-dimensional wing,

an effective angle of attack, $\tilde{\alpha}$, may be quantified by measuring the angle of a line intersecting the centroids of the newly separated portions of the plate, Figure 5.19. Chord flexion here is defined by a deflection about a line situated at the midchord position running the full span of the wing parallel to the leading-edge.

Desired $\tilde{\alpha}$ are achieved employing leading-edge attack angles $\alpha_{\text{LE}} = 50^\circ$ and 60° in conjunction with suitable chord-wise deflection amplitudes. Deflection profiles mirror that of the pitching profile of Equation (5.2). Beginning with lift coefficient $\bar{C}_L$ of the rigid wing, beyond an attack angle $\alpha = 50^\circ$ ($\equiv \tilde{\alpha}$) lift generation declines. Thus, $\tilde{\alpha} = 50^\circ$ is interpreted as the operational limit to be mimicked by a trailing-edge flexion plate. It becomes evident trailling-edge deflection does not produce lift in agreement with the rigid plate lift coefficient trend line. There is little convergence in the deflection lift data with that of the rigid plate trend line. Differences in trailing-edge and rigid plate trend lines decrease with decreasing α_{LE}. The leading-edge orientation largely dictates LEV strength and formation, thus formation about α_{LE} will differ from that of $\tilde{\alpha}$ in a rigid wing, contributing to the differences in lift performance.

It would seem the effective attack angle approach is not sufficient in quantifying a flexion plate analogous to a rigid counterpart based on lift arguments alone. Conversely, inspection of drag profiles reveals the trailing-edge flexion plate agrees rather well with the rigid plate $\bar{C}_D$ trend line, nearly collapsing onto the rigid member. In reconciling the differences observed in lift behavior in response to $\tilde{\alpha}$ between two-dimensional wings [49] and three-dimensional plates it should be noted the two-dimensional wing is tantamount to an infinite aspect ratio three-dimensional plate undergoing translation, rather than revolving kinematics. It remains to be seen if the lift profile of a translating finite aspect ratio rigid plate could be reproduced with a trailing-edge deflection plate with an effective attack angle $\tilde{\alpha} = \alpha$.

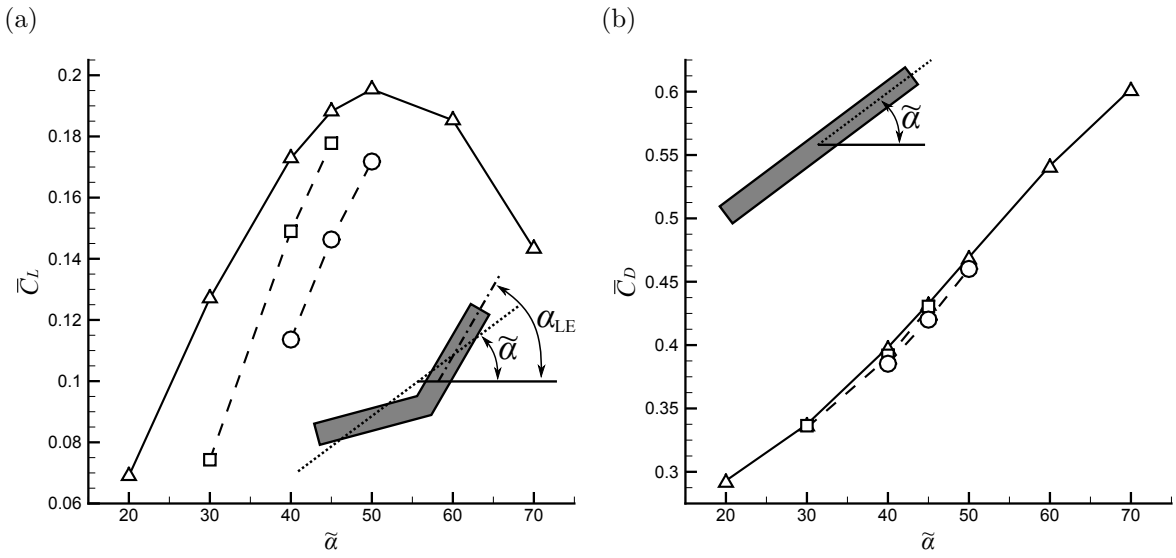

Figure 5.19: Time-averaged (a) Lift and (b) Drag coefficient versus effective angle of attack $\tilde{\alpha}$: Rigid ($\triangle$), $\alpha_{\mathrm{LE}} = 50°$ ($\square$), $\alpha_{\mathrm{LE}} = 60°$ ($\bigcirc$). Plates: Rigid (——), Trailing-edge deflection (– – –).

5.10 Conclusion

Two-dimensional studies of hovering wings have found wing deformation had little effect on leading-edge vortex strength or formation time. For the two generalized deflection modes explored here in three-dimensional rectangular wings it has been shown deformation had a greater role on LEV formation and circulation strength in three-dimensional flow aided by three-dimensional flow phenomena such as axial flow convecting information and disturbances of the root flexion along the span and the tip flexion wing's alteration of the tip vortex and its interaction with the leading-edge vortex. With deformation following a sinusoidal waveform of maximum deflection coincident with the midstroke in hover it was shown the effect of deflection were more pronounced in areas of higher local velocity which correspondingly meant tip deflection resulted in greater modification of lift, drag and efficiency. At Re = 100 the tip deflection produced an enlarged tip vortex over that produced for a rigid wing and also experienced a shift inboard the wing resulting in greater overlap between the tip vortex and the leading-edge vortex. At Re = 1000 the tip vortex suppressed the

formation of secondary vortical structures emanating from the wing tip in rigid and root flexion wings resulting in a simplified wake to encounter in hover. Efficiency gains in flexion wings over that of the rigid counterpart were shown to increase with Reynolds number. The root flexion wing transitions from less efficient than the rigid wing to greater with increasing Reynolds number from Re = 10^2 to Re = 10^3. The leading-edge vortex circulation of the flexion wings exhibited profiles distinct from the rigid wing. At Re = 100 the root flexion profile maintained a near-linear dependence on spanwise position until a maximum and tip flexion assumed a symmetric profile with a maximum at midspan. Flapping at Re = 10^3 hosts a broader range of circulation values within all three wing configurations. All wings experienced a spike in LEV circulation near 70% span in response to the tip vortex redirecting inboard, producing a spanwise component merging with the trailing-edge shear layer in contrast to the tip vortex produced at Re = 100 which develops along a path outlined by the wing tip trajectory. Mapping of the LEV axis highlighted its inherent robustness as the axes of the rigid, root flexion, and tip flexion wings exhibited negligible differences in spatial evolution along the span at Re = 100. At Re = 10^3 axis invariance to deflection continued with all wing configurations experiencing the same axis profile, though the spatial evolution of the LEV now receded from the leading edge approaching the wing tip. The LEV core demonstrated notable responses to wing deflection while satisfying a general trend of core enlargement with span until reaching a maximum near 75% span for both Reynolds numbers considered. Further along the span the rigid and root flexion wings experiences core size reductions while tip deflection supports further enlargement and reorientation congruent with wing tip deflection.

CHAPTER 6

Three-Dimensional Wing in Hover: Passive Deformation

6.1 Introduction

There has been a growing interest in flapping wings operating at elevated Reynolds number. This includes Reynolds on the order of Re = $O(10^4)$. The term elevated is used here to distinguish the flow regime from Reynolds numbers characteristic of biological fliers observed in nature whose Reynolds numbers typically peak at $O((10^3)$. It has been reported flapping at elevated Reynolds numbers activates a host of flow phenomena absent at lower regimes including bursting. However these phenomena are yet to be fully understood. Therefore, attention is increasingly given to the trans-bursting regime for MAV applications. Here flow visualization is performed to provide qualitative insight into the effects of elevated Reynolds number on LEV formation. Naturally a given wing is expected to experience greater aerodynamic loads and correspondingly the potential for greater deformation. As such, the effect of flexibility on LEV formation in maneuvers associated with flapping flight are of primary importance as much of the wing lift can be attributed to the LEV. Flexibility here is represented by a single hinge allowing for a segmental tip or root portion of the wing to passively deflect. The wings considered are dynamically-scaled fruit fly (*Drosophila melanogaster*) wings. The objective is to asses the response of vortical structure development about wings which typically operate at the lower Reynolds number flapping limit Re = $O(10^2)$ to greater flight speeds and acceleration fields.

(a) (b)

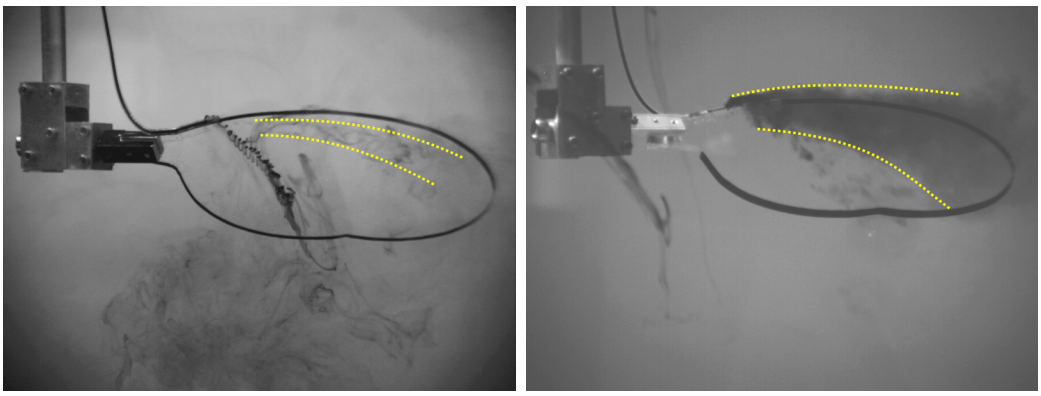

Figure 6.1: Flow visualization of a flapping wing at (a) Re = 100 and (b) Re = 14226 with fixed $\alpha = 45°$.

6.2 Reynolds Number Effects on LEV Growth

With sufficiently increased Reynolds number the leading-edge vortex undergoes a fundamental change in behavior thought to be driven by the interaction between axial flow and the LEV core. In Section 5.5 it was observed a rotating wing experiences axial flow from wing root to tip driven by pressure gradients inherent in the wing's radial velocity gradient. With increasing Reynolds number an order of magnitude it was shown the axial velocity maximum shifted from the trailing edge toward the leading edge, ultimately localizing in the LEV core. Further increasing Reynolds number then results in LEV bursting which is defined here as the sudden expansion of the LEV in size accompanied by significant levels of mixing within the vortex. The deceleration of the newly integrated axial flow into the core is thought to be responsible [41, 54]. The deceleration also implies possible flow reversal within the core.

Figure 6.1 demonstrates the transformation of the leading-edge vortex in response to Reynolds number beyond the trans-bursting limit about a dynamically scaled fruit fly wing of aspect ratio $AR = 2.36$. At Re = 100 the LEV is visualized as a clean spiral in the vicinity of the leading edge across the span. At Re = 14226 there exists significant growth and expansion extending to the trailing edge. Despite the turbulent appearance the LEV remains stable owing to quasi-steady accelerations of centripetal and Coriolis acceleration

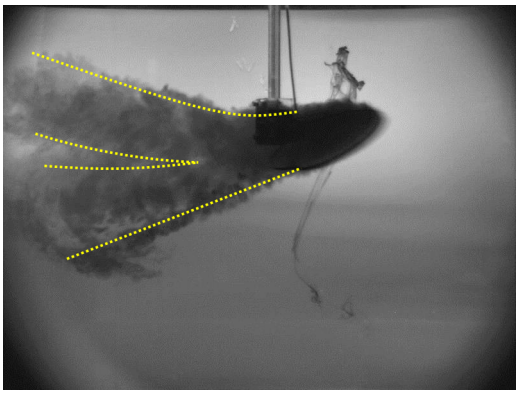

Figure 6.2: Dual vortical wake stemming from a rigid wing tip shortly after midstroke in constant velocity revolution of 360° at fixed $\alpha = 45°$.

which are inversely proportional to Rossby number. Experiments by Lentick and Dickinson on rotating and translating wings found translating wings with Ro = inf could not maintain a stable LEV [68]. Figure 6.2 shows signs of a dual vortex wake stemming from the wing tip undergoing pure rotation impulsively started at Re = 14226. The wake stands as another departure from behavior characteristic of sub-bursting Reynolds numbers. It is worth noting that bursting initiates almost immediately upon startup.

6.3 Passive Deflection in Hover

Increasing quasi-steady acceleration associated with revolving wings has been shown to induce significant growth of the leading-edge vortex. As noted earlier, increased flight speed and acceleration fields is bound to increase aerodynamic loads on the wing as well as inertial effects, resulting in greater deformation for a wing structurally suited for lower Reynolds number flight. With the potential for greater deflection in a flow regime that remains largely unknown, here dye visualization is employed to qualitatively examine the effects of deformation at elevated Reynolds number $\mathrm{Re}_{b/2} = 14226$ ini hover kinematics. Heave is determined by a nearly triangular waveform

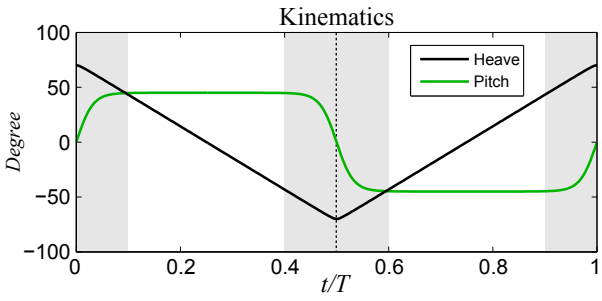

Figure 6.3: Flapping kinematics: heave (——), pitch (——). Shaded regions indicate pitch.

$$\phi(t) = \frac{\phi_m}{\sin^{-1}(M)} \sin^{-1}\left[M \cos\left(2\pi f t\right)\right], \tag{6.1}$$

where in the limit as $K \to 1$ the waveform increasingly becomes triangular rather than sinusoidal as proposed by Berman and Wang [9]. Pitch maintains a constant value of $\pi/4$ for the majority of a stroke, determined by a the hyperbolic tangent function

$$\alpha_p(t) = -\frac{\pi}{2} + \frac{\pi}{4} \tanh\left[N \sin\left(2\pi f t\right)\right], \tag{6.2}$$

where N is a smoothing parameter. Variables are as listed in Table 6.1 and kinematics are plotted in Figure 6.3.

Table 6.1: Hover Kinematic Parameters

Sweep Amplitude	ϕ_m	70°
Triangular Fit	M	0.99
Smoothing Parameter	N	5
Angle of Attack	α	45°
Reynolds Number	$\mathrm{Re}_{b/2}$	14226

Each wing contains a single torsional spring of stiffness $K = 0.035$Nm about the hinge as a restoring force with the undeflected state as the equilibrium state. Through a process of matching CAD reconstructions of the experimental apparatus with high speed imaging of the wings in hover the deflection angles are quantified over the course of a halfstroke as

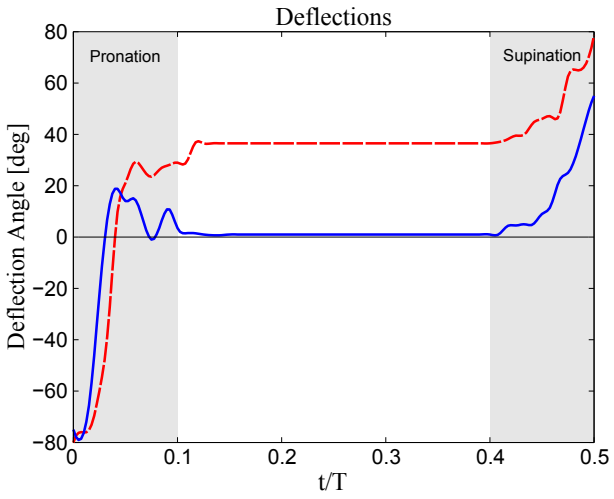

Figure 6.4: Deflection angles in hover over a representative halfstroke: root (———), tip (– – –). Shaded regions indicate pitch.

shown in Figure 6.4. The root deflection wing is most responsive to pitch and after some oscillatory behavior the wing returns to the undeflected state once the desired angle of attack is achieved. Conversely, the tip deflection wing remains in the deflected state well after pitch, holding a steady angle of 38°. The implications here are a given biological wing would be prone to deflection in the distill portion of the wing during heave and most susceptible to root deflection in pitch or stroke reversal. Of course the deflection behavior of a given wing would be dependent on a number of factors including architectural, material and planform.

The effects of these deflections in stroke are explored in Figure 6.5. It has been established the leading-edge vortex experiences significant growth at the Reynolds number under investigation. The dye about the rigid wing appears well mixed and near the 70% span position the LEV growth extends to the wing trailing edge. The LEV growth for the root deflection wing appears very similar to that of the rigid wing in stroke. The root deflection wing returns to an undeflected state after pitch making it geometrically-similar to the rigid counterpart. The greatest variability in LEV formation is observed for tip deflection in stroke. Tip deflection maintains a steady deflection angle and as a result the LEV grows considerably. The very nature of LEV growth at $\mathrm{Re} = O\left(10^4\right)$ has been thought to be indicative

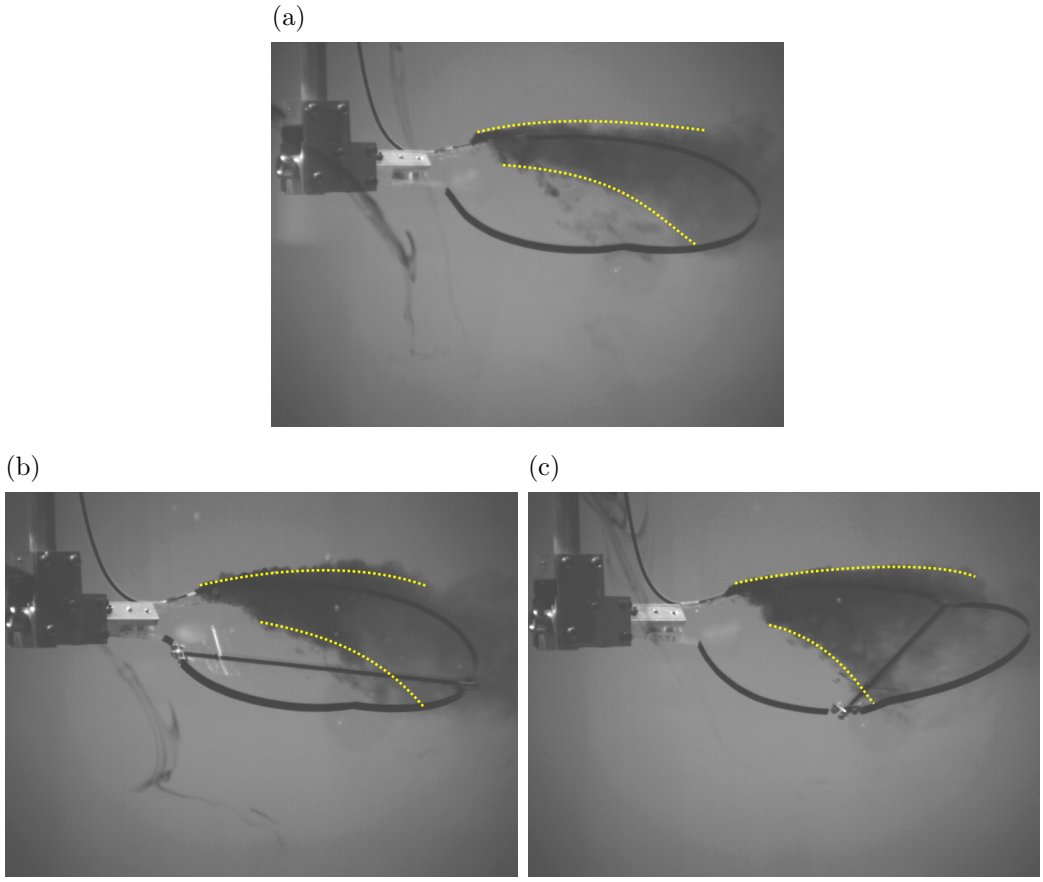

Figure 6.5: Dye visualization of leading-edge vortex about (a) rigid, (b) root, and (c) tip deflection wings prior to pitch. Dotted lines highlight the leading-edge vortex.

of LEV bursting. Khoo *et al.* examined bursting vorticity in an unconfined vortex flow and observed a correlation between abrupt enlargement of the vortex with sudden deceleration of axial flow in the vortex core [54]. Additionally, as Reynolds number is increases there is a shift of axial flow about a flapping wing from the trailing edge toward the leading edge and at sufficiently high Reynolds number this flow is integrated into the LEV core. The great departure of the tip deflection wing may be a greater deceleration of LEV core flow. The deflected tip may provide an obstruction of sorts for core flow and promote greater deceleration which translate to greater enlargement.

6.4 Passive Pitch in Hover

Passivity is extended to pitch in addition to flexion. Various stiffnesses are tested with the addition or removal of torsional springs about the flexion line. In the absence of direct force measurements the degree of pitch in stroke may provide some insight into the nature of resultant force and moment about the wing and LEV formation in response to the variable hinge spring stiffness. Figure 6.6 shows optical encoder readouts installed on the pitch rod of the flapper apparatus. The rigid wing reaches a largely steady pitch angle at approximately one-fourth halfstroke cycle. The pitch phase lags stroke reversal by 16% halfstroke cycle. The measured pitch bears resemblance to high-speed video measurements of wing kinematics in free-flying fruit flies by Fry *et al.* which determined a nearly synchronous relationship between wing reversal and supination during slow ascension [34]. The similarity comes despite differing flow patterns associated with the respective Reynolds numbers which may lead some to believe the driving mechanism behind passive pitch is primarily inertial. However, a study by Bergou *et al.* calculated the rotational power owing to aerodynamic and wing inertias for motions derived from measurements of tethered insect to reveal a negative rotational power suggesting fluid forces assist pitching rather than resist [7].

The pitch behavior exhibited in the rigid, root flexion and tip flexion wing configurations is complicated not just by the aerodynamic resistance presented in their deformation in stroke but also in the distinct wakes created by such deformation which is encountered during the subsequent halfstroke. The exclusion of springs in Figure 6.6 provides the greatest variability among the flexion wings compared to the rigid wing. Root flexion produces greater pitch than the rigid wing initially then reduces pitch below the rigid wing approaching stroke reversal. It is believed this is in part due to the weakening of the trailing-edge vortex at the end of the halfstroke which retards its ability to induce a significant flow field to aid in the downwash of the previous halfstroke's leading-edge vortex under the wing. The rise in pitch angle is the indicative of the wing pitch navigating the passage of the previous leading-edge vortex in a flow field reduced in strength of counter-rotating vortical structures, namely

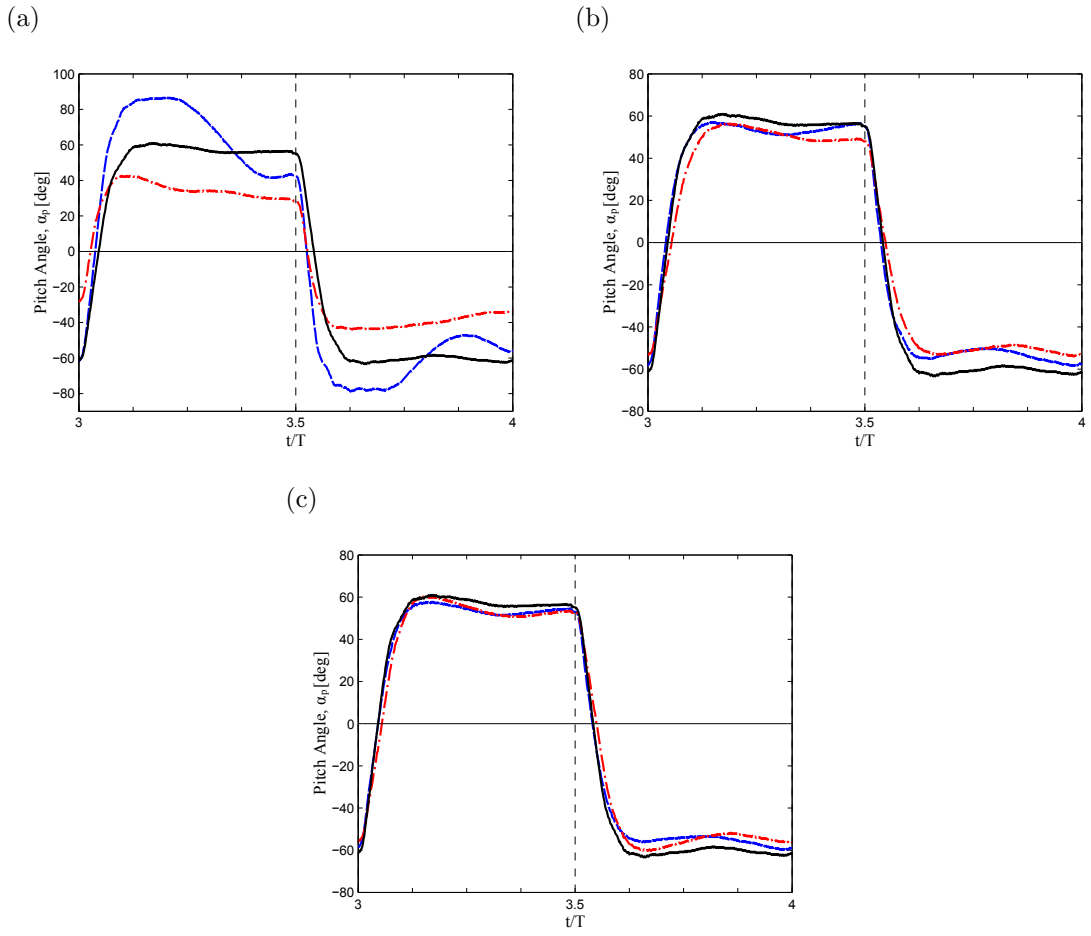

Figure 6.6: Pitch angle in hover over a representative period at Re = 14226 with $\phi_m = 70°$. Wings: rigid (——), root flexion (– – –), and tip flexion (— · —). Torsional springs at the hinge: (a) 0 springs, (b) 1 spring, and (c) 2 springs.

the trailing-edge vortex. The inclusion of springs places the deflection wings profiles in agreement with that of the rigid wing. In tip deflection without torsional springs the wing approaches a maximum pitch angle early on in stroke and begins a process of reduction until stroke reversal. The deflection portion of the wing could potentially shift the resultant pressure forces closer to the leading edge and potentially reduce its contribution to pitch however it has been shown the leading-edge vortex growth is expanded under tip deflection. A significant contributor to the lower pitch angle is the reduction of forces acting on the distal region of the now deflected wing. As the wing is made stiffer with the addition of torsional springs the behavior increasingly approaches that of the rigid wing.

In reducing the heave amplitude in Figure 6.7(a) the pitch profile of the rigid wing transitions to one of smooth gradual increase until reaching a maximum near stroke reversal. Pitch also now experiences a greater lag with respect to stroke reversal. Experiments on free-to-pivot flat plates in hover kinematics by Granlund *et al.* found the stroke amplitude to chord ratio in rectilinear translation determined the vortex production history and aerodynamic load production history with large strokes producing simpler vortex wakes [40]. Additionally, Granlund *et al.* found Reynolds numbers effects in the range considered were insignificant. It is important to note their experiments were focused on two-dimensional kinematics and pitch was confined to a predetermined range via limiters. However, despite these key differences the effects of reduced stroke amplitude are mirrored in the rigid wing passive pitch profiles in Figure 6.7(a), with the increased phase lag and "smoothing" of the pitch profile due to the greater interactions with the wake. In the exclusion of torsional springs in Figure 6.7(b) the root flexion wing now showcases a plateauing behavior reminiscent of the rigid wing at $\phi_m = 70°$. Of the wings configurations presented the root flexion wing's pitch phase is the least affected by the reduction in stroke amplitude. Tip flexion wing does not offer that great a departure from the rigid wing. Once again with the application of torsional springs the pitch profiles approach that of of the rigid wing.

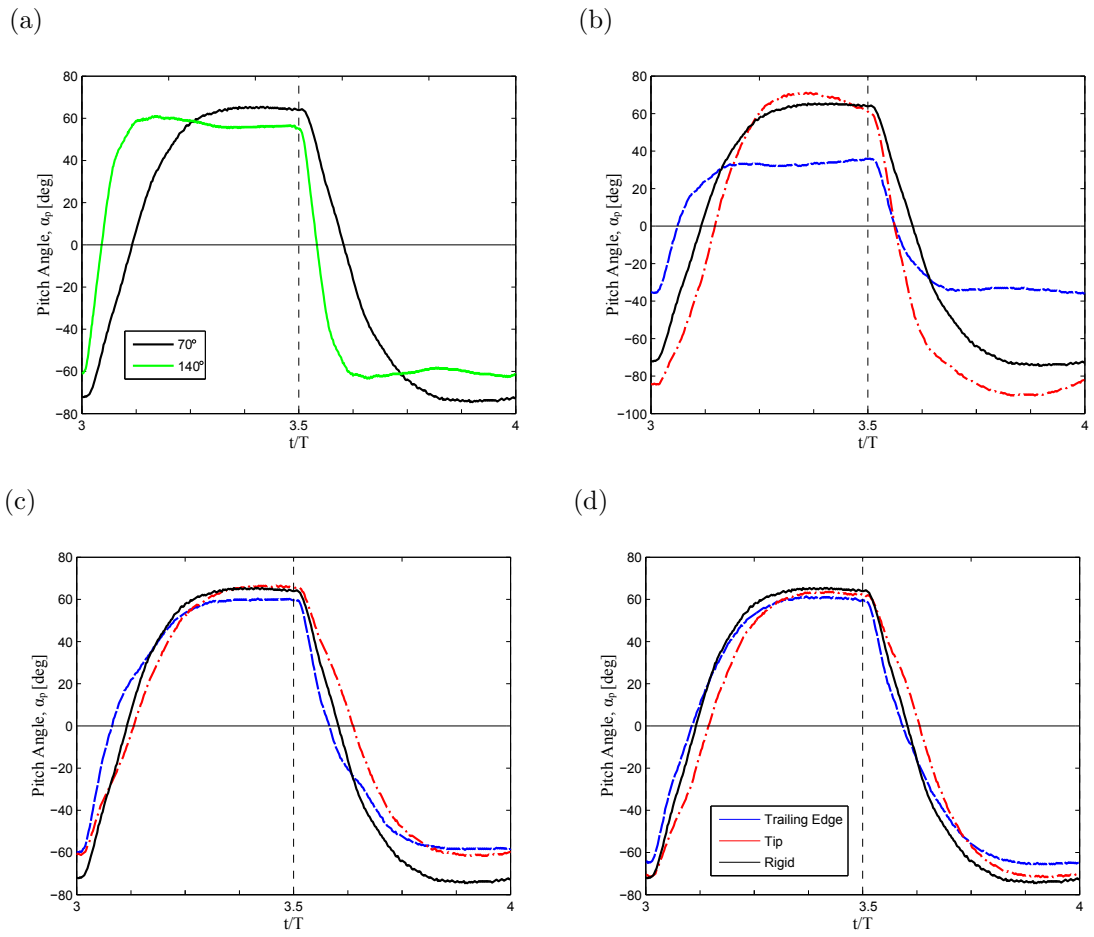

Figure 6.7: Pitch angle in hover over a representative period at Re = 14226 with $\phi_m = 35°$. Wings: rigid (——), root flexion (– – –), and tip flexion (— · —). (a) Pitch behavior comparison between $\phi_m = 70°$ and $\phi_m = 35°$. Torsional springs at the hinge: (b) 0 springs, (c) 1 spring, and (d) 2 springs.

6.5 Conclusion

As demonstrated in Chapter 5 there exists a shift in axial flow maximum about a flapping wing from external to the leading-edge vortex in the vicinity of the wing trailing edge to the wing leading edge with increasing Reynolds number from $\mathrm{Re} = 10^2$ to $\mathrm{Re} = 10^3$. This shift places maximum axial flow coincident with the leading-edge vortex, introducing significant core flow into the LEV. When Reynolds number is increased further there exists a deceleration of core flow which incites enlargement of the leading-edge vortex termed bursting. Dye visualization on flapping wings demonstrated this growth from a compact LEV adhering to the wing leading edge at $\mathrm{Re} = 10^2$ to a well mixed LEV with expansion extending to the wing trailing edge at $\mathrm{Re} = O(10^4)$. Two distinct wing deformation modes were introduced to the wing as root and tip flexion spring-loaded flexion lines allowing for passive deflection. Measurements of in-stroke deflection revealed root deflection was largely isolated to the pitch phases of hover with the wing returning to an undeflected state during much of the stroke. Tip flexion, however, exhibited significant deflection during stroke which was found to further enhance LEV bursting by means of the deflection tip acting as a physical barrier decelerating the LEV core flow and redirecting vorticity.

CHAPTER 7

Three-Dimensional Wings in Rotary Motion

7.1 Introduction

Much of the flapping wing's performance and lift capabilities are largely attributed to the development of a low-pressure suction region above the wing via the formation of a leading-edge vortex. In biological fliers and MAV applications the finite wing stroke ensures the attachment of the leading-edge vortex for the duration of the stroke. In an effort to distill the nature of leading-edge vortex formation and fundamental long-term behavior of the leading-edge vortex, wings undergoing unidirectional rotation kinematics are examined. Wings are maintained at a fixed angle of attack and allotted a single degree to maneuver about the rotary shaft completing one revolution of 360°. The rotation angle is well beyond stroke angles typically observed in flapping flight. In this manner the effects of prolonged sweep on LEV attachment are explored and the sustainability of the LEV influence on lift generation can be quantified via direct force measurements. With the exception of the initial angular acceleration and deceleration, which constitute a mere fraction of the total rotary angle, the simplified kinematics relieve the LEV of influences from secondary acceleration fields associated with pronation and supination. The wings considered include low aspect ratio $AR = [1, 2]$ with rectangular planforms. At such aspect ratios there is expected to be greater interaction between the tip and leading-edge vortex. Reynolds numbers tested are elevated to coincide with the bursting-limit associated with significant enlargement of the LEV. Further, in addition to rigid wings, the effects of chordwise flexibility on aerodynamic performance and the implications on LEV formation are also explored. At the Reynolds numbers considered the LEV growth is known to extend to the wing trailing edge before

reaching saturation. Trailing edge deflection results in a dynamic chord thereby modifying the spatial evolution, and possibly the strength, of the leading-edge vortex.

7.2 Rigid Rotary Wings

Rotary wing experiments were conducted in water and a $50-50$ mixture of water and glycerin by volume. Rectangular planform wings of aspect ratio $AR = [1, 2]$ were accelerated from rest with a constant acceleration to reach a maximum constant velocity for the duration of rotation following a smoothed ramp-up and ramp-down velocity profile which allows for a continuous motion that is differentiable, avoiding discontinuities in the angular acceleration:

$$\Omega(t) = \frac{\dot{\Omega}_{\max}}{2a} \ln\left(\frac{\cosh(a(t-t_1))\cosh(a(t-t_4))}{\cosh(a(t-t_2))\cosh(a(t-t_3))}\right) \tag{7.1}$$

where a is the smoothing parameter, t_1 and t_2 determine initiation and completion of acceleration from rest of an un-smoothed profile, and t_3 and t_4 determine initiation and completion of deceleration to rest for an un-smoothed profile. The deceleration is equal and opposite to that of the angular acceleration. Sample kinematics are shown in Figure 7.1.

Eq. (7.1) is a modified form of a function implemented by Eldredge *et al.* in pitching plate studies [31]. Wings engaged in unidirectional rotation are held at a fixed angle of attack with a root standoff distance off $0.5c$ from the rotary axis to the wing root, Table 7.1. Two Reynolds numbers are tested with differing reference velocities, the first of which is with respect to the room velocity and the second Reynolds number based on three-quarter span position from the wing root as depicted in Figure 7.2. The root Reynolds number aids in isolating effects of span on LEV on aerodynamic performance and three-quarters Reynolds number ensures all wings experience the same conditions at the point along the span where sudden enlargement of the LEV is expected to occur. High-fidelity simulation by Garmann and Visbal on revolving wings showed the enlargement of the vortex loop generated by the wing according to travel distance of the wing tip with the leading-edge vortex lifting slightly off the surface near the outboard section of the wing to form an artch-type structure at

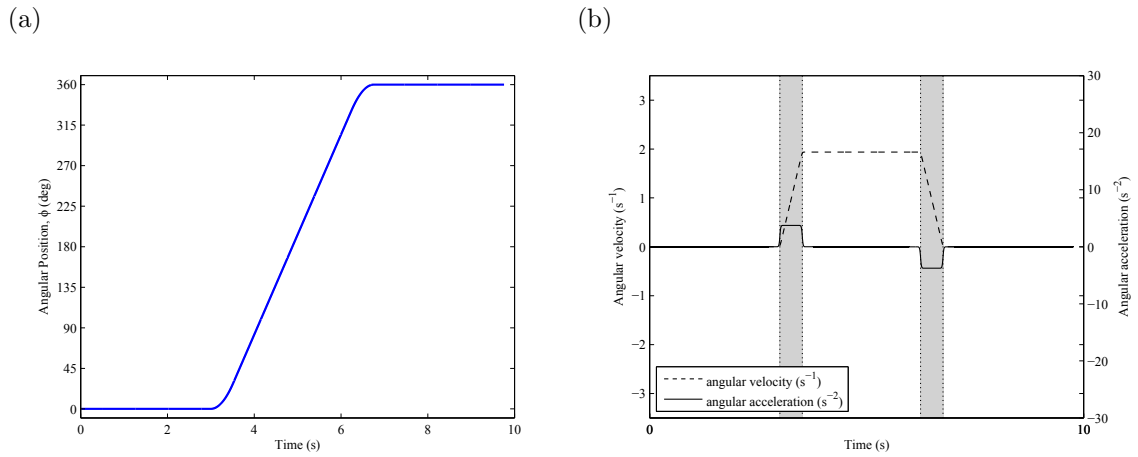

Figure 7.1: Sample rotary kinematics. (a) Unidirectional rotation angular position, (b) angular velocity and acceleration. Shaded regions indicated acceleration phases.

75%-span position that reattaches to the wing tip early on in stroke [36]. Later in stroke as inboard pressure establishes the leading-edge vortex experiences expansion near the midspan position onward as the LEV experiences burst and breakdown.

Table 7.1: Rotary Wings

Aspect Ratio	AR	[1, 2]
Root Standoff	r_s/c	0.50
Angle of Attack	α	30°, 45°, 60°
Reynolds Number	$\mathrm{Re}_{\mathrm{root}}$	10^3
	$\mathrm{Re}_{3/4b}$	10^4

Initial experiments at $\mathrm{Re}_{\mathrm{root}} = 10^3$ utilized the water-glycerin mixture as the working fluid, Table 7.2. The plates are accelerated from rest over 15° of rotation as with deceleration. Figure 7.3 showcases the aerodynamic performance of an aspect ratio $AR = 1$ wing. The angular acceleration phases of rotation are reflected in initial transients of lift and drag owing in part to inertial-driven forces of added mass. Negligible difference is observed in lift behavior of $\alpha = 45°$ and $\alpha = 60°$ with both profile and magnitude in agreement. Lift approaches a maximum near rotation angle $\phi = 115°$. Lift then experiences a gradual, yet

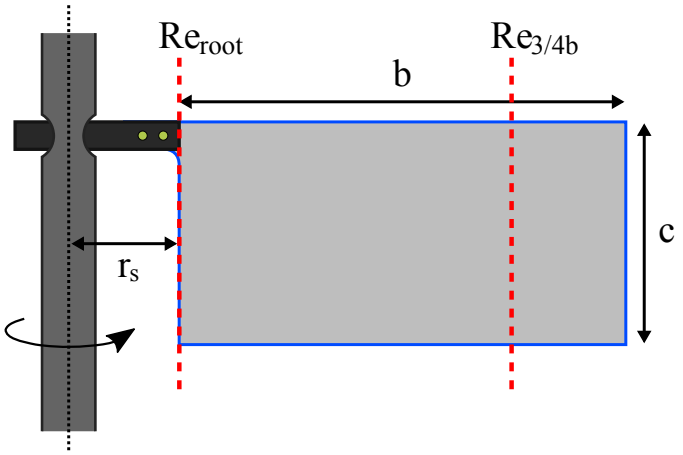

Figure 7.2: Diagram of rigid wing mounted on the rotary shaft. The two Reynolds numbers shown use differing spanwise locations for reference velocity.

slight, decrease until deceleration. Lift generated at $\alpha = 30°$ lies below that of the remaining attack angle though it hosts a delayed maximum near $\phi = 238°$. Additionally, there appears a secondary minor peak in lift near $\phi = 90°$. Drag monotonically increases with angle of attack with maximums near $\phi = 120°$.

On the nature of the initial transient spikes present in all force histories throughout this study, given the wing accelerates from rest and decelerates to a stop it is expected that added mass contributes to the spike. However the acceleration profile is symmetric about the acceleration about the acceleration phases as demonstrated in Figure 7.1(b) which would indicate effects of added mass alone should produce a symmetric spike as added mass force is directly proportional to acceleration. Added mass approximations by Sane and Dickinson in Eq. (7.2) and by Korotkin in Eq. (7.3) are plotted in Figure 7.4. Rather than symmetry, the spike achieves a peak value coincident with the end of the acceleration phase indicating added mass along does not account for initial transients. Dickinson and Gotz observed similar spike behavior in experiments on model wings accelerating from rest [24] where they postulated the peak is also the result of transient vortex formation about the wing and note the ability of the wing to initiate the formation of leading-edge vortex is enhanced with increasing Reynolds number.

On inspection of the spike

$$F_{N,S} = \rho\frac{\pi}{4}R^2\bar{c}^2\left(\ddot{\phi}\sin\alpha\right)\begin{cases}\int_{0.5}^{1.5}\hat{r}^2\mathrm{d}\hat{r}\\ \int_{0.25}^{1.25}\hat{r}^2\mathrm{d}\hat{r}\end{cases} = \rho\frac{\pi}{4}R^2\bar{c}^2\left(\ddot{\phi}\sin\alpha\right)\begin{cases}1.0833 & AR=1\\ 0.64583 & AR=2\end{cases} \tag{7.2}$$

$$F_{N,K} = -\lambda_{22}\left[-0.5\left(b+c\right)\right]\sin\left(\alpha\right)\dot{\Omega} = \left[0.5\left(b+c\right)\right]\sin\left(\alpha\right)\dot{\Omega}\rho Sb\begin{cases}0.46142 & AR=1\\ 0.56605 & AR=2\end{cases} \tag{7.3}$$

Upon extending the wing span to obtain aspect ratio $AR = 2$ wing, while maintaining a root Reynolds number of $\mathrm{Re}_{\mathrm{root}} = 10^3$, lift peak trends are intensified with peaks much more distinct than previously observed. Lift of $\alpha = 45°$ now exhibits a peak near $\phi = 117°$ which develops and diminishes at greater rates than the remaining force history for duration of the stroke, as shown in Figure 7.5. The end of the peak is marked by a dramatic rate of change of lift similar to that reporter for $AR = 1$ with lift experiencing a gradual, yet slight, decrease until deceleration. Lift of $\alpha = 60°$ maintains a profile mirroring that of $\alpha = 45°$ yet the extensional effects of span now provide for a slight reduction in performance with $\alpha = 60°$ producing less lift. At this greater aspect ratio $\alpha = 30°$ lift and drag are both characterized by indifference to rotation angle with both forces maintaining near constant values for the duration of the stroke.

Table 7.2: $\mathrm{Re}_{\mathrm{root}} = 10^3$

Aspect Ratio	AR	[1, 2]
Reynolds Number	$\mathrm{Re}_{3/4b}$	[2500, 4000]
	Re_{R_g}	[2000, 3000]
Acceleration Angle	θ_{acc}	15°

Now the Reynods number is defined by the three-quarter spanwise position with experiments now conducted in water. Sudden enlargement of the LEV has been reported to initiate near $70-75\%$ span at sufficient Reynolds numbers. A Reynolds number value of

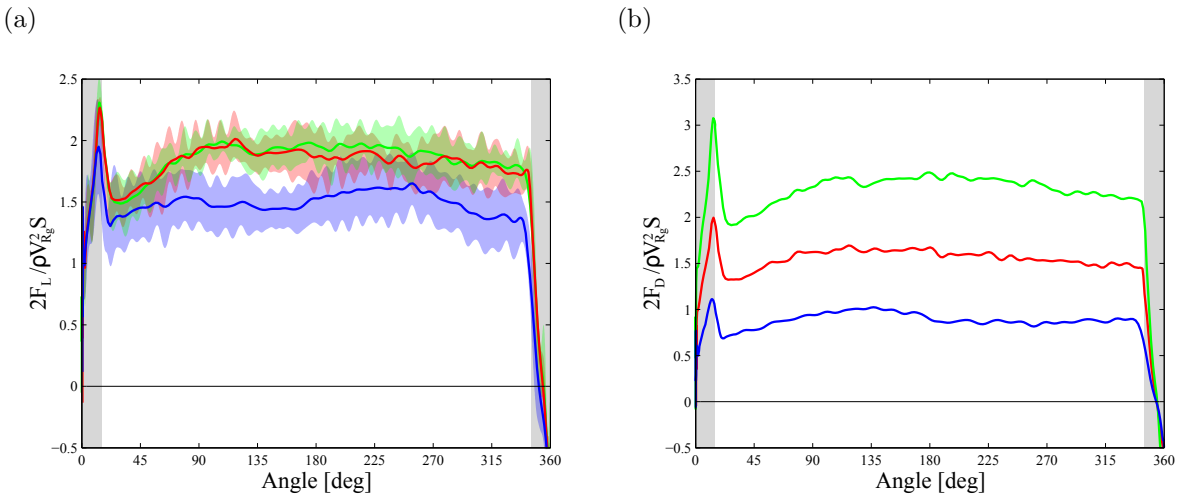

Figure 7.3: (a) Lift and (b) drag over the coarse of one revolution for rigid wing of $AR = 1$ at $\mathrm{Re}_{\mathrm{root}} = 10^3$. Angle of attack: 30° (——), 45° (——), 60° (——). Gray shaded regions indicate acceleration phases and colored shaded regions indicate standard deviation.

$\mathrm{Re}_{3/4b} = 10^4$ is capable of prompting LEV expansion and bursting in addition to a host of enlargement instabilities and secondary vortical structures about the leading edge. Selection of the three-quarter span position is to induce these phenomena on both aspect ratio wings and examine the aerodynamic effects of LEV formation and breakdown. Both wings are now accelerated over one chord length as measured from the reference spanwise position, resulting in varying angles among the two aspect ratios as indicted in Table 7.3. However, xperimental studies on rotating wings by Schlueter and Jones found outside of the acceleration phases force history of the constant-velocity portion of the wing stroke was independent of acceleration distance [91].

In Figure 7.6 the lift and drag of $AR = 1$ at $\mathrm{Re}_{3/4b} = 10^4$ wing are shown. Once again, as was the case for $\mathrm{Re}_{\mathrm{root}} = 10^3$, the lift of $\alpha = 45°$ and $\alpha = 60°$ are comparable to one another in magnitude and share key characteristics, namely the development of twin peaks largely centered about midstroke rotation angle $\phi = 180°$. The peaks are much more defined for $\alpha = 60°$ with one peak near $\phi = 115°$ and the second occurrence near $\phi = 255°$. The lift profile is best characterized as periodic or repeatable, more so for $\alpha = 60°$ than other angle of attack tested. When you entertain the idea of period lift generation it conjures up an

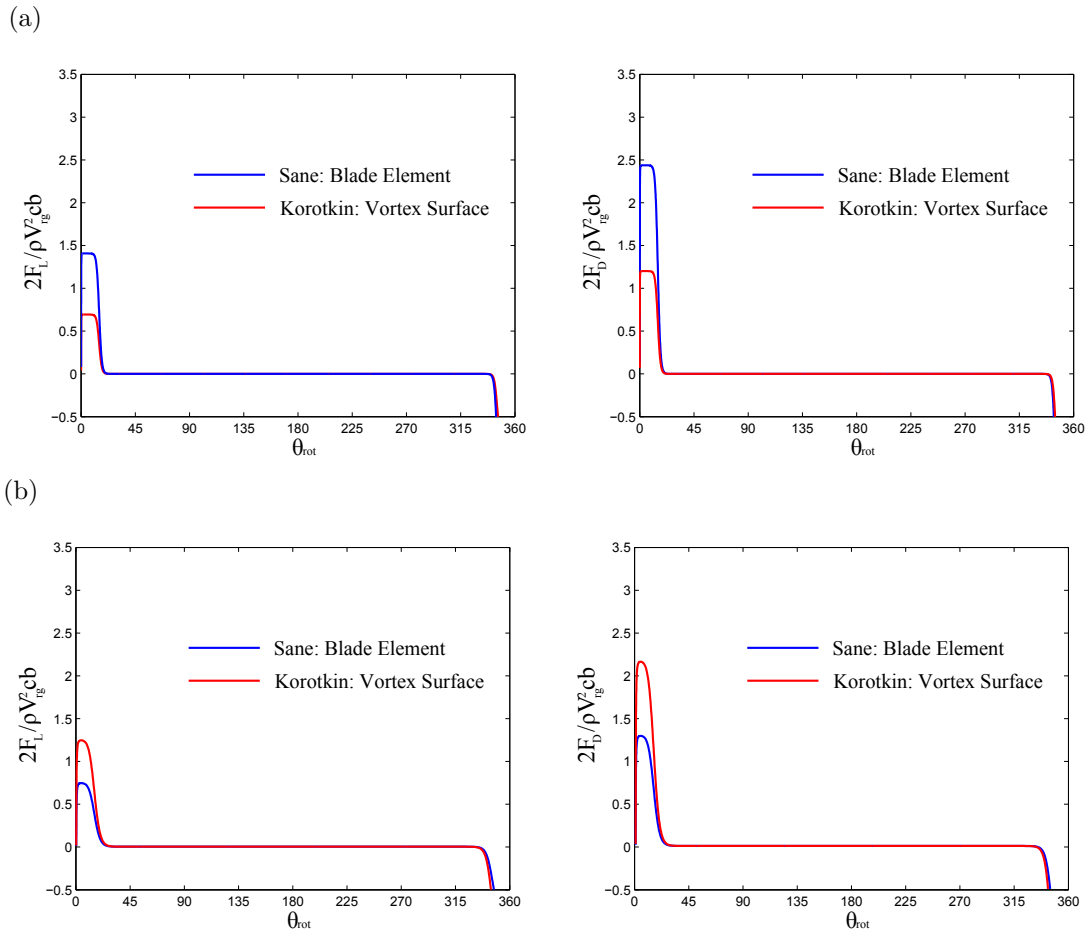

Figure 7.4: Added mass comparisons between the approach of Sane utilizing blade element theory [90] and vortex surface method found in Korotkin [62]. Rows: aspect ratio (a) $AR = 1$, (b) $AR = 2$. $Re_{r_g} = 2$k, attack angle $\alpha = 60°$.

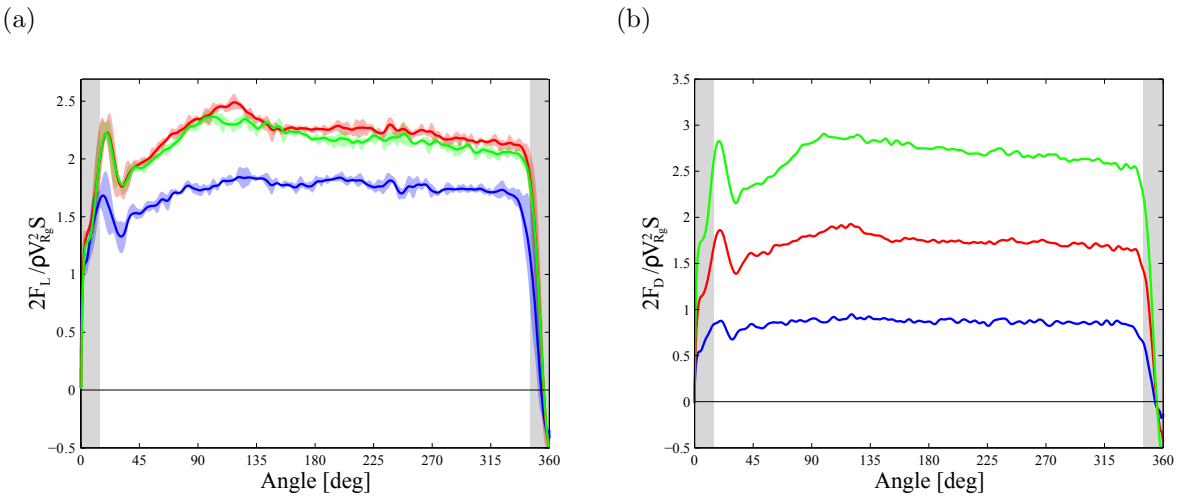

Figure 7.5: (a) Lift and (b) drag over the coarse of one revolution for rigid wing of $AR = 2$ at $\mathrm{Re}_{\mathrm{root}} = 10^3$. Angle of attack: 30° (——), 45° (——), 60° (——). Gray shaded regions indicate acceleration phases and colored shaded regions indicate standard deviation.

image of a two-dimensional wing translating several chord lengths where the periodic nature of life is the result of repeated LEV formation and shedding. Additionally, the subsequent bumps in lift typically attain lower maximum peak values. Even three-dimensional free-to-pivot translating plates of finite aspect ratio, as experimentally studied by Granlund *et al.*, experienced force decay from an initial maximum achieved shortly after attaining a steady attack angle [39]. This is not to suggest the phenomena responsible for the two-dimensional flapping wing's force behavior is responsible for that observed in the three-dimensional rotary wings. The rotary wing does not experience shedding as the LEV remains attached to the wing surface through it will host a number of instabilities. It is remarkable that the mechanism at play produce periodicity in force that also maintains magnitude. The first bump in lift is attributed to the formation of the LEV and the second bump seems driven by the strengthening of the tip vortex at the higher angles of attack which has greater interaction with the flow field about the wing given the aspect ratio $AR = 1$. It could be argued that the true test of periodic lift generation would be in the repeatability of a constantly rotating wing beyond a single revolution, however, such a maneuver would result in the wing encountering its wake.

(a) (b)

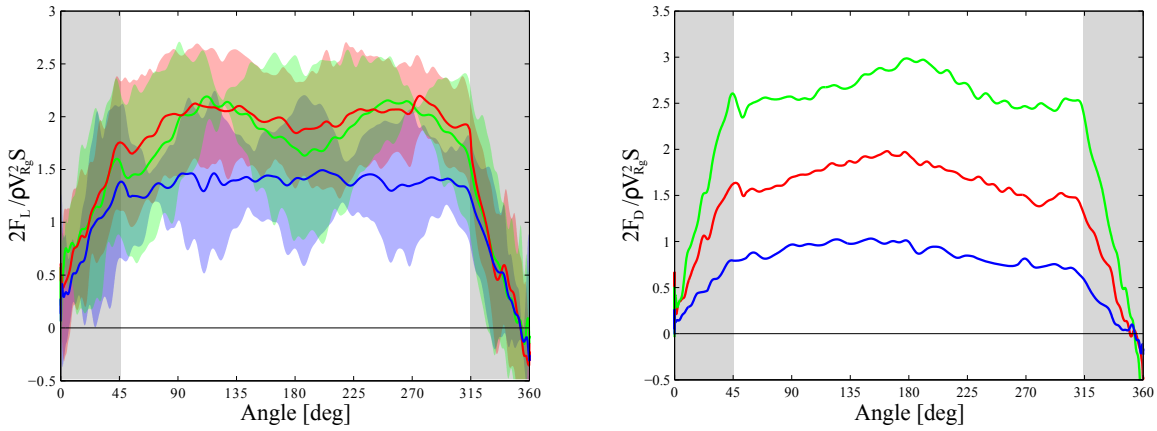

Figure 7.6: (a) Lift and (b) drag over the coarse of one revolution for rigid wing of $AR = 1$ at $\mathrm{Re}_{3/4b} = 10^4$. Angle of attack: 30° (——), 45° (——), 60° (——). Gray shaded regions indicate acceleration phases and colored shaded regions indicate standard deviation.

Low angles of attack are met with relatively constant lift as demonstrated by $\alpha = 30°$, or at least the defining features are on the order of the noise remaining in the signal. Drag profiles for $\alpha = [45°, 60°]$ appears as reciprocals of the lift with the most defining feature of a single peak at midstroke $\phi = 180°$. It should be noted at at lower aspect ratios there is greater interaction between the leading-edge vortex and tip vortex as reported by Ozen and Rockwell [77]. Ringuette *et al.* demonstrated the ability of the tip vortex to stabilize a leading-edge vortex in wings of aspect ratio $AR \leq 1$ highlighting a greater degree of interaction of the LEV with the tip vortex for the lower aspect ratio wing [85].

Table 7.3: $\mathrm{Re}_{3/4b} = 10^4$

Aspect Ratio	AR	[1, 2]
Reynolds Number	$\mathrm{Re}_{\mathrm{root}}$	[4000, 2500]
	Re_{R_g}	[8000, 7500]
Acceleration Angle	θ_{acc}	[45.83°, 28.64°]

Aspect ratio $AR = 2$ lift and drag are shown in Figure 7.7. In the lift of $\alpha = 60°$ there is

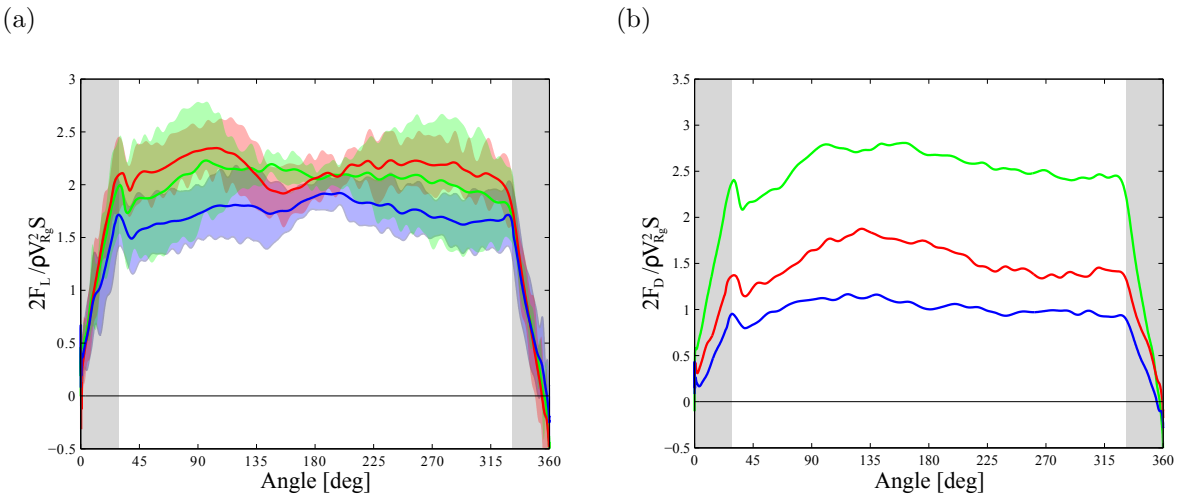

Figure 7.7: (a) Lift and (b) drag over the coarse of one revolution for rigid wing of $AR = 2$ at $\mathrm{Re}_{3/4b} = 10^4$. Angle of attack: 30° (——), 45° (——), 60° (——). Gray shaded regions indicate acceleration phases and colored shaded regions indicate standard deviation.

now a complete decay of the twin peak nature as the profile now bearing semblance to trends observed at $\mathrm{Re}_{\mathrm{root}} = 10^3$ with a single maximum in the vicinity of $\phi = 97°$. For $\alpha = 45°$ there still exist two distinct humps, the first of which appears to be the result of mechanisms responsible for the first peak reported for $AR = 1$ wing though the duration of the peak is shortened in comparison to $AR = 1$ with a trough now present at $\phi = 153°$ rather than 180°. Peak lift is achieved at $\phi = 103°$. The second hump resembles an elevated plateau region of lift. The wing oriented at $\alpha = 30°$ begins to show minor signs of the development of twin lift peaks with a trough coincident with that of $\alpha = 45°$. Drag profiles experience a shift in peak to earlier rotation angles over that of $AR = 1$ wings to $\phi = 130°$ from $\phi = 180°$.

7.3 Trailing-Edge Deflection

Now experiments are extended to include passive wings where passivity is isolated to the wing trailing edge via a single midchord hinge as depicted in Figure 7.8. The leading body is held at the prescribed angle of attack and the trailing body is free to passively pivot about the hinge. The hinge contains no torsional spring or damper and in the unloaded state the

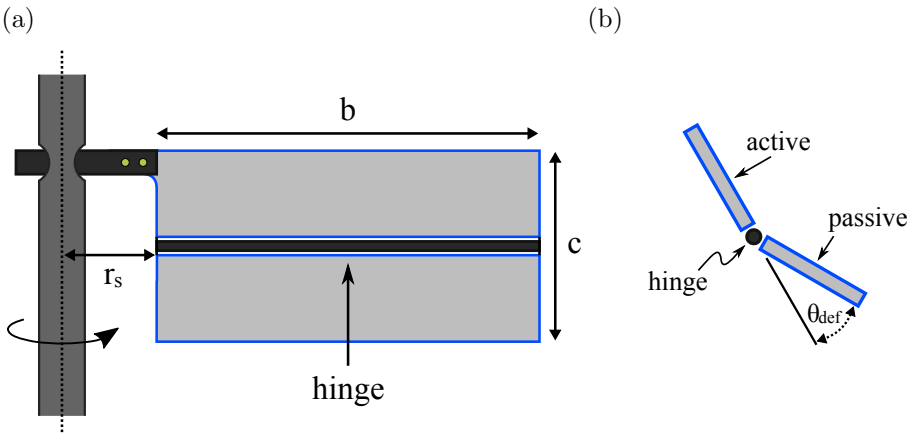

Figure 7.8: Diagram of flexible wing with addition of midchord hinge. The hinge allows for passive deflection of the trailing edge.

trailing body will orient itself vertically under gravitational effects. At the Reynolds numbers considered, both the root and bursting point have been shown to experience LEV growth extending to the wing trailing edge. The LEV growth is said to be limited by the chord length which after the vortex size reaches will then reach a saturation point as demonstrated in freestream plunging studies of rigid plates by Rival *et al.* [87]. By the inclusion of trailling-edge deflection one can asses the modifications dynamic camber may have on LEV formation.

The effect of a passive trailing edge in $AR = 1$ wings at $\mathrm{Re}_{\mathrm{root}} = 10^3$ is simply the a uniform reduction or magnitude shift of all forces as shown in Figure 7.9. Lift and drag trends observed for rigid wings are preserved in their flexible counterparts without excitation of additional modes. Because the trailing body is tugged by the leading body and rotates about the hinge in response to initial accelerations its orientation is much more streamlined than the trailing edge of a rigid wing. The quiescent fluid is imparted with less momentum, facing less resistance to passive deflection. As such the inertial loads of the wing are significantly reduced to magnitudes on par or less than forces generated during revolution at constant angular velocity. The effects of midchord passivity for the $AR = 2$ wing were largely lost given the extreme angles of deflection obtained, as shown in Figure 7.10. The deflection angles effectively reduce the intended lifting surface by half with the trailing body oriented

nearly horizontal in stroke. More so than with the $AR = 1$ wing, the inertial spike in $AR = 2$ is diminished to an even greater extent due to the great deflection angles producing added mass force component opposite those of the leading body.

At $\mathrm{Re}_{3/4b} = 10^4$ Figure 7.11 shows preservation of general rigid wing force trends by flexible counterparts with reduced magnitude and continued reduction of inertial spikes during angular acceleration for $AR = 1$ wings. Passive deflection wing at angle of attack $\alpha = 45°$ seems to incite a disruption of the mechanisms responsible for the second peak in lift of the rigid wing. There still exists a second abrupt rise in lift at $\phi = 225°$ but begins immediate decay for the remainder of stroke. The most notable modification to aerodynamic force is in the lift of $\alpha = 60°$ wings. The passive response of the trailing edge prolongs the development of the leading-edge vortex as indicated in the shift in initial lift peak from $\phi = 115°$ for the rigid wing to $\phi = 147°$. The trough in lift correspondingly is also shift. Consequentially the trailing edge deflection may also retard the mechanisms responsible for the second rise in lift associated with the remainder of stroke.

Aspect ratio $AR = 2$ passive response to trailing edge deflection is similar to that of $AR = 1$ with much of the rigid wing force characteristics preserved. Key differences arise in lift of $\alpha = 45°$ and $\alpha = 60°$. For $\alpha = 45°$ the duration of the first hump for the passive wing remains similar to that of a rigid wing, however, the lift peak associated with that hump is occurs sooner in stroke for the flexible wing at $\phi = 76°$ suggesting trailing edge deflection may hasten the formation of the LEV. As was noted for $AR = 1$, the passive aspect ratio $AR = 2$ wing also experiences a shift or delay in lift peak to beyond the midstroke at $\phi = 200°$. It appears at higher angles of attack trailing-edge deflection dynamics are capable of regulating LEV development and breakdown.

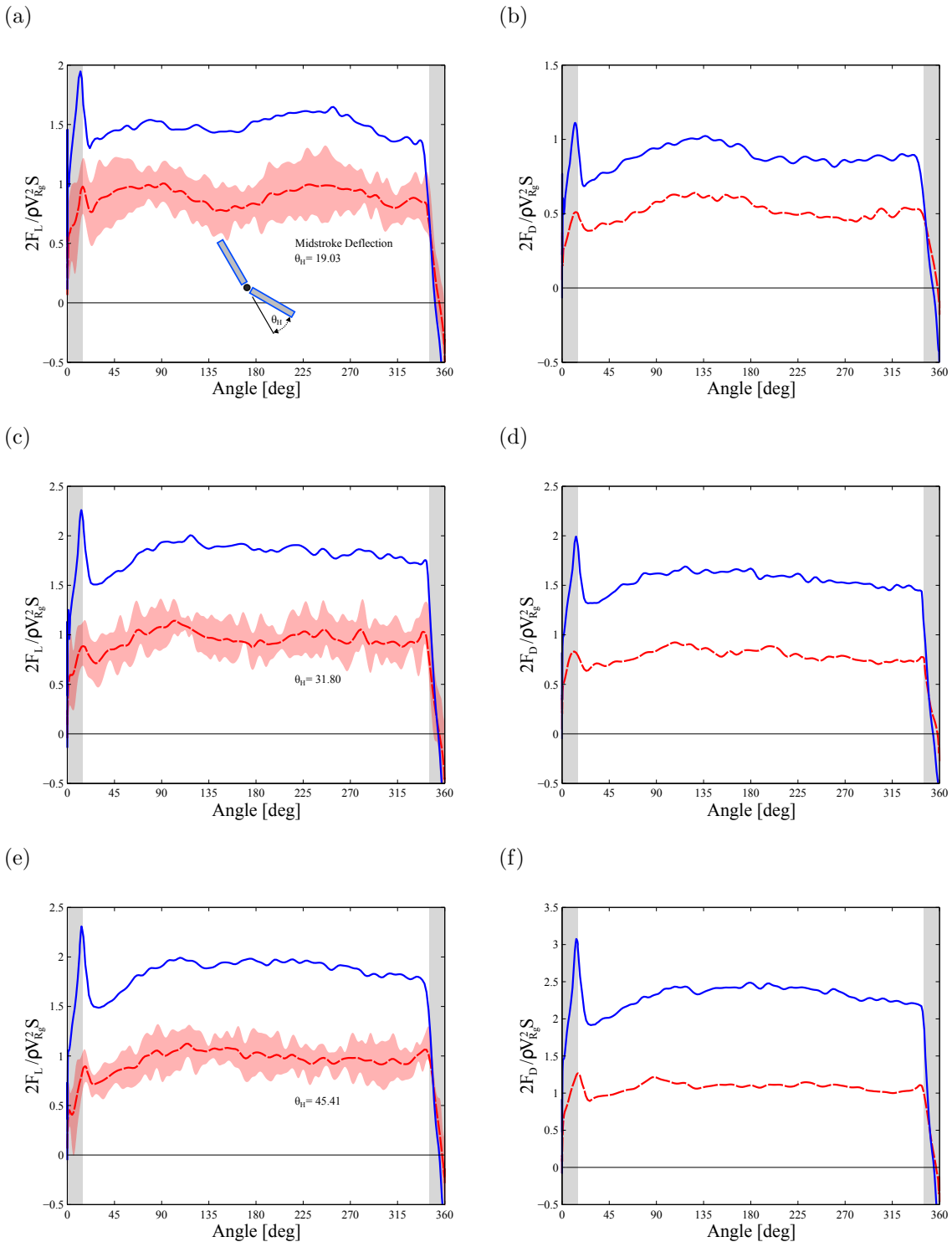

Figure 7.9: Columns: (left) Lift and (right) drag over the coarse of one revolution for rigid wing of $AR = 1$ at $\mathrm{Re}_{\mathrm{root}} = 10^3$. Wings: rigid (——), flexible (– – –). Angle of attack increases with row following $\alpha = [30°, 45°, 60°]$. Gray shaded regions indicate acceleration phases and colored shaded regions indicate standard deviation.

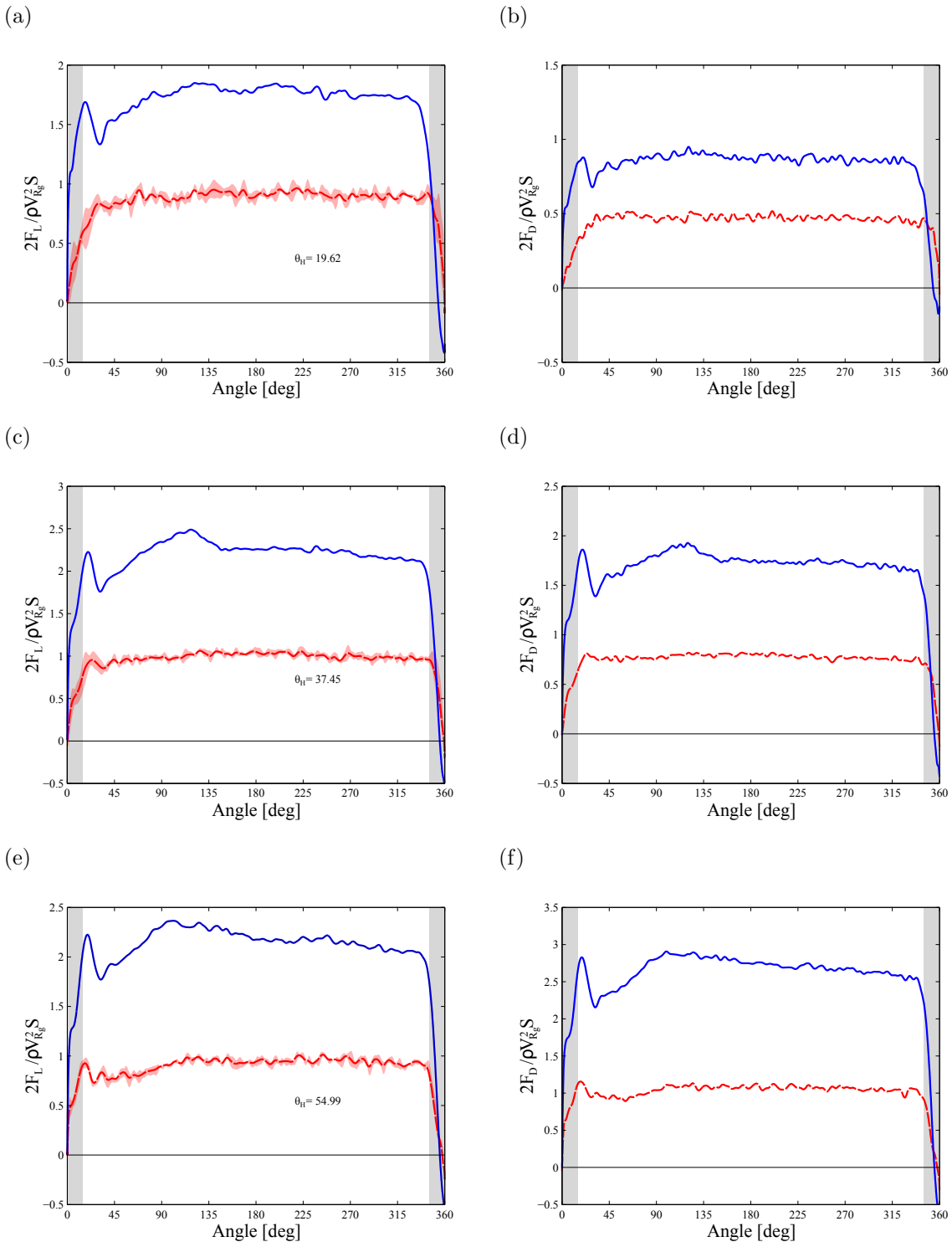

Figure 7.10: Columns: (left) Lift and (right) drag over the coarse of one revolution for rigid wing of $AR = 2$ at $\mathrm{Re}_{\mathrm{root}} = 10^3$. Wings: rigid (——), flexible (– – –). Angle of attack increases with row following $\alpha = [30°, 45°, 60°]$. Gray shaded regions indicate acceleration phases and colored shaded regions indicate standard deviation.

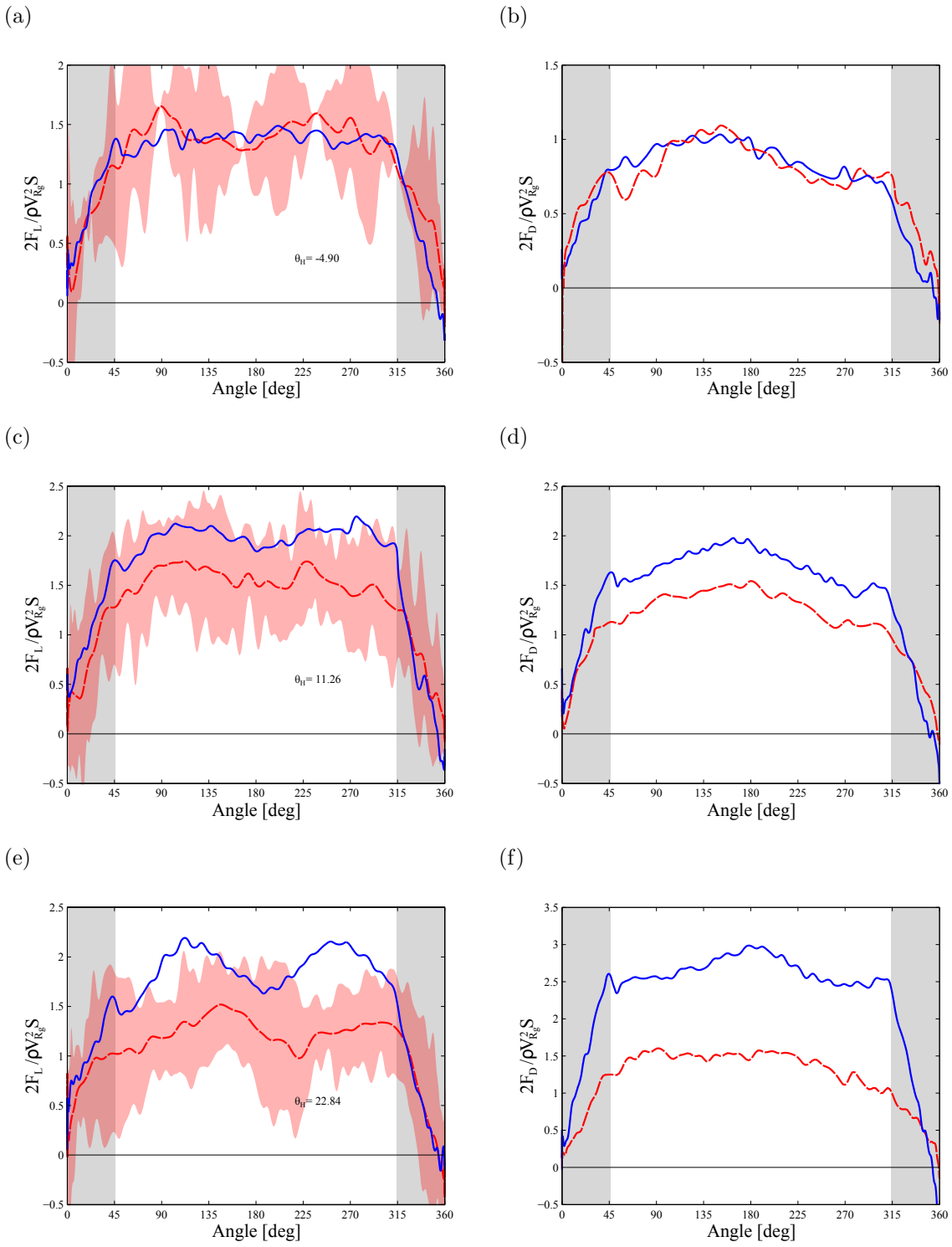

Figure 7.11: Columns: (left) Lift and (right) drag over the coarse of one revolution for rigid wing of $AR = 1$ at $\mathrm{Re}_{3/4b} = 10^4$. Wings: rigid (——), flexible (– – –). Angle of attack increases with row following $\alpha = [30°, 45°, 60°]$. Gray shaded regions indicate acceleration phases and colored shaded regions indicate standard deviation.

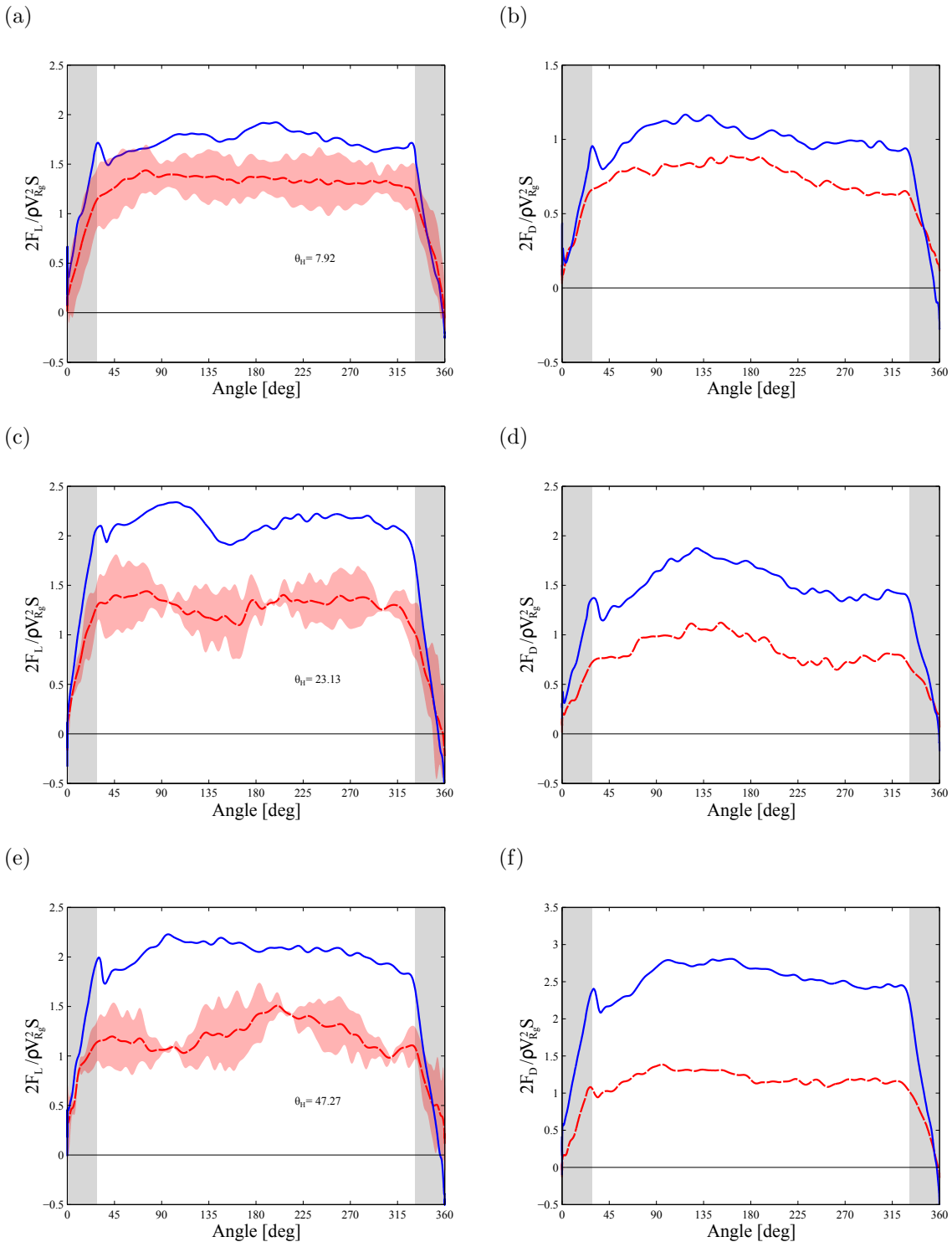

Figure 7.12: Columns: (left) Lift and (right) drag over the coarse of one revolution for rigid wing of $AR = 2$ at $\mathrm{Re}_{3/4b} = 10^4$. Wings: rigid (——), flexible (– – –). Angle of attack increases with row following $\alpha = [30°, 45°, 60°]$. Gray shaded regions indicate acceleration phases and colored shaded regions indicate standard deviation.

7.4 Deflection Reconstruction

To better comprehend aerodynamic trends observed in lift and drag the motions of the hinged wings were captured in a dual high speed camera setup at 90° from one another and through a process of direct linear transformation the wings were reconstructed in three-dimensional space. Motion tracking of points along the wing tip on both the leading and trailing body revealed the deflection angle at the hinge. This allows for the examination of coupling behavior between hinge deflection and aerodynamic forces encountered at $\mathrm{Re}_{3/4b} = 10^4$.

Figure 7.13 revisits $AR = 1$ wing at $\mathrm{Re}_{3/4b} = 10^4$ where the second column of the figure is now dedicated to hinge deflection history. Generally speaking the deflection angles measured at all angles of attack remain relatively stable with minor low frequency undulations within the range of $\pm 5°$ external to angular acceleration phases of rotation. The slight increases in lift in the passive wing at $\alpha = 30°$ are in-part due to the negative deflection encountered for the duration of the stroke which pits the trailing body deflected into the direction of motion resulting in a positive camber effect for the low attack angle. The larger angles of attack have hinges deflection opposite the direction of motion, increasing with α. Undulation patterns of $\alpha = 60°$ show maximum deflections near $\phi = 225°$ or $t/T = 0.6$ coincident with minimum lift.

Aspect ratio $AR = 2$ also resembles stable deflection angles for the later half of the stroke as shown in Figure 7.14. The greatest oscillation in hinge angle occurs near $\phi = 135°$ or $t/T = 0.35$ for both $\alpha = [45°, 60°]$, preceded by the initial trailing edge flick associated with the acceleration phase. As noted for $AR = 1$ wings, the peak in deflection is coincident with momentary reduction in lift. They Reynolds number regime ensures significant enlargement of the LEV, traversing the entire chord for the outboard region of the wing. Further, the LEV is to experience a number of instabilities and in trajectory, strength and the development of secondary vortical structures associated with interruptions of the leading-edge vortex shear-feeding layer. Despite these time-fluctuating behaviors the LEV suction on the trailing body dynamics does not elicit behavior as random as the vortical breakdowns above it.

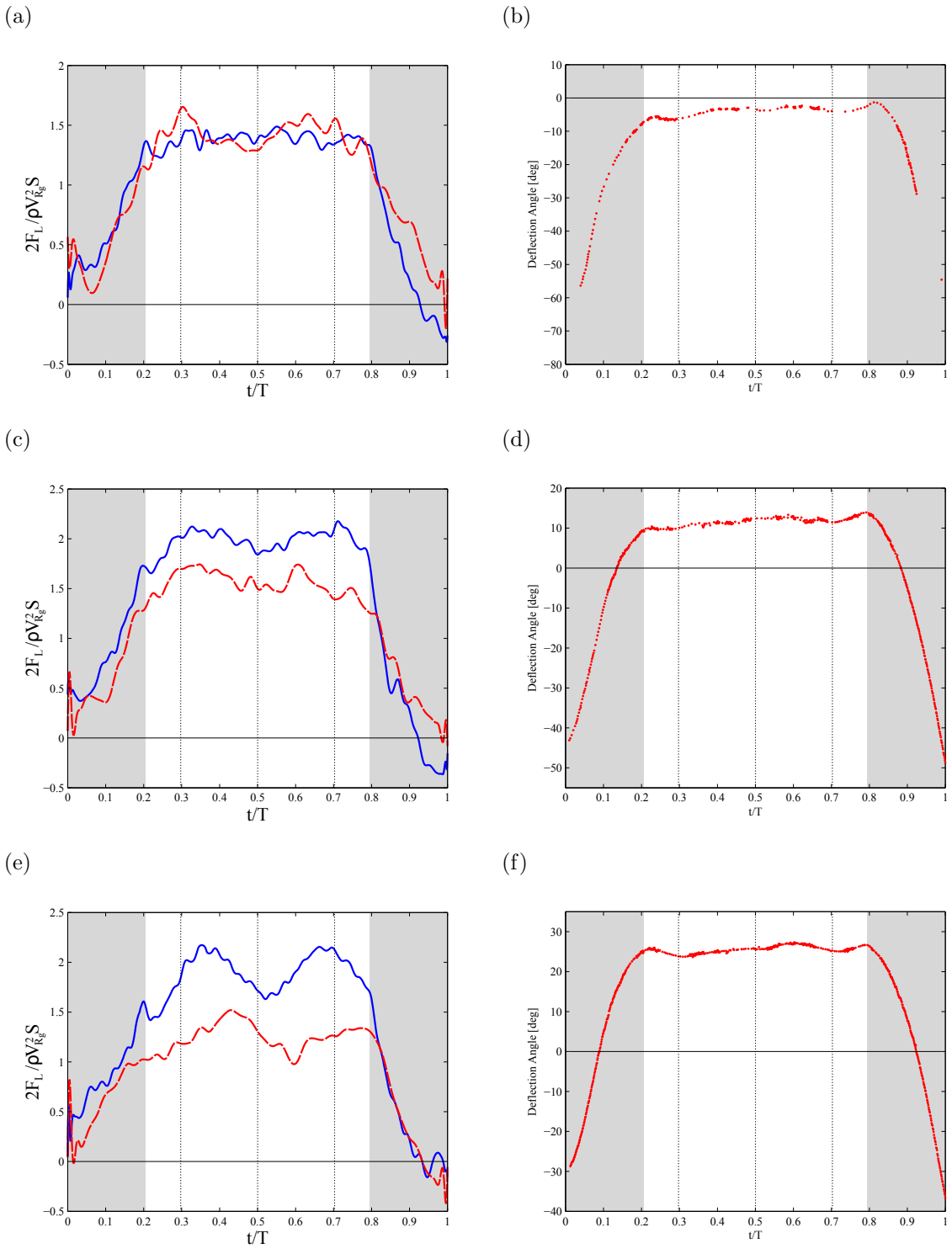

Figure 7.13: Columns: (left) Lift and (right) hinge deflection angle over the coarse of one revolution for rigid wing of $AR = 1$ at $\mathrm{Re}_{3/4b} = 10^4$. Wings: rigid (——), flexible (– – –). Angle of attack increases with row following $\alpha = [30°, 45°, 60°]$. Shaded regions indicate acceleration phases. Dotted lines indicate revolution angles [90°, 180°, 270°] respectively.

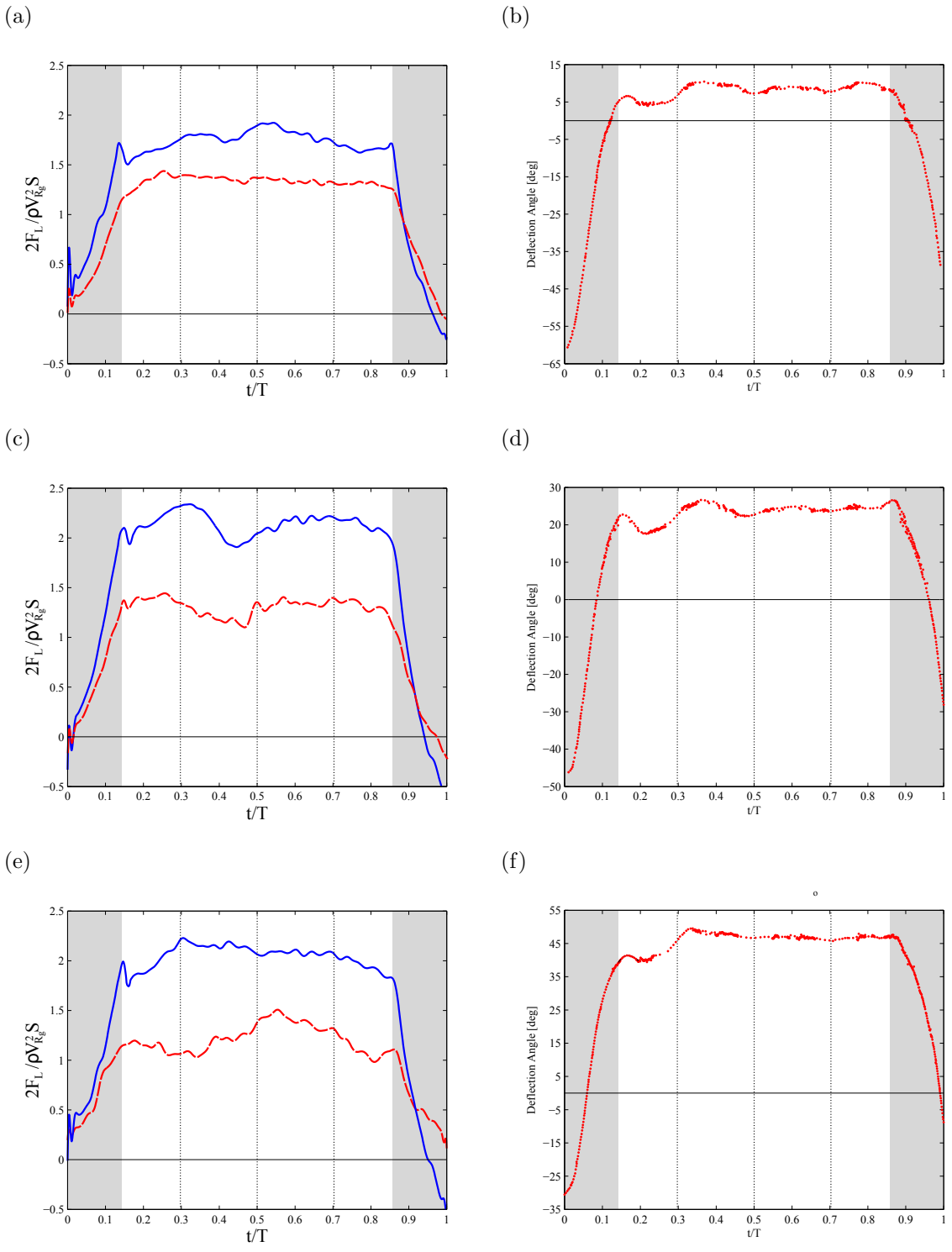

Figure 7.14: Columns: (left) Lift and (right) hinge deflection angle over the coarse of one revolution for rigid wing of $AR = 2$ at $\mathrm{Re}_{3/4b} = 10^4$. Wings: rigid (——), flexible (– – –). Angle of attack increases with row following $\alpha = [30°, 45°, 60°]$. Shaded regions indicate acceleration phases. Dotted lines indicate revolution angles [90°, 180°, 270°] respectively.

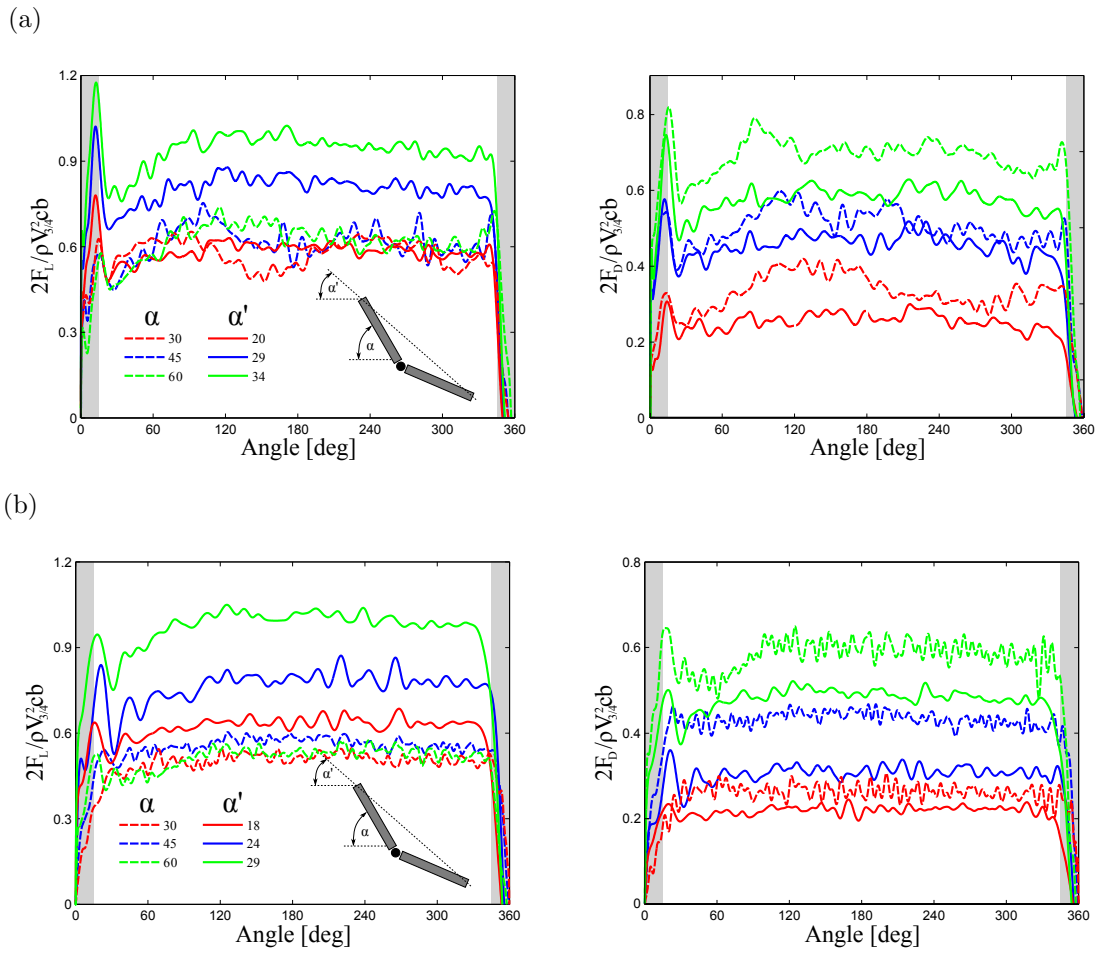

Figure 7.15: Lift and drag of (a) $AR = 1$ and (b) $AR = 2$ wings at $\mathrm{Re}_{\mathrm{root}} = 10^3$. Wings: rigid (——), flexible (– – –). Angle of attack are as indicated in the figure.

Given the relatively steady nature of deflection, a series of force measurements were conducted with a rigid wing oriented at an equivalent angle of attack, α', determined by a vector from trailing to leading edge of the passive wings deflected at midstroke. Figure 7.15 demonstrates the equivalent rigid wing is not strictly interchangeable with that of a deflected wing. The substitution of the rigid wing does not sufficiently encapsulate the disparity in leading-edge shear and trailing-edge shear inherent in the deflected wing's configuration.

7.5 Conclusion

Rotary wing experiments were conducted to examine leading-edge vortex formation at large convective times. Rotation is limited to a single revolution in a simple ramp up and ramp down velocity profile to avoid effects of wake interaction on the on the LEV. Leading-edge vortex behavior is inferred from force measurements in revolution. At $\mathrm{Re}_{\mathrm{root}} = 10^3$, apart from an initial spike during the acceleration phase owing to inertial force and initial LEV development, lift of $AR = 1$ achieves a maximum near rotation angle $\phi = 115°$ that steadily declines in stroke. Force between attack angles $\alpha = 45°$ and $\alpha = 60°$ is only differentiable in the drag produced by the wing. Extending the wing span to $AR = 2$ maintained a maximum near $\phi = 115°$ though the wing now supports a distinct bump or mount accompanying the maximum. The mount in lift is thought is thought to be the result of the additional wing span associated with $AR = 2$ allowing for the leading-edge vortex to fully mature over the a greater arc length in rotation in the distal portion of the wing and incite LEV bursting. Aspect ratio had little effect on sweep angle ϕ of maximum lift, revealing a universal formation time of the leading-edge vortex independent of aspect ratio. Redefining Reynolds number at the three-quarters spanwise position where bursting is often initiated and increasing to $\mathrm{Re}_{3/4b} = 10^4$ prompted the aspect ratio $AR = 1$ wing to also experience bursting such that the leading-edge vortex growth was limited by traversing the chord rather than wing span. The resulting lift profile for $AR = 1$ at attack angles $\alpha = 45°$ and $\alpha = 60°$ showcased oscillatory behavior with two major peaks nearly symmetric about the midstroke with the second peak retaining the magnitude of the initial peak. Such behavior is typically reserved for translating wings periodically shedding the leading-edge vortex. Aspect ratio $AR = 2$ wings experienced a reduction of the second peak noted in $AR = 1$ wings for $\alpha = 45°$ and complete loss of the secondary peak at $\alpha = 60^{circ}$ though peak lift is still achieved near $\phi = 115°$ indicating a LEV formation time independent of Reynolds number and acceleration profile. With $\mathrm{Re}_{3/4b} = 10^4$ it is assumed the leading-edge vortex growth extends to the trailing edge and the inclusion of a mid-chord spanwise hinge demonstrated a passive means of flow control in delaying the development of the leading-edge vortex at $\alpha = 60°$ with a temporal shift in peak lift greater

in the $AR = 2$ wing accompanied by greater hinge deflection over that of the $AR = 1$ wing.

CHAPTER 8

Conclusion

The works presented in this dissertation have examined the influence of wing deformation on force production and vortical structure formation in flapping wing flight with application to next generation micro air vehicles. Our desire to construct agile fliers on the insect scale is complicated by the degradation and eventual breakdown of classical flight mechanics with decreasing scales. This leaves unsteady mechanisms as the only viable solution for lift production at the scales desired and necessitates the study of unsteady separate flows about low aspect ratio wings and the interactions of the resulting vortical structures. The resulting unsteady flow phenomena stands as a great departure from classical lift mechanics and is further complicated by the degree of compliance experienced by an insect wing in stroke owing to its architecture. An insect wing derives much of its stiffness from coalescence of vein members along the leading edge, leaving the posterior region of the wing susceptibility to deformation greater owing to non-uniform venation distribution. The resulting nonuniform stiffness incites various deflection modes of bending and twisting in response to inertial-elastic and fluid forces. The challenge then is studying the various phenomena in isolation given the high level of interdependency. To this end numerical and experimental studies were conducted in two and three-dimensional wings to characterize the vortical structures' response to deformation, with emphasis given to the leading-edge vortex, in a series of simplified biologically-inspired kinematics.

Numerical studies on wings normal to the freestream reveal a vortex-symmetry breaking mechanism in flexible wings unavailable to rigid counterparts. As anticipated the rigid wing produces zero lift, where lift is identified as force normal to the freestream, and a nonzero

drag that quickly settles into to an asymptotic value characteristic of the development of two counter-rotating vortices of the same strength in the wing wake. The flexible wings passively deflect in response to forces applied and as a result of the trailing edge configuration the trailing-edge vortex shear-feeding layer strength is reduced thereby producing a vortex of weaker strength. The leading-edge vortex strength remains largely unchanged resulting in a break in symmetry producing resultant force in the direction of the stronger vortex. The resultant force does not approach a steady value but instead oscillates as the process of vortex formation and subsequent shedding is repeated at a steady frequency. Thus, trailing edge deflection also provides for a vortex shedding mechanism unavailable to rigid counterparts.

To characterize the leading-edge vortex formation time and attachment-cycle prior to shedding rigid and flexible wings at fixed angle of attack were accelerated from rest following a power-law velocity profile. The frequency of LEV formation and shedding was interpreted as the frequency of oscillation in the lift signature. It was shown, in accordance with the findings of Chen*et al.* [16], that the shedding frequency was largely dependent on Reynolds number and not the acceleration profile of the wing. The inclusion of passive deflection of the wing trailing edge was met with continued linear-dependence of shedding frequency on Reynolds number as with the rigid wing however linear profiles are now at a greater slope with flexible wings. Flexibility increased the leading-edge vortex shedding frequency with the most compliant wings experiences the greatest shedding frequency. Increased stiffness resulted in shedding profiles approaching that of the rigid wing.

Flexibility in hover kinematics demonstrated a mechanism by which flexibility may be implemented to recover losses in lift experienced by a rigid wing. Deflection of the wing is most predominant during pitch and approaches an undeflected state during heave. Deflection from pitch in phase with stroke reversal results in a whipping motion of the trailing edge, increasing the trailing edge wing velocity. This mechanism produced greater shear in the end-of-stroke vortex, strengthening its influence on the induction of the previous stroke leading-edge vortex under the wing. Deflection also served to reduce the obstruction or resistance of the wing to sweep the previous shed LEV under the wing in preparation for the

subsequent halfstroke. Stroke-averaged lift over a range of pitch angles demonstrated the flexible wing's ability to utilize symmetry-breaking mechanisms in hover with the flexible wing producing greater lift for small pitch angles until producing comparable averaged lift to the rigid wing at pitch angle 30°. Operational efficiency was shown to be consistently greater for flexible wings at all pitch angles considered. By extending a line extending from the centroid of the trailing and leading bodies of the flexible wing an effective pitch angle can be quantified which shifts the flexible wing data to agree with trend lines associated with the rigid wing.

Numerical simulations on three-dimensional wings in hover reveal a stable leading-edge vortex for the duration of the stroke owing to centripetal and Coriolis accelerations. The modification to lift performance to wing deformation is explored in two candidate deflection modes with each acknowledging a single flexion about which deflection is prescribed by sinusoidal waveform. In-phase deflection, with maximum deflection coincident with the midstroke, was shown to have a greater effect on lift and drag for tip flexion at Re = 100. Force profile trends are maintained though magnitudes vary. Examining the vortical structures about the wing reveal tip flexion is responsible for a thicker tip vortex which occupies a greater region of the flow. The tip vortex now extends inboard toward the wing root, promoting an earlier merger between the tip vortex and the leading-edge vortex. Force profiles of flexion wings at Re = 10^3 maintain much of the characteristics of the rigid wing with the greatest variability presented at the start of the halfstroke with the initial peak. Lift of the flexion plates for the majority of the stroke behave similarly with greater disparity between the two modes exhibited in drag. Visualization of vortical structures about the wings reveal tip deflection suppressing the formation of secondary vortical instabilities in the wake stemming from the tip vortex, as experienced by the rigid and root flexion wings.

Force and vortices visualized by λ_2 criterion appear responsive to the deflection modes considered. On examination of the leading-edge vortex axes to deformation the opposite holds true. The axes were determined following the Γ_1 criterion and for all wing considered the spatial evolution of the axes remained along the leading edge with negligible variation

between the plate configurations at Re = 100. At Re = 10^3 the vortex axes' insensitivity to deflection is continued with the axes of all wing configurations sharing a common spatial evolution along the span. The axes show a response to Reynolds number as they now recede from the leading edge in approaching the tip beginning near the midspan position. The leading-edge vortex cores are also identified using the Γ_2 criterion. Root flexion at Re = 100 bears influence on the core size near the wing root, reducing core size in comparison to rigid and tip flexion wings. General trends support enlargement of the leading-edge vortex core with spanwise position until $0.75b$ where the core now decreases approaching the tip with the exception of tip flexion which supports further enlargement approaching the wing tip. At Re = 10^3 the circulation of the leading-edge vortex cores show a distinct spike nearing the tip due to the tip vortex bending inboard merging with the trailing-edge shear layer producing a spanwise component of tip vortex near the wing tip. In transition from Re = 100 to Re = 10^3 there exists a shift of the axial flow maximum from the trailing edge region of the wing to the leading edge near the leading-edge vortex axis producing greater core flow which is a precursor the leading-edge vortex bursting.

Experiments on dynamically-scaled fruit fly wings at Re = $O\left(10^4\right)$ demonstrated bursting behavior in flapping. Dye visualization at Re = 100 outlines a leading-edge vortex largely confined to the leading edge of a rigid wing with laminar mixing. Flapping at Re = 14226 exhibits significant enlargement of the leading-edge vortex which now extends to the trailing edge. This behavior is believed to be the result of decelerated leading-edge vortex core flow. Numerical simulations have demonstrated a shift in axial flow maximum from external to the LEV core to internal with increasing Reynolds number an order of magnitude. At the Reynolds number considered it is believed the axial flow is decelerated to a near stop, possible supporting reversed flow under the influence of the tip vortex, which incites sudden enlargement of the vortex. The inclusion of flexion lines in a root and tip configuration reveal greater enlargement by the tip flexion as this mode offers a deflected wing in heave whereas the root flexion wing's deflection is almost exclusive to the pitching phase of the kinematics at stroke reversal. The deflected nature of the tip acts an a barrier further decelerating core

flow.

Experiments on low aspect ratio rotary wings explored the sustainability of lift and leading-edge vortex evolution at long convective times unimpeded by secondary acceleration fields characteristic of flapping flight. Two Reynolds numbers are tested with varying magnitude and reference velocity. The root Reynolds number is intended to isolate effects of span while the three-quarter span Reynolds number is intended to ensure bursting conditions in both aspect ratio wings considered to examine the effects of tip vortex influence in the bursting limit. In root Reynolds number revolution of $AR = 1$ there exists a maximum in lift for $\alpha = [45°, 60°]$ near $\phi = 112°$ though the overall lift profile variation is rather slight. At $AR = 2$, in extending the wing span the maximum lift still occurs at $\phi \approx 112°$ though now maximums appear as distinct peaks. The leading-edge vortex is in a sense given more time to develop in $AR = 2$ by virtue of the greater span sweeping through a greater arc length. Despite the differences in sweep arc length the maxima occur at the same revolution angle suggesting LEV formation is independent of aspect ratio. In raising Reynolds number an order of magnitude and using the three-quarter span velocity reference the lift maxima maintain a $\phi = 112°$ dependence. For $AR = 1$ there exists a departure from other lift profiles of $\alpha = 60°$ in that the initial bump or maximum is repeated nearly symmetric about the midstroke position $\phi = 180°$. Periodicity in lift is highly characteristic of two dimensional flows by way of shedding, however revolving wings do not shed the vortex which remains attached to the wing surface for the duration of stroke. At lower aspect ratios it is expected that the tip vortex plays a more dominant role on the force behavior. The role of the tip vortex is only strengthen by the angle of attack $\alpha = 60°$ producing stronger vorticity at the tip. The intensified interaction and proximity of the tip vortex to the bursting plane results in repeatable force generation rather than a signature that decays over time.

The introduction of chordwise passive deflection at root Reynolds number $\mathrm{Re}_{\mathrm{root}} = 10^3$ in $AR = 1$ produced force signatures maintaining the profile trends of the rigid wing lift and drag now shifted in magnitude. At three-quarter span Reynolds number $\mathrm{Re}_{3/4b} = 10^4$ a three-dimensional reconstruction of the revolving wings allowed for the quantification of

the deflection angle history during the stroke. Peaks in deflection wing lift are likely to be shift now away from the $\phi = 112°$. Additionally, there appears to exist a correlation between oscillations in deflection history and reductions in lift signature, namely near the first 40% of the stroke. The belief is as the leading-edge vortex growth extends to the trailing edge the deflection experienced redefines the effective chord thereby passively regulating the leading-edge vortex. The hinge on the wings used here are completely undamped and provide no resistance. The addition of torsional springs of specific stiffness could provide a passive means of tuning the lift behavior to reflect desired attributes.

Future work entails further dye visualization on rotary wing configurations as well as stereoscopic particle image velocimetry to draw conclusions on lift and drag profiles observed thus far and evaluation of the relative contributions of leading-edge, tip, root and starting vortices in force generation. Degrees of flexibility are to be expanded upon in the form of several articulated bodies constituting a single wing and the inclusion of fully elastic wings deriving stiffness from venation. Three-dimensional reconstruction of experimental wings via motion capture will then provide a means to study passive deformation in the scope of prescribing measured deformation to a computational wing. Kinematics in future work will also examine perching maneuvers as a possible means of bolstering aerial dexterity of next generation micro air vehicles. Nature has demonstrated the breadth of maneuverability achievable with flapping wing configuration which also poses an inherent ability to hover, strengthening their aerial repertoire. However despite the many advances in recent years the aerodynamics of flapping flight remain poorly understood. Flapping wings take advantage of short-time unsteady processes such as dynamic stall which do not lend themselves to classical aerodynamics, where the term short-time is reserved for timescales on the order of a halfstroke. The unsteady nature of force generation afford highly responsive maneuvers with even the most subtle of wing motions inciting complex, rapid flight patterns. Current micro air vehicles rely on stroke-averaged force where simplified locomotion is achieved only after several wing beat cycles and remain a far cry from biological counterparts which utilize instantaneous flow phenomena to achieve a greater level of agility in fewer strokes. In order

to distill how MAVs may modulate their wings to increase force production in a given stroke and induce sharp maneuvers the vortical structure formation about low aspect ration wings undergoing pitching and perching kinematics will be examined. Both pitching and perching motions provide potential short-time solution to achieving greater maneuverability by modifying the leading-edge vortex strength and reorienting the resultant force acting on the wing.

APPENDIX A

Lower-Order Modeling: Inviscid Brown-Michael Equation

A.1 Introduction

High fidelity simulations can prove quite demanding on computational resources. By exploring inviscid models we wish to reduce the computational expenses such as runtime and memory. We make use of an inviscid model assuming incompressible fluid initially at rest. Of interest is a two-dimensional flat plate translating at an angle of attack α with a specified acceleration profile. Our aim is to capture much of the physics observed in high fidelity simulations which see the formation of point vortices at both ends of the plate. In fact, this lower order model may be extended to a general body with N_c number of corners or sharp edges. Each edge releases a point unsteady point vortex into the flow with monotonically increasing strength. A plate contains two edges $N_c = 2$ corresponding to the trailing and leading edges and thus introduce a a total of two point vortices representing the trailing and leading-edge vortices experienced in higher order models.

The point vortices represent a lower order model to the rolling-up of the vortex sheet, however, vorticity strictly remains at the point vortices and the sheets themselves are neglected. The vortex strength is updated each timestep in accordance with the cancellation of the singularities produced at the edges of the body. The point vortex represents the roll-up of the vortex sheet which physically cannot unroll itself, such behavior would amount to a negative diffusion within the vortex core [71]. This requires that the strength magnitude to monotonically increase with time. As a given wake vortex matures and reaches a maximum,

its strength is frozen for the remainder of time. It is still free to update its position and velocity in the flow in response to the velocity field produced by the vortices in the wake and bound on the body. When a given vortex is frozen, a new vortex is introduced into the flow from the edge of the body corresponding to that of the newly frozen vortex.

A.2 Governing Equations

Initial trials will examine a translating plate the long-term goal of extend the kinematics to flapping. We take a thin airfoil theory approach and begin by discretizing the plate into panels satisfying a *cosine* distribution. This allows for greater resolution near the tips of the plate where we expect the most variability in the bound circulation strength. The bound circulation γ is determined by point vortices of strength Γ located at the ends of each panel, satisfying:

$$\gamma = \frac{\mathrm{d}\Gamma}{\mathrm{d}s} \tag{A.1}$$

where s is the direction along the plate surface. The wake is viewed as shed vortices with branch cuts spanning from the vortices to their respective edge of introduction (Fig. [A.1]). However, the branch cut does not bear any influence on the plate or wake vortices, with all vorticity in the wake is localized in the point vortices. In analyzing Newton's second law about a contour enclosing a wake point vortex and its branch cut, we arrive at the Brown-Michael equation [71]:

$$\dot{z}_n + (z_n - z_{n,o})\,\frac{\dot{\Gamma}_n}{\Gamma_n} = \overline{\tilde{\omega}_n} \tag{A.2}$$

where subscript n denotes point vortex n in the wake, z is the complex position, $z_{n,o}$ is the time varying position of the edge from which a wake point vortex was introduced, Γ the point vortex strength, $\overline{\tilde{\omega}_n}$ the desingularized complex velocity of vortex n, and $\dot{()}$ indicating derivative in time. Using equation (A.2) we can update the position of a given point vortex each time step of the simulation.

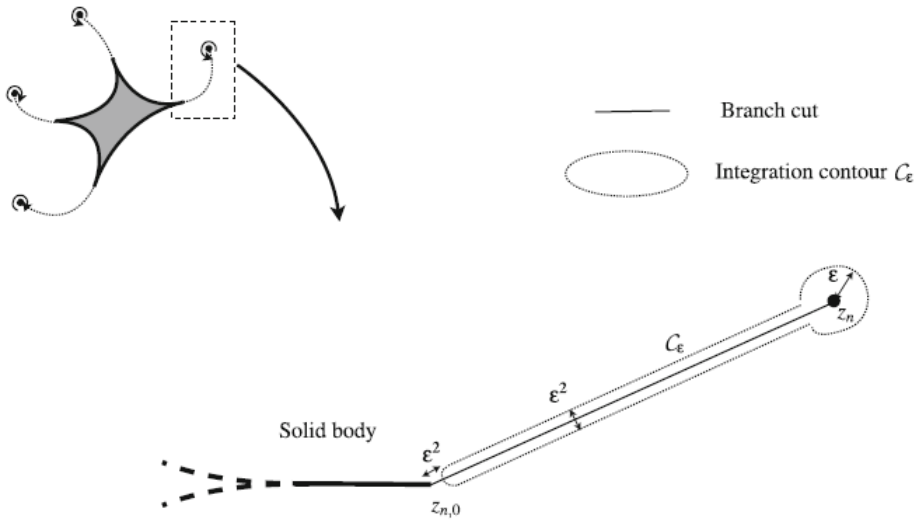

Figure A.1: Convservation of momentum applied to an unsteady point vortex and its branch cut [71].

The Brown-Michael model reduces the problem to one of $N_p + 3$ initial point vortices, where N_p is the number of panels on the plate. The number of vortices is subject to change, increase with the freezing of a current wake vortex and the subsequent introduction of a newly shed vortex from the same edge. The no-flow through condition is satisfied at collocation points located at the midpoint of each panel:

$$\mathbf{u} \cdot \mathbf{n} = \mathbf{u}_b$$
$$\sum_{j=1}^{N_p+3} \Gamma_j / \left(2\pi r_j^i\right) = \mathbf{u}_b^i$$

where superscript i denotes a collocation point on the plate. This allows for bound vortex strengths to be solved. The wake vortex strengths are governed by the unsteady Kutta condition:

$$\mathrm{d}\Gamma_{wake}/\mathrm{d}t = \gamma \bar{U} \tag{A.3}$$

which states wake vortex strength rate of change is equal to bound vortex sheet strength γ times the velocity average U taken above and below the plate at the vortex's respective edge of introduction. Conventionally the Kutta condition is applicable only to the trailing-edge

of an airfoil. However, in lieu of a complementary theory for flow separation at the leading-edge the Kutta condition is applied at both edges of the wing. The trajectory of the wake is determined Brown-Michael equation. In addition to this, Kelvin's circulation theorem must also be satisfied:

$$\mathrm{d}\Gamma_{total}/\mathrm{d}t = 0 \tag{A.4}$$

When the leading-edge vortex reaches a maximum in magnitude the vortex is frozen in strength and a new vortex is shed from the corresponding edge of the plate. The frozen vortex now follows a trajectory determined by the flow field induced by remaining point vortices and the newly formed vortex satisfies Brown-Michael equation once again. One advantage to panel method over complex potentials is the panel method allows us to examine multiple bodies. Additionally, we are more easily able to examine deflected bodies.

Resultant force can be expressed as:

$$\mathbf{F} = -\frac{\mathrm{d}}{\mathrm{d}t}\int_{A_f} \mathbf{x} \times \omega dA - \frac{\mathrm{d}}{\mathrm{d}t}\oint_{S_b} \mathbf{x} \times (\gamma + \mathbf{n} \times \mathbf{u}_b)\, ds \tag{A.5}$$

It is worth noting this particular model only sought to conserve force using Newton's second law. The method does not take into account moment balance and therefore may not be suitable for passively deflecting plates. It may still be utilized for deflecting bodies, however, it would be restricted to active deflection prescribed a priori.

A.3 Results

Thus far in this body of work the process of dynamic stall and the formation of a leading-edge vortex has been studied via high-fidelity simulations in the context of flapping flight where the underlying wing motions occur at shorter time scales than that associated with the fully developed stall condition. In fact, the dynamic stall of been studied in a host of aerodynamic contexts beyond MAVs where the process has been exploited to enhance maneuverability and lift. Though high-fidelity simulations have proven invaluable to the advancement of unsteady

aerodynamics their implementation proves computationally expensive. Lower order modeling is motivated by the desire to develop computationally inexpensive methods while retaining much of the relevant physics of the problem.

Here the feasibility of an inviscid lower-order Brown-Michael model is tested as a potential tool for reliably predicting LEV dynamics about wings at elevated angels of attack. Additionally, the lower-order model is employed to examine qualitative trends in performance associated with wing deflection. Previous lower-order methods have modeled the wake as a sheet [93] [3] or a continuous release of point vortices [6]. In the current method circulatory forces on the plate are accounted for by potential point vortices in the wake. At startup the wake is to consist of two point vortices emanating from the leading and trailling-edge representing the LEV and TEV respectively. This approach would reduce unsteady viscous vortical phenomena to point vortices with evolving strengths of three degrees of freedom. Lower-order models have proven quite accurate at low angles of attack flow regimes where there is no leading-edge vortex present.

A.3.1 Normal Flat Plate

Here the Brown-Michael equations are solved for a normal flat plate accelerating from rest. Experiments conducted on viscous flow around nominally two-dimensional flat plates reveal the formation of counter-rotating circulatory regions in the plate's wake which remain symmetrical and stable as they approach a steady state [21] [47] [48]. For a normal plate ($\alpha = 90°$) translating in an inviscid fluid following a nearly impulsive start given by:

$$X = t + \frac{1}{C_\varsigma}\exp\left(-C_\varsigma t\right) \tag{A.6}$$

$$\dot{X} = 1 - \exp\left(-C_\varsigma t\right) \tag{A.7}$$

$$\ddot{X} = C_\varsigma \exp\left(-C_\varsigma t\right) \tag{A.8}$$

where C_ς (= 100) is the ramping parameter and the term "nearly impulsive" stems from the resulting kinematic profile quickly accelerating to a constant velocity from rest.

Figure A.2 shows the streamlines of the resulting flow at a representative point in translation. It is quite clear the Brown-Michael equation adequately captures major components of the flow physics in maintaining symmetry in the wake with counter rotating regions well accounted for situated behind the plate. Figure A.3(a) shows the circulatory strength evolution of both point vortices. As anticipated, the strengths are equal and opposite one another, maintaining symmetry throughout the simulation. And although the circulatory strengths never quite reach a steady-state value for the duration of translation distance considered here, it is worth noting the asymptotic nature the strengths approach after approximately five chord lengths of travel by the plate. In Figure A.3(b) the normal and tangential distance of a given point vortex from its respectively plate-feeding edge also exhibits an asymptotic behavior. Over the course of translating thirty chords the vortices can be found slightly beyond of one chord length aft of the plate.

Lastly, the forces generated on the plate are strictly drag as shown in Figure A.4, as anticipated for a normal plate. The lift coefficient defined as forces perpendicular to the direction of motion is consistently zero at all times for the duration of translation and drag maintains a non-zero value with an initial spike at the onset of motion in response to the acceleration profile.

A.3.2 Angle of Attack and Deflection Effects

Now the planar airfoil is oriented at an angle of attack α representative of that characteristic of biological fliers. If the Brown-Michael equation is to potentially be a design tool it must be able to produce lift and drag trends similar to high-fidelity simulations. The wing still translates following Eq. (A.6) and α is increased from 40° to 90° in increments of 5°. Figure

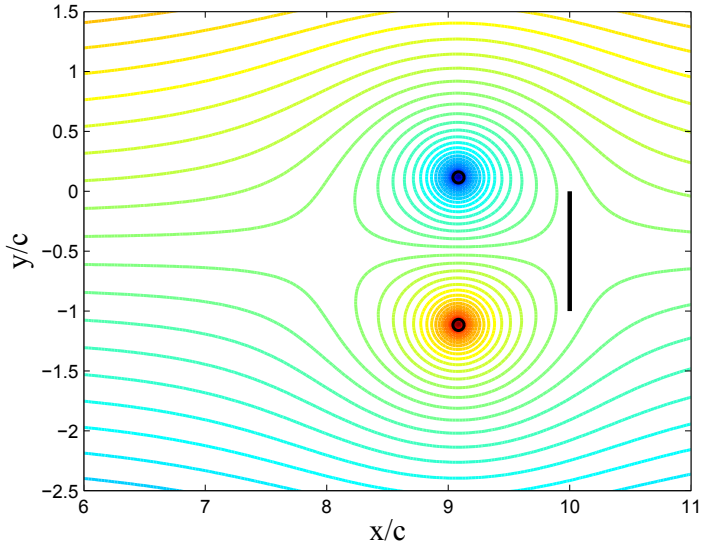

Figure A.2: Brown-Michael equation solution for a normal plate translating (left to right) in an inviscid fluid: streamlines (contours), plate (——), wake point vortices (o). Convective time is $T_c = 10$, matching chords traversed $X/c = 10$.

(a) (b)

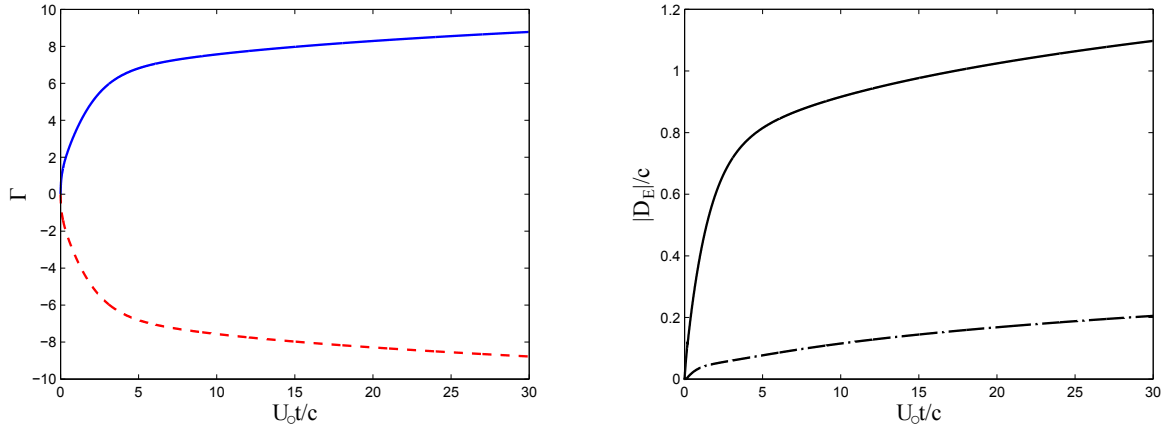

Figure A.3: Wake vortices' (a) circulation: Γ_1 (——), Γ_2 (– – –). (b) A representative point vortex distance from its respective feeding-edge, D_E: normal distance from plate to point vortex (——), tangential distance from plate edge to point vortex(– · –).

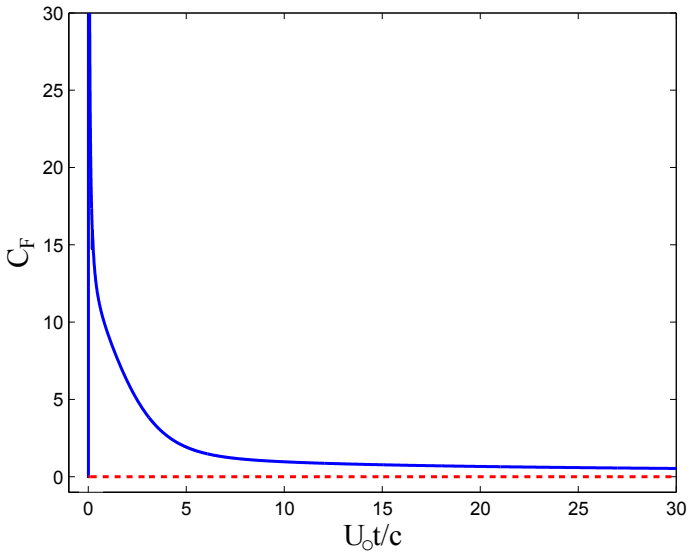

Figure A.4: Force coefficient for normal translating plate: C_L (——), C_D (– – –).

A.5(a) depicts effect of attack angle on lift coefficient for the translating wing.

With increased angle of attack there is a monotonic decrease in lift which stands at odds with viscous simulations which experience maximum lift near $\alpha = 50°$. For α range $[45° - 65°]$ lift abruptly drops near 3.5 chords of travel. This drop in lift can be interpreted as the point in which shedding of the leading-edge vortex would occur at the onset of a von Karman street. However, the current method is not well suited for vortex shedding for reasons to be discussed in Section A.3.4. For greater attack angles we see the drop in lift is postponed to greater chords traversed. Drag as shown in Figure A.5(b) does not experience a monotonic increase in drag with increasing attack angle as would be expected from the increased projected area in the cross flow. The maximum drag coefficient corresponds to $\alpha = 55°$ and minimum corresponds to 90°.

The decision to represent the wing by a series of panels hosting point vortices rather than mapping the wing to a circle that houses image vortices via Joukowski mapping was purely for the ease of introducing deflection in the wing or introducing multiple bodies within a given simulation. Figure A.6 demonstrates the effect of midchord deflection on lift and drag for wing translating at $\alpha = 45°$. Deflection angle is increased in increments of 5° to a

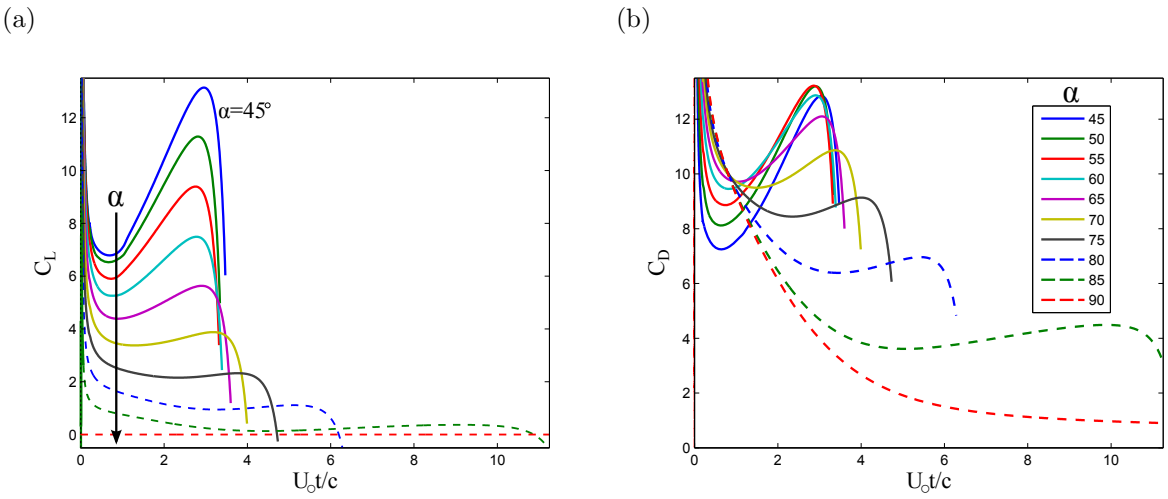

Figure A.5: Angle of attack effects on (a) lift and (b) drag of a planar translating wing accelerated from rest.

maximum of 40°. Force production monotonically decreases with the increased deflection of the trailing-edge. The loss in force on the plate is reflected in the wake vortices' circulation as shown in Figure A.7 where both the leading and trailing-edge vortex circulation decreases with increased deflection angle. The trailing-edge deflection works to modify the distribution of the wake vortices and correspondingly their strengths about the newly configured wing.

A.3.3 Comparison to Viscous Methods

Comparison between lower order inviscid streamfunctions and high fidelity viscous vorticity contour plots gives an idea of the method's capability in qualitatively capturing the wake as demonstrated in Fig. A.8. Both results show a clearly defined leading-edge vortex above the wing and a trailing-edge vortex residing in the wake. However, the figures also reveal the fundamental difference in the vortices' representations: the viscous case exhibits vortices dispersed over a region of the flow field and the inviscid method idealizes the vortices as singular points in the flow.

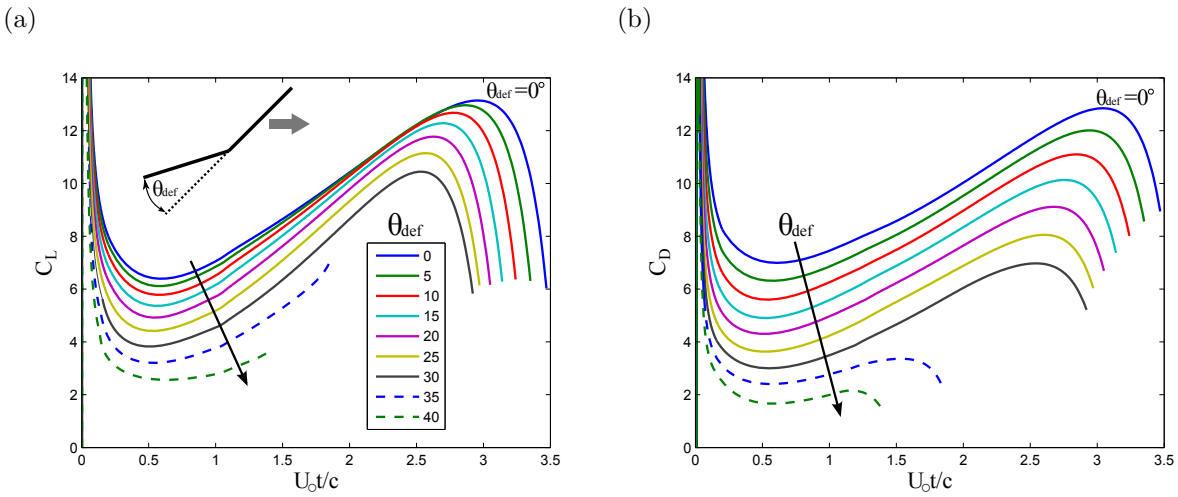

Figure A.6: Deflection angle effects on (a) lift and (b) drag of a wing translating at $\alpha = 45°$. Deflection is introduced midchord and is maintained at a constant value throughout translation.

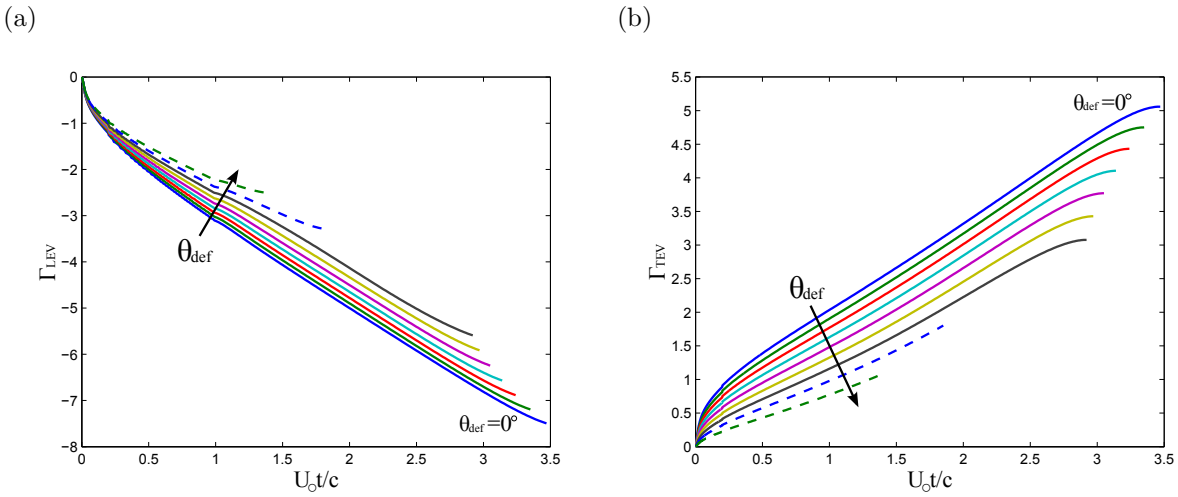

Figure A.7: Deflection angle effects on (a) leading-edge vortex circulation and (b) trailing-edge vortex circulation. Deflection is introduced midchord and is maintained at a constant value throughout translation.

(a) VVPM vorticity field (b) Brown-Michael streamfunctions

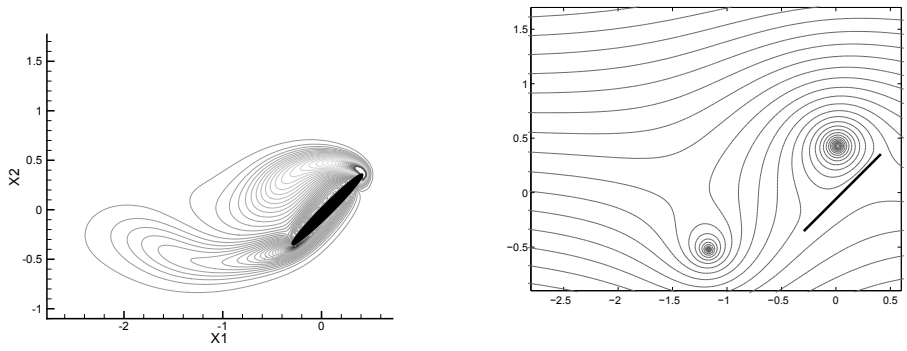

Figure A.8: Vortex representation in high fidelity (VVPM) and lower order modeling (Brown-Michael) at $\alpha = 45°$.

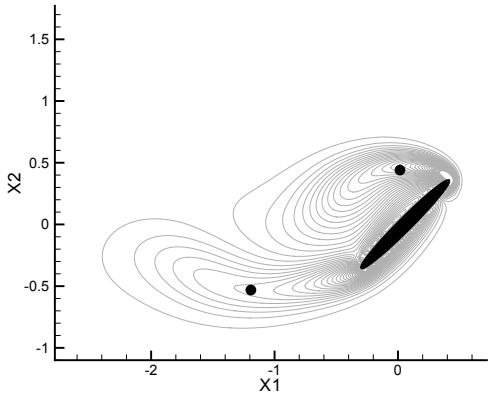

Figure A.9: Overlay of viscous wake with inviscid point vortices (•).

Results for lift and drag of the Brown-Michael model show a tendency to diverge from high fidelity results at Re = 100. Presented here is a flat plate undergoing sinusoidal translation for a fourth of a stroke at angle of attack $\alpha = 45°$. It seems the model has difficulty in preserving the physics to the extent desired for Reynolds number Re = 100. Higher Reynolds number may see better agreement, indicating Brown-Michael's model may be better suited for high *Re* flows. Additionally, because the model calls on shedding a point vortex from all edges of a given body in the flow, it is meant for applications at high angles of attack, α. In our experience, $\alpha \leq 35°$ was met with error. Despite the differences in resultant force

magnitudes, the lift-to-drag ratio of the model was also examined and found this ratio too experienced values exceeding those of the viscous case. The differences is most pronounced when acceleration is largest. As the plate approaches its maximum velocity, acceleration and the lift-to-drag difference is minimal.

(a) Lift (b) Lift-to-Drag ratio

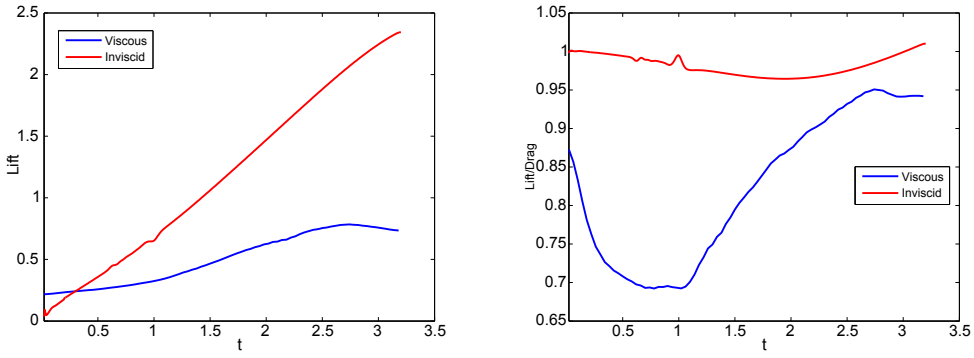

Figure A.10: Nondimensional force on a sinusoidally translating plate from rest in VVPM (blue) and Brown-Michael model (red) at $\alpha = 45°$.

In attempts to enduce von Karman street shedding from the plate it became apparent the method is problematic for long-time solutions. Despite angle of attack, trajectory, and speed of the plate, the leading-edge vortex often becomes artificially trapped above the plate such that it enduces shedding of the trailing-edge vortex. The problem then arrises with the releases of the new vortex from the trailing edge: under the influence of the leading-edge vortex, the TEV encounters the plate, resulting in a singularity. This does not render the method obsolete, but perhaps more suitable for short-time kinematics. It may prove more applicable to high speed perching maneuvers where shedding does not occur.

A.3.4 Vortex Shedding

As mentioned in Section A.3.2 and reflected in the chords traversed for various α Figure A.5 there seems to be a a direct link between the finite run time of simulation and the wing's orientation and thus the resulting wake vortices' strength and dynamics. Just as in a viscous sense, the wake vortices strength and dynamics are highly dependent on the

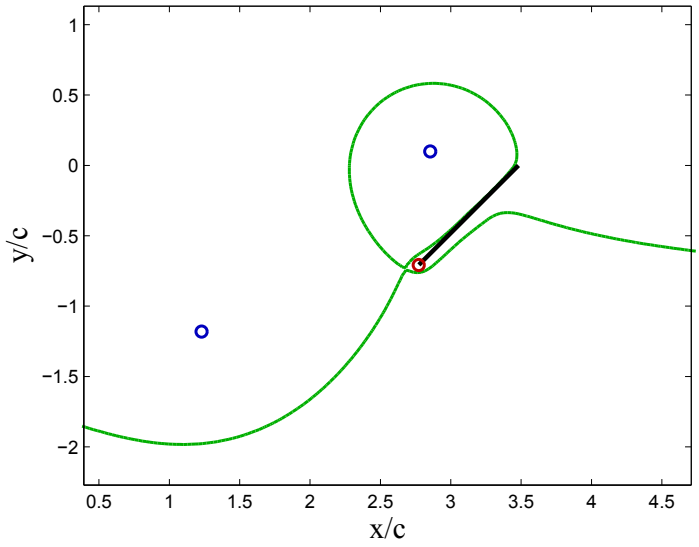

Figure A.11: Body streamline (——) at point of TEV shedding from trailing-edge of planar wing translating at $\alpha = 45°$. Initial wake vortices (○), newly shed vortex (○). The body streamline now encapsulates the leading-edge point vortex, extending from the wing leading-edge to the trailing-edge.

wing's orientation as they are fed by the wing edges via the Kutta condition. The sudden drop lift experienced by translating wings can be interpreted as vortex saturation, signifying the necessity to initiate shedding. It is here that the current method encounters the most difficulty.

Figure A.11 captures a translating wing at $\alpha = 45°$ at the point of shedding as stipulated by the initial trailing-edge vortex obtaining an extremum Γ_{TEV} value. The value of the initial TEV is now frozen, no longer fed by the trailing-edge and from the same edge a new vortex emanates. Isolating the body streamline contour reveals a streamline encapsulating the initial leading-edge vortex and extends from the wing leading-edge to the trailing-edge. And therein lies the problem. The body streamline re-encountering the trailing-edge and dictates the trajectory of the newly shed TEV to encounter the body and its representative point vortices, resulting in a singularity. Efforts to assign the new TEV an initial circulation value or an initial standoff distance from the trailing-edge upon release have done little

to offset the influence of the streamline in question and ultimately lack definitive selection criteria and remain arbitrary.

Wang and Eldredge (2012) would go on to develop a lower-order point vortex model where the motion and evolution of the variable-strength vortices is determined by equating the rate of change of its impulse with that of a surrogate vortex of identical properties but constant strength [104]. Their approach has afforded a more generalized shedding criteria since the variable-strength vortex can be exchanged with the constant-value surrogate vortex at any instant, no longer prompted by vortex extremum values. Ultimately, Wang and Eldredge demonstrated improved qualitative agreement in lift and drag trends between viscous and lower-order model results for perching and translating wings over that produced by the Brown-Michael equation.

References

[1] Internal Energy Agency. Ocean energy systems, status and research and development priorities 2003: Wave and marine current energy. 2003.

[2] S. Alben and M. Shelley. How flexibility induces streamlining in a two-dimensional flow. *Phys. Fluids*, 16:1694–1713, 2004.

[3] Silas Alben and Michael J. Shelley. Flapping states of flag in an inviscid fluid: bistability and the transition to chaos. *Phys. Rev. Lett.*, 100:074301, 2008.

[4] J. J. Allen and A. J. Smits. Energy harvesting eel. *Journal of Fluids and Structures*, 15:629–640, 2001.

[5] A. Anderson, U. Pesavento, and Z. J. Wang. Analysis of transitions between fluttering and tumbling and steady descent of falling cards. *J. Fluid Mech.*, 541:91–104, 2005.

[6] S. A. Ansari, R. Zbikowski, and K. Knowles. Non-linear unsteady aerodynamic model for insect-like flapping wings in the hover. part 1: methodoloty and analysis. *Proc. IMechE Part G J. Aerosp. Eng.*, 220:61–83, 2006.

[7] A. J. Bergou, X. Xu, and Z. J. Wang. Passive wing pitch reversal in insect flight. *J. Fluid Mech.*, 591:321–337, 2007.

[8] Attila J. Bergou, Leif Ristroph, John Guckenheimer, Itai Cohen, and Z. Jane Wang. Fruit flies modulate passive wing pitching to generate in-flight turns. *Phys. Rev. Lett.*, 104, 2010.

[9] G. J. Berman and J. Z. Wang. Energy-minimizing kinematics in hovering insect flight. *J. Fluid Mech.*, 582:153–168, 2007.

[10] Michael M. Bernitsas, Kamaldev Raghavan, Y. Ben-Simon, and E. M. H. Garcia. Vivace: A new concept in generation of clean and renewable energy from fluid flow. *J. Offshore Mech. Arct. Eng.*, 130, 2008.

[11] J. M. Birch and M. H. Dickinson. Spanwise flow and the attachment of the leading edge vortex on insect flight. *Nature*, 412:729–733, 2001.

[12] J. M. Birch and M. H. Dickinson. The influence of wing-wake interactions on the production of aerodynamic forces in flapping flight. *J. Exp. Biol.*, 206:2257–2272, 2003.

[13] M. Bozkurttas, R. Mittal, H. Dong, G. V. Lauder, and P. Madden. Low dimensional models and performance scaling of a highly deformable fish pectoral fin. *J. Fluid Mech.*, 631:311–342, 2009.

[14] S. L. Brunton and C. W. Rowley. Modeling the unsteady aerodynamic forces on small scale wings. In *47th AIAA Aerospace Sciences Meeting, January 2009*, number 2009-1127, 2009.

[15] Jinsheng Cai, Shijun Luo, and Feng Liu. Stability of symmetric and asymmetric vortices over slender conical wing-body combinations. *AIAA Journal*, 44(7):1601–1608, 2006.

[16] K. K. Chen, T. Colonius, and K. Taira. The leading-edge vortex and quasi-steady shedding on an accelerating plate. *Phys. Fluids*, 22, 2010.

[17] S. A. Combes and T. L. Daniel. Flexural stiffness in insect wings: I. scaling and the influence of wing venation. *J. Exp. Biol.*, 206:2979–2987, 2003.

[18] S. A. Combes and T. L. Daniel. Flexural stiffness in insect wings: Ii. spatial distribution and dynamic wing bending. *J. Exp. Biol.*, 206:2989–2997, 2003.

[19] S. A. Combes and T. L. Daniel. Flexural stiffness in insect wings: effects of wing venation and stiffness distribution on passive bending. *American Entomologist*, 51(1):42–44, 2005.

[20] T. L. Daniel and S. A. Combes. Flexible wings and fins: bending by inertial or fluid-dynamic forces. *Interg. Comp. Biol.*, 42:1044–1049, 2002.

[21] S. C. R. Dennis, Wang Qiang, M. Coutanceau, and J.-L. Launay. Viscous flow normal to a flat plate at moderate reynolds numbers. *J. Fluid Mech.*, 248:605–635, 1993.

[22] M. H. Dickinson, F. O. Lehmann, and S. P. Sane. Wing rotation and the aerodynamic basis of insect flight. *Science*, 248:1954–1960, 1999.

[23] Michael H. Dickinson. Unsteady mechanisms of force generation in aquatic and aerial locomotion. *Amer. Zool.*, 36:537–554, 1996.

[24] Michael H. Dickinson and Karl G. Gotz. Unsteady aerodynamic performance of model wings at low reynolds number. *J. Exp. Biol.*, 174:45–65, 1993.

[25] W. B. Dickson and M. H. Dickinson. The effect of advance ratio on the aerodynamics of revolving wings. *J. Exp. Biol.*, 207:4269–4281, 2004.

[26] G. Du and M. Sun. Aerodynamic effects of corrugation and deformation in flapping wings and hovering hoverflies. *J. Theor. Biol.*, 300:19–28, 2012.

[27] R. H. Edwards and H. K. Cheng. The separation vortex in weis-fogh circulation-generation mechanism. *J. Fluid Mech.*, 120:463–473, 1982.

[28] J. D. Eldredge. Numerical simulation of the fluid dynamics of 2d rigid body motion with the vortex particle method. *J. Comput. Phys.*, 221(626), 2007.

[29] J. D. Eldredge. Dynamically coupled fluid-body interactions in vorticity-based numerical simulations. *J. Comput. Phys.*, 227:9170–9194, 2008.

[30] J. D. Eldredge, T. Colonius, and A. Leonard. A vortex method for 2d compressible flow. 2001.

[31] Jeff D. Eldredge, Chengjie Wang, and Michael Ol. A computational study of a canonical pitch-up, pitch-down, wing maneuver. *AIAA*, pages 2009–3687, 2009.

[32] A. R. Ennos. Mechanical behaviour in torsion of insect wings, blades of grass and other cambered structures. *Proceedings: Biological Sciences*, 259(1354):15–18, 1995.

[33] A. Roland Ennos and Robin J. Wootton. Functional wing morphology and aerodynamics of panorpa germanica (insecta: mecoptera). *J. Exp. Biol.*, 143:267–284, 1989.

[34] S. N. Fry, R. Sayaman, and M. H. Dickinson. The aerodynamics of hovering flight in drosophila. *J. Exp. Biol.*, 208:2303–2318, 2005.

[35] D. Garmann, M. Visbal, and P. Orkwis. Three-dimensional flow structure and aerodynamic loading on a low aspect ratio, revolving wing. In *42nd AIAA fluid dynamics conference and exhibit, 2012-3277*, pages 1–22, 2012.

[36] Daniel J. Garmann and Miguel R. Visbal. Investigation of aspect ratio and dynamic effects due to rotation for a revolving wing using high-fidelity simulations.

[37] S. A. L. GLegg, W. J. Devenport, and N. Spitz. Application of proper orthogonal decomposition of trailing edge noise. *AIAA Journal*, 47(6):1543–1548.

[38] L. Graftieaux, M. Michard, and N. Grosjean. Combining piv, pod and vortex identification algorithms for the study of unsteady turbulent swirling flows. *Meas. Sci. Technol.*, 12:1422–1429, 2001.

[39] K. Granlund, M. Ol, and L. Bernal. Experiments on free-to-pivot hover motions of multi-hinged flat plates. In *AIAA Atmospheric Flight Mechanics Conference, 08-11 August 2011, Portland, Oregon*, 2011.

[40] K. Granlund, M. Ol, L. Bernal, and S. Kast. Experiments on free-to-pivot hover motions of flat plates. In *40th Fluid Dynamics Conference and Exhibit 28 June-1 July 2010, Chicago, Illinois*, 2010.

[41] D. I. Greenwell. Simple engineering model for delta-wing vortex breakdown. *J. Aircraft*, 40:402–405, 2002.

[42] S. Heathcote and I. Gursul. Flexible flapping airfoil propulsion at low reynolds numbers. In *43rd AIAA Aerospace Sciences Meeting and Exhibit*, 2005.

[43] T. Y. Hou, V. G. Stredie, and T. Y. Wu. A 3d numerical method for studying vortex formation behind a moving plate. *Commun. Comput. Phys.*, 1(2):207–228, 2006.

[44] M. S. Howe. Emendation of the brown-michael equation with application to sound generation by vortex motion near a half-plane. *J. Fluid Mech.*, 329:89–101, 1996.

[45] Marcus Hultmark, Megan Leftwich, and Alexander J. Smits. Flowfield measurements in the wake of a robotic lamprey. *Exp. Fluids*, 43:683–690, 2007.

[46] D. Hummel. Aerodynamic aspects of formation flight in birds. *J. Theor. Biol.*, 104:321–347, 1983.

[47] D. B. Ingham and T. Tang. Steady two-dimensional flow past a normal flat plate. *Journal of Applied Mathematics and Physics*, 42:584–604, 1991.

[48] D. B. Ingham, T. Tang, and B. R. Morton. Steady two-dimensional flow through a row of normal flat plates. *J. Fluid Mech.*, 210:281–302, 1990.

[49] J. Toomey J. D. Eldredge and A. Medina. On the roles of chord-wise flexibility in a flapping wing with hovering kinematics. *J. Fluid Mech.*, 659:94–115, 2010.

[50] T. Jardin, A. Farcry, and L. David. Three-dimensional effects in hovering flapping flight. *J. Fluid Mech.*, 702:102–125, 2012.

[51] J. Jeong and F. Hussain. On the identification of a vortex. *J. Fluid Mech.*, 285:69–94, 1995.

[52] M. A. Jones. The separated flow of an inviscid fluid around a moving flat plate. *J. Fluid Mech.*, 496:405–441, 2003.

[53] E. Kanso, J. E. Marsdon, C. W. Rowley, and J. B. Melli-Huber. Locomotion and articulated bodies in a perfect fluid. *J. Nonlinear Sci.*, 15:255–289, 2005.

[54] B. C. Khoo, K. S. Yeo, D. F. Lim, and X. He. Vortex breakdown in an unconfined vortical flow. *Expt. Thermal Fluid Sci.*, 14:131–148, 1997.

[55] H. Kikitsu, Y. Okuda, M. Ohashi, and J. Kanda. Pod analysis of wind velocity field in the wake region behind vibrating three dimensional square prism. *J. Wind Engineering and Industrial Aerodynamics*, 96:2093–2103, 2008.

[56] D. Kim and H. Choi. Immersed boundary method for flow around an arbitrarily moving body. *J. Comp. Phys.*, 212:662–680, 2005.

[57] Dokyun Kim and Haecheon Choi. Immersed boundary method for flow around an arbitrarily moving body. *J. Comput. Phys.*, 212:662–680, 2005.

[58] J. Kim, D. Kim, and H. Choi. Immersed-boundary finite-volume method simulations of flow in complex geometries. *J. Comp. Phys.*, 139:132–150, 2001.

[59] Jungwoo Kim, Dongjoo Kim, and Haecheon Choi. An immersed-boundary finite-volume method for simulations of flow in complex geometries. *J. Comput. Phys.*, 171:132–150, 2001.

[60] T. Kinsey and G. Dumas. Parametric study of an oscillating airfoil in a power-extraction regime. *AIAA Journal*, 46:1318–1330, 2008.

[61] Christopher Koehler, Zongxian Liang, Zachary Gaston, Hui Wan, and Haibo Dong. 3d reconstruction and analysis of wing deformation in free-flying dragonflies. *J. Exp. Biol.*, 215:3018–3027, 2012.

[62] Alexandr I. Korotkin. *Added mass of ship structures*. Springer, 2009.

[63] J. Kweon and H. Choi. Sectional life coefficient of a flapping wing in hovering motion. *Phys. Fluids*, 22, 2010.

[64] Fritz-Olaf Lehmann. The mechanisms of lift enhancement in insect flight. *Naturwissenschaften*, 91:101–122, 2004.

[65] Fritz-Olaf Lehmann. When wings touch wakes: understanding locomotor force control by wake-wing interference in insect wings. *J. Exp. Biol.*, 211:224–233, 2007.

[66] Fritz-Olaf Lehmann. Wing-wake interaction reduces power consumption in insect tandem wings. *Exp. Fluids*, 46:765–775, 2009.

[67] D. Lentick and M. H. Dickinson. Biofluiddynamic scaling of flapping, spinning and translating fins and wings. *J. Exp. Biol.*, 212:2691–2704, 2009.

[68] David Lentick and Michael H. Dickinson. Rotational accelerations stabilize leading edge vortices on revolving fly wings. *J. Exp. Biol.*, 212:2705–2719, 2009.

[69] Y. C. Liang, H. P. Lee, K. H. Lim, W. Z. Lin, K. H. Lee, and C. G. Wu. Proper orthogonal decomposition and its applications - part i: theory. *J. Sound Vib.*, 252(3):527–544, 2002.

[70] Hao Liu, Charles P. Ellington, Keiji Kawachi, Coen van den Berg, and Alexander P. Willmott. A computational fluid dynamic study of hawkmoth hovering. *J. Exp. Biol.*, 201:461–477, 1998.

[71] S. Michelin and S. G. L. Smith. An unsteady point vortex method for coupled fluid-solid problems. *Theor. Comput. Fluid Dyn.*, 23:127–153, 2009.

[72] D. Mueller, H. A. Bruck, and S. K. Gupta. Measurement of thrust and lift forces associated with drag of compliant flapping wing for micro air vehicles using a new test stand design. *Experimental Mechanics*, 2009.

[73] Jonathan A. Muse, Andrew A. Tchieu, Ali T. Kutay, Rajeev Chandramohan, Anthony J. Calise, and ANthony Leonard. Vortex model based adaptive flight control using synthetic jets. In *AIAA Guidance, Navigation, and Control Conference*, 2009.

[74] S. Nair and E. Kanso. Hydrodynamically coupled rigid bodies. *J. Fluid Mech.*, 592:393–411, 2007.

[75] R. Ake Norberg. The pterostigma of insect wings an inertial regulator of wing pitch. *J. Comp. Physiol.*, 81:9–22, 1972.

[76] B. J. O'Donnell and B. T. Helenbrook. Proper orthogonal decomposition and incompressible flow: an application to particle modeling. *Computers and fluids*, 36:1174–1186, 2006.

[77] C. A. Ozen and D. Rockwell. Flow structure on a rotating plate. *Exp. Fluids*, 52:207–223, 2012.

[78] Z. Peng and Q. Zhu. Energy harvesting through flow-induced oscillations of a foil. *Phys. Fluids*, 21:123602–123602–9, 2009.

[79] U. Pesavento and Z. J. Wang. Falling paper: Navier-stokes solutions, model of fluid forces, and center of mass evaluation. *Phys. Rev. Lett.*, 93, 2004.

[80] Umberto Pesavento and Z. Jane Wang. Flapping wing flight can save aerodynamic power compared to steady flight. *Phys. Rev. Lett.*, 103, 2009.

[81] C. Poelma, W. B. Dickson, and M. H. Dickinson. Time-resolved reconstruction of the full velocity field around a dynamically-scaled flapping wing. *Exp. Fluids*, 41:213–225, 2006.

[82] D. I. Pullin and Z. J. Wang. Unsteady forces on an accelerating plate and application to hovering insect flight. *J. Fluid Mech.*, 209:1–21, 2004.

[83] D. Rempfer. On low-dimensional galerkin models for fluid flow. *Theor. Comput. Fluid Dyn.*, 14:75–88, 2000.

[84] M. Ringuette, M. Milano, and M. Gharib. Role of the tip vortex in the force generation of low-aspect-ratio normal flat plates. *J. Fluid Mech.*, 581:453–468, 2007.

[85] M. Ringuette, M. Milano, and M. Gharib. Role of the tip vortex in the force generation of low-aspect-ratio normal flat plates. *J. Fluid Mech.*, 581:453–468, 2007.

[86] Leif Ristroph, Gordon J. Berman, Attila J. Bergou, Z. Jane Wang, and Itai Cohen. Automated hull reconstruction motion tracking (hrmt) applied to sideways maneuvers of free-flying insects. *J. Exp. Biology*, 212:1324–1335, 2009.

[87] David E. Rival, Jochen Kriegseis, Pascal Schaub, Alexander Windmann, and Cameron Tropea. A criterion for vortex separation on unsteady aerodynamic profiles. In *51st AIAA Aerospace Sciences Meeting including New Horizons Forum and Aerospace Exposition 07-10 January 2013, Grapevine (Dallas/Ft. Worth Region), Texas*, 2013.

[88] C. W. Rowley, T. Colonius, and R. M. Murray. Model reduction for compressible flows using pod and galerkin projection. *Physica D*, 189:115–129, 2003.

[89] M. Rutten and H. G. Pagendarm. Fast vortex axis calculation suing vortex features and identification algorithms. In *Bonneau, G. P. and Ertl, T. and Nielson, G. M. (Eds.), Scientific visualization: the visual extraction of knowledge from data*. Springer, Berlin, 2006.

[90] Sanjay P. Sane and Michael H. Dickinson. The control of flight force by a flapping wing: lift and drag production. *J. Exp. Biol.*, 204:2607–2626, 2001.

[91] Kristy Schlueter and Anya R. Jones. Force coefficients of low reynolds number rotating wings.

[92] J. K. Shang, S. A. Combes, B. M. Finio, and R. J. Wood. Artificial insect wings of diverse morphology for flapping-wing micro air vehicles. *Bioinsp. Biomim.*, 4, 2009.

[93] R. K. Shukla and J. D. Eldredge. An inviscid model for vortex shedding from a deforming body. *Theor. Comput. Fluid Dyn.*, 21:343–368, 2007.

[94] M. Sun and J. Tang. Lift and power requirements of hovering flight in drosophila virilis. *J. Exp. Biol.*, 205:2413–2427, 2002.

[95] Kunihiko Taira and Tim Colonius. Three-dimensional flows around low-aspect ratio flat-plate wings at low reynolds numbers. *J. Fluid Mech.*, 623:187–207, 2009.

[96] Kunihiko Taira, William B. Dickson, Tim Colonius, Michael H. Dickinson, and Clarence W. Rowley. Unsteadiness in flow over a flat plate at angle-of-attack at low reynolds numbers. In *45th AIAA Aerospace Sciences Meeting and Exhibit*, 2007.

[97] H. Tanaka and I. Shimoyama. Forward flight of shallowtail butterfly with simple flapping motion. *Bioinsp. Biomim.*, 5(2), 2010.

[98] A. A. Tchieu, A. T. Kutay, J. A. Muse, A. J. Calise, and A. Leonard. Validation of a low-order model for closed-loop flow control enable flight. In *AIAA 4th Flow Control Conference*, 2008.

[99] T. Theodorsen. General theory of aerodynamic instability and the mechanism of flutter. *Report National Advisory Committee for Aeronautics*, (496):291–311.

[100] Jonathan Toomey and Jeff D. Eldredge. Numerical and experimental study of the fluid dynamics of a flapping wing with low order flexibility. *Phys. Fluids*, 20, 2008.

[101] C. van den Berg and C. P. Ellington. The three-dimensional leading-edge vortex of a hovering model hawkmoth. *Philosophical Transactions: Biological Sciences*, 352(1351):329–340, 1997.

[102] M. Vanella, T. Fitzgerald, S. Preidikman, E. Balaras, and B. Balachandran. Influence of flexibility on the aerodynamic performance of a hovering wing. *J. Exp. Biol.*, 212:95–105, 2009.

[103] S. M. Walker, A. L. R. Thomas, and G. K. Taylor. Deformable win kinematics in free-flying hoverflies. *J. R. Soc. Interface*, 7:131–142, 2010.

[104] Chengjie Wang and Jeff D. Eldredge. Lower-order phenomenological modeling of leading-edge vortex formation. *Theor. Comput. Fluid Dyn.*, pages 1–22, 2012.

[105] Z. J. Wang. Two dimensional mechanism for insect hovering. *Phys. Rev. Lett.*, 18:2216–2219, 2000.

[106] Z. J. Wang. Vortex shedding and frequency selection in flapping flight. *J. Fluid Mech.*, 410:323–341, 2000.

[107] Z. J. Wang, J. M. Birch, and M. H. Dickinson. Unsteady forces and flows in low reynolds number hovering flight: two-dimensional computations vs robotic wing experiments. *J. Exp. Biol.*, 207:449–460, 2004.

[108] Z. Jane Wang. Aerodynamaic efficiency of flapping flight: analysis of a two-stroke model. *J. Exp. Biol.*, 211:234–238, 2007.

[109] J.P. Whitney and R.J. Wood. Aeromechanics of passive rotation in flapping flight. *J. Fluid Mech.*, 660:197–220, 2010.

[110] C. H. K. Williamson and A. Roshko. Vortex formation in the wake of an oscillating cylinder. *Journal of Fluids and Structures*, 2:355–381, 1988.

[111] R. J. Wootton, R. C. Herbert, P. G. Young, and K. E. Evans. Approaches to the structural modelling of insect wings. *The Royal Society*, 358:1577–1587, 2003.

[112] Robin J. Wootton. Function, homology and terminology in insect wings. *Sys. Entomol.*, 4:81–93, 1979.

[113] Robin J. Wootton. Functional morphology of insect wings. *Annu. Rev. Entomol.*, 37:113–140, 1992.

[114] Robin J. Wootton. Geometry and mechanics of insect hindwing fans: A modeling approach. *Proceedings: Biological Sciences*, 262(1364):181–187, 1995.

[115] Jianghao Wu and Mao Sun. The influence of the wake of a flapping wing on the production of aerodynamic forces. *Acta Mech Sin.*, 21:411–418, 2005.

[116] Yao-Tsu T. Wu. Hydromechanics fo swimming propulsion. part 1. swimming of a two-dimensional flexible plate at variable speeds in an inviscid fluid. *J. Fluid Mech.*, 46:337–355, 1971.

[117] J. Young, S. M. Walker, R. J. Bomphrey, G. K. Taylor, and L. R. Thomas. Details of insect wing design and deformation enhance aerodynamic function and flight efficiency. *Science*, 325:1549–1552, 2009.

[118] L. J. Zhang and J. D. Eldredge. A viscous vortex particle method for deforming bodies, with application to biolocomotion. *Int. J. Numer. Meth. Fluids*, 59:1299–1320, 2008.